Stiffness Characterization of Mechanically-Compressed Cohesive Soils Using Wave Propagation

by

Jana Marjanovic

S.B. in Civil and Environmental Engineering, Massachusetts Institute of Technology (2010)
S.M. in Civil and Environmental Engineering, Massachusetts Institute of Technology (2012)

Submitted to the Department of Civil and Environmental Engineering
in partial fulfillment of the requirements for the degree of

Doctor of Philosophy in Geotechnical and Geoenvironmental Engineering

at the

MASSACHUSETTS INSTITUTE OF TECHNOLOGY

February 2016

Signature redacted

Author .....
Department of Civil and Environmental Engineering
December 29, 2015

Signature redacted

Certified by .....
John T. Germaine
Research Professor, Tufts University
Thesis Supervisor

Signature redacted

Accepted by .....
Heidi M. Nepf
Donald and Martha Harleman Professor of Civil and Environmental Engineering,
Chair, Graduate Program Committee

Stiffness Characterization of Mechanically-Compressed Cohesive Soils Using Wave Propagation

by

Jana Marjanovic

Submitted to the Department of Civil and Environmental Engineering
on December 29, 2015, in partial fulfillment of the
requirements for the degree of
Doctor of Philosophy in Geotechnical and Geoenvironmental Engineering

Abstract

Wave propagation through soils is a non-destructive method used to characterize soil stiffness properties and is the basis for geophysical interpretations. Due to the difficulty of measuring shear waves through soft cohesive soils with ultrasonic transducers, bender elements are typically used, which couple to the soft clay. Unfortunately, the stress limitation of bender elements precludes it from testing above 1.5 MPa. A novel setup using ultrasonic transducers, with electronic conditioning, is developed in order to overcome the difficulties of transmitting a shear wave through a soft material. The successful fabrication of triaxial cell endcaps fitted with ultrasonic piezoceramic elements has enabled the measurement of compressional and shear wave velocity of clays over a wide stress range (0.5 - 10 MPa). This research compares the shear modulus measurements using three different technologies that encompass a stress range of 0.1 to 70 MPa.

A variety of resedimented materials and plasticities are tested in order to characterize the V_p and V_s as a function of stress during K_0-consolidation. Resedimentation creates controlled, uniform specimens whose results can develop a backbone for velocity behavior independent of field heterogeneities and disturbance. The V_p and V_s results show different trends as a function of stress for the different plasticity materials. However, the V_p/V_s ratio, which is a common indicator of unloading and lithology, has a strong dependence on the liquid limit (w_L). A model is developed to predict the V_p/V_s as a function of stress for a given w_L.

In addition to K_0 loading, the effects of unloading are investigated. Unloading introduces secondary compression, which significantly alters the stiffness results. A method is developed to integrate the secondary compression data with normally consolidated data based on the concept of apparent preconsolidation pressure.

Finally, the dynamically-obtained stiffness parameters are compared to statically-obtained constrained modulus values from static compression. By using Gassmann's fluid substitution and a corrective X factor, a new technique is developed that can predict the dynamic bulk modulus based on the static CRS measurements.

Thesis Supervisor: John T. Germaine
Title: Research Professor, Tufts University

Acknowledgments

There are many people I would like to thank, but can't possibly name them all, so these are a select few.

I am extremely grateful to have had an advisor and mentor like Prof. Jack Germaine, or dearly referred to as Dr. G. Without the continuous support in the lab, as well as the encouragement and positive feedback, this journey would have been a lot more painful. His cynical humor always brightened up my day. I would like to thank the rest of my committee, including Prof. Herbert Einstein, Prof. Alison Malcolm, and Dr. Ronny Hofmann. Their support and advice was invaluable. I cannot leave out Steve Rudolph, who spent so many hours with me, designing and fabricating my experimental equipment.

In addition to the MIT community, I need to acknowledge the folks at UT Austin, led by Prof. Peter Flemings. Being part of the UT Geofluids team has exposed me to industry members and has taught me how to effectively communicate with the technical community.

Some of the testing in this thesis was performed at Shell E&P. I would like to thank the rock testing team at the Westhollow location in Houston, in particular Ronny for inviting me to do the tests, and Jorge for being patient with me and executing the tests.

I was supported by the Department of Defense (DoD) through the National Defense Science & Engineering Graduate Fellowship (NDSEG) Program. Other support was provided by UT Geofluids Consortium.

Over the many, many years I've spent at MIT, different friends have come and gone. The range of people has changed tremendously. Special acknowledgment much be given to those first few, that helped me in my first years in the lab: Amy, Aiden, and Brendan. Most recently, Amer has struggled through these last few years with me, dealing with the "change", and moving our labs to Tufts.

Outside of my departmental friends, I would like to thank Dave for being a pretty cool roommate, always being super considerate. Another thanks goes out to Jon, for always being down to hang out, and of course having the birthday party that led me to Brian.

Finally, I need to profusely thank my family: MOM, DAD, Nikola & Katie, and my future in-laws Sandy, Eric, and Erica Pearson. Lastly, my future husband – Brian, your unconditional love and support, as well as your ability to perk me up any time I'm feeling down, has meant so much to me. I am truly excited about our future.

Contents

List of Figures

List of Tables

Chapter 1

Introduction

1.1 Problem Statement

Clay stiffness properties have been widely tested in the geotechnical field. Many different techniques are utilized, ranging from destructive static tests like torsional shear experiments, to dynamic non-destructive tests using bender elements. These tests are usually limited to the stress regime pertaining to practical geotechnical engineering practice, up to 1 MPa. On the other hand, considerable research has been performed in the high stress regime on sand and rock samples using wave propagation with ultrasonic transducers, from 1 MPa and higher. Few studies exist that investigate the stiffness behavior of fine-grained, unlithified clays above 1 MPa. It is necessary to characterize the compressional and shear wave velocity for a variety of clays over a wide stress range and different loading conditions. The velocities depend on the elastic stiffness of the materials, thus rendering velocities a useful parameter in the stiffness characterization of soils. With an understanding of how the elastic stiffness of clays varies as a function of type, stress, and loading conditions, the small strain stiffness behavior can be predicted, with applications to subsurface construction projects. Furthermore, the stress-velocity-porosity characterization can facilitate safer well designs and improve seismic imaging interpretations.

The major challenge with measuring velocity through soft clays beyond 1 MPa is the difficulty in obtaining a signal – the high impedance contrast between the

piezomaterial adjacent to the soft soil inhibits energy transfer. In order to obtain a continuous velocity curve for a clay from 0.1 to 100 MPa, we use three different experimental setups: 1) low stress bender elements that are inserted orthogonally into the clay and have excellent coupling, 2) medium stress piezoceramic elements embedded in endcaps that sit flush to the specimen, and 3) high stress piezoceramic elements specialized to overcome the decay in vibration at the upper stress range.

Velocity behavior through clay is not well understood. The upper 5 km of the Earth's crust is primarily hard, lightly lithified or unlithified clays, with the smectite-to-illite transition occurring at a depth of 1 - 4 km (Freed and Peacor, 1989b), and many basins at these depths are smectite/illite dominated (Alberty et al., 2003). Drilling through a material whose behavior is unknown can be problematic, incurring failures such as well collapse or mechanical failures. Thus there exists a need to ameliorate this void in understanding.

The overall goal of this research is to develop the technology that enables wave propagation through soils over the medium stress range of 1 - 10 MPa. This work aims to populate the P and S-wave velocity behavior for a variety of clays in this stress range in order to provide some insight into clay behavior that can be applied to clay-rich oil reservoirs.

1.2 Scope and Objectives

The primary focus of this research is to fulfill the aforementioned need in understanding velocity behavior in clay through a detailed experimental program using resedimented specimens.

The first, and possibly most critical, objective is to develop the hardware and protocols to enable separate evaluation of velocity during K_0-consolidation and swelling in the medium stress range. The technological challenges of achieving an interpretable signal for a shear wave through clay cannot be underestimated. Furthermore, to incorporate this into a standard triaxial cell capable of fine-tuned controls renders this piece of technology valuable for many applications, including velocity testing while

shearing in compression and extension. The development of a velocity-enabled triaxial cell, in conjunction with using resedimented clay samples, allows the user to isolate a single parameter and observe the subsequent effect on velocity.

The second major objective is to build a database of velocity results for a variety of clays. By using a range of plasticities, we can observe the mineralogical effect on velocity measurements. Furthermore, by performing unloading cycles in addition to K_0-consolidation, the stiffness reduction as a function of overconsolidation ratio (OCR) and maximum past stress is analyzed. In addition to the medium stress level, the low and high stress levels are included from different experimental techniques in order to compare the feasibility of stitching together velocity results across a continuous stress range from 0.1 - 100 MPa. Moreover, static testing methods are compared to the dynamic velocity tests. A methodology of relating the drained static compression test to the dynamic velocity test is established.

The final object of this thesis is to describe the velocity behavior by creating a predictive model for the velocity-stress behavior in a variety of clay types.

This work is part of the UT Geofluids Consortium, populated with members from Tufts University (formerly MIT) and UT Austin. This consortium provides a wide breadth of data on all the materials tested in this research, focusing on the "evolution of pressure, stress, deformation and fluid migration through experiment, models, and field study".

1.3 Organization of Thesis

The content of each chapter is this thesis is briefly described as follows:

Chapter 2 provides background on the topic of wave propagation through soils. The general motivations for this research are included, as well as an elementary introduction to velocity calculations and stiffness parameters. Furthermore, and extensive investigation into the literature is performed to validate the novelty of this research, including both wave propagation techniques and other static measurement techniques. A concise introduction to the clay microstructure gives the reader a better

understanding of the behavior of clays, followed by a description of the many different fitting techniques that have been previously used to characterize velocity and stiffness behavior in soils and rocks.

Chapter 3 outlines the soils tested, including all the parameters available describing their behavior, including index values, permeability, mineralogy, Cation Exchange Capacity (CEC), Specific Surface Area (SSA), and grain size distributions. Since resedimentation is extensively used in this research, a detailed account of the procedure is included. The experimental setup and procedures are described to the point where the reader can replicate the test, including the fabrication of the velocity endcaps.

Due to the extensive difficulties experienced with electronics and signal conditioning, Chapter 4 examines which factors are important for obtaining clear digital signals, and reports the exact setup used in this thesis.

Chapter 5 firstly introduces the signal interpretation methods, and an error analysis of the results. This is followed by a description of the compression behavior for all materials tested, and the velocity results as a function of vertical effective stress. Many different permutations of the velocity results are presented, including modulus values, velocity as a function of density and porosity, and the V_p/V_s and Poisson's ratio. A model is developed based on the liquid limit that predicts the V_p/V_s ratio as a function of vertical effective stress. Finally, the chapter is concluded with a look at the creep and unloading behavior of clays.

Chapter 6 explains the interpretations of the results, including links to the plasticity and microstructure. A few fitting techniques are selected and applied to the velocity and modulus results, assessing their merit. The velocity results from this thesis are also compared to other published results, drawing conclusions from their relative agreement. A comparison of the velocity-derived modulus values with drained, static modulus values leads to the development of a methodology that links the two.

Chapter 7 summarizes the need for this research and the key findings. Ideas that should be considered for future work are enumerated.

Chapter 2

Background

2.1 Introduction

The stiffness behavior of soils and rocks has been extensively tested using many different techniques. Soft soils have been tested using both destructive and nondestructive methods, including triaxial, torsional shear, resonant column and bender element testing. Alternatively hard materials such as rocks have been primarily tested using wave propagation, in particular using ultrasonic transducers. All these testing methods and their strain levels are listed in Table 2.1. The geotechnical field has tested the soft, low-stress regime, while the geophysics field has tested the hard, high-stress regime. Although there are some studies that have compared different testing techniques, such as Brignoli et al. (1996), Nishimura (2005), Abdulhadi and Barghouthi (2012), Valle-Molina (2006), and Yamashita et al. (2004), there have been no studies that bridge the two fields and cover a wide range of stresses, as well as a wide range of materials with different plasticities.

This chapter aims at introducing the topic of velocity testing through clays, the different testing techniques and attempts at comparing them, as well as previous studies analyzing the velocity data.

Section 2.2 discusses some of the motivations for this thesis, followed by Section 2.3, which talks about the background of velocity testing in general and how it has been historically performed. Section 2.4 briefly reviews the compression behavior

of clays. Section 2.5 begins to introduce some of the previous experimental studies carried out on different materials using ultrasonic transducers, the main technology used in this thesis. After introducing other studies using the same instrumentation, other methods of obtaining velocity or stiffness parameters of soils are described, as well as some experimental results in Section 2.6. In Section 2.7, the topics of attenuation and dispersion are introduced, as well as the effects they potentially have on the velocity results. In order to understand the velocity behavior presented in this thesis, a discussion of the clay microstructure is necessary, thus an overview of the current knowledge of clay microstructure and possible effects it has on the stiffness of clay is included in Section 2.8. Finally, in Section 2.9, various fitting methods are presented, including empirical and theoretical models that are used as predictive tools in industry. With a better understanding of the current state of research on this topic, the significance of this research is highlighted.

2.2 Motivations

Observing the velocity (and elastic modulus) behaviors in soils has been a topic of interest for many fields, including the geotechnical field with its application to soil behavior and infrastructure design (Wair et al., 2012), the geophysics field for more accurate seismic imaging (Claerbout and Green, 2008), and the oil industry for the purpose of interpreting velocity results in their drilling operations (Ebrom et al., 2002).

Measuring the small strain stiffness properties of soils is a primary interest for the geotechnical field in order to predict ground movements during construction projects. The elastic parameters of the soil, most notably the small strain shear modulus (G_{max}), allows the engineer to predict soil movements around structures in deep excavations, especially in urban environments with a high density of adjacent complex structures (Santagata, 1998). With a better comprehensive understanding of the evolution of stiffness with stress and stress history allows for a more comprehensive soil characterization, aiding in an accurate assessment of geomaterial performance

and stability. There has historically been a discrepancy between the stiffness parameters observed in the lab and field, with the lab data underestimating the stiffness of the soil. Although traditionally attributed to sampling disturbance (Lambe and Whitman, 1969), the strain softening effect is considered one of the primary drivers of the difference (Shibuya, 2000). For this thesis, only techniques with extremely low strains were used, far below the 0.0001% strain level.

Velocity measurements have been a key component in predicting the subsurface composition of the Earth. Seismic imaging techniques enable a rather detailed depiction of the subsurface profile based on multiple wave sources and many staggered acoustic receivers or geophones. The interpretation of the signals acquired by receivers can be greatly altered with an incorrect interpretation or assumption, such as an incorrect V_p/V_s ratio[1], or not accounting for anisotropy. In fact, the V_p/V_s ratio is often used as an indicator of increased overpressure or gas saturation (Prasad, 2002).

Velocity measurements are often used as a means to estimate the porosity and pressures in the field. There exist many empirical correlations between velocity, pressure, and porosity; however, due to the wide variety of different textural factors among these correlations, including mineralogy, cementation, deposition, grain size distribution, as well as other factors like pore fluid salinity, stress state, and stress history, it becomes difficult to apply any single correlation to field data. Rather than establishing a trend in a localized source material, observing the trend between many materials and many locations allows us to normalize the behavior and apply it more generally to non-similar cases. Extensive testing has been performed on the porosity and stress effect on velocity in rocks and sandstones (Wyllie et al., 1958, Han et al., 1986, Spencer, 1981, Castagna et al., 1985, Gregory, 1976, Yin et al., 1992), with some even looking at the effect of clay content on velocities (Han et al., 1986, Castagna et al., 1985, Ayres and Theilen, 1999); however, the behavior of velocities through pure clays is much less studied.

As mentioned in the previous paragraph, velocity measurements are a method

[1] V_p is compressional wave velocity, and V_s is shear velocity. This ratio typically ranges from 1.5 to 5, depending on the material

used to predict in situ pressures. To further extend this application, many have tried to use velocity measurements to predict pore pressures, such as Ebrom et al. (2002) and Bowers (1995). Since high pore pressures can cause an "overpressure" effect, rendering the formation overconsolidated, the unloading portion of the consolidation curve is of great interest to the oil industry (also oversonsolidated). At a given velocity, depending on whether the material is normally consolidated or overconsolidated can greatly affect the corresponding effective stress. This can lead to overwhelming errors in field pressure predictions – especially harmful during drilling operations if the well design under-predicts pressures. In simple terms, a compression curve is developed relating porosity to stress, with velocity acting as a proxy for porosity, and depth acting as a proxy for stress, assuming a normally-pressured formation. Compression curve is also referred to as a compaction trend in literature. An error in the compaction trend leads to incorrect pressure predictions (Alberty et al., 2003). Furthermore, it is well-known that many basins have smectite or illite-dominated shales. The smectite to illite transition is a temperature-driven transformation that is seen as a gradient of a 80%/20% smectite/illite mix, eventually transforming into an 80% illite mixture with increased depth/stress (Freed and Peacor, 1989a). This smectite/illite (S/I) transformation produces a large volume of water, which can act as a transporter of hydrocarbons. Distinguishing where this transformation occurs based on velocity logs can enhance oil exploration efforts; however, the presence of abnormal fluid pressures caused by the transformation hinders velocity interpretations. This thesis contributes to a better understanding of velocity measurements through illitic (RBBC) and smectitic (RGOM-EI) materials both during the loading portion, as well as the unloading portion that resembles overpressure.

The S and P-wave velocities are known to be affected by the pore aspect ratio, porosity, and mineral properties of the medium through which they are traveling (Kuster and Toksöz, 1974). Therefore, being able to predict these parameters based on velocity measurements is an overarching goal. This capability would provide as much information about the material as many different tests would equivalently give, thus cutting down on time and cost of soil characterization testing. Although this

thesis is not attempting to infer pore structure from velocity, knowing the plasticity properties and velocity behavior through a material can help predict porosity, density, and stress behavior with the aid of these experimental results.

2.3 Description of Velocity Measurements

Velocity testing, which includes Bender Element (BE) and Ultrasonic Transducer (UT) technology, is revered for its ability to dynamically measure the shear and compressional wave velocities through a material in a nondestructive experiment. The fact that it is nondestructive means that the specimen can be tested continuously over a wide stress range, whereas a destructive test usually provides one data point at a single stress level. The bender elements used by the author were only capable of measuring the shear wave (S-wave), whereas the ultrasonic transducers propagate and measure both the S-wave and the compressional wave (P-wave).

This research encompasses test results obtained from three stress regimes: low, medium, and high. These ranges correspond to 0.1 - 1MPa, 1 - 10 MPa, and 10 - 100 MPa, respectively. The focus of this work is on the medium stress range; however, results from all three stress ranges are presented in Chapter 5, all performed directly or supervised by the author. The background and setup conditions for the low stress regime (using bender elements for S-waves) are described in Marjanovic (2012), thus will not be repeated here. The medium and high stress regimes use ultrasonic transducers, which are described in Section 3.4.1, to measure P and S-waves.

The measurement of the S-wave velocity (V_s) is used to calculate the shear modulus (G_{max}) when the bulk density of the material (ρ) is known:

$$G_{max} = \rho \times V_s^2 \tag{2.1}$$

where the subscript "max" signifies the initial stiffness, which is the maximum stiffness measured.

The elastic parameter obtained from the P-wave velocity (V_p), on the other hand,

depends on the boundary conditions. Based on the boundary conditions, it could be either an elastic, bulk, or constrained modulus. The elastic modulus is the case where a theoretical elastic rod is uniaxially loaded and lateral deformation is permitted. The bulk modulus is in the case of an infinite medium. Finally, the constrained modulus is when an elastic rod is uniformly loaded under uniaxial conditions with no lateral deformations (Johnson, 2011). When using an ultrasonic P-wave transducer, the P-wave propagates directly down the path orthogonal to the surface of origin. Since the P-wave can be appropriately described as a compressional wave that moves in the vertical direction (without lateral movement), the measured P-wave velocity is used to calculate the constrained modulus (M):

$$M = \rho \times V_p^2 \tag{2.2}$$

While the constrained modulus is directly calculated from the compressional velocity, the more commonly used modulus to describe the behavior of materials is the bulk modulus (K) (Mondol et al., 2008). (K) can be calculated using the following relationship:

$$K = M - \frac{4G}{3} \tag{2.3}$$

All the elastic parameters, including the moduli and Poisson's ratio, are related to each other. More extensive derivations can be seen in Stein and Wysession (2003) and Van Der Hilst (2004), but the final simplified versions can be seen as follows:

$$G = \frac{E}{2(1+\nu)} \tag{2.4}$$

$$M = \frac{2G(1-\nu)}{1-2\nu} \tag{2.5}$$

$$E = \frac{G(3M-4G)}{M-G} \tag{2.6}$$

where ν is Poisson's ratio and E is Young's modulus. Although these relations are

useful tools, they abide by the assumption that the material is linearly elastic and isotropic. The materials tested during this research are not isotropic but the equations are still used, since they all stay in a single direction and do not deal with the cross anisotropy present. The degree to which clays abide by these equations has not been rigorously tested; however, since no further adjustments have been made to these relations to account for clays, they are still used.

2.4 Compression Behaviors in Clays

The evolution of clay properties as a function of increasing stress is an important parameter used in both subsurface exploration and construction projects. The civil engineering field clearly needs a comprehensive understanding of the state of stress and void ratio in the soil to adequately design for foundations, tunnels, and earthworks. In addition, the oil industry is interested in the compression behavior for petroleum exploration, drilling, and production. It should be clarified that the term *compaction* is a common oil industry term that is equivalent to the geotechnical term *consolidation*. *Compaction* has a different meaning in terms of the geotechnical industry. Henceforward, *consolidation* will be used when referring to the oil industry equivalent of *compaction*. In addition, *compression behavior* is used in lieu of the oil industry term *compaction behavior*. The term compression refers to the process of densifying the material.

Many studies have attempted to describe mudstone and shale compression behavior. A summary of some of these studies is listed in Mondol et al. (2007), including a graph of many compression curves from the literature in Figure 2-1. Rather than list all the studies that have observed compression trends in clays, I will simply reference Casey (2014), who tested most of the same materials in this thesis, and has comprehensive compression curves ranging all the way to 100 MPa (Figure 2-2). All tests performed by him were one-dimensionally consolidated, with strain only in the vertical direction. This was the case for his research, as well as this thesis, since one-dimensional consolidation (K_0) is a more appropriate representation of in situ

conditions. Many studies test using isotropic consolidation, and although this simplifies testing conditions tremendously, it is a very rare occurrence in nature.

Krushin (2014) attempts to take into account shale mineralogy and the thermal, mechanical, and chemical components of consolidation behavior that control porosity. Krushin uses the Cation Exchange Capacity (CEC) as a means to describe the mineralogy, while desorption water vapor isotherms are used to describe the compression behavior. Using these two components results in a single trend, as seen in Figure 2-3. The isotherms are normalized by the CEC in this figure. Finally, the effective stress can be predicted by applying thermodynamic equations to the relative humidity. This technique seems to provide one collapsed trend of all different types of materials; however, when this technique was applied to data obtained in this research, the results did not collapse to one trend. The compression curves of the void ratio as a function of vertical effective stress were normalized by the CEC, and rather than collapse the curves, it seemed to have the opposite effect.

The evolution of clay compression is still in question today. Some, such as Olsen (1962) believe that cluster rearrangement is the primary contributor to high porosity compression. Lambe (1958) and Mitchell (1956) are proponents of particle orientation driving the evolution of clay behavior as a function of stress. Another theory is that a "collapsing aggregate structure" is at play during compression (Delage and Lefebvre, 1984). The exact description of what is happening during compression still needs to be proven.

2.5 Previous Studies Using Ultrasonic Measurements on Different Types of Materials

There exist many models in the oil and gas industry that take into consideration velocity, electrical resistivity, and depth-profile estimates of porosity. Unfortunately most of these models are calibrated to specific locations, thus extrapolating the models to new locations becomes an issue. This thesis will focus on results found in the

laboratory that can be used to infer general behavior without focusing on a particular material or location.

2.5.1 Sands

There have been many researchers who have studied velocity behavior through sands (and glass beads) due to relative ease of testing, with reference to time. Sand can be tested relatively quickly (hours as opposed to weeks for clays), producing many identical specimens is streamlined, and they can be tested in the dry or saturated conditions. There have also been many numerical models that have adequately captured the behavior of sands, including in MIT-S1 (Pestana-Nascimento, 1994), Li and Dafalias (2002), and Yao et al. (2008).

There are a few studies performed on sands using ultrasonic transducers that should be highlighted. First is the work of Prasad and Meissner (1992) that looked at V_p and V_s as a function of grain size and pressure in water-saturated sands. They found that grain size had a larger effect on V_p, while stress has a larger effect on V_s, as is shown in Figure 2-4. Increased coarseness increases P-wave velocity and attenuation, while it only increases S-wave attenuation, rendering the velocity largely unaffected. The same data is shown in Figure 2-5 and 2-6 in terms of V_p/V_s ratio and Poisson's ratio, indicating there is not a strong grain-size effect on these ratios, at least for the grain sizes observed. Another study by Prasad (2002) focused on testing fully saturated, clean beach sands at low effective stresses (< 2 MPa) using ultrasonic transducers. Her tests covered the kHz and MHz frequency range. In addition to her own results, she compared other studies on sands to examine the effect of stress on the V_p/V_s ratio, finding no significant frequency effect. The results from Prasad (2002), Ayres and Theilen (1999), Yin et al. (1992), and Prasad (1988) are combined in Figure 2-7, and Figure 2-8 where a best-fit line is fit to the data. The best-fit equation for all the data, $V_p/V_s = 5.6014\sigma_v'^{-0.2742}$, has an $R^2 = 0.80$. The work of Prasad (1988) shows no clear trend of the V_p/V_s ratio as a function of grain size, besides the largest grain size being shifted slightly higher (larger V_p/V_s ratio) than the rest.

As presented in Figure 2-7, the work of Ayres and Theilen (1999) measured velocity in surface marine sediments in the Barents Sea. They found that lithology and mechanical properties have a larger effect on the S-wave velocity than the P-wave velocity. S-wave velocity tended to increase with increasing clay content, but decrease with increasing silt content, as shown in Figure 2-9. From the figures, it also becomes apparent that the V_s seems to be more strongly correlated to silt content than for clay content in this study. Finally, they concluded that the V_p/V_s ratio could not be used to differentiate the lithology of the sea floor. Perhaps this is the case for the particular lithology experienced in this study; however, later in this thesis it will become clear that there is a distinct trend in V_p/V_s ratio as a function of clay type.

Further studies on sand performed by Zimmer (2003) included grain size, sorting effects, and partial saturation. The S-wave velocity was seen to depend on effective stress as a function of the fourth root ($V_s \propto p'^{1/4}$), while dry P-wave velocity has a stress dependence of $V_p \propto p'^{0.22}$. Although the wet P-wave velocities were obtained by Gassmann fluid substitution rather than directly measured, the results of the V_p/V_s ratio and Poisson's ratio can be seen in Figure 2-10 for a wide variety of grain sizes of glass beads and Santa Cruz sand. In porosity space, the different grain sorting is distinguished by the spaces between porosities, i.e. the data points between a porosity of 0.23 - 0.24 are the smallest glass beads. He concluded that sorting has no significant impact on the pressure dependence of the elastic moduli. He also compiled velocity results from many sources to observe the global pressure sensitivity of rocks and sediments. He concluded that you can approximate a universal power-law trend to characterize velocity laboratory measurements from 100 kPa to 600 MPa, including unconsolidated sediments, consolidated sandstones and shales, and crystalline limestones and granites (Figure 2-11). Since the models he used (including Hertzian contact and O'Connell and Budiansky's crack model) to describe this universal trend were unable to describe the velocity and pressure sensitivity of all the samples, he hypothesized that the differences lie in the pore space geometries and their evolution with stress.

2.5.2 Clays

Testing resedimented materials lets us focus on the micro-level clay fabric rather than the macro-level. The macro-level includes heterogeneities usually associated with deposition and environmental effects, such as fissures, varved deposits, presence of detritus, and heterogenous silty/sand layering. The complications added by the macro-level have made it difficult to focus on the micro-level effects, such as flocc structure, mineralogy, and application of stresses and the development and breaking of contacts.

The study of clay content effect on velocity has been documented by many researcher, including Ayres and Theilen (1999) mentioned in the previous section with sand, as well as Han et al. (1986) who tested 75 different sandstones with varying clay content. Han et al. (1986) found that the clay content affected the velocity as follows:

$$V_p(km/s) = 5.59 - 6.93n - 2.18C \tag{2.7}$$

$$V_s(km/s) = 3.52 - 4.91n - 1.89C \tag{2.8}$$

where n is porosity, and C is clay content in percent. Clay content and porosity have a more significant impact on the S-wave velocity than on the P-wave velocity. Although the clay content decreases the velocity measurements, ultimately porosity has approximately a 3.2x's and 2.6x's stronger effect than clay content on the P and S-wave velocity, respectively (Han et al., 1986). Similarly Castagna et al. (1985) tested clastic silicate rocks and developed the following equations, showing the P and S-wave velocities as a function of porosity and clay content:

$$V_p(km/s) = 5.81 - 9.42n - 2.21C \tag{2.9}$$

$$V_s(km/s) = 3.89 - 7.07n - 2.04C \tag{2.10}$$

Tosaya (1982) had similar equations, but they are left out for brevity. Unfortunately the clay content and porosity were interpreted through neutron-density logs

and gamma ray logs, which introduce some uncertainty. Although these clay content trends provide some insight into the effect of clay on velocity measurements, they do not take into consideration the depositional environment and pore space evolution that can greatly affect the velocity values. Furthermore, the type of clay is not considered in these studies, which can significantly impact the velocity results, whether it be a smectitic or illitic clay.

An example of ultrasonic velocity measurements done on clay minerals can be seen in the work of Mondol et al. (2008). They tested oven-dried clay powder that was mixed with brine to form a slurry, which was subsequently poured into an oedometer cell, where stress was applied up to 50 MPa. The salinity of 34,000 ppm (34 g/L) was used for both kaolinite and smectite. Although they did mixtures of kaolinite and smectite in different proportions (seen in Mondol et al. (2008) and Mondol et al. (2007)), only the extremes are presented in Figures 2-12 and 2-13, where P-wave (Vp) and S-wave (Vs) velocity are shown as a function of stress and porosity, respectively. The ultrasonic measurements indicate that although the velocities are relatively close for smectite and kaolinite as a function of stress, the graph in porosity-space separates out the results significantly. This led to the observation that porosity has more of an influence on the S-wave velocity than the P-wave velocity. Furthermore, their results indicate that at a given porosity, smectite has a much higher P and S-wave than kaolinite, whereas the reverse can be said for a given stress state. These results were ultimately used by Jensen et al. (2011) to develop a model describing this behavior. Although the study performed by Mondol et al. (2008) and Mondol et al. (2007) are a useful comparison, the compression behavior in this study does not agree with that performed at the MIT Geotechnical lab, since these studies found kaolinite to be more compressible (both in the dry and brine-saturated states) than smectite, while the MIT Geotechnical lab found the converse to be true. Furthermore, taking a pure smectite sample from a slurry state to 50 MPa in 21 days might not have given sufficient time for consolidation to occur. The porosity at 50 MPa for smectite in the Mondol et al. (2008) study was the same as RGOM-EI at 10 MPa found in this thesis.

There are a few examples of clay mixtures, in addition to Mondol et al. (2008), made synthetically to observe the shift in velocity behavior as a function of mineralogy. Holt et al. (2011) mixes kaolinite and smectite with Ottawa sand, measuring the P-wave anisotropy in an oedometer cell. It was observed that pure smectite had the lowest anisotropy, while kaolinite mixed with 25% sand had the highest anisotropy. They also showed how important stress paths are for anisotropy evolution. Grande et al. (2013) also conducted tests on "synthetic clays", comprised of different mixtures of illite, kaolinite, silt, smectite, and sand. They showed that a mix of 30% illite and 70% kaolinite had the slowest vertical P-wave velocity, and the fastest horizontal P-wave velocity. On the other hand the fastest and slowest S-wave velocity was the horizontal and vertical 50% illite and 50% kaolinite mixture, respectively. Finally, Marion et al. (1992) measured the P-wave velocity through mixtures of Ottawa sand and kaolinite, finding that the maximum P-wave velocity occurs between 20 - 40 % clay content (Figure 2-14).

Finally, some logging sonic data published by Alberty et al. (2003) indicate that the P-wave velocity through illite-rich formations are faster than smectite-rich formations. Figure 2-15 plots the vertical effective stress versus the transit time of a wave through smectite and illite, showing a general schematic of the trend.

With all these results, it leaves the reader confused and lost with the different mixtures and trends available. It also becomes difficult to know how to apply these mixtures to field situations. With the results found in this thesis, a more concise relationship is shown in an attempt to simplify the interpretations.

2.5.3 Shales and Rocks

There is an impressive number of sources in the literature that have conducted velocity testing on shales and sands. The velocity behavior through these materials is very complex and is dependent on many parameters, justifying this large repertoire of results. Just to name a few, Gregory (1976) did extensive testing on sedimentary rocks, including the fluid effects. Some of the more interesting studies include Domenico (1984) who analyzed the differences between sandstone, limestone, and

dolomite, Sarout and Gueguen (2008), who tested the anisotropy velocity measurements in Callovo-Oxfordian shale, and Pervukhina et al. (2010), who tested loading and unloading behaviors in sandstones. These materials are very different from this research, so they will not be described in further detail.

2.6 Other Methods of Stiffness Characterization

Geotechnical measurements have long been characterizing the stiffness properties of soils. Some of these include triaxial test, torsional shear, resonant column, and bender element tests. All of these will be briefly mentioned in the following subsections, with key advantages and disadvantages of each method, as well as some key work performed.

One of the overlying questions regarding the different ways of measuring modulus values of soils is whether one method provides the necessary values to accurately assess in situ conditions. Historically, the laboratory-measured stiffness parameters have underestimated the actual values seen in the field; however, this was usually thought to have been caused by sampling disturbance Santagata (1998). In Section 2.6.4, some comparisons between these methods and a few explanations for the discrepancies will be referenced.

2.6.1 Mechanical Testing via Triaxial Apparatus

A nice review of triaxial testing instrumentation and the importance to civil engineers is in Scholey et al. (1995). They summarize the various methods used to obtain deformation characteristics of soils, highlighting the importance of internal strain measurements on the middle one third of the specimen, and radial measurements performed at mid-height.

There are two primary methods of obtaining stiffness parameters of clays using a triaxial test – the small strain measurements during undrained triaxial compression using a specimen-mounted yoke apparatus, and a conventional K_0-consolidation undrained compression (CK_0UC) test that provides the secant modulus based on an

external LVDT. Both of these tests have been conducted on Resedimented Boston Blue Clay (RBBC), thus providing a convenient way of comparing results of this research to other published results without concern for material heterogeneity.

Obtaining elastic stiffness parameters using triaxial test results can be difficult due to the generally large strains exhibited during this type of testing. Before proceeding, it is worth defining the levels of strain that are needed to fall within the elastic, elasto-plastic, and plastic zones. The small strain behavior of soil is typically taken to be less than 0.1%; however, this small strain region can be divided into a linear and non-linear section. The linear portion is any strain at 0.001% or less, while non-linear portion is from 0.001-0.1%. Finally, the plastic region is strain above 0.1%. While these are the boundaries for the types of clays investigated, other materials such as sands tested by Da Re (2000) are quoted to have a linear elastic strain boundary of 0.01% or less.

The first method mentioned above, using on-specimen mounted strain measuring devices, allows for much finer strain measurements. The work done by Santagata (1998) used two LVDT's mounted on the specimen that measured displacement with reference to the spring anchor post also attached onto the specimen. Santagata was able to achieve strain resolution at 0.0001%, which is within the linear small strain region. A stiffness degradation curve measured by Santagata et al. (2005) for RBBC can be seen in Figure 2-16. The figure indicates that although the typical limit quoted for the linear small-strain region is 0.001% (i.e. Clayton (2011)), for RBBC the limit for the linear region appears to be at 0.005%.

The measurements performed by Santagata (1998) were done during shearing of the specimen, thus the *undrained* Elastic modulus (E_u) is measured. The results for RBBC at various overconsolidation ratios (OCR) can be seen in Figure 2-17. The normalized Young's modulus decreases as a function of increasing vertical effective stress. It is also clear from the different OCR's that as the OCR increases, the stiffness increases as well. The research performed by Santagata et al. (2005) provides an in-depth look at the low-stress behavior of RBBC, even characterizing the behavior with

the following equations:

$$E_{u,max} = 617 \times OCR^{0.15} \times p'^{0.80}_{mc}(MPa) \tag{2.11}$$

$$E_{u,max} = 273 \times e^{-2.44} \times \sigma'^{0.44}_{vc}(MPa) \tag{2.12}$$

where p'_{mc} is the mean effective stress[2], e is the void ratio, and σ'_{vc} is the vertical effective consolidation stress. While the work does have a thorough analysis of the small strain behavior, it is unclear how the trends will develop over a wider stress range. Furthermore, while the strain range measured is very low, it is a static (destructive) measurement that does not allow for a continuum of results on the same specimen over the stress ranges and OCR's given. A comparison of these results with the velocity-derived E_u is presented in Section 6.4.2.

Although the small-strain method using the specimen-mounted yoke more accurately provides an elastic parameter, which inherently needs to be very low strain, it can be difficult to perform. A more typical approach to obtaining the secant modulus is to shear the specimen and measure the stress-strain behavior externally. This was successfully performed by Abdulhadi (2009) for a wide stress range. His results can be seen in Figure 2-18, where the normalized undrained secant modulus is plotted as a function of stress. In this figure, the three strain levels are obtained from the same test, while the different consolidation stresses indicate the different tests that were performed. There is clearly a strain-softening effect, indicated by the drastic drop in the modulus with increasing strain level. Furthermore, the normalized modulus decreases as a function of stress, which similarly occurs in the strength trends seen in work performed by Casey (2014). Since the definition of an elastic parameter requires a strain of $< 0.01\%$, the results from Abdulhadi (2009) do not fulfill the small-strain criterion; however, they can be used as a lower boundary for the expected modulus value.

[2] $p'_{mc} = (\sigma'_1 + 2\sigma'_3)/3 = (\sigma'_v + 2\sigma'_h)/3$

2.6.2 Resonant Column & Torsional Shear

Literature shows that resonant column and torsional shear tests have been performed both separately, as well as in a single device, such as in Isenhower et al. (1987), Ellis et al. (2000), and Ferreira et al. (2007) to name a few. The resonant column test, first introduced in the 1960's, is usually run in a fixed-free configuration, where one end is stationary, while the other end is vibrated, propagating a wave through the soil specimen due to an excitation force. The excitation force is produced by a coil and magnet system that generates an electromagnetic force, moving the top plate. The resulting behavior yields the the shear modulus and shear velocity. A detailed description of the test can be seen in ASTM D4015. The resonant column can only test one stress state at a time, however once the specimen is tested, it can be consolidated to a higher stress and tested again repeatedly.

The torsional shear test, explained in ASTM D6467 and d'Onofrio et al. (1999), is a test in which a torque is applied to a cylindrical specimen, where the reaction of the soil will be equivalent to the shear modulus. Usually the applied torque is small enough that it is considered non-destructive, and multiple measurements can be taken. One of the disadvantages of torsional shear tests is that the amount of strain experienced in the specimen varies as a function of the distance from the center of the specimen, thus causing a non-uniform strain distribution. Also, much like the resonant column, only one stress level measurement can be taken per specimen.

2.6.3 Bender Elements

Bender elements are piezoceramic plates used to propagate waves through soils, first used by Shirley and Hampton (1978), and subsequently by many more researchers, including Cho and Finno (2010), Fioravante and Capoferri (2001), Gajo et al. (1997), and Leong et al. (2009), just to name a few. The most common use of the bender elements is to insert the protruding element orthogonally into the soft soil, so that it directly couples with the soil around it to propagate shear waves through the specimen, with another bender element on the receiving end as well. Another technique is

to place the plate parallel to the surface of the soil, so that when it is agitated with the application of a voltage, it displaces orthogonally to the surface, creating a compressional wave. It is ideal for soft soils, and once the soil has been consolidated to higher stresses, the soil restrains the movement of the bender element, thus weakening the signal to a point where interpretation of the arrival is impossible. There exists much skepticism about the interpretation of the signal, highlighted by the parametric study reported by Yamashita et al. (2004). Both Marjanovic (2012) and Marjanovic and Germaine (2013) discuss some of the difficulties of bender element testing.

2.6.4 Discussion

There are numerous studies that compare the modulus values obtained by using different techniques, in an attempt to explain the mechanisms that causes these differences and how to understand which method is most "accurate". One study was performed by Valle-Molina (2006), where he used bender elements, ultrasonic transducers, resonant column, and torsional shear tests, all on samples of washed mortar sand. In his setup, he installed bender elements and ultrasonic transducers into a combined resonant column and torsional shear (RCTS) device. The shear velocity (V_s) was 3 - 7% higher when using bender elements versus resonant column. The results are clear in Figure 2-19. In Figure 2-20, three testing methods (TS, RC, BE) are compared when using different driving frequencies. The differences in the results were thought to be caused by differences in frequency and strain level. Unfortunately the piezoelectric transducers were only for P-waves, thus could not be directly compared to RC, TS, and BE results.

On the other hand, Brignoli et al. (1996) compared shear measurements from resonant column, bender elements, and piezoelectric plate, as well as P-wave velocity results obtained from BE and ultrasonic transducers (UT). The P-wave velocity using BE and UT were virtually the same, with slightly higher velocities using UT. They found that in Ticino sand, V_s using BE was 3% higher than when using UT, while BE was 8% higher than RC. The Pontida silty clay showed the converse, where UT was 2% higher than BE, which were about 8% higher than RC. For undisturbed offshore

clay, all the results aligned with each other. See Figures 2-21a through 2-21c.

Another study, performed by Nishimura (2005) on London Clay, compared different methods of measuring the stiffness parameters using bender element testing, resonant column, and cross-hole field measurements. The results are shown in Figure 2-22, where the subscripts hh indicate horizontally propagating, horizontally polarized shear wave velocity values and vh indicates vertically propagating, horizontally polarized shear waves. Ranges for the various testing methods are given, with arrows spanning the range of the measured parameters. It was evident that the field measurements demonstrated the highest stiffness values, followed by resonant column, and then bender element results.

While the discrepancies between field measurements and laboratory measurements have been well-documented and widely accepted, few systematic attempts have been made at establishing a correlation that resolves this misalignment of laboratory stiffness parameters. There have been a few studies done on rectifying the gap, such as Gist (1994) who used the gas pocket model and corrected for local flow to translate ultrasonic velocity measurements to seismic field measurements.

One of the large differences arising from using different methods is not only the frequency range used (whose effects are discussed in Section 2.7), but also the strain amplitude. Below a strain of 10^{-7}, there is an insensitivity to strain level; however, strains above this limit show a marked increase in attenuation and decrease in velocity as a function of increasing strain (Winkler and Nur, 1982). Iwasaki et al. (1978) also showed that the shear modulus greatly diminishes after a shear strain of 10^{-5} for sands tested by cyclic torsional shear loading.

Another factor that might be at play is the possibility of creep affecting the results. As seen in Lohani et al. (2001) and Shibuya (2000) (and later discussed in Section 5.9), creep, also known as secondary compression, can cause up to a 30% increase in shear modulus if sufficient time is permitted. In tests such as bender element and ultrasonic transducer tests, if a selected stress is maintained after K_0-consolidation, and the velocity is measured after the stress has been held for a long time, the results could yield stiffer modulus values. Resonant column and torsional

shear tests are not actively being consolidated, thus don't run the risk of staying at a select stress after a long period of plastic deformation. During triaxial testing the small strain displacements are measured after the rate of secondary compression has reduced dramatically and is not a driving factor.

2.7 Attenuation and Dispersion

Some of the mechanisms causing attenuation also cause dispersion, and vice versa. There are four primary causes of attenuation of a wave: geometric spreading, scattering, multipathing, and anelasticity (intrinsic attenuation). Geometric spreading is simply the attenuation of the wave amplitude as a function of $1/r$, where r is the distance traveled, explained using ray theory (Shearer, 2009). Scattering occurs when there are discontinuities or heterogeneities present. If the heterogeneities are much smaller than the wavelength, then the wave will likely pass through it as it does through the medium. When the heterogeneities are much larger than the wavelength, multipathing takes over. Multipathing is when the wave is focused or defocused by changes in refractive properties of the medium. Finally, intrinsic attenuation occurs when energy is lost, such as in the form of heat or fluid flow (Stein and Wysession, 2003).

Dispersion is when the velocity differs as a function of frequency. Different wavelengths travel at different velocities (Stein and Wysession, 2003). The different scales affecting dispersion are nicely described in Muller et al. (2010). Mesoscopic heterogeneities are present when the size of the pore (a_{pore}) is much smaller than the size of the heterogeneity (a), which is much much smaller than the wavelength of the propagating wave (λ). This is the scenario where fluid flow occurs. Macroscopic heterogeneities, when λ is much bigger or much smaller than a, is when scattering attenuation is relevant. In this research, the wavelength of the P-wave is between $\lambda = 1 - 1.8$ cm, while the wavelength of the S-wave is between $\lambda = 1 - 8$ cm. Since this wavelength is much much bigger than the average size of the clay particles and pores, it resides in the realm of possibility for local fluid flow.

2.7.1 Fluid Flow Models

Fluid flow models have been formulated to describe the change in velocity behavior as a function of frequency and saturation. A number of these models deal with partial saturation (both uniform and patchy), which can lead to fluid flow between the saturated and dry regions; however, the experiments performed in this thesis are fully saturated, thus any partial saturation fluid flow is neglected. Furthermore, there are many models that distinguish between fractures and pore space. In the case of the fully-saturated resedimented clays, these models are not applicable in the absence of cracks or fractures.

There are many effective medium models, explaining the change in stiffness parameters (or velocity values) as a function of fluid substitutions. Biot (1956) was one of the first to attempt to describe the frequency-dependent velocity of saturated rocks based on the dry rock properties by adding a term that incorporates some mechanisms of viscous and inertial interaction between the rock matrix and pore fluid. He included a term ρ_{12} that described the relative acceleration of the soil frame and pore fluid that caused an inertial drag, resulting in an induced mass (Mavko et al., 2003).

Wave induced flow described by Biot (1956) assumes a homogeneous and isotropic porous rock frame, fully saturated by one medium, and λ is much larger than the largest grain/pore. Later Biot (1962) made adjustments for anisotropic media. In reality, wave induced flow is much more difficult to model than described by Biot (1956), which does not account for squirt dispersion. Thus more complicated explanations have been formulated to account for the squirt dispersion, which can be equal or larger than the Biot dispersion. The Gassmann-Biot theory and Mavko-Jizba squirt theory are commonly used to account for the low and high frequency limits, respectively. There are many effective medium models between the two limits, most notably the Bam-Marion bounding average method and Brown-Korringa relations (Mavko et al., 2003); however, they will not be discussed here.

Finally, wave induced fluid flow can occur where there are heterogeneities in the matrix, much larger than the pore scale, but smaller than the wavelength, which is

called mesoscopic flow. This is the case of fluid flow occurring at seismic frequencies (Muller et al., 2010). Since this can occur for heterogeneities from the size of a pore to the size of the wavelength, it encompasses a broad range of scales. The greatest impact of mesoscopic flow occurs in patchy saturation and fractured media Muller et al. (2010), which is not the case in this thesis.

Low Frequency Limit : Gassmann-Biot

The Gassmann-Biot theory explains an increased stiffness is caused by a passing wave/compression that causes a change in the pore pressure, which resists the wave/compression and stiffens the rock (Mavko et al., 2003). This theory is only valid for isotropic rocks and the low-frequency regime ($<$ 100 Hz) since it assumes equilibration in the pore space occurs. This is the "relaxed" state.

High Frequency Limit: Biot Dispersion and Squirt Flow

At high frequencies, Biot dispersion and squirt flow dominate. The Mavko-Jizba squirt relations were introduced to describe the squirt or local flow caused by passing waves at high frequencies. In the presence of a fully saturated material, both dispersion and attenuation are thought to be caused by a squirt-flow mechanism (Dvorkin et al., 1995). This localized flow occurs on the pore scale within a single pore or between two pores of different shape or different compliance, such as two differently-oriented cracks, seen in Figure 2-23. As the wave passes over the pore, it causes a local pore pressure gradient. Squirt flow is typically important in the medium/high frequency range (10-100 kHz), where equilibration does not occur and causes an unrelaxed stiffness increase, and not as much in the seismic and logging frequencies ($<$10 kHz). An exception to this trend is when the permeability of the material is very low. The system stays unrelaxed at low frequency when the permeability is sufficiently low (Dvorkin and Nur, 1993). Biot dispersion, caused by inertial coupling, occurs at ultrasonic frequencies, around 1 MHz (Hofmann, 2006).

Summary

Effective medium models have incorporated the fluid flow aspect of a passing wave, which can affect the velocity behavior. The Biot mechanism describes how the fluid moves with the solid due to viscous friction and inertial coupling (macroscopic level). The squirt-flow mechanism describes how fluid is squeezed from one pore to another due to the passing wave (pore/micro level) (Dvorkin and Nur, 1993). At low frequencies, the fluid pressure does have time to equilibrate and the contacts remain soft. At high frequencies, pressure does not have enough time to equilibrate, which stiffens the contacts and dispersion occurs. Biot's dispersion is dominant at ultrasonic frequencies and the squirt flow dispersion is dominant at high frequencies. In materials with high porosity and well-connected pores, the Biot mechanism is the dominant driver of dispersion rather than the squirt mechanism (Mavko et al., 2003). A unified model, named the Biot-squirt (BISQ) model was introduced by Dvorkin and Nur (1993), and is depicted in Figure 2-24. The model, however, is limited to high pressure rocks with closed compliant cracks. The testing performed in this thesis is on the order of sonic logging frequencies (P-wave =100 - 180 kHz, S-wave = 5 - 80 kHz), thus it is uncertain which dispersion mechanism is at play.

2.8 Clay Microstructure

In order to describe the behavior of velocities through the different clays tested, an investigation into the differences in clay microstructure is needed. Knowledge on the clay microstructure is limited, primarily lacking the support of high resolution micro-scale images to justify the theories prominent in the geotechnical field. Most recently Deirieh (2015) has provided some insight into the microstructural behavior of clay particles ranging from the slurry state to the high stress states up to 40MPa using Cryo-SEM and conventional oven-dried SEM; however, most theories of how the microstructure forms and behaves are based on macro-scale observations, some of which are discussed in the following sections.

2.8.1 Diffuse Double Layer

The diffuse double layer is a layer of adsorbed water on the surface of the clay particle. This adsorption is caused by most importantly hydrogen bonding and cation hydration, but also van der Waals forces. The layer is typically around 1 - 1.5 nm in thickness, but this can greatly vary depending on the mineral and the pore fluid chemistry. The two extremes of the spectrum as far as double layer thickness are smectite and kaolinite, having the largest and smallest double layers, respectively. Furthermore, the thickness increases with decreasing cation valence, increasing dielectric constant, and decreasing salt concentration of the pore fluid (Ladd, 1996). Double layers tend to inhibit particle contact. Repulsive forces are caused by water molecules entering the double layer in an attempt to reduce the cation concentration, thus affecting the microstructure during deposition. The flocculation occurs when van der Waals forces overcome electrostatic repulsion (McBride and Baveye, 2002). The initial microstructure during sedimentation greatly affects the rate of particle reorientation with stress application, which in turn affects the velocity results. More about the role of the double layer on velocity is discussed in Section 5.5.

2.8.2 Microstructural Imaging

Many publications have been including micro-scale images of fine-grained clays to support their findings – Flores et al. (2010) (cement-treated kaolinite), Shibuya (2000) (natural v. reconstituted clays), Dewhurst et al. (2002) and Dewhurst et al. (2011) (intact shale), Sarout and Gueguen (2008) (Jurassic Callovo-Oxfordian shale), Emmanuel et al. (2015) (sandstones), and Schneider et al. (2011) (BBC) just to name a few. Some have even gone further and analyzed the images to quantify particle orientation, such as Day-Stirrat et al. (2011) on BBC and kaolinite, describe quantitattively the microstructure of Opalinus Clay (Houben et al., 2014), and Hemes et al. (2015) uses many types of imaging to characterize the pore space an its connectivity in Boom Clay. Most recently the work of Deirieh (2015) quantitatively analyzes the porosity based on imaging and compares it to other conventional porosity measure-

ments.

A recent effort, by Adams (2014), was done to quantitatively look at the mean particle orientation of RBBC. She compared her quantitative analysis performed on SEM (Scanning Electron Microscope) images to the March model (March, 1932). The March model assumes random initial particle orientation at 45° when no stress is applied to the slurry. The model is described as follows:

$$\theta_{\epsilon_v} = tan^{-1}[(1 - \epsilon_v)tan\theta_0] \tag{2.13}$$

where ϵ_v is volumetric strain and θ is mean particle orientation relative to the horizontal. The model is applied to RBBC and RGOM-EI, and compared to quantitative analysis of SEM images by Adams (2014) in Figure 2-25. The results of Adams (2014) are described by a best fit equation as follows:

$$\theta_{RBBC} = 16.8e^{1.8n} \tag{2.14}$$

where ϵ is particle orientation and n is porosity. The agreement between RBBC of the March model and experimental results from Adams (2014) agree quite well. Based on this relatively good agreement, one can get a rough idea of the mean particle orientation of RGOM-EI based on the March model prediction. At the same porosity, the mean particle orientation for RBBC is expected to be greater than for RGOM-EI.

2.9 Fitting Methods

Many studies have tried to concisely summarize experimental data into a single equation that can describe the clay stiffness behavior. This is especially useful when it comes to modeling soil behavior.

Hardin (1978) suggested the form:

$$\frac{G_0}{p_a} = S * f(e) * OCR^k(\frac{p'}{p_a})^n \tag{2.15}$$

to describe the small strain shear modulus as a function of stress. In the above equation, G_0 is the small strain shear modulus, p_a is atmospheric pressure, $f(e)$ is a decreasing function of the void ratio, p' is the mean effective stress, and OCR is the overconsolidation ratio. The p_a term serves as method of normalization for stress, thus eliminating the issue of using different units. Finally, the terms S, k, and n are material constants. An updated version of equation 2.15 that ensures objectivity is presented in Hardin and Blandford (1989) as follows:

$$G_{ij}^e = \frac{OCR^k}{f(e)} \frac{S_{ij}}{2(1+\nu)} p_a^{1-n} (\sigma_i' \sigma_j')^{n/2} \tag{2.16}$$

The terms i and j indicate the directions of wave propagation and particle motion, respectively. ν is Poisson's ratio. The available test data for soils indicates that the coefficient values are $n = 0.5$, $\nu = 0.1$, and $S = 1400$ (Hardin and Blandford, 1989). The S value, which is a measure of the stiffness of the particles, can vary from 700 for cohesive soils, to much greater than 1400 for uniform gravels and cemented soils. The plasticity effect of the soil is also seen in the OCR exponent k, which goes to zero as plasticity decreases. This implies that high plasticity clays are more sensitive to stress history (Hardin, 1978, Vucetic and Dobry, 1991, Santagata, 1998). Equations 2.15 and 2.16 are not limited to but are most commonly used for sands.

Rampello et al. (1997) have also attempted to adjust the parameters of the original Hardin equation (equation 2.15) by producing the following equation:

$$\frac{G_0}{p_r} = S^* (\frac{p'}{p_r})^{n*} OCR^m \tag{2.17}$$

where OCR is the overconsolidation ratio, S^*, n^*, and m are material constants, p' is mean effective stress, and p_r is a reference stress used to eliminate units. Rampello et al. (1997) concluded that for a clay under isotropic stress conditions, one of the following is redundant and not needed: e (void ratio), p' (mean effective stress), and OCR. With a few substitutions and incorporating the Cambridge space (ln(p')-ν) nomenclature, the following was derived:

$$\frac{G_0}{p_r} = S * f(e) * (\frac{p'}{p_r})^{n*-c} \tag{2.18}$$

where

$$f(e) = \frac{A}{exp(Be)} \tag{2.19}$$

and $A = exp[B(N-1)]$ and $B = c/\lambda$ are constants that depend on N and λ (compressibility parameters) and c (stiffness index). N is the specific volume ($\nu = 1 + e$) at the reference mean effective stress, and λ is the slope of the virgin compression line in ln(p')-ν space. See Figure 2-26 for clarification of the nomenclature. Although this type of fitting is appropriate for isotropic stress conditions, it is not appropriate for the K_0-consolidation experiments run in this thesis. Equation 2.16 is more appropriate in this case.

Shibuya et al. (1997) created a new void ratio term and a new empirical expression proposed for practical use in natural soil deposits. The new void ratio is based on the assumptions that K_0 is constant, the compression behavior is linear on a double log plot (of σ'_v and ν, the specific volume), and G_{max} increases exponentially with σ'_v. Based on these, the new void ratio function is:

$$f(e) = (1 + e)^{\alpha} = v^{\alpha} \tag{2.20}$$

where α is a constant. m is the constant relating the increase of stress with increase of shear modulus as follows:

$$\frac{G_{max}}{G_{maxr}} = (\frac{\sigma'_v}{\sigma'_{vr}})^m \tag{2.21}$$

The relationship between m and the compression index C' for many clays was taken. The slope of this relation was found to be 2.4, thus α= -2.4. The final resulting equation was found to be:

$$G_{max} = A(1 + e)^{-2.4}\sigma_r^{0.5}\sigma_v'^{0.5} \qquad (in \quad kPa) \tag{2.22}$$

σ_r is a reference stress used to normalize out the units. This equation can be applied to any soil, where A is a constant that accounts for different soils, and includes an aging effect present between reconstituted versus intact samples.

Other attempts at fitting trends to experimental data have focused on using the velocity values rather than the stiffness moduli (which included the velocity plus a density term). Hardin and Richart Jr (1963) described the shear wave velocity of isotropically consolidated sands as follows:

$$V_s = (m_1 - m_2 e)(p')^{0.25} \tag{2.23}$$

where m_1 and m_2 are material constants, e is the void ratio, and p' is the mean normal effective stress. To account for non-isotropic stress application, Roesler (1979) devised

$$V_s = (m_1 - m_2 e)(\sigma'_a)^{na}(\sigma'_p)^{nb} \tag{2.24}$$

Exponents na and nb were usually equal to 0.125.

Transitioning over to rocks, Dvorkin (2008) altered an equation typically reserved for describing P-wave velocity. This classical equation, named the Raymer-Hunt-Gardner (RHG) equation, was quoted as an improvement over the Wyllie time-average equation (WTA) (Wyllie et al., 1956). The WTA and two RHG equations are as follows, respectively:

$$\frac{1}{V_p} = \frac{\phi}{V_{pF}} + \frac{1-\phi}{V_{pS}} \tag{2.25}$$

$$V_p = (1-\phi)^2 V_{pS} + \phi V_{pF}, \qquad \phi < 37\% \tag{2.26}$$

$$\frac{1}{\rho V_p^2} = \frac{\phi}{\rho_f V_{pf}^2} + \frac{1-\phi}{\rho_S V_{pS}^2}, \qquad \phi > 47\% \tag{2.27}$$

where ϕ is porosity, V_{pS} and V_{pF} correspond to the P-wave velocity in the solid and pore-fluid phase. The RHG was selected since it closely aligns with the analytical stiff-sand model, introduced by Gal et al. (1998), hence was presumed to be the best

type of equation to fit S-wave velocity. The resulting equation is

$$V_{sDry} = (1 - \phi)^2 V_{sS} \tag{2.28}$$

with V_{sS} being the S-wave velocity in the solid phase. The wet S-wave velocity is then obtained by the Gassmann assumption that the wet and dry shear modulus are equivalent:

$$V_s = V_{sDry}\sqrt{\frac{\rho_{bDry}}{\rho_b}} \tag{2.29}$$

where ρ_{bDry} and ρ_b are the dry and wet bulk densities respectively. Equations 2.28 and 2.29 can predict dry and saturated S-wave velocity in consolidated clastic and carbonate rocks. The advantages of this equation is the lack of reliance on the P-wave velocity, and its simplicity. The pervasiveness of using the V_p to predict V_s is evident by the many sources listed by Dvorkin (2008). The simplicity, although an advantage, also means that applying it to a clay, which contains various quantities of different clays and minerals could prove to be challenging. Furthermore, the RHG was selected by Dvorkin (2008) since it agreed with the "stiff-sand" model; however, for a fine-grained clay, certainly an equation that aligns with the "soft-sand" model (developed by Dvorkin and Nur (1996))would be more appropriate, if at all any sand model is used.

Xu and White (1995) recognized that the presence of clay obscures the validity of these models, and proposed a relation based on log data case studies. They used an inclusion effective-medium theory (developed from the Kuster and Toksöz (1974) model), acknowledging that aspect ratios for pores in sand are vastly different from those in clay. The results of the iterative differential-effective-medium scheme are seen in Figure 2-27, showing the incremental increase from 0% clay (labeled clean sand) to 60% clay (labeled pure shale[3]). Xu and White (1995) concluded that clay pores had much smaller aspect ratios than sand pores – about 0.02-0.05 for clay pores, and 0.12 for sand pores.

Another fit commonly applied to P-wave velocity in the field is a Gardner-type fit

[3]Shales usually contain between 35-70% clay content (Sayers and den Boer, 2011)

Gardner et al. (1974) as follows:

$$\rho = aV_p^b \tag{2.30}$$

where a and b are fitting parameters, and ρ is density. This is a purely empirical equation, where the fitting parameters are always site-specific. Castagna and Backus (1993) suggested extending the equation to

$$\rho = aV_p^2 + bV_p + c \tag{2.31}$$

This equation is used for P-wave velocity, with the S-wave velocity usually calculated by assuming a Poisson's ratio and applying it to the V_p.

One of the most commonly used predictors of S-wave velocity is the Greenberg and Castagna (1992) model. It can predict the S-wave velocity within 3% accuracy and 7% precision if given the P-wave velocity, lithology, porosity, and water saturation. It calculates the S-wave velocity based on averaging the harmonic and arithmetic means of the V_s's of the pure lithology, much like the Voight-Reuss-Hill average for elastic moduli. For the saturation component, it utilizes the Gassmann (1951b):

$$K_{sat} = K_{dry} + \frac{(1 - \frac{K_{dry}}{K_0})^2}{\frac{\phi}{K_{fl}} + \frac{1-\phi}{K_0} - \frac{K_{dry}}{K_0^2}} \tag{2.32}$$

K_{sat} is the effective bulk modulus of the rock with pore fluid, K_{dry} is the effective bulk modulus of dry porous solid, K_0 is the bulk modulus of the solid mineral material, ϕ is porosity, and K_{fl} is the bulk modulus of the fluid. Since the Greenberg and Castagna (1992) V_s prediction is an iterative method with many equations, it will not be repeated here (also described in Chapter 7.8 of Mavko et al. (2003)). This method does not make any predictions with respect to porosities, but assumes they are implied in the V_p values. The same assumptions are pointed out with lithology, with the regression coefficients for pure lithologies (empirical correlations) obtained from Castagna and Backus (1993). Finally, the saturation state is accounted for in the Gassmann model, thus combining empirical relations with a theoretical model to predict the V_s.

Sayers and den Boer (2011) takes a look at multiple techniques, including the Gardner relation (Gardner et al. (1974)) assuming the parameters of Castagna et al. (1993), the Greenberg and Castagna (1992) model, and the mudrock line from Castagna et al. (1985) ($V_s = 0.862V_p - 1.172$), as well as the Mori-Tanaka rock physics model (Mori and Tanaka, 1973) to see which one most closely predicts the behavior in two deepwater subsalt wells in the Green Canyon area of the Gulf of Mexico. They showed that the best model that described the data was the effective field theory of Mori-Tanaka, which includes and aspect ratio of the pores. Although the M-T method was able to achieve the best fit, this was due to the selection of the appropriate aspect ratio (c/a) that yielded the best fit. This meant a ratio of approximately 0.02 for the P-wave and 0.015 for the shear wave.

Finally, a Bowers-type fit is commonly used to describe the loading and unloading behavior of shales and rocks (Bowers, 1995). Since it accounts for the unloading effect, it is often used as a pore pressure predictor. The equation is as follows:

$$V_p = C + A(\sigma'_{max}(\frac{\sigma'}{\sigma'_{max}})^{\frac{1}{U}})^B \tag{2.33}$$

where A, B, and C are fitting parameters, it is assumed that $C = 5000ft/s$ in all cases, U is a fitting parameter for the unloading portion, σ'_{max} is the maximum past stress, and σ' is the current effective stress. U is referenced by Bowers (1995) as falling between 3 - 8, with $U = 1$ being a perfectly elastic unloading, and $U = \infty$ being a perfectly plastic unloading. This type of fit is shown to be quite effective on P-wave velocity in rocks and shales, without an explicit intention to model S-wave velocity behavior. In Section 6.2.2, the equation above is applied to the P-wave velocity through clays.

2.9.1 Summary

It is clear from the number of models and empirical relations available, establishing a relationship between velocity, porosity, and stress is highly desirable. While there are a few equations focused on fitting the low-stress shear modulus (G_{max}), others develop

models to predict velocities based on mixing two components or predicting V_s from V_p. Despite the success of some of the theoretical effective medium models, empirical fits to data are most often used in the field (Mavko et al., 2003). Furthermore, many of them are appropriate for rocks, sands, and in some cases a certain amount of clay content added to a primarily rock or sand formation. Few attempts have been made, besides most notably Hardin and Blandford (1989), to describe clay behavior. There is an insufficient amount of data and empirical attempts at describing how velocities behave through clays, including different clay types and their plasticities, and as a function of evolving stress conditions and porosity.

Table 2.1: List of experiments classified as dynamic or static and their stain levels (adapted from Santagata (1998))

	Test	Strain (%)
Static	Triaxial (TX)	> 0.05 external, > 0.0001 on specimen
	Torsional Shear (TS) ML (Monotonic)	> 0.0001
	Torsional Shear (TS) CL (Cyclic Loading)	$0.0005 - 0.001$[1]
Dynamic	Resonant Column (RC)	$0.00001 - 0.01$[2]
	Bender Element (BE)	< 0.001
	Ultrasonic Transducer (UT)	$\ll 0.0001$

[1]From Youn et al. (2008)
[2]From Nishimura (2005)

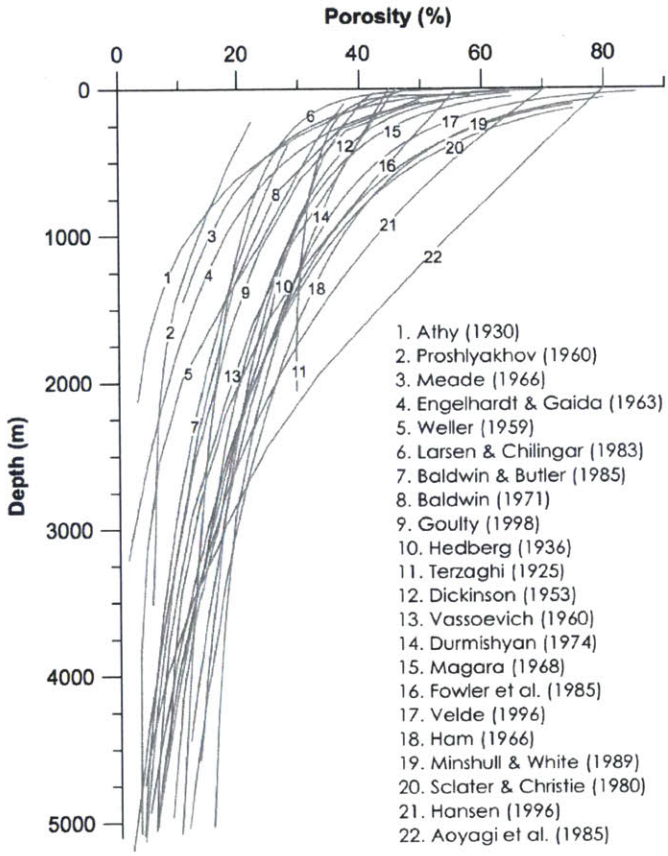

Figure 2-1: Compression trends for shales and argillaceous sediments from different parts of the world (Mondol et al., 2007)

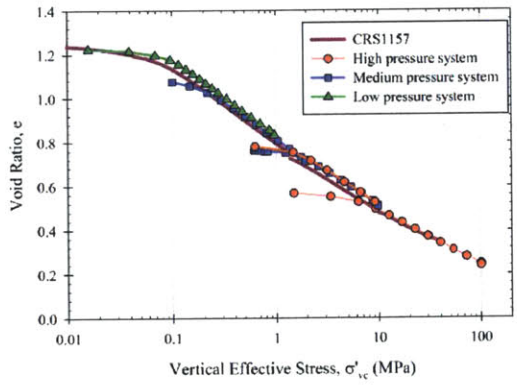

(a) Compression curve for RBBC

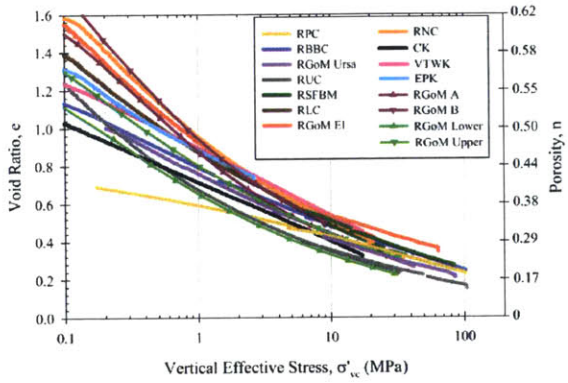

(b) Compression curve for all materials tested by Casey (2014) and UT Geofluids Consortium

Figure 2-2: Figure (a) includes the compression curves for RBBC using three different capacity cells. Figure (b) includes all the materials tested in this research (tested by others) as well as other materials (Casey, 2014)

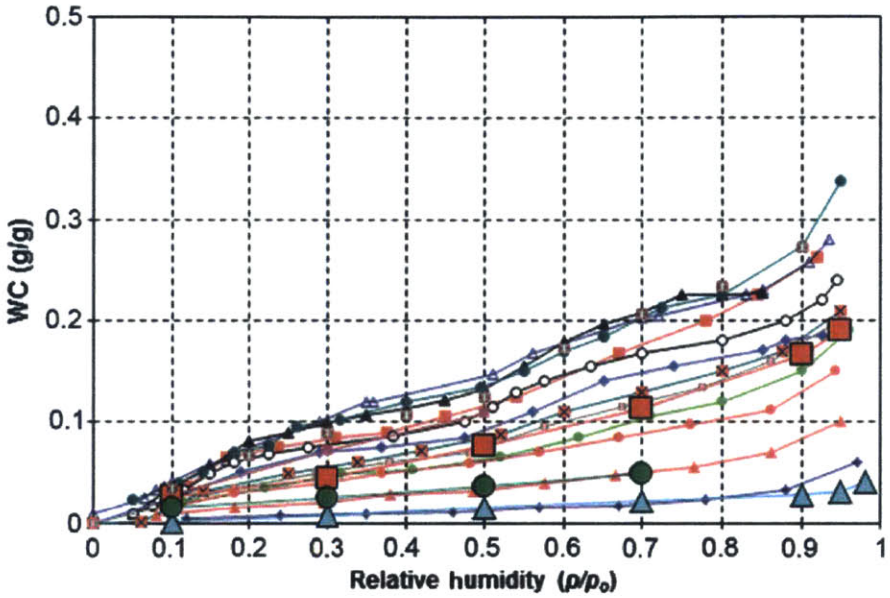

(a) Water vapor desorption isotherms

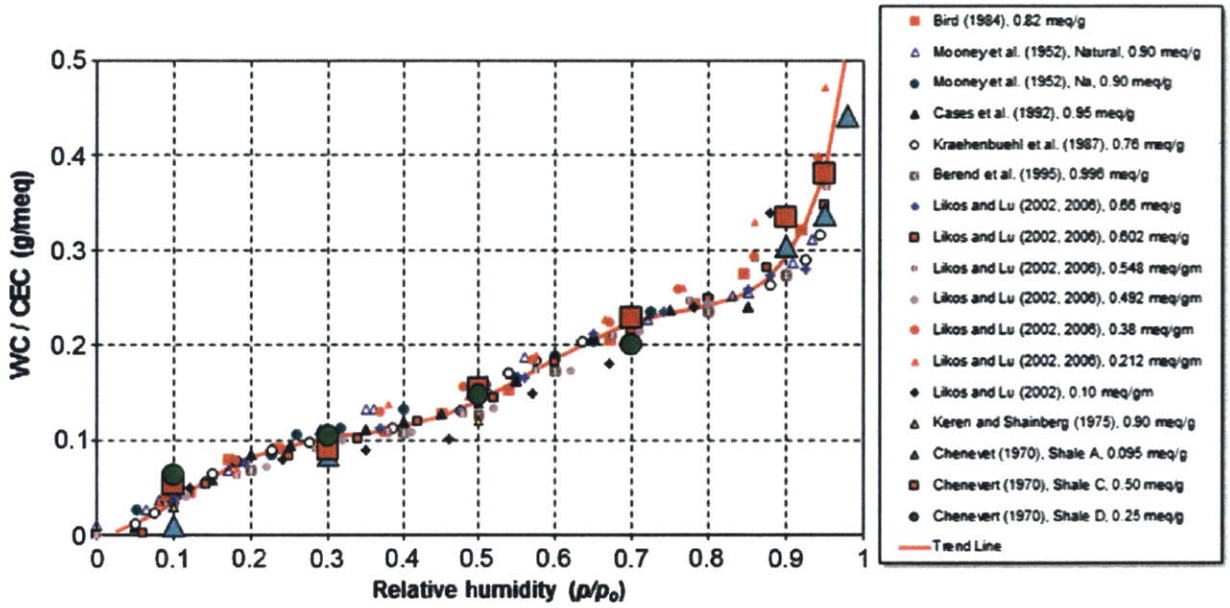

(b) Water vapor desorption isotherms normalized by CEC

Figure 2-3: Analysis performed by Krushin (2014) shows that for many different types of clays (small symbols for pure clays and clay mixtures, while large symbols are for shales), the water vapor desorption isotherm can be normalized by the CEC. Figure a) shows the water vapor desorption isotherms, while Figure b) shows the same isotherms normalized by the CEC for each clay

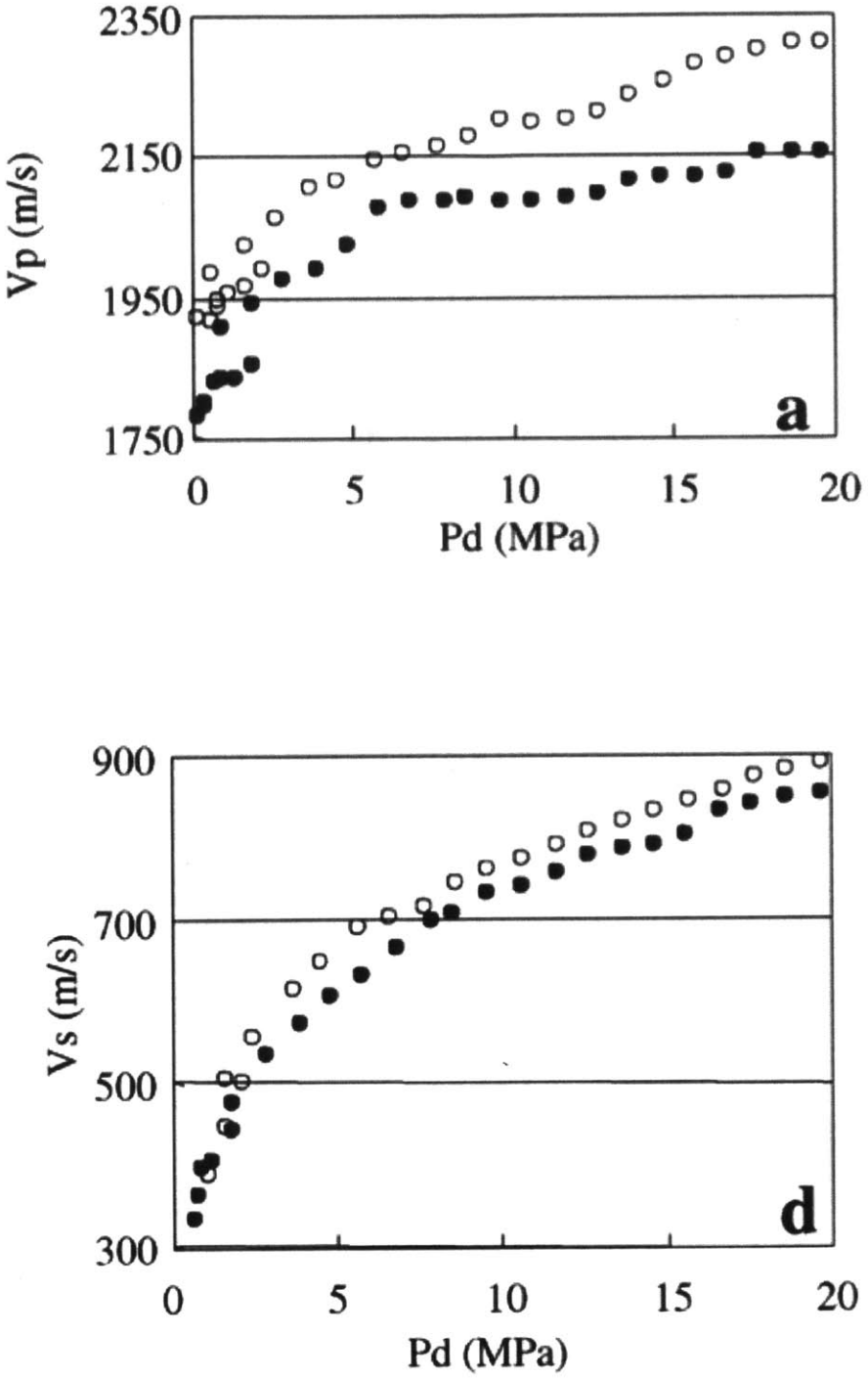

Figure 2-4: The P-wave (Vp) and S-wave (Vs) velocities are measured using ultrasonic transducers. Pd is the vertical effective stress. The hollow circles are coarse grained ($d = 550\mu m$), closed circles are fine grained ($d = 220\mu m$), Prasad and Meissner (1992)

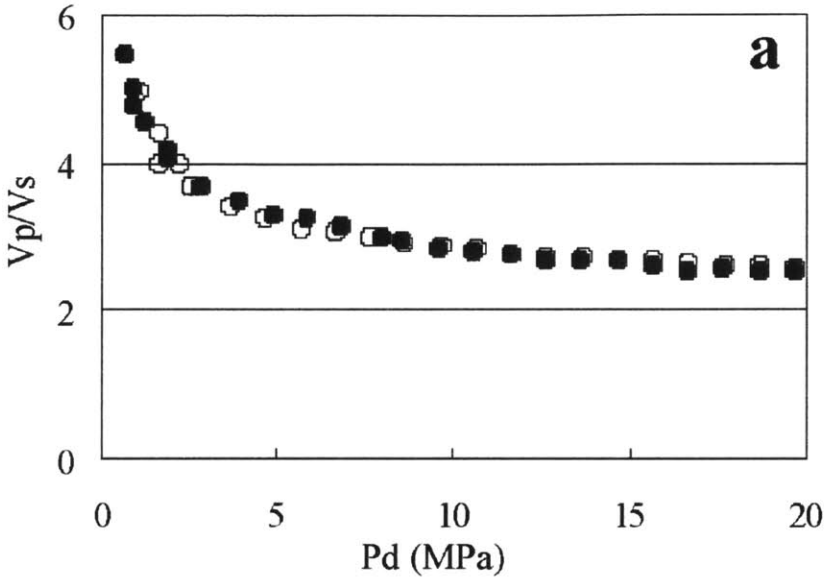

Figure 2-5: The ratio of P-wave (Vp) to S-wave (Vs) velocities measured using ultrasonic transducers. Pd is the vertical effective stress. The hollow circles are coarse grained sand ($d = 550\mu m$), closed circles are fine grained sand ($d = 220\mu m$), Prasad and Meissner (1992)

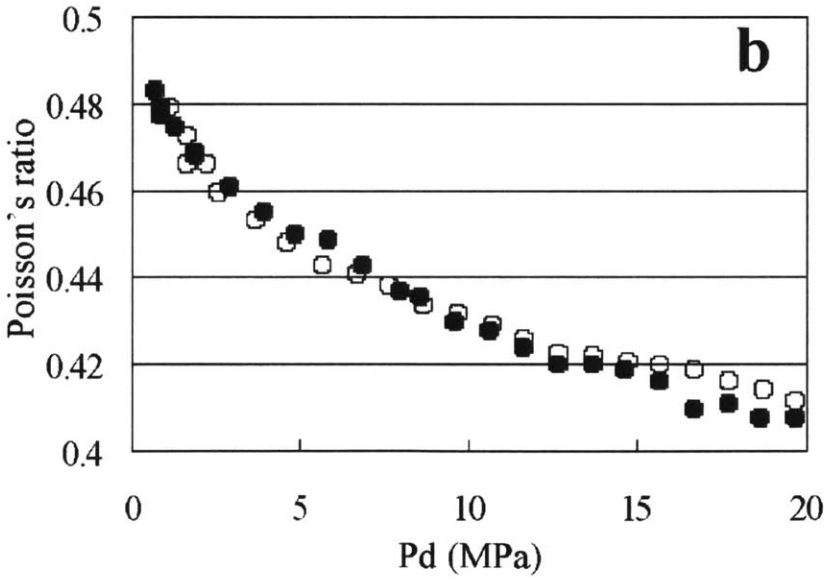

Figure 2-6: The Poisson's ratio measured using ultrasonic transducers. Pd is the vertical effective stress. The hollow circles are coarse grained sand ($d = 550\mu m$), closed circles are fine grained sand ($d = 220\mu m$), Prasad and Meissner (1992)

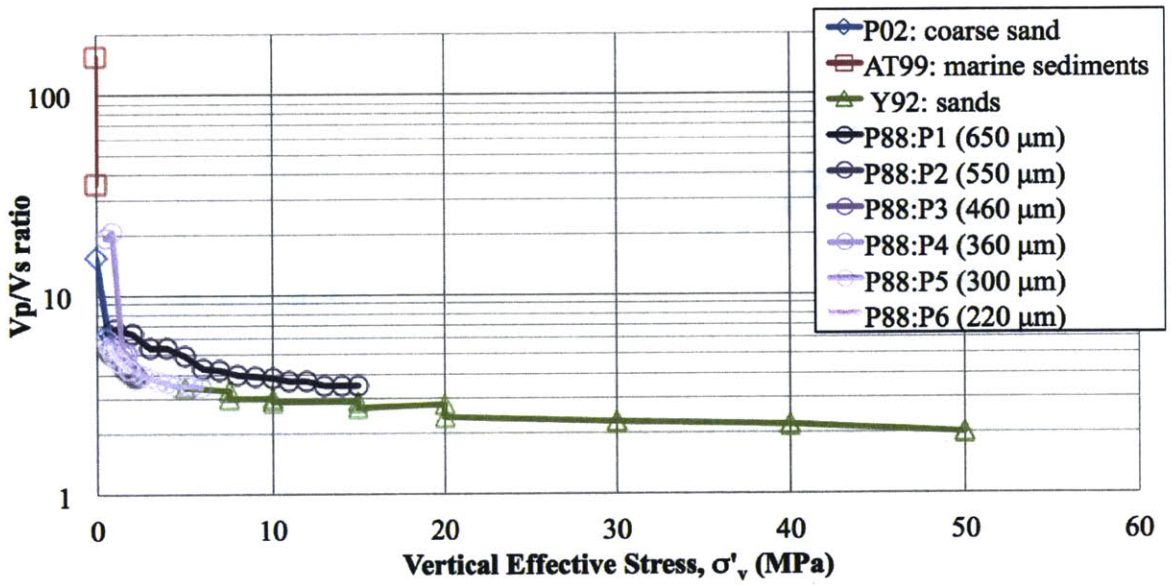

Figure 2-7: A comparison of the V_p/V_s ratio from various sources for sands. P02=Prasad (2002), AT99=Ayres and Theilen (1999), Y92=Yin et al. (1992), P88=Prasad (1988), with P88 showing a distribution of different grain sizes, listed in parentheses. Modified from Prasad (2002)

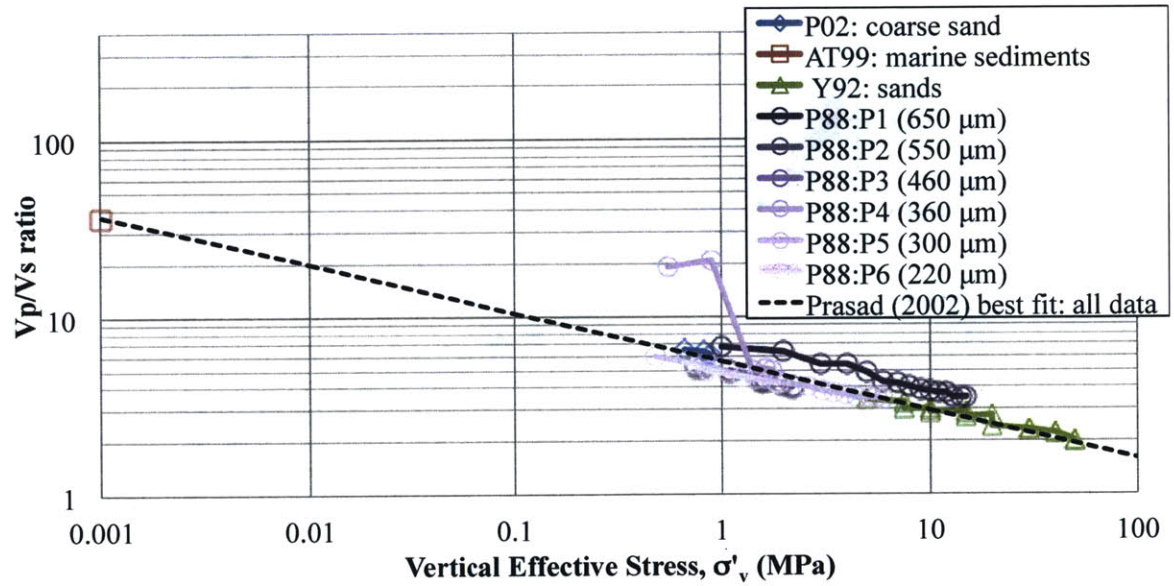

Figure 2-8: A comparison of the V_p/V_s ratio from various sources for sands. Legend is same as previous figure, but with a best-fit line included: $V_p/V_s = 5.6014\sigma_v'^{-0.2742}$. Modified from Prasad (2002)

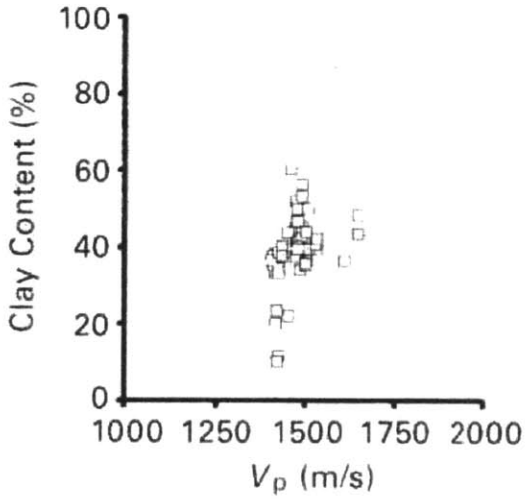

(a) V_p as a function of clay content

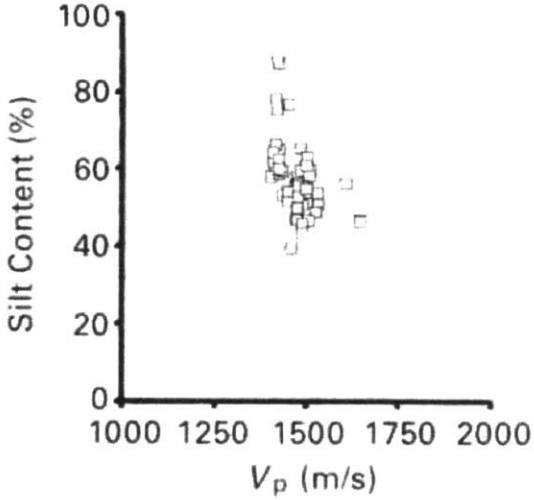

(b) V_p as a function of silt content

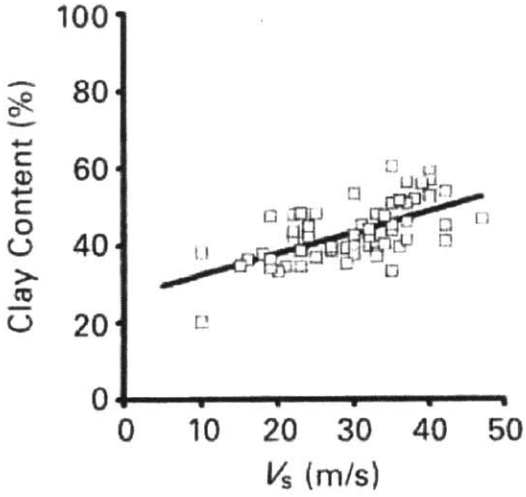

(c) V_s as a function of clay content

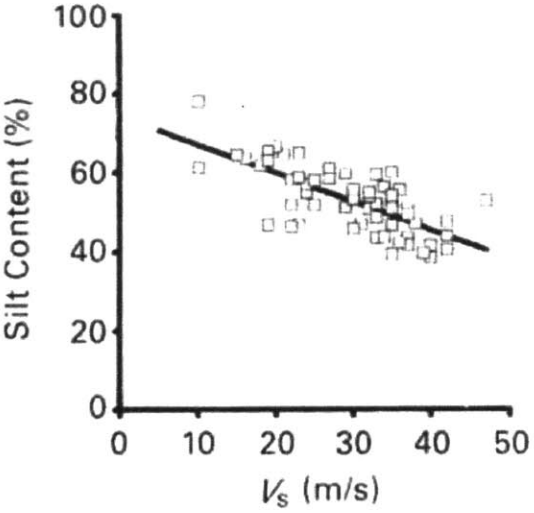

(d) V_s as a function of silt content

Figure 2-9: V_p and V_s as a function of silt and clay content for intact sandy marine sediments (Ayres and Theilen, 1999)

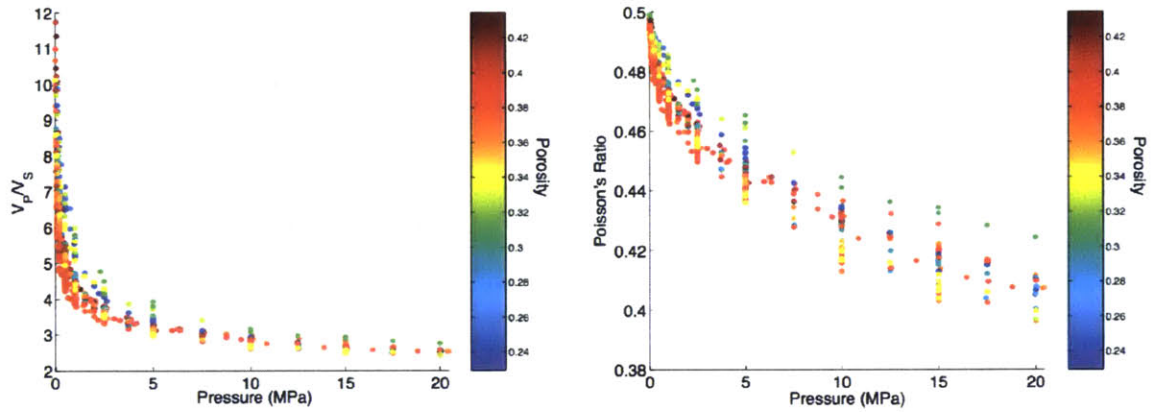

(a) V_p/V_s ratio and Poisson's ratio for differently-sorted sands as a function of stress

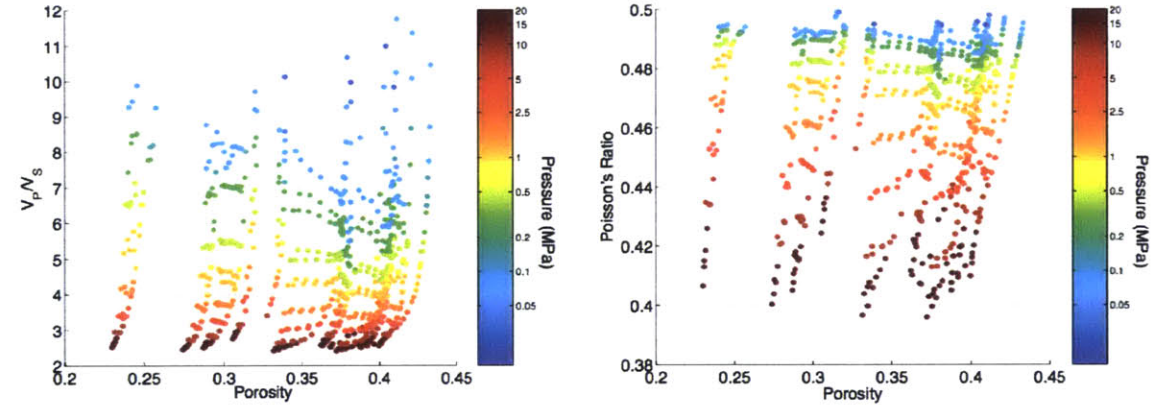

(b) V_p/V_s ratio and Poisson's ratio for differently-sorted sands as a function of porosity

Figure 2-10: The V_p/V_s ratio and Poisson's ratio for differently-sorted sands and glass beads as a function of stress show that there is no strong effect of sorting on these trends (Zimmer, 2003)

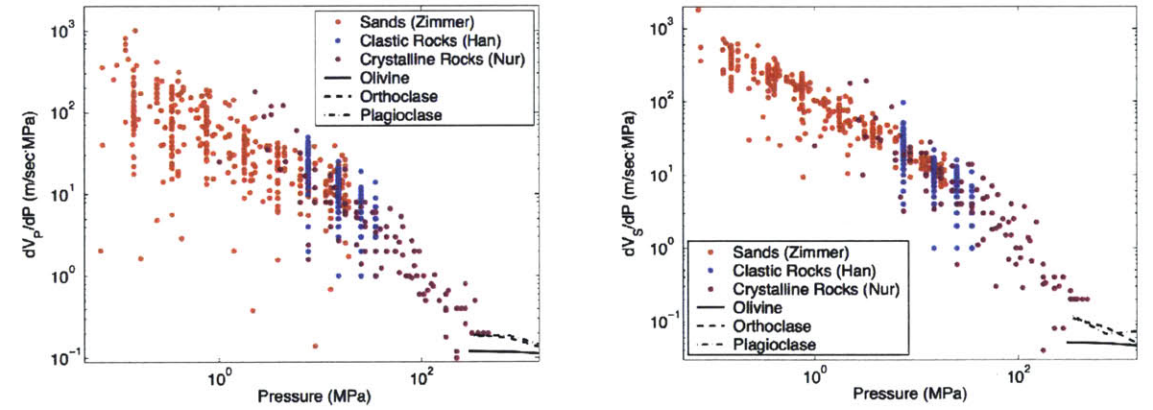

(a) V_p sensitivity as a function of stress

(b) V_s sensitivity as a function of stress

Figure 2-11: V_p and V_s sensitivity as a function of stress for a variety of rocks, shales, and sediments (Zimmer, 2003)

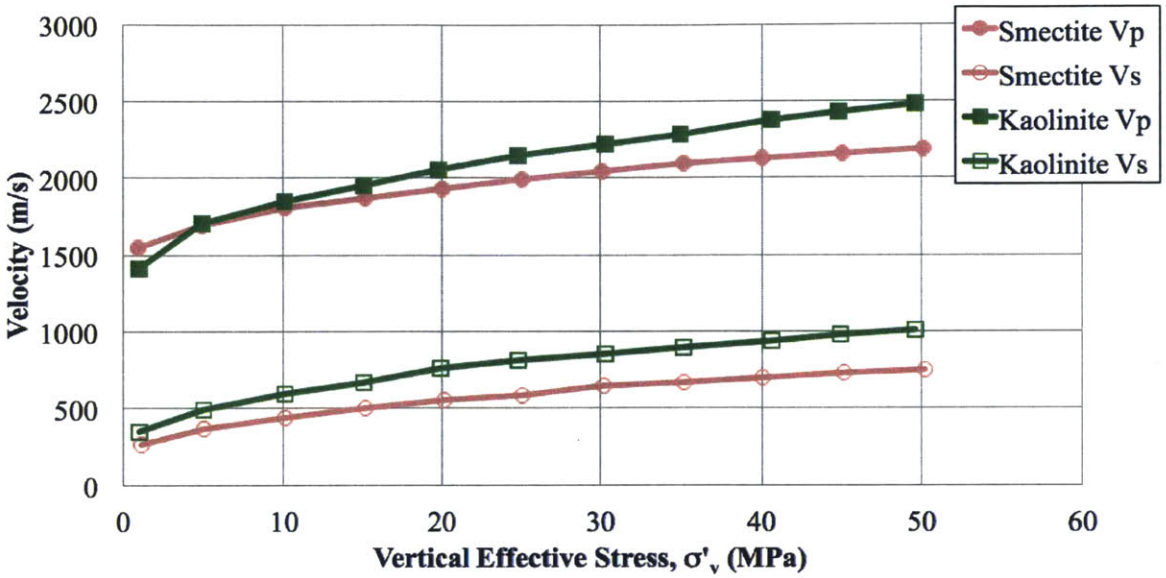

Figure 2-12: The P-wave (Vp) and S-wave (Vs) velocities are measured in an oedometer cell as a function of vertical effective stress for brine-saturated kaolinite and smectite (adapted from Mondol et al. (2008))

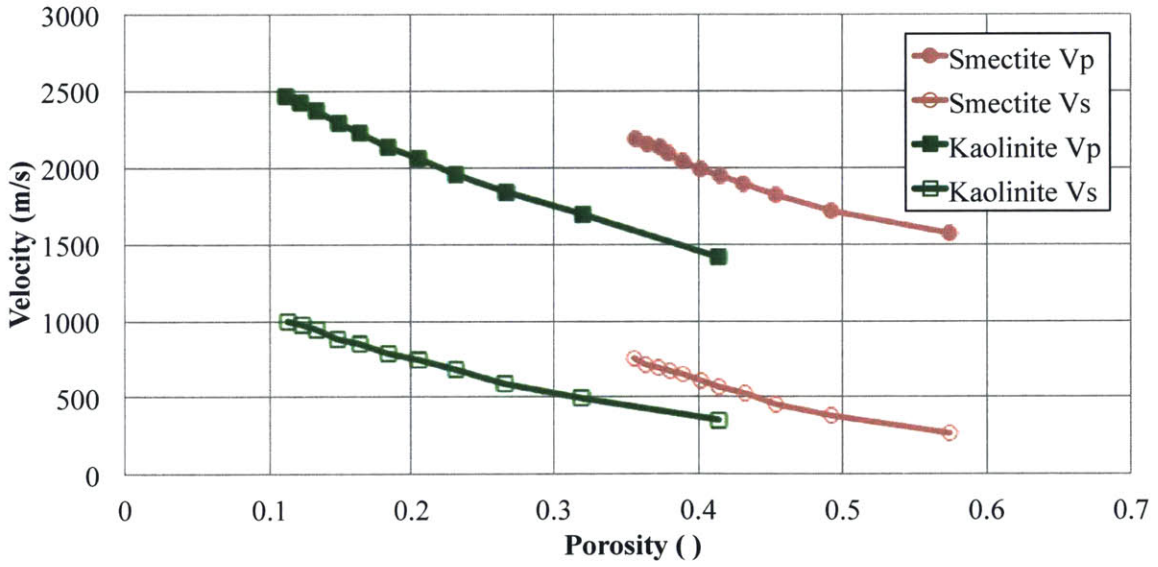

Figure 2-13: The P-wave (Vp) and S-wave (Vs) velocities are measured in an oedometer cell as a function of porosity for kaolinite and smectite (adapted from Mondol et al. (2008))

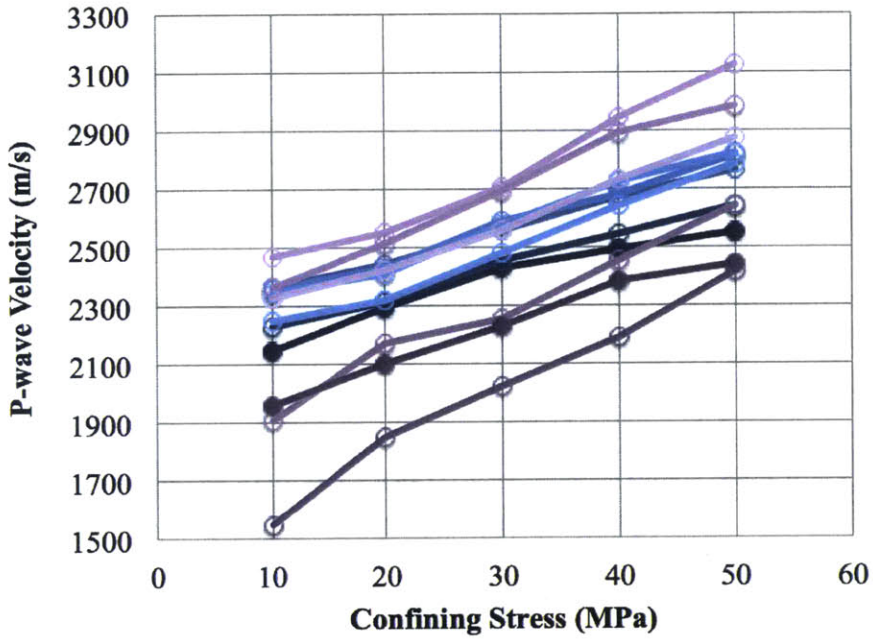

(a) V_p for sand/clay mixtures as a function of stress

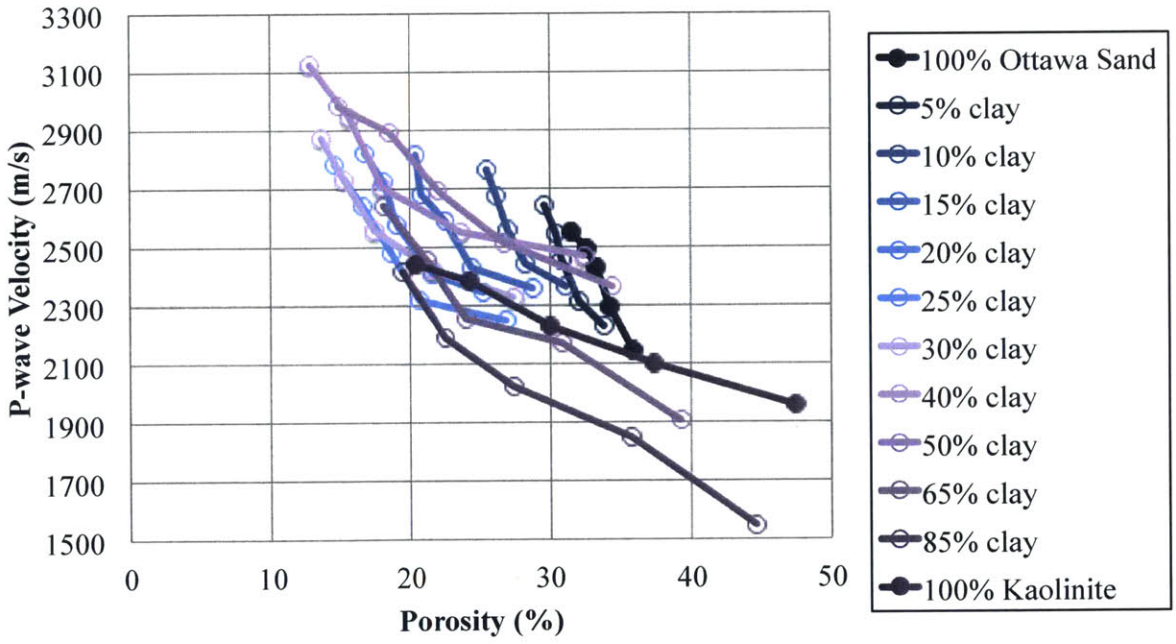

(b) V_p for sand/clay mixtures as a function of porosity

Figure 2-14: V_p for Ottawa sand and Kaolinite mixtures. Adapted from Marion et al. (1992)

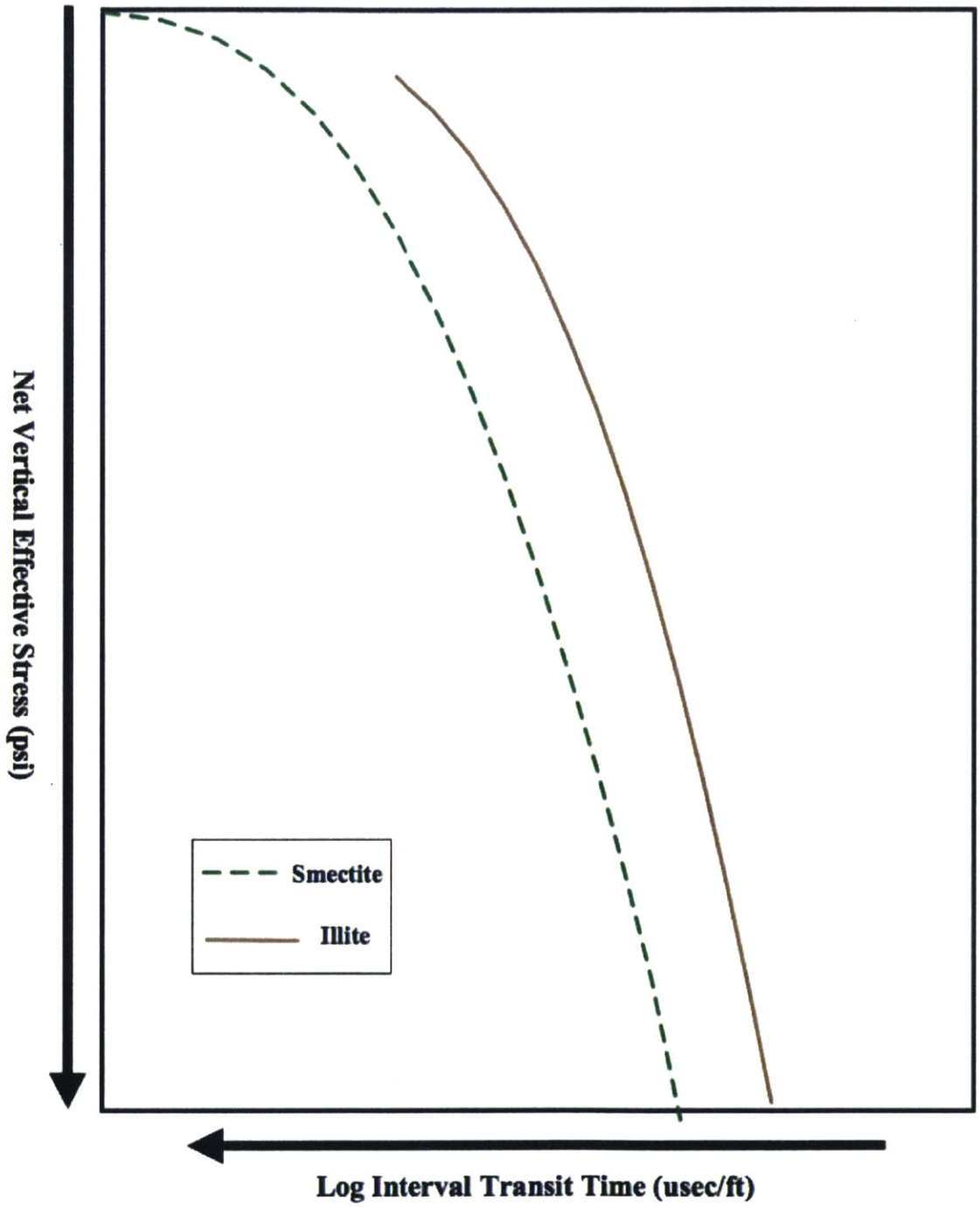

Figure 2-15: Crossplot of the sonic velocity versus vertical effective stress for illite and smectite-rich formations, showing a higher P-wave velocity for illite than for smectite (Alberty et al., 2003)

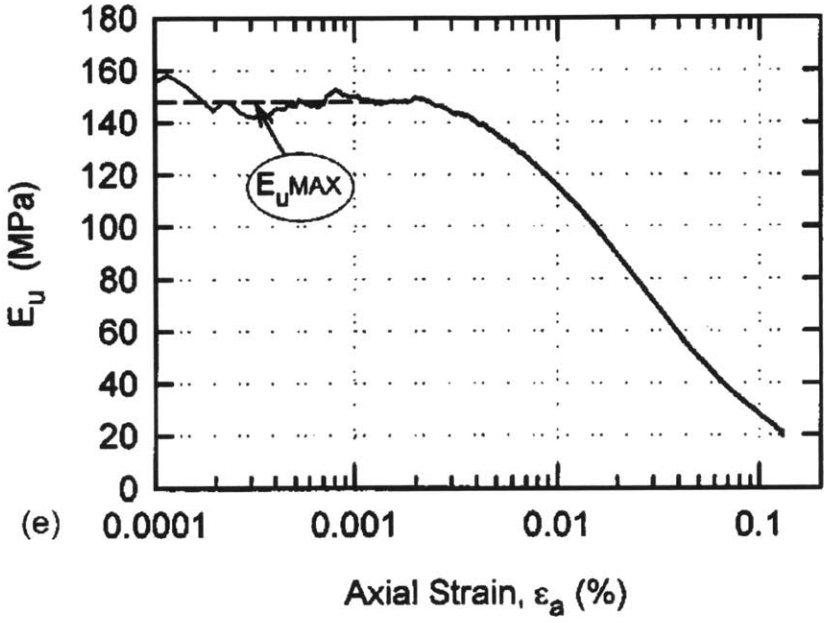

Figure 2-16: Stiffness degradation curve for RBBC shows that linear behavior prevails until a strain of 0.005% (Santagata et al., 2005)

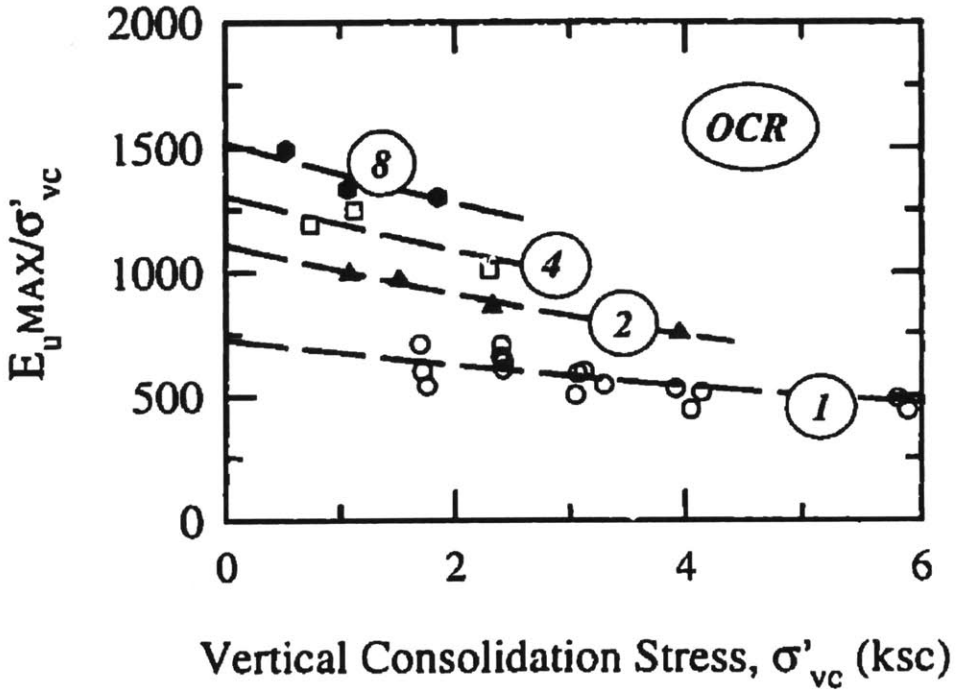

Figure 2-17: Undrained secant modulus as a function of axial strain for RBBC for both NC and OC RBBC (Santagata, 1998)

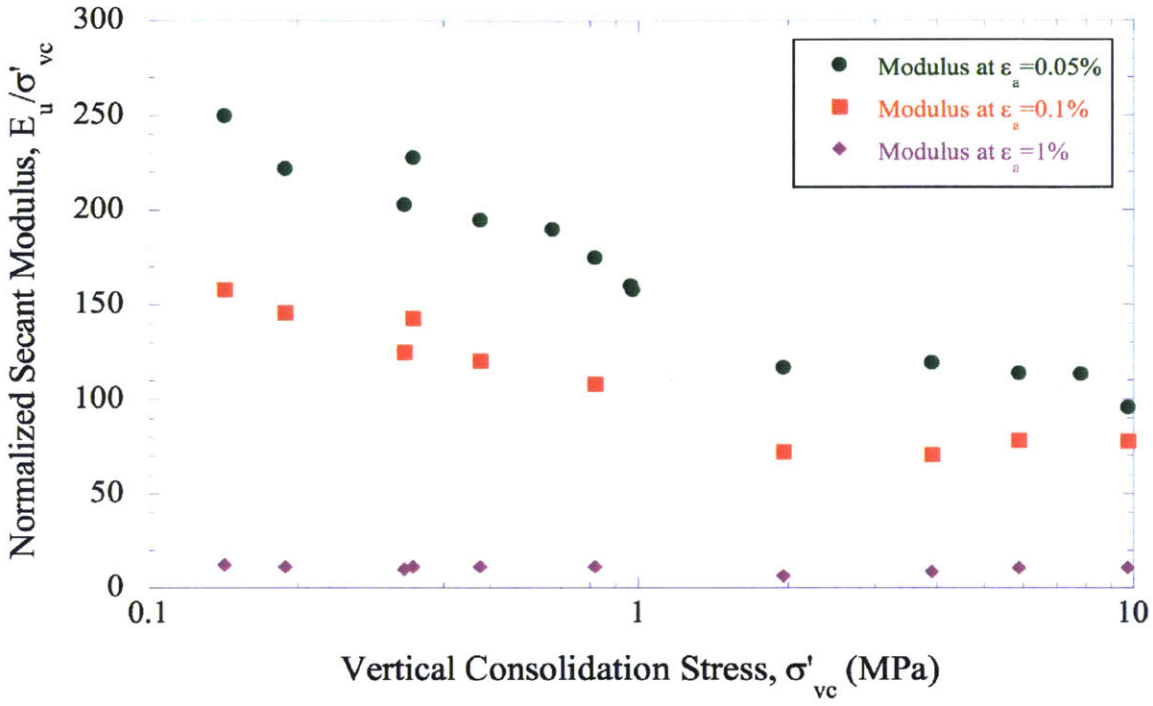

Figure 2-18: Normalized undrained secant modulus versus stress level for NC RBBC from CK_0UC triaxial tests (Abdulhadi, 2009)

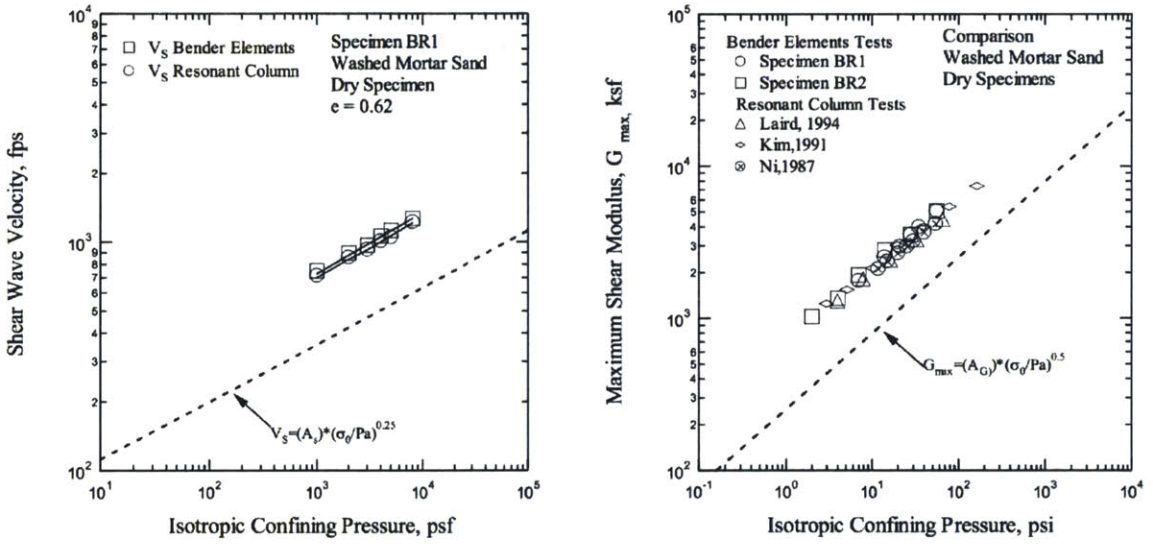

(a) V_s results on sand using RC and BE

(b) G_{max} results on sand using BE and other sources of RC

Figure 2-19: V_s and G_{max} results for both resonant column (RC) and bender elements (BE). Various sources of RC tests were used in figure (b) (Valle-Molina, 2006)

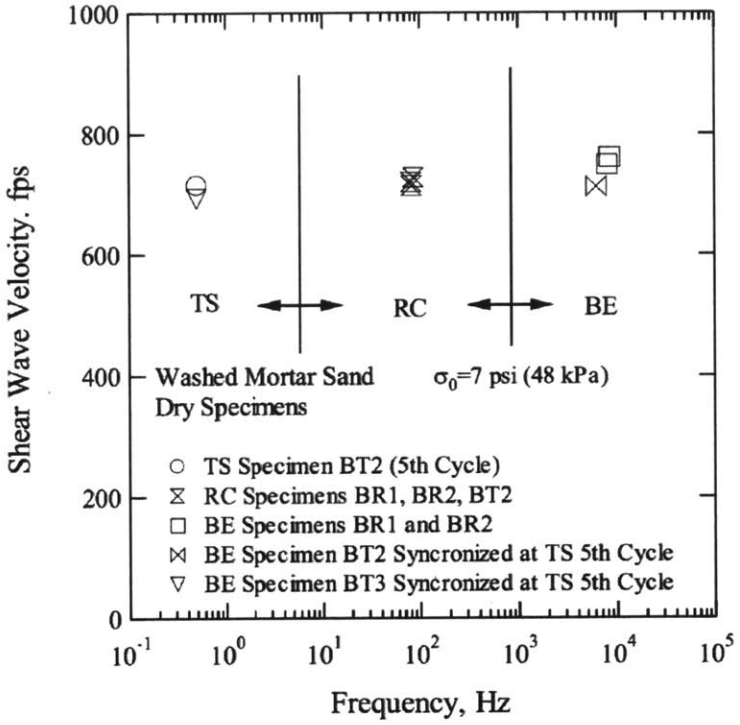

Figure 2-20: Comparison of torsional shear, resonant column, and bender element tests on washed mortar sand specimens at 7 psi (48 kPa), with varying driving frequencies (Valle-Molina, 2006)

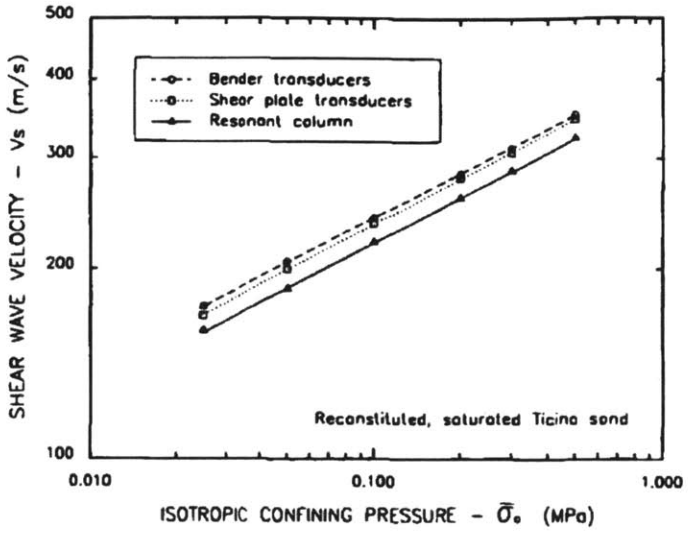

(a) V_s results on Ticino sand using RC, UT, and BE

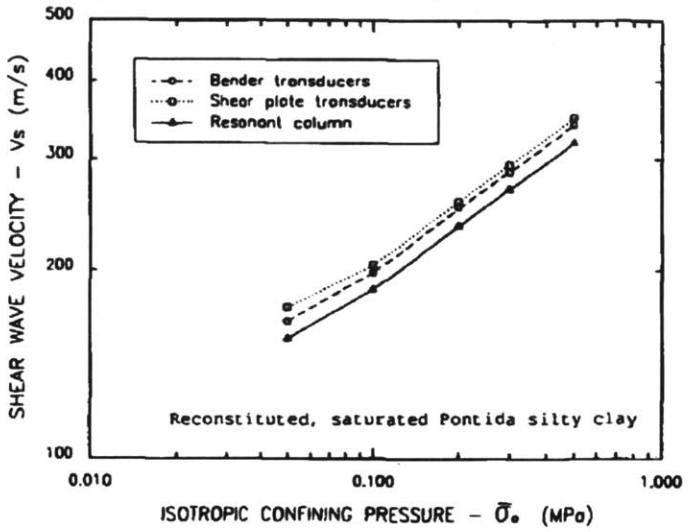

(b) V_s results on Pontida clayey silt using RC, UT, and BE

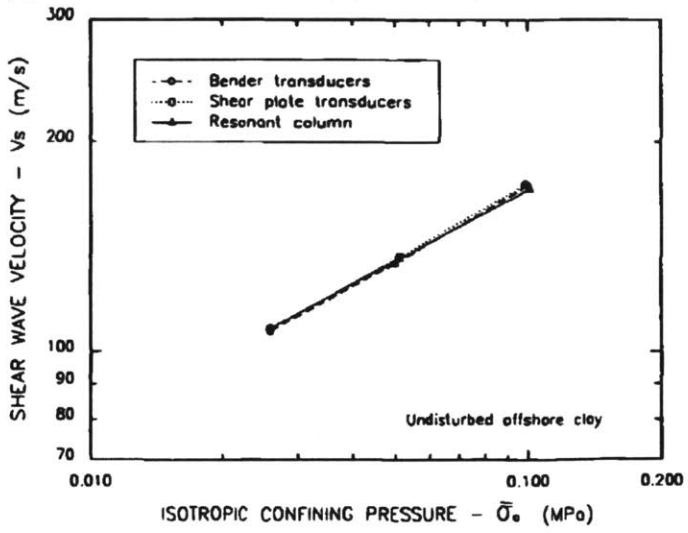

(c) V_s results on offshore clay using RC, UT, and BE

Figure 2-21: V_s for different materials using bender elements, ultrasonic transducers, and resonant column (Brignoli et al., 1996)

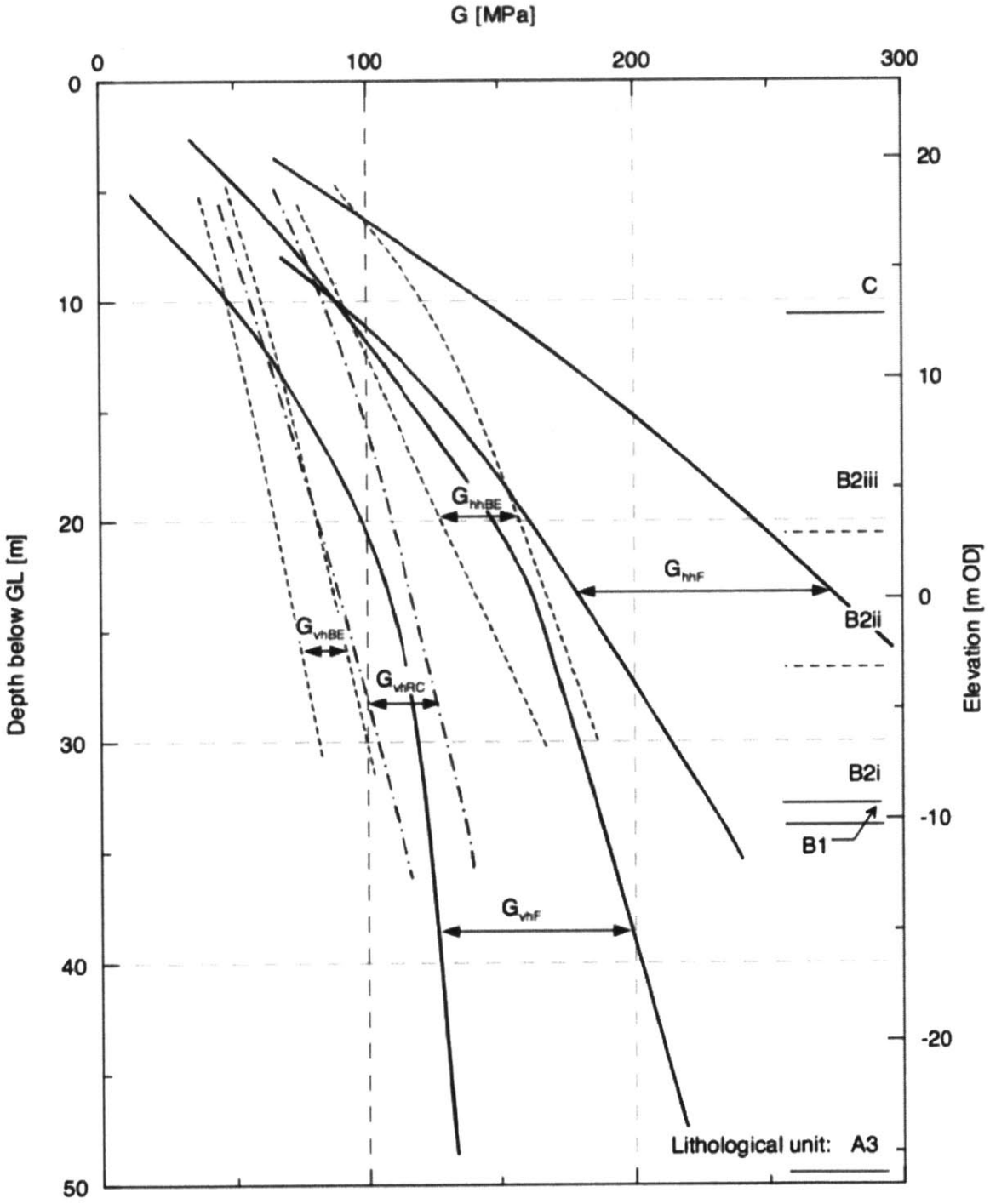

Figure 2-22: This study on London clay compare the vertical and horizontal velocities obtained with down-hole seismic (field = F), bender elements (BE), and resonant column (RC), as a function of depth. Ranges are given for each method, indicated by the arrows (Nishimura, 2005)

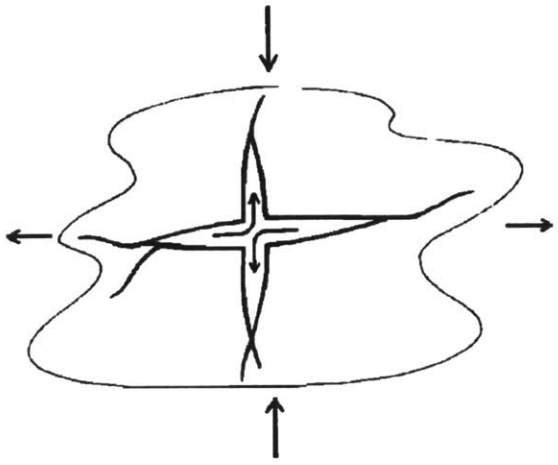

Figure 2-23: The squirt flow mechanism caused the movement within a pore of between two pore spaces, such as the two differently-oriented cracks here (Mavko and Nur, 1975)

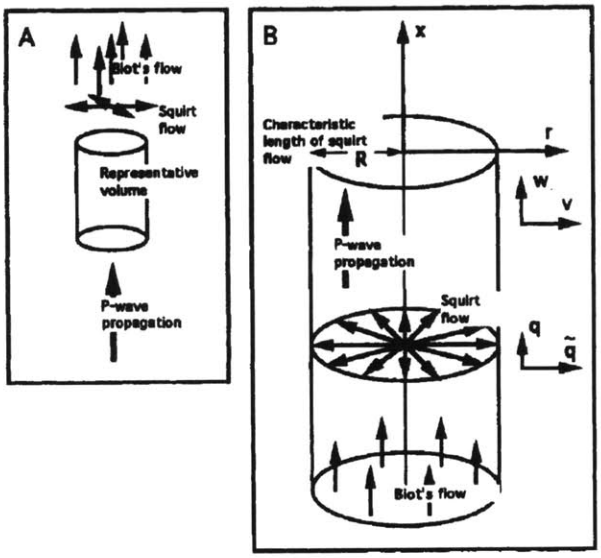

Figure 2-24: The BISQ model, which is a combination of the Biot and squirt-flow mechanism is depicted here with the respective dominant direction of flow for each mechanism (Dvorkin and Nur, 1993)

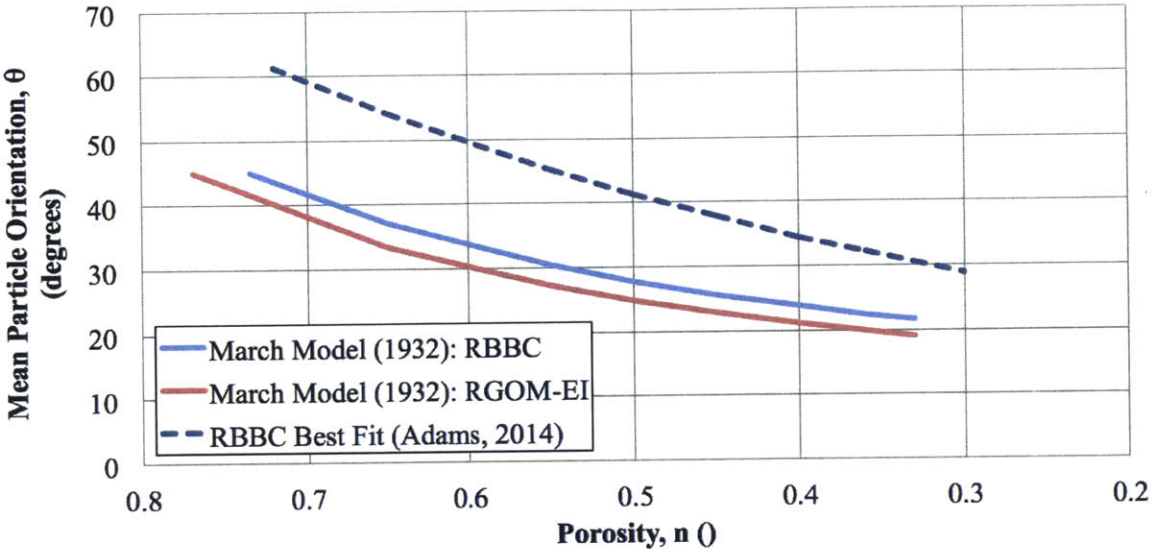

Figure 2-25: The mean particle orientation of RBBC and RGOM-EI is predicted using the March (1932) model, and is compared to the best fit line of the experimental results obtained from Adams (2014). Figure adapted from Adams (2014)

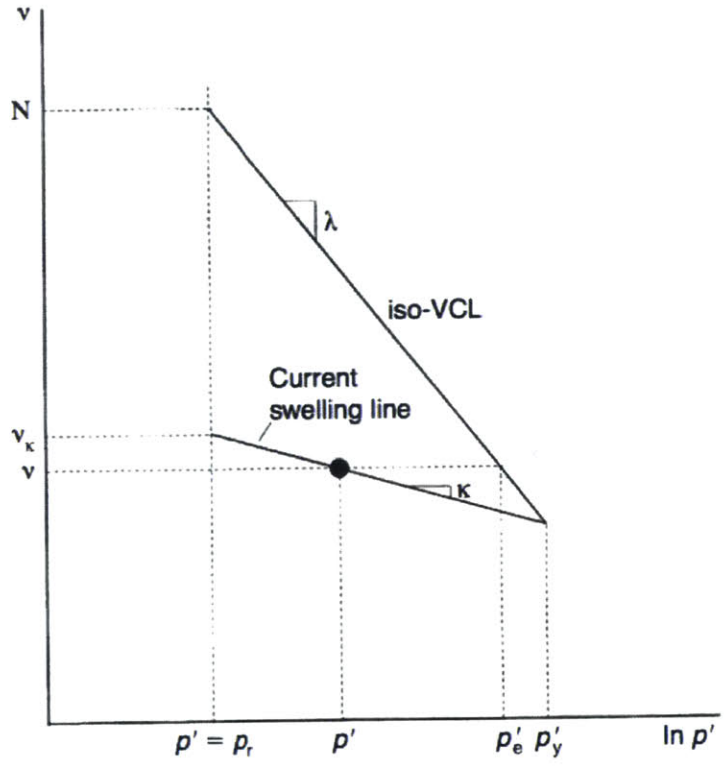

Figure 2-26: Example compression curve using nomenclature in Equation 2.18 (Rampello et al., 1997)

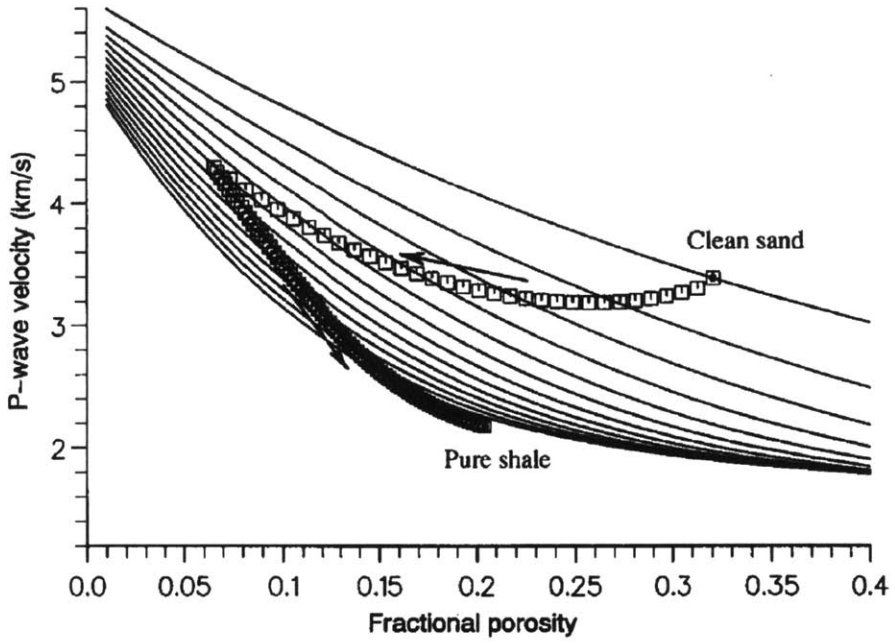

Figure 2-27: Porosity-velocity relationship obtained from the Xu and White (1995) model, an inclusion effective-medium theory. The clay content ranges from 0% (labeled clean sand) to 60% clay (labeled pure shale). Arrows show increasing clay content. Based on pore aspect ratios of 0.15 and 0.04 for sand and clay respectively. The squares are the model applied to a sandstone with originally 32% porosity, and the porosity behavior reduced to 20% for pure shale, per Marion et al. (1992)

Chapter 3

Materials, Equipment, and Procedures

3.1 Introduction

In the following sections, a detailed description of the source materials, how the test specimens are made (using resedimentation), as well as the equipment setup and procedures is provided. The source materials used in this research, including Presumpscot Clay, Boston Blue Clay, Gulf of Mexico-Eugene Island, and Gulf of Mexico Upper and Lower, were selected for their wide variety of properties. They cover a broad area on the plasticity chart, as seen in Figure 3-1, as well as a wide grain size distribution (Figure 3-2) and permeabilities (Figure 3-3). The plasticity of the materials was obtained from the liquid limit and plastic limit, where the liquid limit was determined using either the Casagrande cup method (ASTM D4318) or the falling cone method (BS 1377), as specified in Table 3.1. The grain size distribution was obtained using the hydrometer test (ASTM D422). A compilation of the index properties and origin of the soils can be seen in Table 3.1. The clay fraction listed is defined by the percentage of particles finer than $2\mu m$. The Unified Soil Classification System (USCS classification) (ASTM D2487) is based on the materials' properties, coinciding with their location on the plasticity chart, as labeled in Figure 3-1. The specific gravity, a measure of the grain density of the soil (ASTM D854-14), is also provided in Table 3.1.

Finally, the Cation Exchange Capacity (CEC) and Specific Surface Area (SSA) are listed in Table 3.2. Many of these materials have been extensively tested by other researchers, in particular those working at the MIT Geotechnical Laboratory. Credit is given to those that conducted the index tests.

The process of resedimentation allows for the iterative testing of a single source material with limited variability. One major concern with velocity testing is the proclivity to have variable source material as well as significant sample disturbance, especially for intact samples obtained from deep locations or offshore. The inability to differentiate between intact specimen variability and testing constraints has been a major damper to the investigation of velocity behavior in soils and rocks. With the use of resedimentation, a rather large number of undisturbed, fully saturated samples were produced to the desired pore fluid salinity and stress level. This would not be possible with natural intact samples. Instead of designing the equipment to fit the conditions of the material (such as load and cell capacity, amount of strain, etc.), the specimen was designed to fit the equipment. Furthermore, with the abundant supply of identical samples, proof of concept for new equipment has become quite seamless. Finally, the reliability and repeatability of this research has relied on following the precise protocols established in this chapter.

3.2 Source Materials

The materials used in this research were primarily made using resedimentation, signified by the R in the abbreviation for the material[1]. The only intact material used in this research was Presumpscot Clay. In the tables and figures, when Presumpscot Clay is described as RPC, it means that material in the powder state was used for the test, such as when performing the index testing or mineralogy analysis. For all the triaxial tests performed in this thesis, intact material is used, thus the material is labeled as Presumpscot clay.

[1]Intact Boston Blue Clay is abbreviated BBC, while Resedimented Boston Blue Clay is RBBC. This is consistent for all the abbreviations

The clay mineralogy of each material used in this research was determined using X-ray Diffraction (XRD) and was performed by Macaulay Scientific Consulting Ltd. of Aberdeen, U.K. Both a sample of the bulk material and the clay fraction ($< 2\mu m$) was tested. The results for the bulk material can be seen in Table 3.3, while the results for the clay fraction are in Table 3.4. The clay fraction was separated using timed sedimentation and then it was glycolated, heated, and air dried. The graphical representation of the mineralogy is seen in Figures 3-4 to 3-8. Each material has a combination of quartz, plagioclase, illite + illite-smectite, and varying amounts of other minerals.

3.2.1 Presumpscot Clay

Presumpscot Clay is a glacial marine clay located in Central Maine. This soil was extensively tested by Reynolds and Germaine (2007), and further information about its mechanical behavior can be found in their paper. The material used in this research was intact material from shallow bore tubes. The samples are from above the water table, thus possible cementation occurred due to oxidation, and there might be some organics present. The Resedimented Presumpscot Clay (RPC), such as that used in the index property tests, was a mixture of numerous bored tubes of clay that were air-dried, ground into a powder, and homogenized. This procedure provided a uniform source material that is a representative sampling of the material properties. Presumpscot clay has a liquid limit of w_L=33.1%, a clay fraction of 37%, and a specific gravity of G_s=2.772. Its bulk material is primarily comprised of quartz, muscovite, and plagioclase (Figure 3-4a), while the clay fraction is over 75% illite (Figure 3-4b).

3.2.2 Boston Blue Clay

The most widely tested material at the MIT Geotechnical Laboratory, Boston Blue Clay (BBC) is a low plasticity glacio-marine clay that is revered for its testability. Due to its low sensitivity and mid-range consolidation times, as well as its abundant supply at MIT, it is an excellent soil for testing. Currently found in most of the Boston

area, MA, it was originally deposited about 12,000 to 14,000 years ago (Kenney, 1964) in a marine environment following deglaciation. This illitic clay therefore is mainly comprised of glacial outwash. BBC can be found mostly in the shallow ground layers and is usually 20-40m thick. The top 12-20m forms a stiff, overconsolidated crust, while below 20m is normally consolidated (Santagata, 1998). The material used in this research is Series IV BBC powder. The series number corresponds to the location of the source material. While Series I-III were obtained from various regions around Boston, Series IV was obtained from an excavation site at MIT's Koch Biology Building (Building 68) in Cambridge, MA in 1992. In order to use BBC for resedimentation, in needs to be transformed into a powder form. This was accomplished by adding tap water to the excavated material to soften it into a thick slurry. It was then sieved with a #10 standard US sieve to move debris such as shells and twigs. This slurry was then oven-dried at 60° C and ground fine enough to have 95% passing a #100 US sieve. The Sturtevant Company accomplished this with a roller mill. Finally it was homogenized for uniformity and stored in 40-gallon buckets (Cauble, 1996).

Boston Blue clay has been extensively tested at MIT, starting with Bailey (1961) to most recently Casey (2014), Adams (2014), and Horan (2012). An extensive list of tests conducted on BBC can be found in Abdulhadi (2009). BBC has extremely well-known stress-strain behavior, strength anisotropy, strain rate dependency, permeability, and consolidation characteristics. Most recently its strength properties are known up to 100MPa and its resistivity, resistivity anisotropy, and permeability anisotropy behaviors are known. Although the intact material has some minimal variability, the homogenized batches used over the past 50 years have been very consistent. Comparisons between intact and resedimented BBC have been conducted by numerous researchers including Berman (1993), Casey (2011), House (2012), Horan (2012), thus will not be repeated here. BBC has a liquid limit of w_L=46.5%, clay fraction of 56%, and specific gravity of G_s=2.778. It's bulk material is primarily quarry, plagioclase, and muscovite (Figure 3-5a), while the clay fraction is about 92% illite (Figure 3-5b).

3.2.3 Gulf of Mexico - Eugene Island

As the name implies, this high plasticity clay originates from the Eugene Island area in the Gulf of Mexico, about 70 miles off the coast of Louisiana. The location can be seen in Figure 3-9. The RGOM-EI material used in this research was obtained by mixing the material bored from two wells: The A-20ST2 well in Block 330 and the A-12 well in Block 316 (Stump and Flemings, 2002). These areas are mostly comprised of Pliocene and Pleistocene sedimentary fill deposited over a salt-weld. As the gamma ray logs in Figure 3-10 suggest, the depth interval of the cores ranged from 2200m to 2500m. This figure also notes where the samples tested by Stump and Flemings (2002) are tested. As described by Betts (2014), the cores were processed at the University of Texas at Austin. The sandy intervals in the core were discarded while the clayey materials were kept and broken into baseball-sized chunks, spread on plastic sheeting, and air-dried for 18 days. It was subsequently ground into a powder by an external company to the specification that 99% passes a #100 sieve (diameter of 0.15mm), and then thoroughly homogenized. RGOM-EI clay has a liquid limit of w_L=87.0%, a clay fraction of 65.0%, and a specific gravity of G_s=2.775. Its bulk material is primarily comprised of quartz, illite and illite-smectite (Figure 3-6a), while the clay fraction is over 65% interlay smectite (Figure 3-6b), which is calculated using the expandability and illite-smectite percentage. In-situ salinity measurements were reported as ranging from 63g/L to 116g/L by Losh et al. (2002).

While RGOM-EI has been tested by other researchers to obtain its mechanical properties, including Casey (2014), Betts (2014), and Fahy (2014), there are additional velocity tests done on this source material. In-situ velocity measurements were obtained by wireline logging tools for well A-20ST2. Furthermore, Stump and Flemings (2002) conducted laboratory velocity measurements on intact samples from both the A-12 and A-20ST2 wells. The results of these experiments are presented later in Chapter 5.

3.2.4 Gulf of Mexico Upper & Lower

The Gulf of Mexico Upper and Lower material is sourced from a proprietary location; however, the material properties were obtained at the MIT Geotechnical Laboratory and are subsequently specified. The primary challenge of this material was its initial processing to obtain the dry powder needed for resedimentation. These soils were originally drill cuttings obtained from a borehole and thoroughly mixed in with drilling fluid. The drilling fluid was removed with washing the cuttings with Toluene, sieving out the clay chunks, and repeating this process four more times to remove all the drilling fluid. An image of the material before and after cleaning can be seen in Figure 3-14. The difference in appearance between the Upper and Lower intervals is apparent – the Upper interval contains brittle, dark grey chips about 1-2 cm in size, while the Lower interval consists of similar dark grey chips but only 0.5-1cm in size and much easier to break apart. The same procedure of drying, grinding, and sieving was followed for these materials as previously mentioned. For more detailed description and pictures of cleaning, refer to Fahy (2014)

RGOM Upper clay has a liquid limit of w_L=64.7%, a clay fraction of 70%, and a specific gravity of G_s=2.804. Its bulk material is primarily comprised of quartz, illite and illite-smectite (Figure 3-7a), while the clay fraction is 66% smectite (Figure 3-7b). RGOM Lower clay has a liquid limit of w_L=62.7%, a clay fraction of 54%, and a specific gravity of G_s=2.71. Its bulk material is primarily comprised of quartz, illite and illite-smectite (Figure 3-8a), while the clay fraction is 54% illite (Figure 3-8b).

3.2.5 Ticino Sand

Although tested in very limited quantities, Ticino sand was used as a convenient proof of concept for the testing equipment. Ticino sand is sourced from Italy and its properties can be seen in Tables 3.5 and 3.6. During setup of this material, a rodding method was used to make sure no large voids were present. Furthermore, it was tested in the dry state, and then saturated during the experiment with flash vacuum saturation to test the wet state. Unfortunately no density values were measured for

the Ticino sand experiments, hence no modulus values are presented for this material, only velocity values.

3.3 Resedimentation

Since its introduction by Bailey (1961) to the MIT Geotechnical Laboratory, resedimentation has been extensively used as a means of producing identical clay specimens for testing in the laboratory. The process has transformed significantly over the last 50 years, starting for partially saturated specimens, then progressing to fully saturated specimens, and finally allowing for high stress (40 MPa) saturated specimens. The benefits of resedimentation include not only the supply of an abundant amount of homogeneous samples, but also the ability to alter the fabric in a way that can isolate specific factors that affect soil behavior, such as salinity and silt content. Although this research does not vary these factors, resedimentation does allow for the creation of samples at *specific* salt concentrations, and take the specimens to desired stress levels needed for this research before testing them in the triaxial cell.

3.3.1 Salinity

The water content and salinity used for resedimentation varies greatly from one material to the next. The values used for each material can be seen in Table 3.7. The ideal water content is achieved when the slurry is pourable but not too watery that it begins to separate. The amount of salt added during resedimentation depends on the original salinity of the material, listed in Table 3.7 as "Natural Salts". Thus the water content and the natural salt content roughly determine the resedimentation salinity. For example, BBC has a natural salt amount of 2.19 g/kg. At 40% water content, which is typical for in-situ conditions, this would correspond to a pore fluid salinity of 5.5 g/L. It is usually beneficial to batch the material at a salinity *higher* than the in-situ pore water salinity in order to take into account the variability of the material, thus a 16 g/L batching salinity was selected.

It should be noted that for all the samples in this research, the material is batched

at a salinity without originally considering the natural salinity of the material. The salinity at which we attempted to create the slurry is a the "Resedimentation Salinity" column of Table 3.7. However, this is an inaccurate representation of the sample salinity since it does not take into account the natural salinity present in the dry clay powder. When the natural salts are taken into consideration, the *actual* total salinity of the slurry is computed in the "Actual Salinity" column. The salinity at which the specimen is originally made during mixing is assumed to remain constant during the consolidation process – i.e. the fluid expelled is homogenous and is not preferentially more/less saline than the remaining pore fluid[2].

3.3.2 Resedimentation Procedure

For this research, a standard technique for resedimentation was used for all the clay types, with slight differences in salinity and batching water content. The steps followed for resedimentation are specified below.

Powder

Before beginning the resedimentation process, the powder form of the soil needs to be made. All of the materials used in this research were originally extracted from the field. Although the methods to produce the powder do not vary greatly, there are a few difference that are enumerated in the previous sections. Overall, the intact material is essentially dried and ground to pass 95% through a #100 standard U.S. sieve.

Slurry and Deposition

Distilled water, sea salt, and clay powder are mixed to form a slurry. The amount of water used depends on the clay and salinity. Enough water is used to make the slurry pourable into the consolidation tubes; however, not too much water is added

[2]It has been hypothesized that depending on the stress level, the pore fluid versus the clay-bound fluid can preferentially be expelled from the specimen, which would progressively change the cumulative salinity of the specimen. This topic is not investigated in this research

that separation of the water and clay occurrs (i.e. no free water at surface). As a first order of approximation, a water content of about twice the liquid limit is used. The slurry is mixed with an electric mixer at a low speed until it is sufficiently homogenized and no lumps present (Figure 3-12). The slurry is left to hydrate overnight. Next, it is de-aired by applying a vacuum to a large Büchner flask at 15 to 25 inches of mercury, as seen in Figure 3-13. The slurry is then poured into an acrylic tube using a funnel, as seen in Figure 3-14a. On both ends of the slurry is a porous stone and nylon filter paper, which allows for double drainage.

Consolidation

In order to reach the desired stress state, the slurry needs to be incrementally loading using a load increment ratio of one, which means the stress is doubled at each increment. The first load is the weight of the porous stone, followed by various PVC spacers, and then the load frame and hanging weights (Figure 3-14b). If too much load is added at once, there is too much extrusion around the sides of the stone. The duration of each increment depends on the time to End of Primary (EOP) consolidation. This time is quite high for the high plasticity clays like RGOM-EI, while RBBC has a much faster EOP time. Whenever possible, a floating setup was used during resedimentation, which means that both the top spacer and bottom spacer can displace soil, thus the acrylic tube needs to be floating and not touch the bottom. This setup is used for two reasons: reduce friction and have uniform water content.

Once the target stress level is reached, the sample is allowed to sit at that maximum stress level for a full log cycle longer than the time to EOP in order to achieve secondary compression. Finally, it is unloaded to an OCR=4 using one load increment over the time span equivalent to the final time to EOP. Unloading brings the sample to an isotropic stress state, where K_0=1 and there is minimal shearing during extrusion. K_0 is the ratio of the horizontal to the vertical effective stress:

$$K_0 = \frac{\sigma'_h}{\sigma'_v} \tag{3.1}$$

Extrusion and Trimming

The last steps before commencing the triaxial test are extrusion and trimming. The sample can either be extruded manually or with a hydraulic jack. Once the sample is free, it is trimmed with a wire saw and a mitre box. The final step of precise cutting is performed with a large razor blade. The tube in Figures 3-14a and 3-14b is bigger than the ones used for this research's triaxial tests. A tube with the same diameter as a triaxial specimen was selected (1.4 inches or 3.56 cm) so that only vertical trimming and no lateral trimming was needed. The trimmings are typically used for water content measurements.

3.3.3 High Stress Resedimentation

While the gravity hanger system works well for the low stress samples, it is limited to 50kg of weight before the hangers begin to break down. This means that for a sample made to be the size of a triaxial specimen (Area = 9.93 cm^2) reaches approximately 0.5 MPa. If further loading is needed, the pneumatic actuator is used, which has the capability of applying up to 1000 kgf of load.

3.3.4 Evaluation of Specimen Uniformity

There are two possible causes of heterogeneities in the resedimented samples that are discussed here. One is the vertical variation in composition of the sample. The other is the radial heterogeneity introduced by the sidewall friction.

The vertical variation in the sample is briefly addressed by the mention of the floating setup. This research observes that if the fixed setup is used, where the deformation is only applied from one end of the sample, there tends to be about 1-5% difference in water content from the top to the bottom of the sample. This can be explained by the fact that stress at the bottom of the sample is about 20% less than that exhibited at the top of the sample, caused by the sidewall friction (Casey, 2014). Finally, although trimmings are taken as a first order approximation of the water content of the sample, it is prone to well-documented errors, induced by handling

of the trimmings (human contact) and the migration of water to the surface during the trimming process and subsequent evaporation. Previous researchers (Germaine, 1982, Seah, 1990) have evaluated the uniformity of their resedimented samples via water content measurements, checking vertical and radial slices for stratification, and x-ray diffraction pattern methods, all confirming adequate homogeneity.

Another concern is smearing at the interface of the soil and acrylic tube, causing radial heterogeneities. The presence of slight smearing is supported by the plastic-like, smooth appearance of the exterior of the sample after extrusion. Since this research uses tubes with the same inner diameter as the diameter of a triaxial specimen, no trimming is needed, thus retaining the "smeared" surface. To investigate whether an untrimmed specimen behaves differently from one whose exterior has been trimmed away, Abdulhadi (2009) performed triaxial tests on both scenarios. The graph in Figure 3-15 compares the compression curves of two specimens: 1) a specimen consolidated in a "Stnd" device with a diameter d=6.35 cm and trimmed down to 3.45cm and 2) a specimen consolidated in a "Plexi" device with d=3.45 cm, with no need for trimming. Both specimens were loaded to a target stress of $\sigma'_p = 0.1MPa$ during resedimentation, and $\sigma'_p = 0.35MPa$ during pre-shear K_0 consolidation. The void ratio for the "Plexi" case is initially higher than the "Stnd" case due to the larger amount of sidewall friction experienced. The sidewall friction reduces the amount of load that the sample experiences, thus for the same applied load, the "Stnd" sample feels more of it than the "Plexi" sample. They do, however, converge at the end of K_0 consolidation, indicating that any disturbances and smearing effects are quickly overcome. Furthermore, Abdulhadi (2009) saw that the behavior during undrained shearing for the two specimens was nearly identical. Based on these results, the sidewall friction effect was considered negligible, especially for the stress ranges experienced in this research.

3.4 Triaxial Experimentation

This section describes the testing equipment and procedures used to conduct velocity testing on mechanically-compressed cohesive soils. More than one type of testing technique is used to encompass such a wide stress range. The low and medium stress testing (0.1-1M Pa and 1-10 MPa, respectively) was done at the MIT Geotechincal laboratory. While the low-stress results will be briefly presented in Chapter 5, they will not be discussed in detail. The experimental setup for the low stress is described in Marjanovic (2012) and will not be repeated here. The medium stress equipment is discussed in Sections 3.4.1 through 3.4.4, followed by the testing procedures in Section 3.4.5. The high-stress testing was conducted at off-site facilities and is described in Section 5.6.

3.4.1 Triaxial Equipment

Overview of Triaxial System

The medium pressure triaxial system used in this research was originally developed by Andersen (1991) for testing frozen and unfrozen sands, but was subsequently modified by Abdulhadi (2009) and eventually the endcaps were further modified by this author to measure wave propagation.

K_0 conditions and stress path control are performed in the automated medium stress triaxial cell. Although the apparatus is capable of shearing the specimen in both extension and compression, these capabilities are not used by the author. The triaxial device itself has been used by previous researchers, and the evaluation of the testing system can be seen in Abdulhadi (2009), Casey (2014), and Fahy (2014). The evaluation of the velocity, however, was more difficult to test, since the materials tested in this research had not been tested before with this type of velocity equipment. Sections 6.4.1 and 5.8 contain some comparisons between the velocity data from this research and other published research, while Sections 6.3 and 6.5.2 compare this research with theoretical boundaries and fluid substitution models.

The general triaxial test setup consists of a triaxial cell connected to Pressure Vol-

ume Actuators (PVAs) that are monitored by a control box connected to a computer. The schematic is shown in Figure 3-16. Although the medium stress triaxial setup is slightly modified from this figure, the general concept is the same. The setup can be roughly divided into the triaxial cell and load frame, the PVAs, the control system, and the data acquisition system.

Triaxial Cell & Load Frame

The triaxial cell can accommodate a 3.5 cm diameter specimen with top and bottom drainage. The pressure cell, which is designed to have a cell pressure capacity of up to 20 MPa, is a 10 mm zinc-plated carbon steel wall. Figure 3-17 shows a schematic of the triaxial cell when it is fully assembled, while Figure 3-18 shows a cross-sectional view of the cell. The height of the specimen is not listed intentionally, since the height can vary.

The load is applied with a 9 Tonne (89 kN) hydraulic ram controlled by a Pressure Volume Actuator (PVA) filled with silicon oil. The load frame has a pedestal that is pushed upward against a stationary cross bar. The load is transmitted to the specimen through a 2.54 cm diameter hardened steel piston, which is sealed with an O-ring. An internal 2,000 lb capacity (8.9 kN) load cell is attached to the piston in order to avoid the effects of O-ring friction at the seal. An image of the piston assembly is seen in Figure 3-19. This image shows a spacer between the piston and the load cell, as well as an alignment cap with tubing that connects it to the spacer. This setup allows the application of suction on the specimen top cap in the case of a triaxial extension test (negative deviator load). The alignment cap in this case has an O-ring that seals with the top cap. Although this research did not apply suction in any of the experiments, the same alignment cap is used without connecting the alignment cap to atmosphere, but rather open to the cell fluid.

The chamber is filled with Dow-Corning "200 fluid", 20 centistokes silicon oil. This particular fluid was selected due to its non-conductive nature in the presence of electronics. Since both the load cell and the velocity endcaps have wires running from the inside of the cell, through the triaxial base (via 9-pin amphenol connectors), and

out to the atmosphere, silicon oil prevents short circuits. Furthermore, silicon oil is known to have exceptionally low viscosity at a wide range of temperatures, thus can be used in many different testing conditions. Finally, it does not react with the latex membranes used in testing and leakage is not an issue.

The modifications to this setup included hollowing out the top cap and pedestal to house the acoustic actuators. Figure 3-20 shows a zoomed version of the pedestal. In order to reduce the complexity in the waveforms introduced by having a porous stone between the actuators and the soil, an annular cut is made around the pedestal. This allows an annular stone to sit on the pedestal and enable free drainage from the specimen to a drainage line specifically angled to coincide with the stone.

Although not included in the schematics, there is a drainage line that connects the top cap to the base. This drainage line is copper tubing coiled entirely around the specimen to allow for the large vertical deformation during consolidation. A picture of the coil can be seen in Figure 3-22. The top and bottom drainage lines connect to a pressure transducer through a series of valves and tubes, seen at the bottom of Figure 3-17.

The specimen is sealed with two thin membranes ordered from Durham Geo Enterprises. The membranes are 0.03 cm (0.012 inches) thick and fit a 3.5 cm (1.4 inch) diameter specimen (Part #S-54014). This configuration is used since Abdulhadi (2009) saw leakage beyond 3 MPa when two extra-thin membranes (unlubricated condoms) were used. While two thin membranes work well for testing RBBC up to a vertical effective stress of 10 MPa (i.e. confining pressure up to 6 MPa), some of the other materials that have higher K_0 values (thus higher confining pressures for the same σ'_v), and longer consolidation times had leakage. When the test took longer than two weeks, there was a reaction between the porous stone/brass endcap/membrane interface. The membrane became discolored and fused to the stone. It seems to be a time-dependent reaction. Two tests performed at the exact same stresses, but one was done under two weeks, while the other took three weeks. The shorter experiment did not exhibit leaking, while the other did. Whether leaking was caused by the fusing or some other time-dependent degradation of the membrane is unclear. It is

advisable to use at least one thick membrane (0.06 cm or 0.025 inches thick) in lieu of a thin membrane for tests that run for longer than two weeks.

In addition to the PVA that applies axial load to the specimen, there are two PVAs that control the pore (water) pressure and cell pressure. The pore pressure PVA also has a string pot that measures the displacement of the PVA piston, thus enabling the measurement of volume change in the pore pressure. The string pot measures piston displacement, and given the area of the PVA piston (2.85 cm^2), a volume is calculated. This is a critical component to the PID (proportional-integral-derivative) control algorithm that allows allows for K_0 consolidation. These PVAs (Figure 3-23) have a pressure capacity of 14 MPa and a volume capacity of 47 cm^3. A 0.5 ton Duff-Norton® inverted ball screw jack is driven by Maxon Motors® servomotor with 80 mNm continuous output (geared at 84:1). Finally, all the PVAs have a limit switch at both extreme ends of the stoke, which triggers the shut down of power to the servomotor. Both the pore pressure and cell pressure are connected to 1,000 psi (7 MPa) capacity pressure transducers.

The triaxial chamber, the three PVAs, and the load frame are all enclosed in a temperature-controlled environment. This enclosure is located in an air-conditioned room set to a low temperature, which enables the heating device in the enclosure to turn on and off to maintain a stable temperature a few degrees above the room temperature.

Data Acquisition

The original control system was developed by Sheahan (1991) in order to automate the existing manual system components. This allows for precise automated stress path control that can run without continual supervision, greatly decreasing the manual labor needed for triaxial testing. The integration of automation into the medium stress triaxial setup was performed by Andersen (1991).

The measurement instrumentation acquires data in the most raw form: an analog signal. Measurement instrumentation includes the elements both inside and outside of the cell that measure pressure, load, and displacement. In the medium stress triaxial

setup, this includes the following:

- External LVDT (Linear Variable Differential Transformer) that measures vertical displacement
- Pore pressure transducer that can measure both back pressure and specimen pressure
- Cell pressure transducer for chamber pressure
- String pot that measures vertical displacement but is subsequently transformed into volumetric strain of pore fluid
- Internal load cell measures vertical deviator load applied to the specimen

The analog signal obtained from the instrumentation is run to a box housing a multichannel analog-to-digital converter (MADC) device developed by Sheahan (1991). This MADC device, which is the Analog Devices AD1170 analog to digital (A/D) converter[3], can be seen in Figure 3-24. The AD1170 has a high degree of signal averaging, thus eliminating noise and producing a very stable reading. The signal is then sent to a USB interface card (also housed in the MADC box), which is then sent to the computer. This interface card is specifically used for newer computers that do not have a an expansion slot to house the A/D converter. The computer runs a control program written in QBASIC, and uses this signal to evaluate which commands to send back out to the motors controlling the pressures and loads in the test, implementing either intermittent proportional or continuous PID control. USB to ISA emulator requires DOSBOX, which hosts the QBASIC software.

In order to send the digital signals from the computer to the motors controlling the PVAs, the digital signal is sent into the MADC box to be converted from digital to 12 bit analog (through the digital to analog (D/A) converter board made by Strawberry Tree Inc.), and then a custom-designed control card, housed in the control box seen in

[3]The AD1170 is a high resolution integration-type converter which allows integration times from 1 to 350 ms and a resolution from 7 - 22 bits. Based on a 10 V range, there is a maximum precision of 0.0024 mV

Figure 3-25. The control box contains the control card as well as sevoamplifiers, a 50 V dc power supply, and a fan. The motors are energized by pulse width modulation from the servoamplifiers, which is derived from a combination of the control card signal, power supply, and tachometer feedback from the motors.

In addition to the locally-obtained information and signal transmission described above, the information from the transducers, LVDTs, and load cell need to be stored for further analysis. To do this, there is a central data acquisition system that collects all the data from all the different test setups at the MIT Geotechnical Laboratory. The central data acquisition system uses a 486 microprocessor PC driven by Windows based software interfaced with a Hewlett Packard HP3497 data acquisition unit. This unit uses a low noise integrating A/D converter with auto-ranging signal amplification. The system could monitor up to 180 channels simultaneously at a rate of 1Hz.

3.4.2 Wave Propagation Equipment

The endcaps that contain P and S-wave actuators can both send and receive signals. One endcap (in this case the bottom endcap) is designated as the source, while the other (top) endcap is set as the receiver of the signal. The piezoceramic material used in the endcaps can convert strain to an electric charge, and vice versa. An image of the piezoceramics can be seen in Figure 3-26.

To excite the piezoceramics, a pulse is needed. The exact specifications of how the pulse was selected and its characteristics are explained in Chapter 4. The pulse (sent by the pulser) goes through a series of electronics that condition the pulse (also discussed in Chapter 4) before it is sent to the bottom endcap, where it excites the piezo actuator. The excited actuator transmits a pulse through the soil, which is received by the top endcap. The top endcap is connected to an oscilloscope (Tektronix TDS2001C), where the pulse is seen and saved. The schematic in Figure 3-21 shows this stepped process.

The wiring configuration connecting the endcaps is set up so that only a P-wave or an S-wave can be sent at one time. Once one of the waves has been acquired, the wiring configuration needs to be changed to connect to the other scenario. Au-

tomation was not an option at the time of testing. Furthermore, due to the aged state of the pulser, it was not advisable to keep it running nonstop for two weeks at a time. The pulse sent by the pulser was split with a BNC T-adapter so that the input signal could be sent directly to the oscilloscope in addition to being sent to the signal processing stage and eventually to the endcap. The input pulse is always used as the trigger for the oscilloscope to acquire the readings.

3.4.3 Fabrication of Piezoceramic Actuators

The novel implementation of velocity testing within the medium stress triaxial cell was accomplished by altering the traditional brass endcaps and installing piezoceramic actuators, as seen in Figure 3-27. Each endcap is fitted with an element that can propagate and receive both a compressional (P) and shear (S) wave. The description of the piezoceramic actuators purchased from Micromechatronics Inc. is listed in Table 3.8. The construction of the specialized endcaps can be seen in Figure 3-28, and is described as follows:

1. Cut copper shim stock of thickness 0.08mm to the size of the shear actuator, with one edge slightly longer to provide enough clearance to adhere a wire to it. The goal is to adhere one shim stock on either flat edges of the shear actuator, with the longer edge sticking out on opposite ends. The wires are bonded to the shim stock with silver conductive epoxy.

2. The wired shim stocks need to be adhered to the shear actuator with stiff epoxy (Loctite®$E30-CL$). The shim stock needs to be electrically connected to the shear actuator, thus when bonding, the layer of epoxy should be as thin as possible, since the epoxy is not conductive. Only a small drop of epoxy should be used and a weight of 20 kg should be applied to the sandwiched element during curing. Furthermore, other methods can be utilized to ensure the thinnest layer of epoxy possible, such as heating up the epoxy so that it has a lower viscosity, or applying a heating gun to the area after the weight is applied to encourage the epoxy to squeeze out.

3. To ensure that the shear and compressional actuators are electrically isolated from each other and the brass endcap, non-conductive DuPont^{TM} Kapton® HN is used. Two square pieces of Kapton sheets are cut and adhered to the faces of the compressional plate actuator. The sheets are slightly oversized (e.g. 11x11 mm) to make sure that when all components are assembled, the wires do no touch the other components. The Kapton sheets are adhered to the multilayer actuator with nonconductive Loctite® E30-CL epoxy, with a small pressure applied during curing to keep the two materials from sliding out of place.

4. The shear actuator and compressional plate actuator need to be adhered to each other, and then the pedestal in the endcap. Best results are obtained when the two actuators are first attached to each other using Loctite® E30-CL epoxy, wired together, and then attached as a unit to the brass pedestal. The wiring scheme includes 3 wires going through the endcap: one ground and two positive leads. The ground wires for the shear and compressional plate actuators are combined to reduce the complexity of wiring.

5. With the actuators in place, the cavity needs to be filled with a soft epoxy that reduces the restraint on the displacement of the actuators. Loctite® E-90FL epoxy is used for the purpose. The outlet of the bored holed is plugged up with some cotton, and the epoxy is poured liberally in the opening, until the top level of the epoxy reached the top shim stock.

6. Finally the hard epoxy (Loctite® E30-CL) is used to coat the surface of the metal shim stock and fill in any gaps at the top. Excess epoxy is used so that a curved surface is formed due to surface tension. This surface is then machined down with a fine grinder to ensure that any surface bubbles or discontinuities are eliminated. Furthermore, the outlet wires are attached to a 3-hole pitch socket receptacle, and the receptacle is pushed into the slot hollowed out in the endcap, finished off with some epoxy to seal it in place. This scheme is chosen to facilitate a safer design that eliminated wire fraying, as well as simplifying the setup of the membrane and O-rings in the experimental procedures.

3.4.4 Calibration of Endcaps

There is a lag in the arrival time of any signals received by the oscilloscope. This lag is caused by the finite speed needed for the signal to travel across the electronics and wires before it arrives at the oscilloscope. Additionally there is a slight lag due to the epoxy between the actuators, as well as the S-wave actuators that are directly between the two P-wave actuators due to the stacking sequence of the elements. This lag time is calculated by using different length spacers and back-calculating the travel time for a spacer with zero length using linear interpolation. The materials used for the spacers were aluminum, Teflon (polytetrafluoroethylene or PTFE), and PEEK (polyetheretherketone). These materials were used since they have very different properties from each other:

- Aluminum is very stiff, non-dispersive, and non-attenuative
- Teflon is very soft and very dispersive and attenuative
- PEEK is soft and has low dispersive behavior. It also has significantly more attenuation for the S-wave than the P-wave

Rather than present all the figures for each of the materials, the procedure will be presented for a longitudinal wave through aluminum. Figure 3-29 shows the P-wave arrival times for the waves for each respective length of spacer. The best fit linear line for the three data points provides an equation of the form $y = mx + b$. b is the y-intercept of the line, which would correspond to a spacer with zero height. This value is taken as the lag time, in this case a lag time of $t_{lag} = 1.583\mu s$. In order to test the validity of this offset time, the velocity of the P-wave is computed before and after correcting for the lag time. Figure 3-30 is the unadjusted velocity as a function of spacer height, while Figure 3-31 shows the velocity profile corrected for the lag time. The corrected profile shows a constant velocity as a function of height, which is evidence that the lag correction is accurate.

This time lag back-calculation is performed for both the P and S-wave for all three materials. The resulting lag times are presented in Table 3.9, as well as a culminating

average lag time that was subsequently used for all the velocity interpretations in this research.

As a secondary means of verifying that this correction technique is accurate, the same best fit line seen in Figure 3-29 is used. The m value in the equation (a.k.a. the slope) is the reciprocal of the velocity. Thus $m = 161.304$ μs/m gives a velocity of $V_P = 6199.5$ m/s. The velocity for the P and S-wave is calculated for all the materials and compared to published results, seen in Table 3.10. The velocities measured in this research agree very well with the published results; therefore, two methods of validating this technique deemed it satisfactory to proceed with use in this research.

3.4.5 Triaxial Testing Procedures

The setup procedures for the low, medium, and high stress triaxial tests are very similar in the beginning, with slight divergences during the later stages of setup. This section will focus on the medium stress triaxial, while the high stress triaxial will be briefly described in Section 5.6.

Since the stress range of primary concern during medium stress triaxial testing is between 0.5 - 10 MPa, the samples of resedimented materials are consolidated to 0.5 - 1 MPa. The high smectite clays that have a long consolidation time are generally resedimented to the higher end of the range since, as mentioned previously, the membrane would sometimes leak if left in the cell for over two weeks. In the case that an intact sample is used, such as for Presumpscot clay, a deep section with relatively high stiffness is selectively chosen.

All the resedimented materials are made in an acrylic tube with the exact diameter needed for triaxial testing (3.5 cm), thus no trimming is required after extrusion, besides the vertical trimming to make the specimen the appropriate height. The initial height of the specimens ranges from 8 - 9 cm. The trimmings from the ends are used to obtain an estimate of the initial water content. The water content is obtained by measuring the wet mass of the material before and after 24hrs of oven drying at 90°. Although this initial water content is not used for the void ratio calculations, it is a good point of reference to which to compared the final water

content. The trimmings are generally 2 - 4% drier than the correct water content measurement based on the entire sample.

For the intact samples used, the brass sample tube is first cut with a horizontal bandsaw, the burrs are smoothed, and a wire is run around the perimeter of the tube to dislodge the clay from the tube. The clay is then pushed out of the tube, and trimmed using a cylindrical miter box and a wire saw.

Once the specimens are trimmed with a wire saw, they are put in an aluminum mold where the ends are squared off with a large razor blade. The dimensions are measured with a caliper and the wet mass recorded. The moist porous stone and nylon filter paper are placed on the endcaps before the specimen is placed between the endcaps. The nylon filter paper is placed between the porous stone and specimen. The porous stone is annular, thus does not cover the transducer; however, the nylon filter paper does cover the transducer. A membrane is stretched out using a membrane stretcher attached to a vacuum, which allows for the placement of the membrane onto the specimen without disturbing it. Once the membrane is in position, the vacuum is released and the membrane fits snuggly onto the specimen. Two O-rings are positioned at each end of the specimen, where the membrane overlaps with the endcap. A space is left between these two O-rings for the next O-ring. Next, the outer membrane is placed over the specimen, followed by the final O-ring on each side of the specimen that fits tightly between the first set of O-rings. There should be six O-rings in total. The top drainage line is then connected to the triaxial base. The final configuration should look like Figure 3-22. All the wires for the acoustic components are connected.

Next, the steel chamber is lowered down using a cantilever pulley system. Before it reaches its final position, the load cell wire is connected to the triaxial base and the load is zeroed. This enables load monitoring during the last few centimeters as the chamber is lowered to ensure that the specimen is not preloaded. The cell chamber is tightened down with six washers and nuts, and the piston is slowly tapped down with a rubber mallet until contact is established between the alignment cap and top endcap. The chamber is filled with silicon oil. A small amount of cell pressure is applied before the drainage lines are flash saturated with water of the same salinity as the

pore fluid in the specimen. The flash saturation occurs by applying a vacuum to the specimen for about 5-10 minutes, and then releasing the vacuum while the drainage lines have free access to water. At this point the specimen enters the "pressure up" stage, where approximately 0.05 - 0.1 MPa cell pressure is applied and the specimen is allowed to equilibrate overnight. The specimen is then back-pressure saturated until a satisfactory B-value[4] is obtained. Back-pressure typically applies 0.4 MPa of cell pressure and 0.3 MPa of pore pressure, while the B-value check applies 0.025 MPa. During back-pressure saturation, a small deviator load is applied ($\approx$1 kg) to ensure contact between the alignment cap and top endcap is maintained.

The next stage is K_0-consolidation. The PID control algorithm used to control consolidation is set to a strain rate of 0.15%/hr for RBBC and Presumpscot clay, while the high smectite clays are typically consolidated at a slower rate (0.07%/hr). The volumetric strain measured from the pore water being expelled from the specimen is used as a means to monitor the K_0-consolidation. Since the axial deformation is being measured, the volumetric strain should be exactly that axial strain multiplied by the initial area of the specimen in order to maintain zero lateral strain.

The specimens are consolidated to 5 MPa, at which point they are left until sufficient creep has occurred. This corresponds to an axial strain rate of less than 0.015%/hr, which takes about 24hrs, depending on the material. Next the specimens are taken through unloading cycles, to an OCR=2 and OCR=4, whenever possible. When unloading the specimen to the desired OCR, stress path consolidation is performed instead of K_0-consolidation. Although K_0-consolidation could work for some materials that have low strain rates, there is some lash-back during load reversal in the load frame, which changes the strain reading, and can affect the specimen area in the K_0-consolidation algorithm used. In order to keep test setup procedures universal, stress path consolidation is always used for the unloading portion, while the K_0-consolidation algorithm is used for the loading portion. The stress state during the unloading part is determined by calculating the K_0 during unloading using the

[4]B-value is the ratio of change in pore pressure divided by change in applied cell pressure while the pore pressure valves are closed off. A B-value of 0.95 means 95% saturation

following equation:

$$K_0 = K_{0NC}(OCR)^n \tag{3.2}$$

where K_{0NC} is the lateral stress ratio during the normally consolidated region, OCR is the overconsolidation ratio[5], and $n = 0.4$ for RBBC, and was similarly used for all the other materials. K_{0NC} is computed based on the final K_0 exhibited before unloading at each cycle. At each unloading stage, the specimen is again left to enter secondary compression before proceeding. Once the maximum OCR is reached, the specimen is reloaded using the same staged progression until it reaches the virgin compression line. For each of the tests, at least two unloading/reloading cycles were performed, usually at 5 MPa and 10 MPa whenever possible.

During the entire test, velocity measurements are taken periodically. During the K_0-consolidation, measurements are taken approximately every 0.5 MPa. During the unloading sections, a velocity measurement is only taken when the target stresses are reached. Furthermore, some measurements were made immediately when the target stress was reached, as well as after it has entered secondary compression to observe the creep effect.

3.4.6 High Stress Equipment & Procedures

The high stress testing (5M Pa-100 MPa) was done at Shell Westhollow Technology Center (SWTC) in Houston. This was the first equipment was used to tested clays, and to the knowledge of this author, the first time velocity measurements were taken on a resedimented clay at such a high stress. Usually these high stress triaxial cells are used to test hard rocks, shales, or sandstones. The test was supervised by the author; however, the author is not familiar with the detailed use of the equipment found at Shell, so only a brief description of the setup will be provided.

[5] $OCR = \sigma'_{max}/\sigma'_{current}$

Shell Exploration and Production in Houston

The triaxial cell at SWTC was made by MetaRock Laboratories in Houston, with customized software specifically made for the laboratory at SWTC. The triaxial cell has a capacity up to 100MPa, but due to some experimental difficulties, only 70 MPa was reached. There is top and bottom drainage, two internal vertical displacement LVDT's, and two radial strain gauges. The initial attempt at maintaining K_0 using the radial strain gauge measurements was not successful. The K_0 was unstable and kept dropping as the test progressed. The two possible explanations for this are that the software program was not able to maintain control and make incremental adjustments in the axial and radial load that would correspond with zero lateral strain, or the strain gauges were unable to give accurate results for a specimen that is much softer than it was designed to test. As soon as it became evident that an automated K_0 stress path was not working, the control method was changed to loading the specimen by increments of 10 MPa. The K_0 value for RBBC at high stresses was taken from Casey (2014) in order to calculate the exact stresses to apply. The signal used to excite the peizoelectric elements had a frequency of 1 MHz and a voltage of 100 V. The diameter of the specimen is 2.54 cm (1 inch) and it is confined by shrink-wrap tubing during testing.

Table 3.1: Index properties and origin of soils tested [6]

Material	Abbreviation	Origin	Liquid Limit, w_L (%)	Plastic Limit, w_P(%)	Plasticity Index, I_p(%)	Clay Fraction (%)	USCS Classification	Specific Gravity, G_s	Performed by
Presumpscot Clay	RPC	Maine, USA	33.1^{FC}	19.4	13.7	37	CL	2.772	Casey (2014)
Boston Blue Clay	RBBC	Boston, Massachusetts	46.5	23.8	22.7	56	CL	2.778	Casey (2014), Horan (2012), Abdulhadi (2009), Santagata (1998)
Gulf of Mexico - Eugene Island	RGOM-EI	Eugene Island, Gulf of Mexico	87.0	24.0	63.0	65.0	CH	2.775	Casey (2014), Fahy (2014), Betts (2014)
Gulf of Mexico Upper	RGOM Upper	Proprietary location	64.7^{FC}	25.5	39.2	70	CH	2.804	Fahy (2014), Taylor Nordquist
Gulf of Mexico Lower	RGOM Lower	Proprietary location	62.7^{FC}	26	36.7	54	CH	2.71	Fahy (2014), Taylor Nordquist

[6] FC done using fall cone method. Rest is done using Casagrande cup method

Table 3.2: Available CEC and SSA data for materials tested. SSA was performed by Adams (2014) using MB Spot Test Method. CEC was performed with a Cu-complex at University at Buffalo, SUNY

Material	CEC (meq/100g)	SSA (m^2/g)
Presumpscot Clay	-	-
Boston Blue Clay	10.7	49
Gulf of Mexico - Eugene Island	32.8	267
Gulf of Mexico Upper	31.8	230
Gulf of Mexico Lower	23.8	171

Table 3.3: The mineralogy obtained from performing XRD on the bulk materials is shown here in %. Testing performed by Macaulay Scientific Consulting LTD

	RPC	RBBC	RGOM-EI	RGOM Upper	RGOM Lower
Quartz	38.3	21.3	27.8	21.6	36.0
Plagiclase	17.0	20.5	5.3	5.5	3.3
K-Feldspar	2.9	8.2	4.0	3.3	1.8
Calcite	-	0.5	1.2	8.7	2.4
Dolomite	0.7	0.8	0.8	0.8	0.1
Siderite	0.1	-	1.0	1.7	2.6
Pyrite	0.3	-	0.7	0.9	0.7
Anatase	-	-	0.2	0	0.2
Barite	-	-	3.2	0.4	1.6
Halite		0.2	0.2	2.9	0.4
Muscovite	17.3	13.8	1.9	3.3	3.0
Illite+Illite-Smectite	9.8	7.3	44.4	44.4	37.8
Kaolinite	-	2.9	9.1	6.1	8.9
Chlorite	13.0	6.2	0.4	0.4	1.3
Amphibole	0.6	3.8	-	-	-
Tri-mica	-	9.2	-	-	-
Hydrobiotite	-	5.4	-	-	-

Table 3.4: The mineralogy obtained from performing XRD on the clay fraction ($< 2\mu m$), from Macaulay Scientific Consulting LTD

Material	Chlorite (%)	Kaolinite (%)	Illite (%)	Illite-Smectite (%)	Expandibility (%)
RPC	20	2	66	12	< 10
RBBC	5	2	65	28	5
RGOM-EI	1	4	8	87	70-80
RGOM Upper	1	3	8	88	70-80
RGOM Lower	1	6	6	87	40-50

Table 3.5: Range of test setup parameters for Ticino sand

Unit	Range
Porosity, $n()$	0.33 - 0.45
Density, $\rho(g/cm^3)$	1.4 - 1.6
Void ratio, $e()$	0.6 - 0.85

Table 3.6: Material properties of Ticino Sand (Fioravante and Capoferri, 2001)

Property	Specific gravity:	$G_S = 2.681$
	Mean particle size:	$D_{50} = 0.55$ mm
	Uniformity coefficient:	$C_U = 1.6$
	$\gamma_{min} = 13.65kN/m^3$	$e_{max} = 0.927$
	$\gamma_{max} = 16.67kN/m^3$	$e_{min} = 0.578$
Description	Uniform coarse to medium sand	
Morphology	Angular (20%), Sub-angular (55%), Sub-rounded (25%)	
Mineralogy	Quartz (30%), Feldspar (30%), Mica (5%), Opaque (35%)	

Table 3.7: Salinity and water content at which the materials were mixed during resedimentation [7]

Material	Natural Salts (g/kg)	Resedimentation Salinity (g/L)	Water Content (%)	Actual Salinity (g/L)
Presumpscot Clay	-	-	-	-
Boston Blue Clay	2.19*	16	100	18.2
Gulf of Mexico - Eugene Island	10.95**	80	122	89.9
Gulf of Mexico Upper	29.4***	70^{NaCl}	100	98.8
Gulf of Mexico Lower	7.5***	70^{NaCl}	100	78.5

Table 3.8: Specifications for the piezoceramics used in this research, from Micromechatronics Inc.

	P-wave	S-wave
Part number	NAC2015	CSAP03
Dimensions (mm)	10x10x2	10x10x0.5
Operational voltage (V)	150	+/-320
Material	NCE51F	NCE51
Capacitance (nF)	760	3.32

[7] * Average value from Adams (2014), Casey (2014), Horan (2012)
** Average value from Adams (2014), Casey (2014), Betts (2014)
*** Measured by Amy Adams for Fahy (2014)
^{NaCl} indicates that material was resedimented with NaCl. If not specified, Sea Salt was used

Table 3.9: Lag times for the different materials tested based on an interpreted $h = 0$ for the spacers. The average of the three materials was used as the official lag time for the P and S-waves in this research

	P-wave lag time (μs)	S-wave lag time (μs)
Aluminum	1.584	0.554
Teflon	2.479	1.614
PEEK	1.801	1.206
Average	**1.955**	**1.125**

Table 3.10: The reciprocal of the slope of the line in Figure 3-29 yields the velocity of the material being tested. The measured results are presented here and are compared to published data found in literature (see footnotes for sources)

	P-wave		S-wave	
	Measured Velocity (m/s)	Published Velocity (m/s)	Measured Velocity (m/s)	Published Velocity (m/s)
Aluminum[8]	6199	6380	3148	3180
Teflon[9]	1352	1333	516	506
PEEK[10]	2590	2550	1149	1290

[8]Lee and Waite (2009)
[9]Rae and Dattelbaum (2004)
[10]Hu et al. (2015)

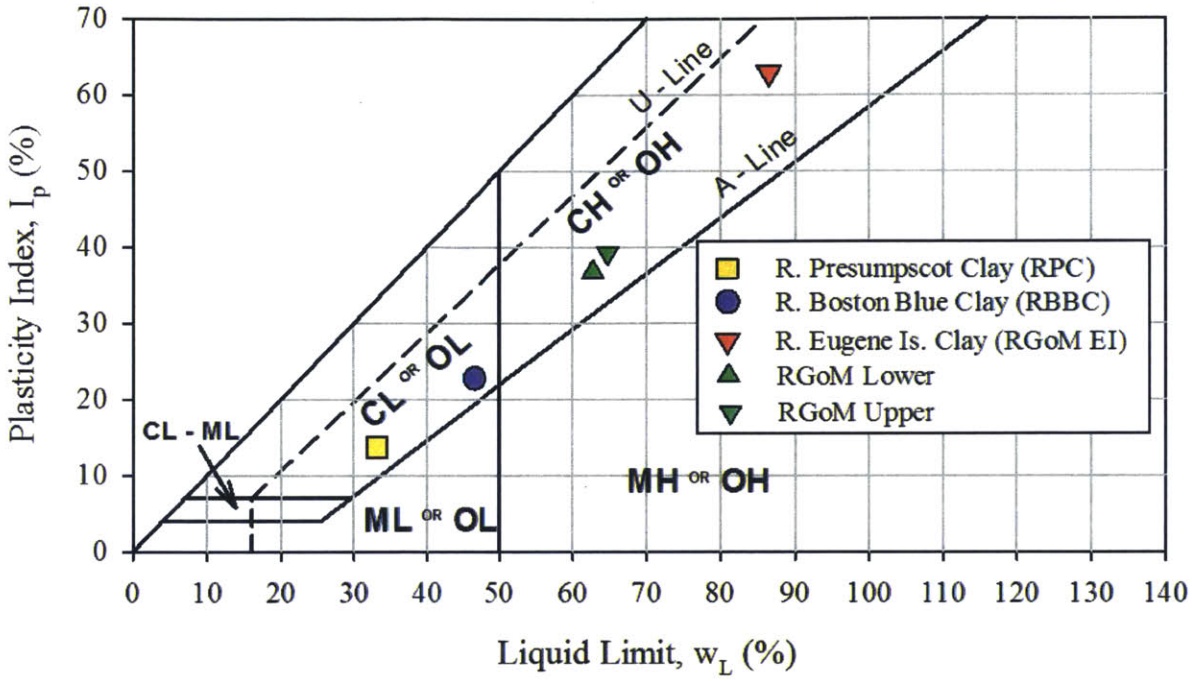

Figure 3-1: All the materials used in this research are plotted on the plasticity chart

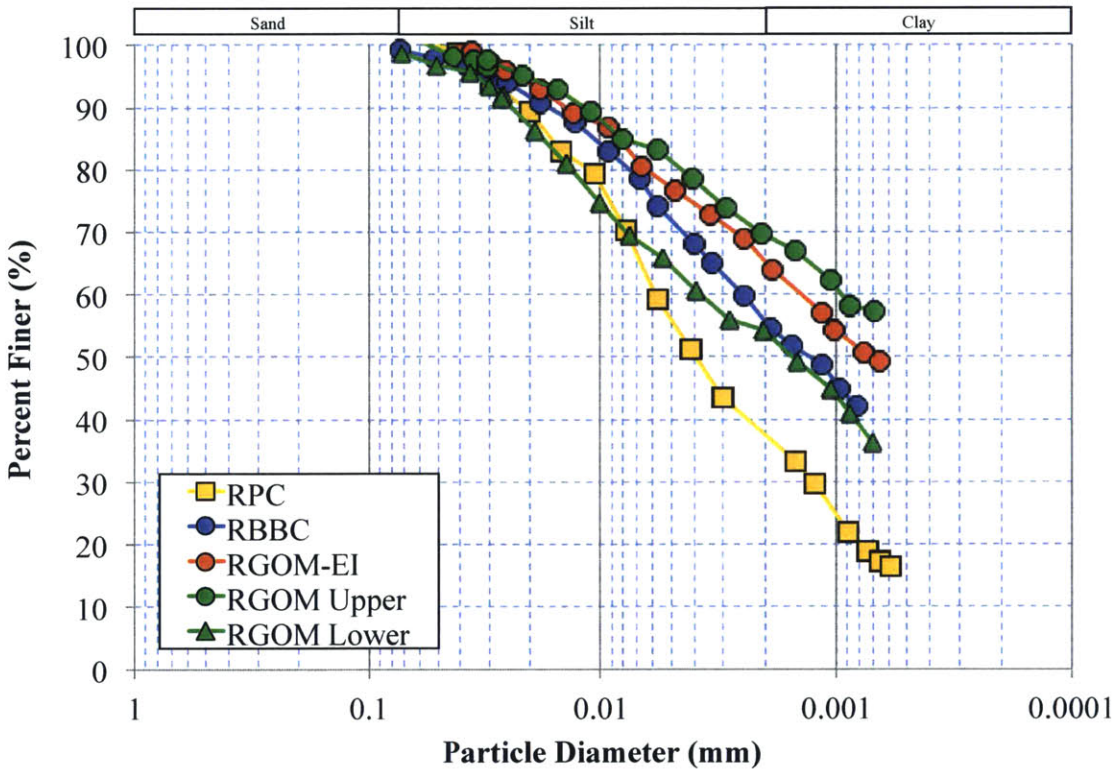

Figure 3-2: This grain size distribution chart shows the spread of the particle size as a function of % passing. The clay fraction ($<2\mu$m) was obtained using a hydrometer test

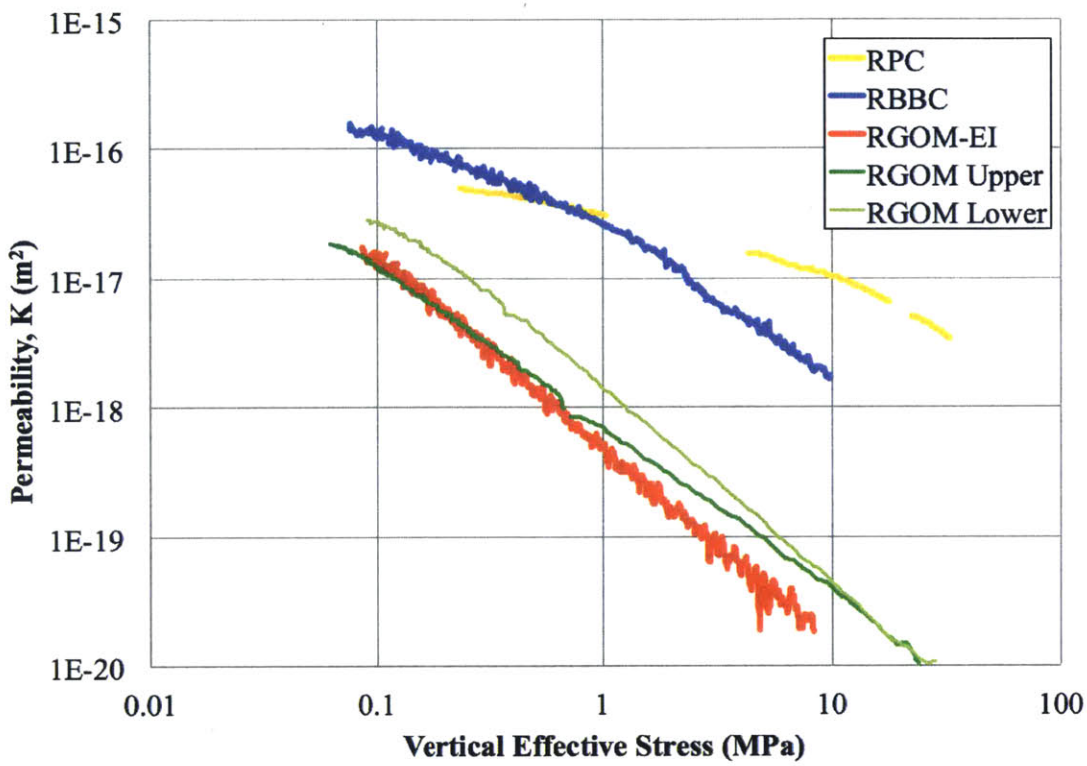

(a) Permeability as a function of stress

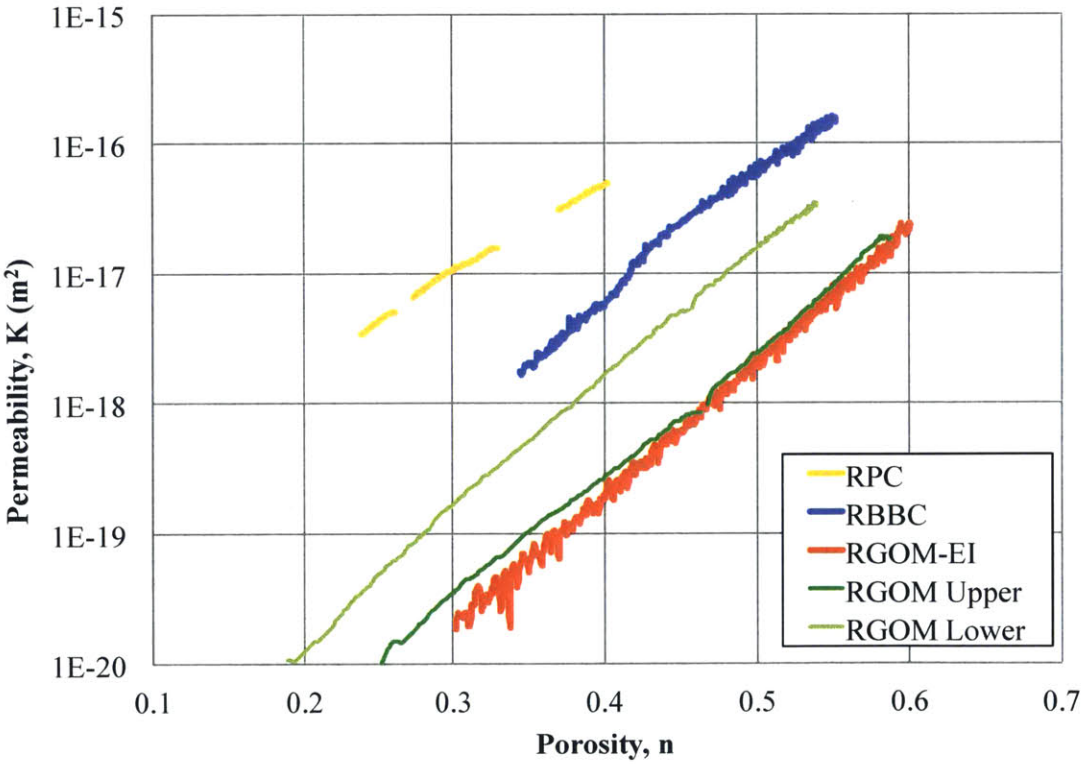

(b) Permeability as a function of porosity

Figure 3-3: Permeability curves of all the materials tested. Tests performed by members of UT Geofluids Consortium

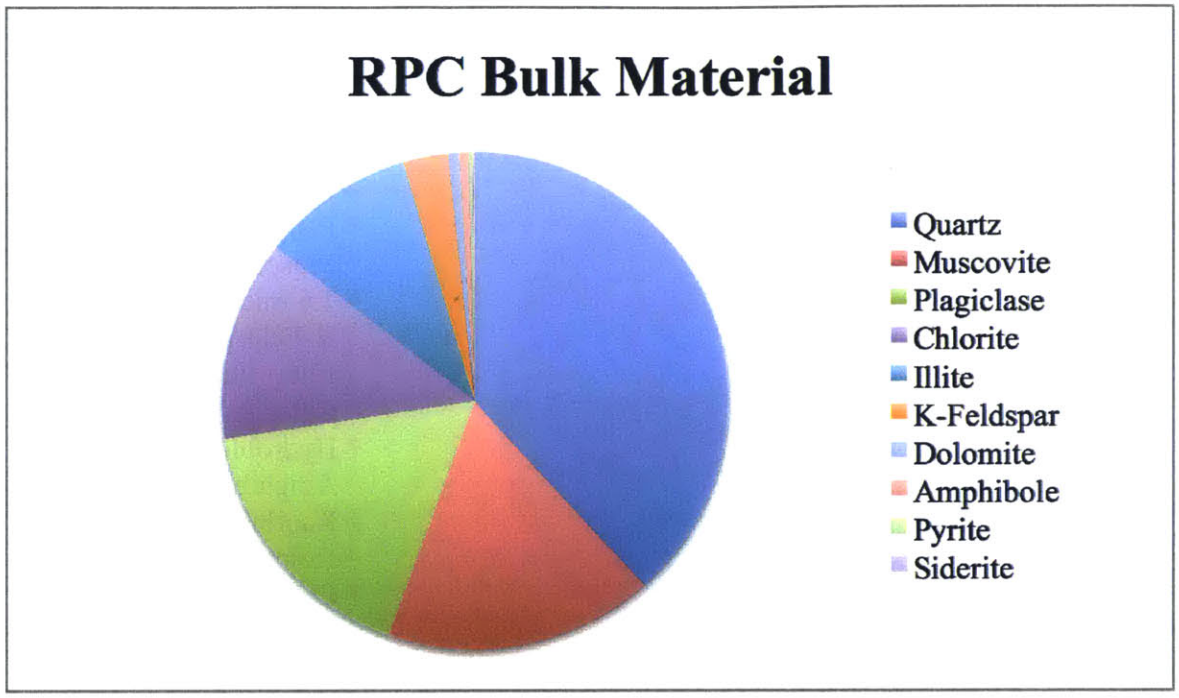

(a) Bulk XRD properties of RPC

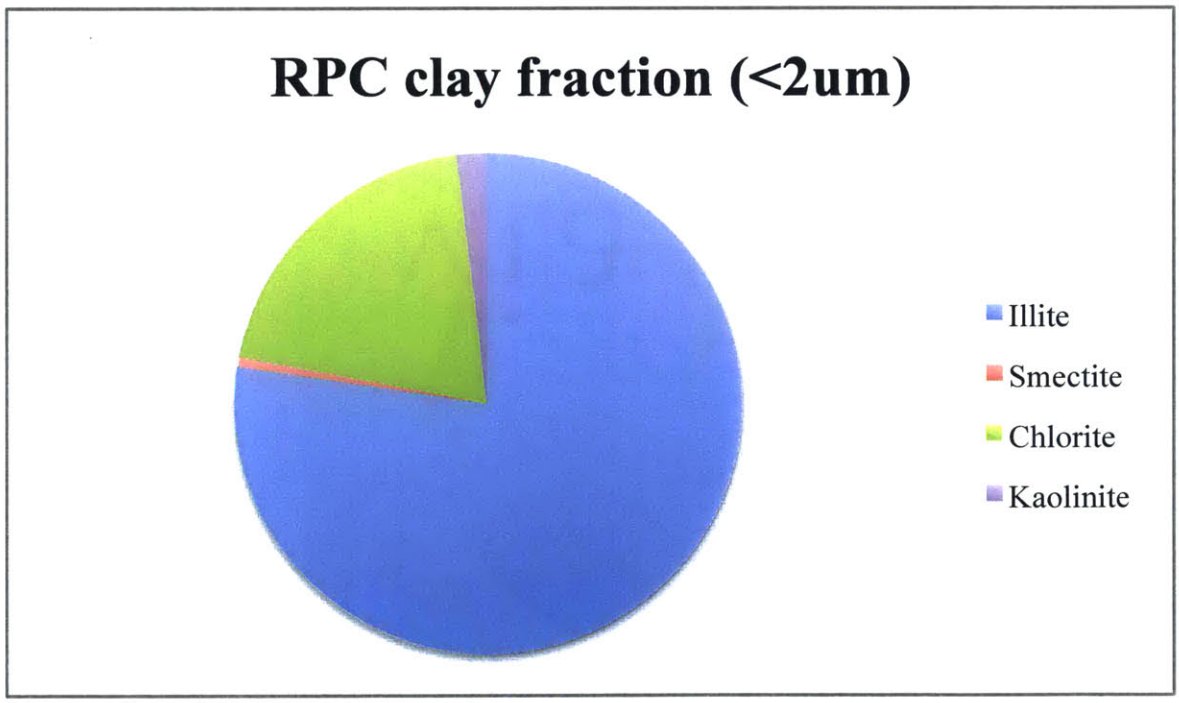

(b) Clay fraction ($< 2\mu m$) XRD properties of RPC

Figure 3-4: XRD analysis shows the distribution of components found in Presumpscot clay

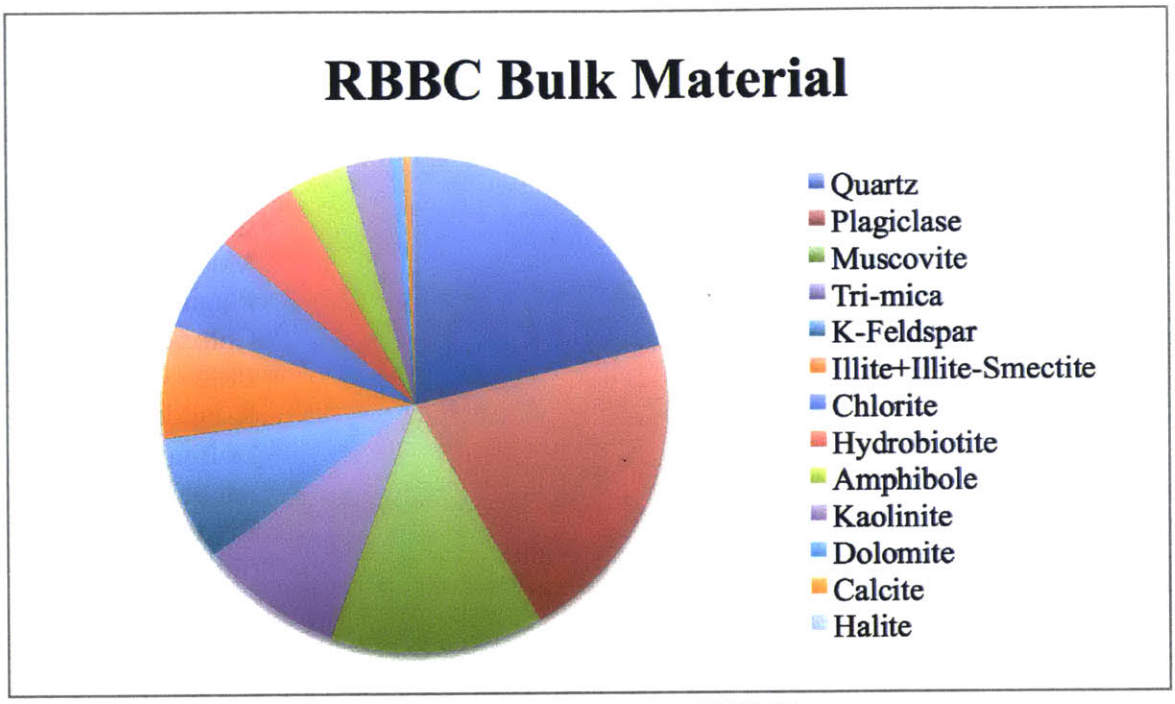

(a) Bulk XRD properties of RBBC

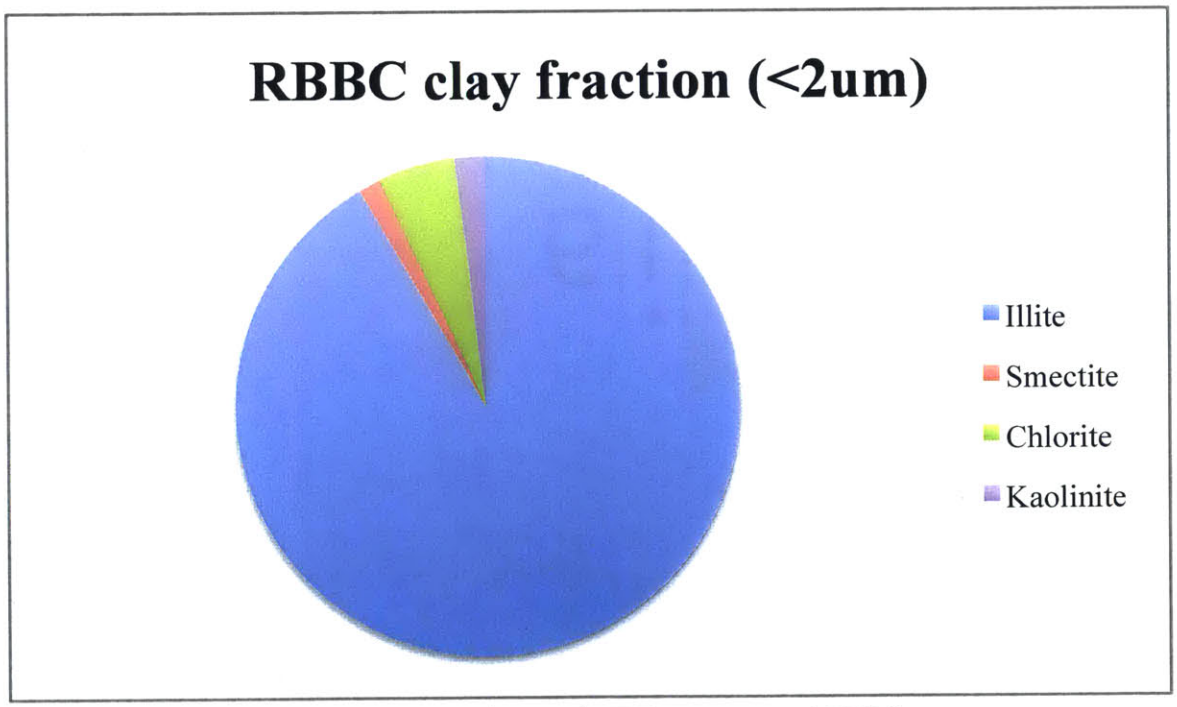

(b) Clay fraction ($< 2\mu m$) XRD properties of RBBC

Figure 3-5: XRD analysis shows the distribution of components found in Boston Blue Clay

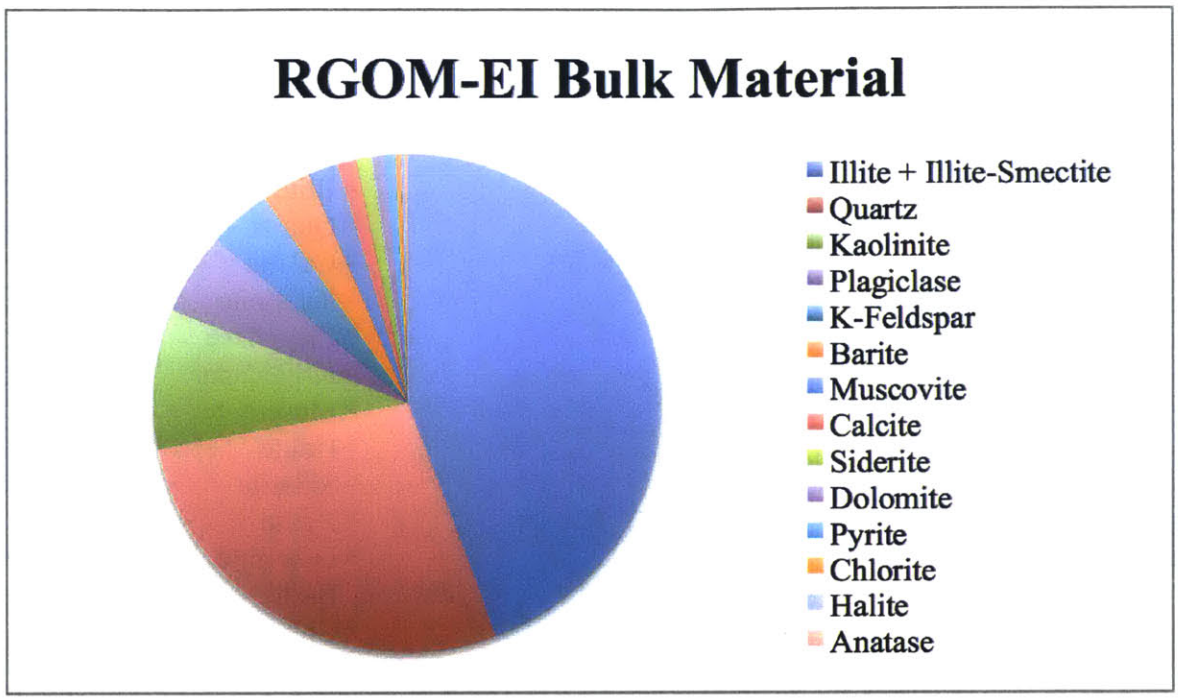

(a) Bulk XRD properties of RGOM-EI

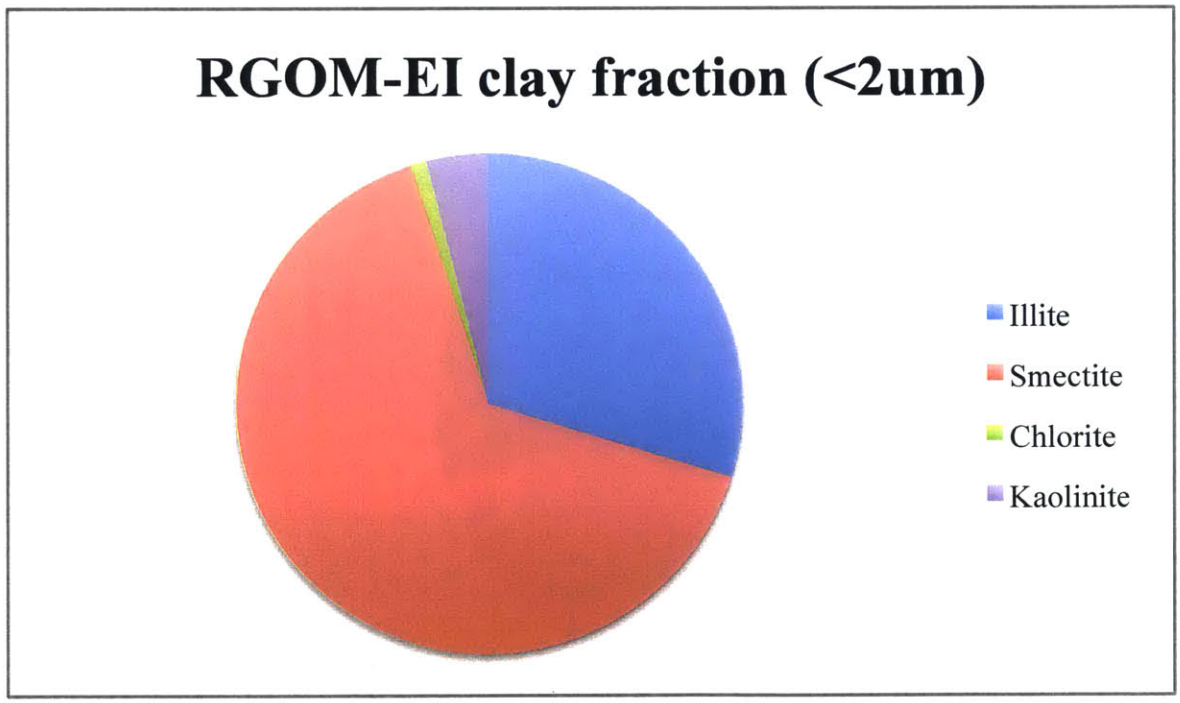

(b) Clay fraction ($< 2\mu m$) XRD properties of RGOM-EI

Figure 3-6: XRD analysis shows the distribution of components found in Gulf of Mexico - Eugene Island Clay

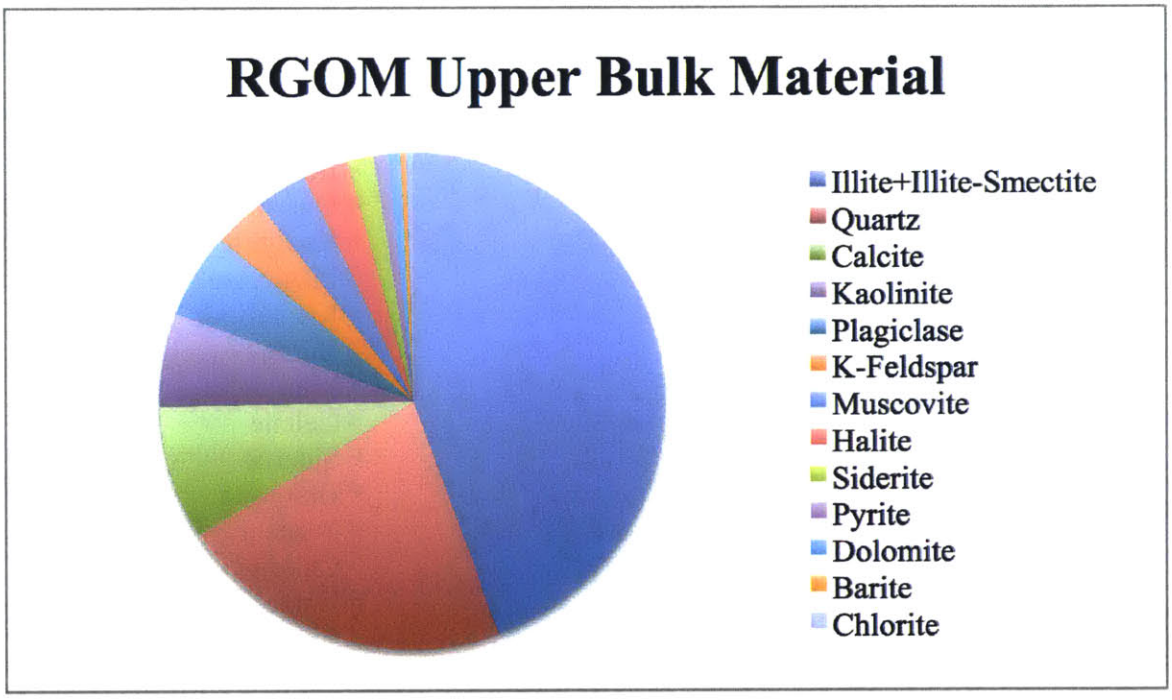

(a) Bulk XRD properties of RGOM Upper

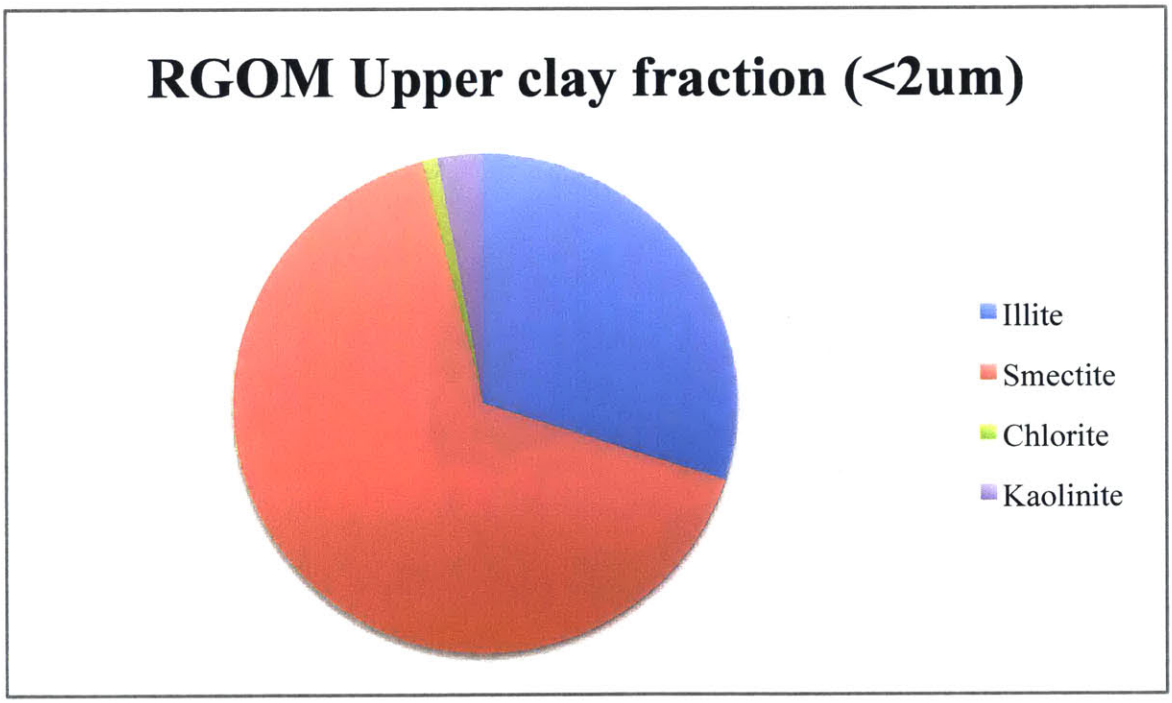

(b) Clay fraction ($< 2\mu m$) XRD properties of RGOM Upper

Figure 3-7: XRD analysis shows the distribution of components found in Gulf of Mexico Upper Clay

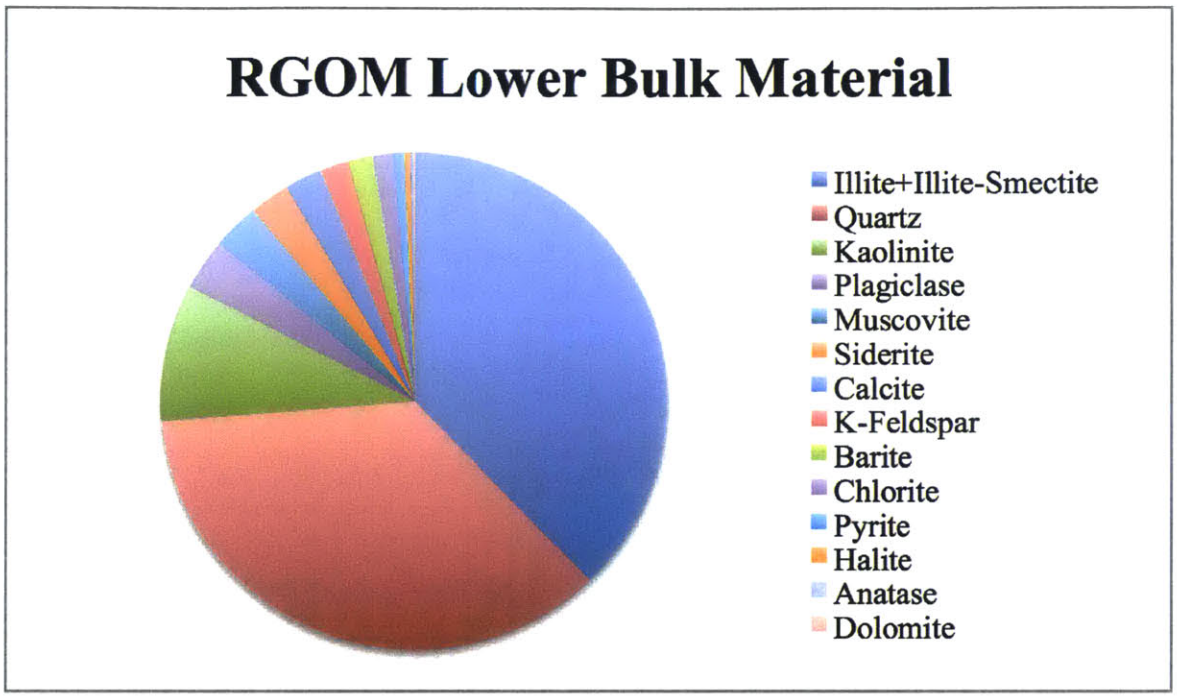

(a) Bulk XRD properties of RGOM Lower

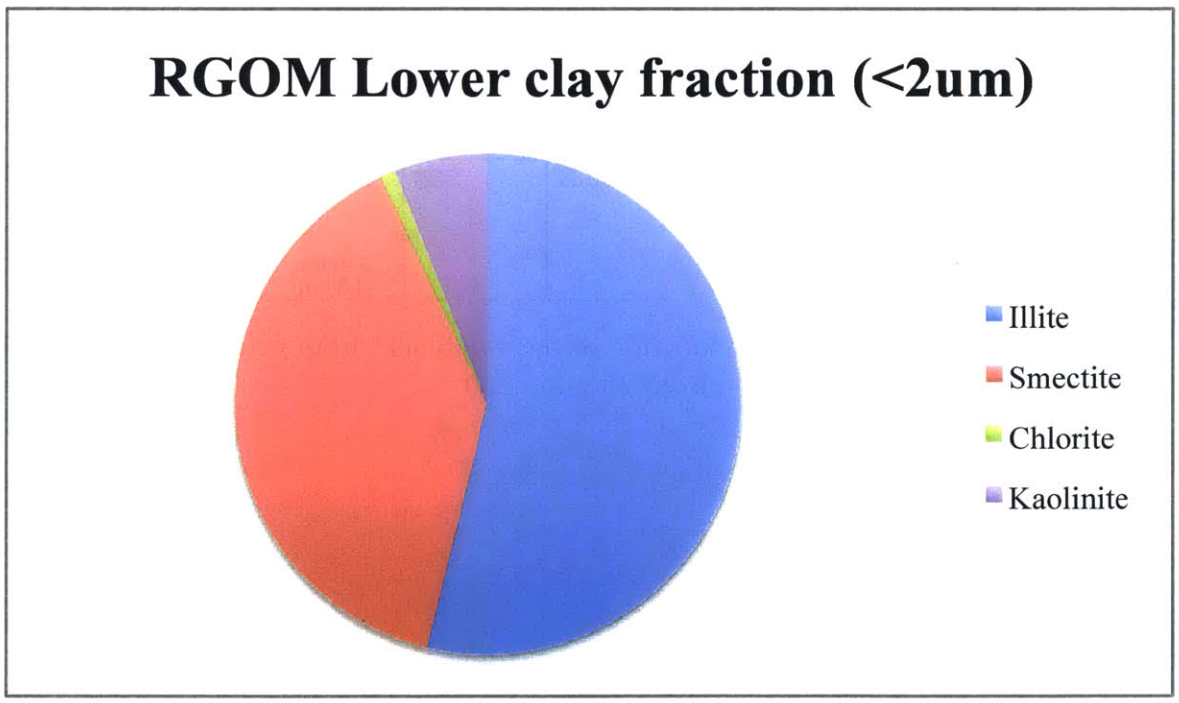

(b) Clay fraction ($< 2\mu m$) XRD properties of RGOM Lower

Figure 3-8: XRD analysis shows the distribution of components found in Gulf of Mexico Lower Clay

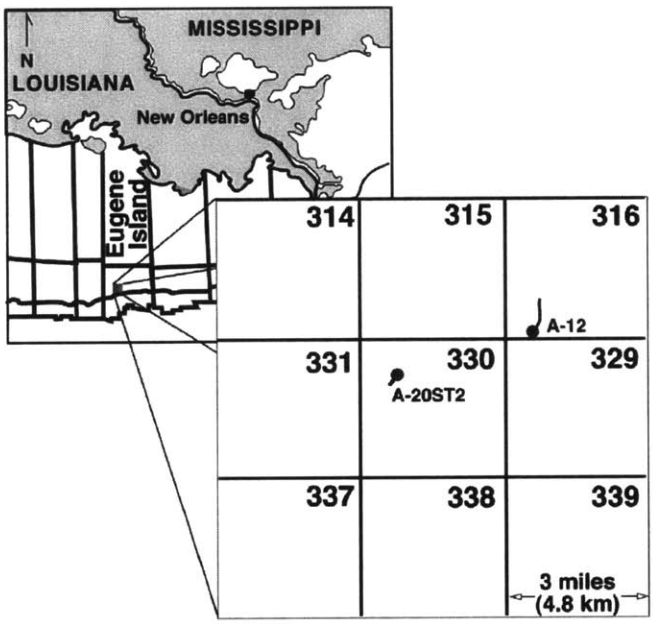

Figure 3-9: This map shows the location of the two blocks from which the RGOM-EI source material was obtained – blocks 316 and 330

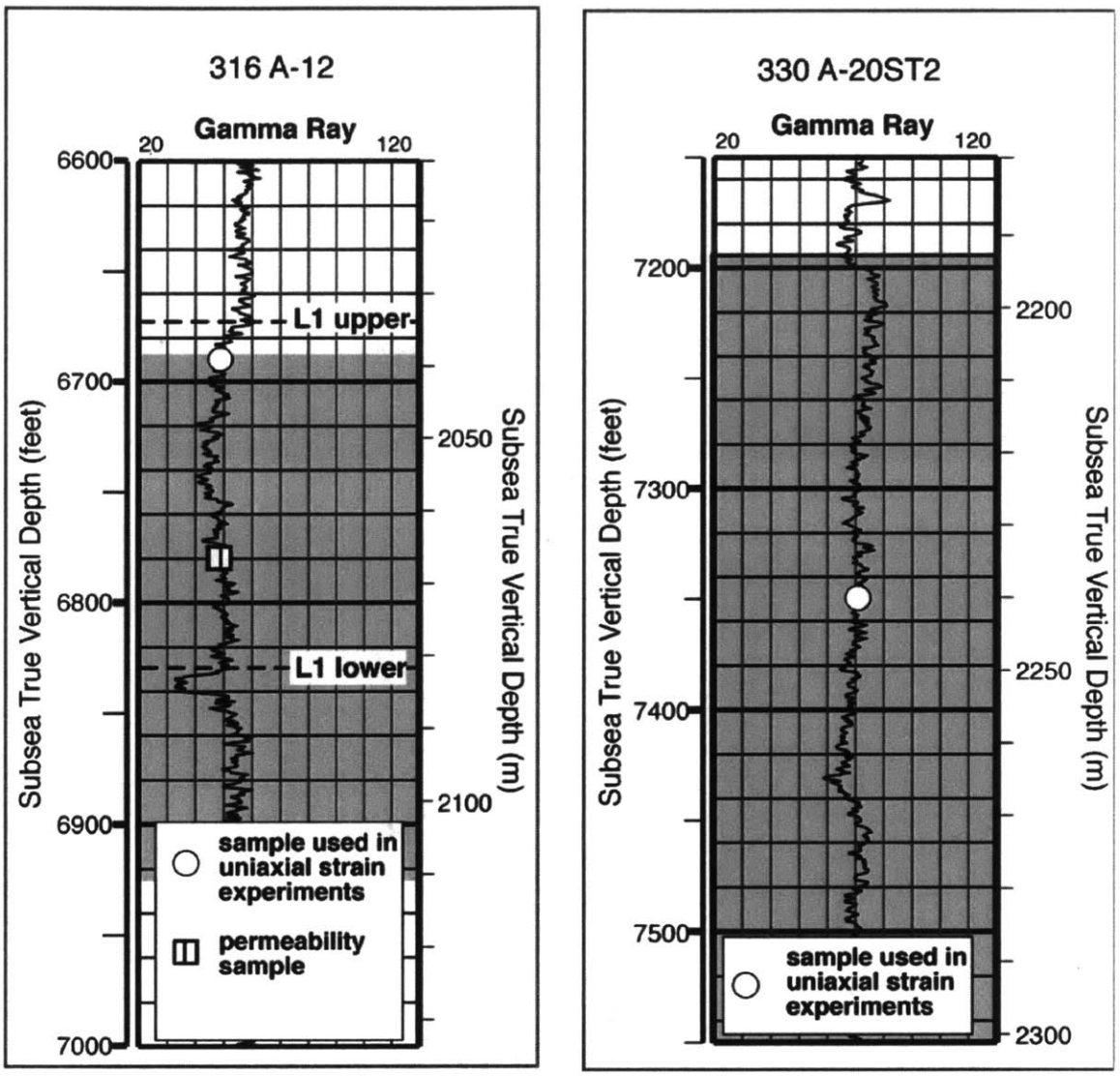

Figure 3-10: These are the gamma ray profiles for the two wells where the RGOM-EI material was excavated, also indicating the depths at which the materials were taken. This figure also shows the location of samples tested by Stump and Flemings (2002), presented in Section 6.4.1

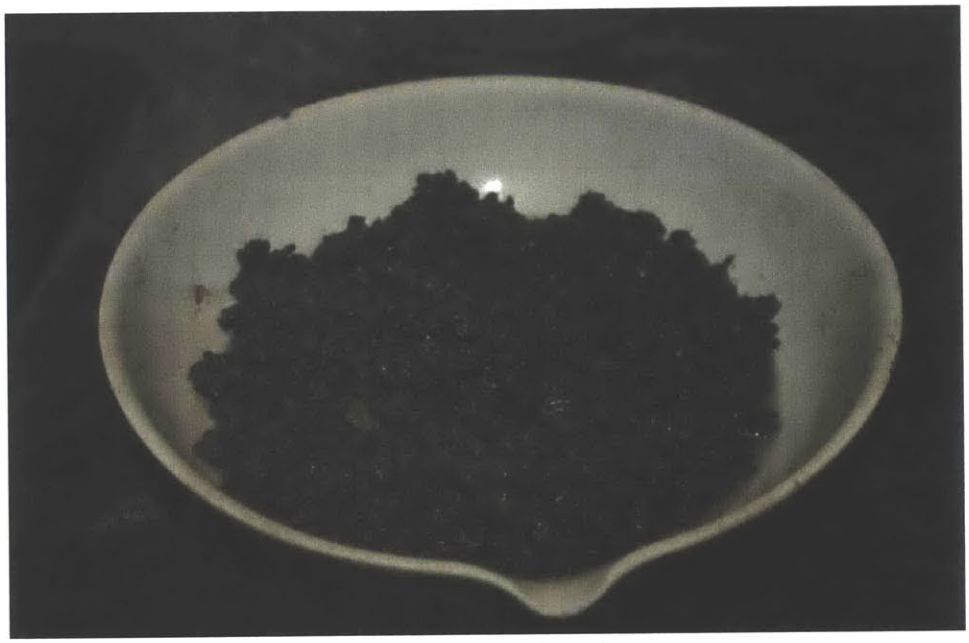

(a) RGOM Upper before cleaning

(b) RGOM Upper after cleaning

Figure 3-11: RGOM Upper interval clay before and after cleaning with Toluene. Before cleaning it is coated in drilling fluid (Fahy, 2014)

Figure 3-12: This is the second step of resedimentation, where clay powder is mixed with saline water until thoroughly homogenized and no lumps are present

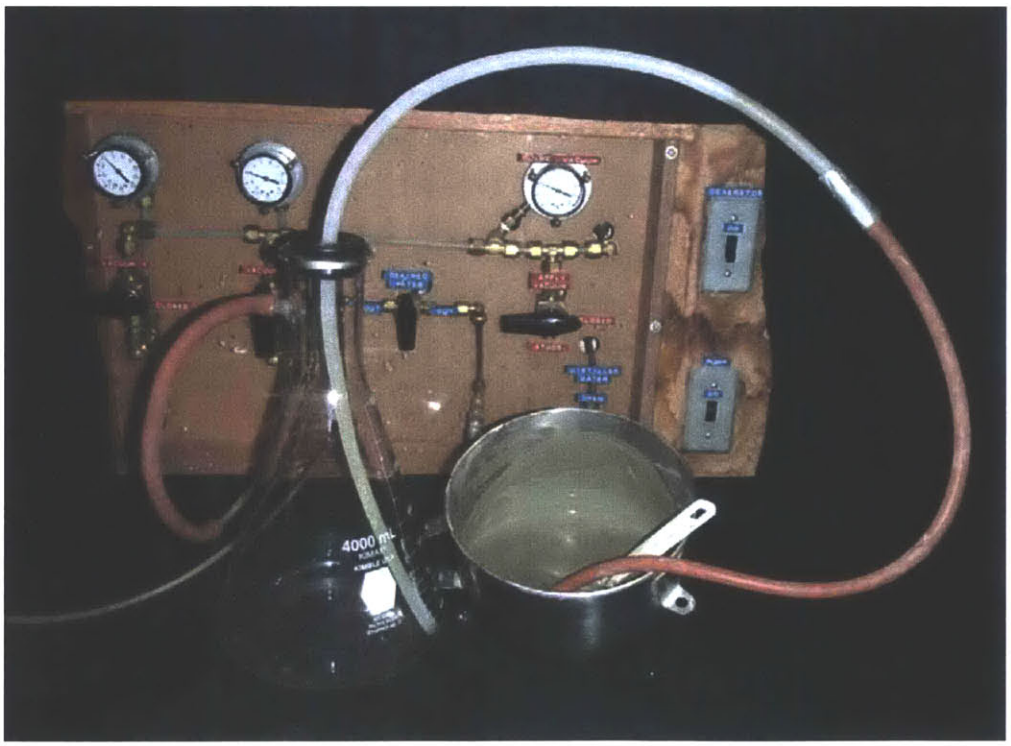

Figure 3-13: This is the third step of resedimentation, where clay slurry is held under vacuum until majority of bubbling subsides

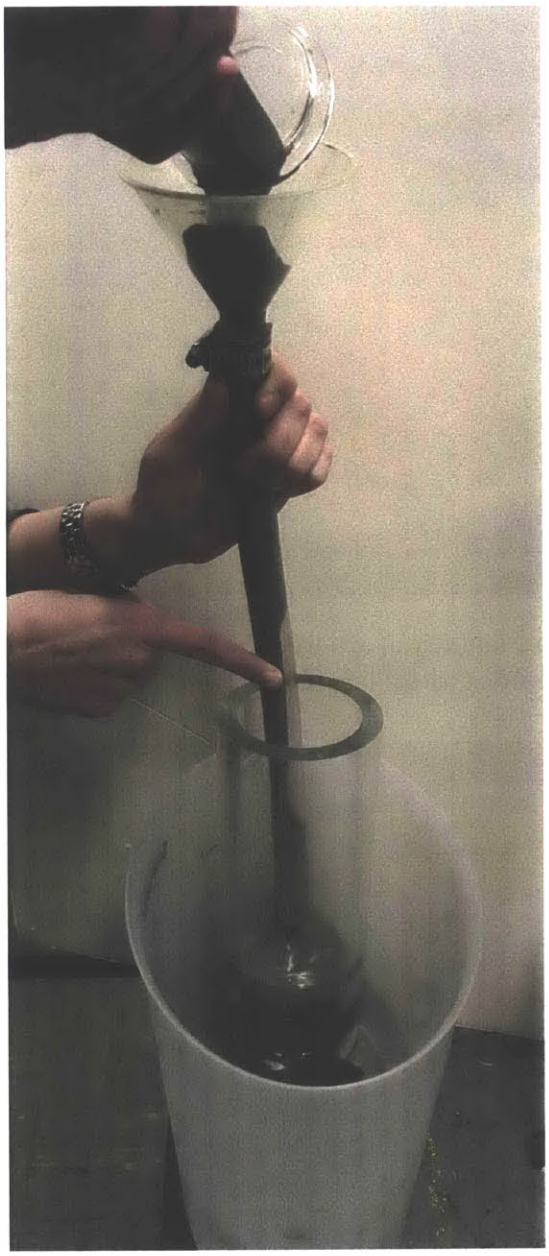

(a) Pouring stage of resedimentation

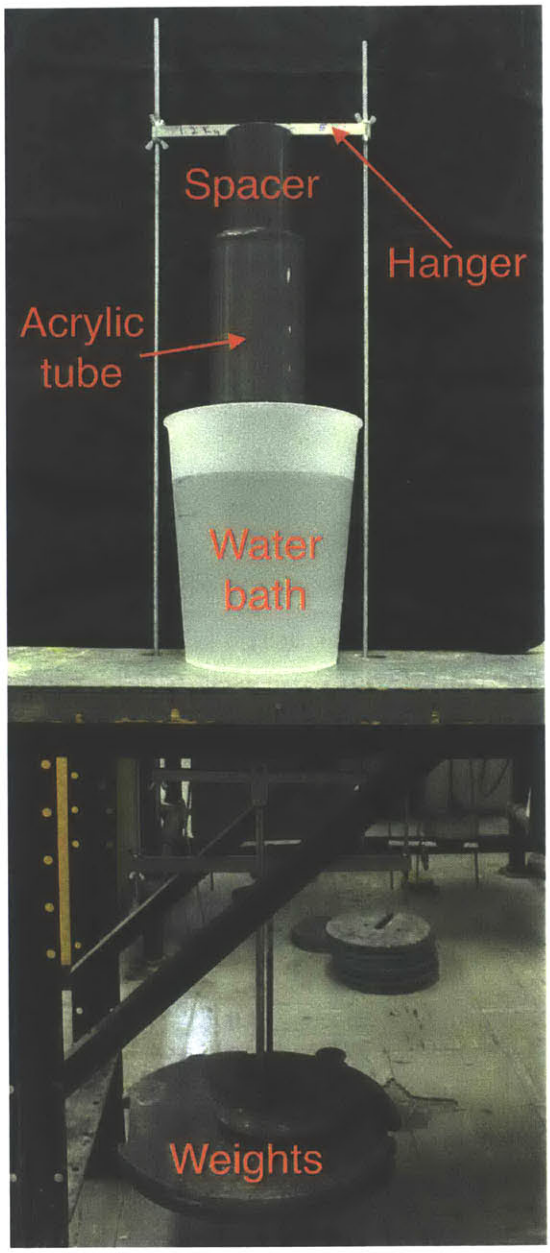

(b) Loading stage of resedimentaiton

Figure 3-14: The last two steps of resedimentation include pouring the slurry into an acrylic tube (confined by pourous stones on either end), and applying load to the slurry with a gravity hanger system. The hanger rests on spacers that extend beyond the cylinder

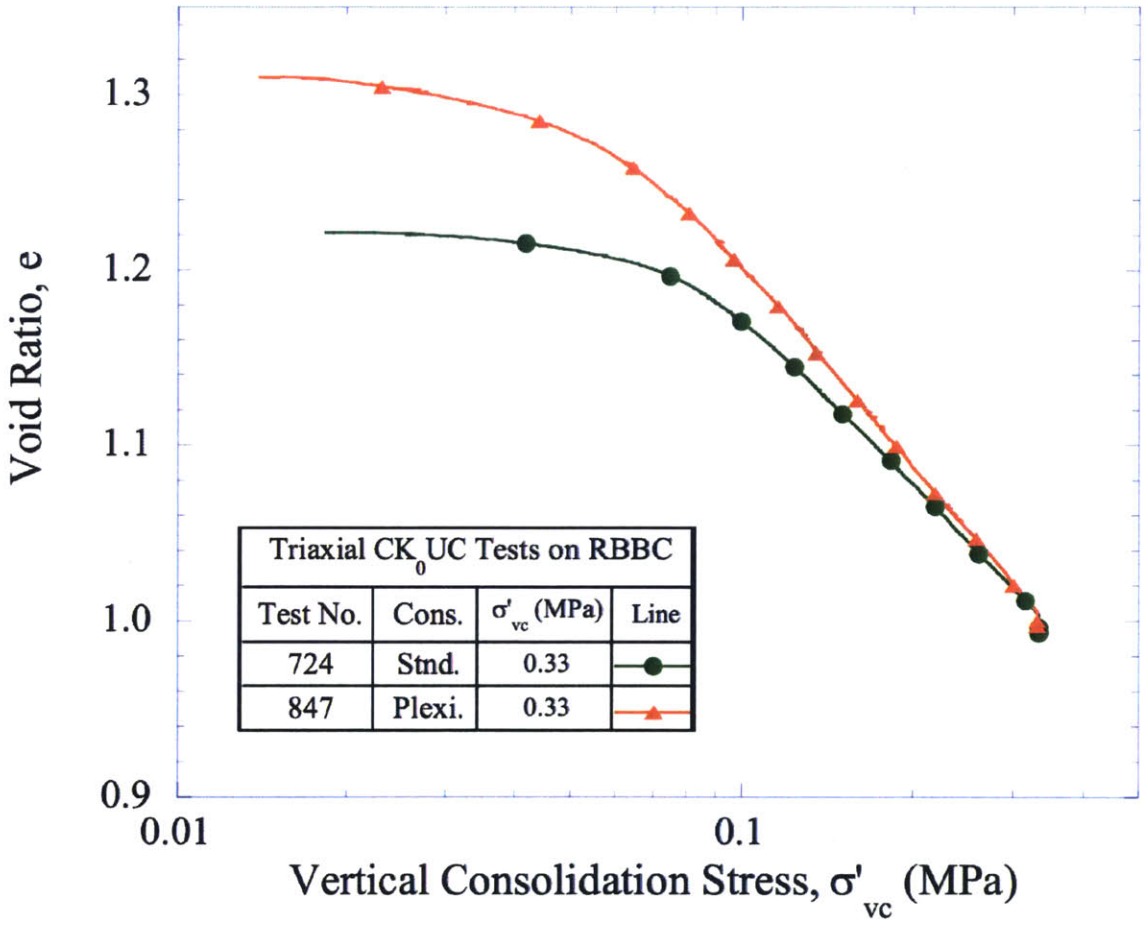

Figure 3-15: The compression curves measured during a triaxial test from two different resedimented samples are shown. The "Stnd" indicates a wide tube was used and the sample was trimmed down to size, while the "Plexi" indicates that a narrow tube that has the same diameter as a triaxial test was used so that no trimming was needed (Abdulhadi, 2009)

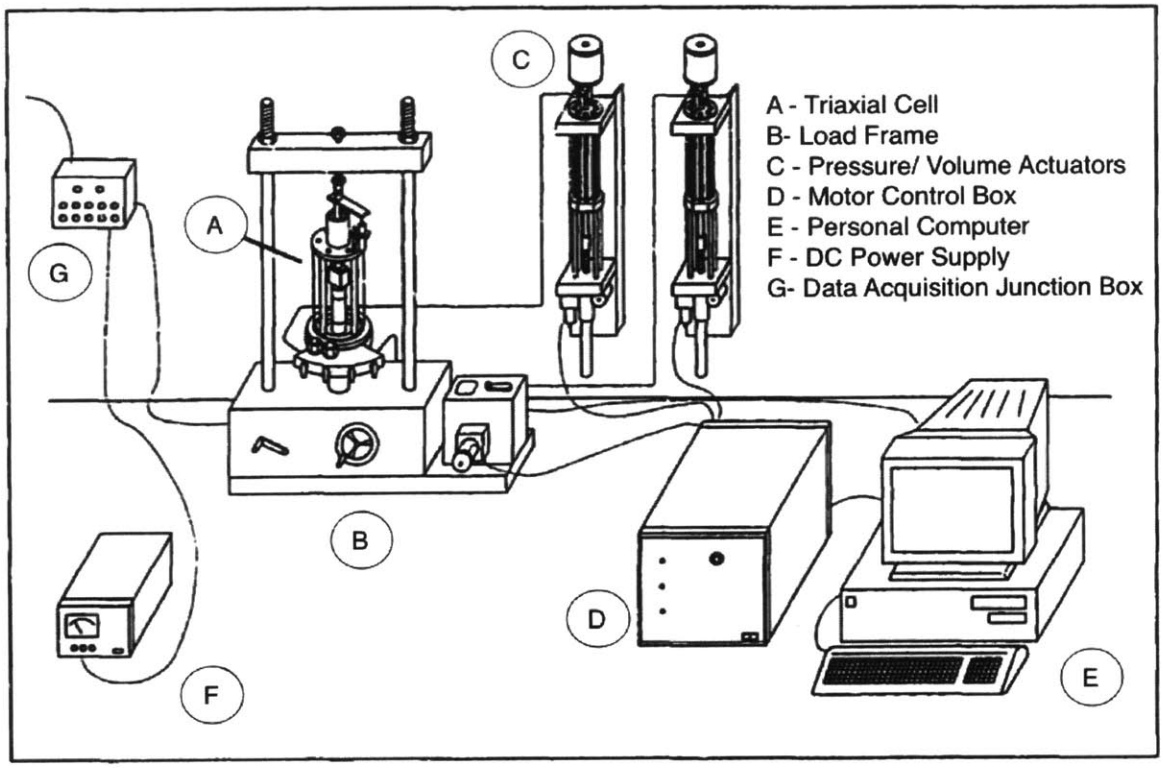

Figure 3-16: This schematic shows the major elements that are combined to create the triaxial cell system (Santagata, 1998)

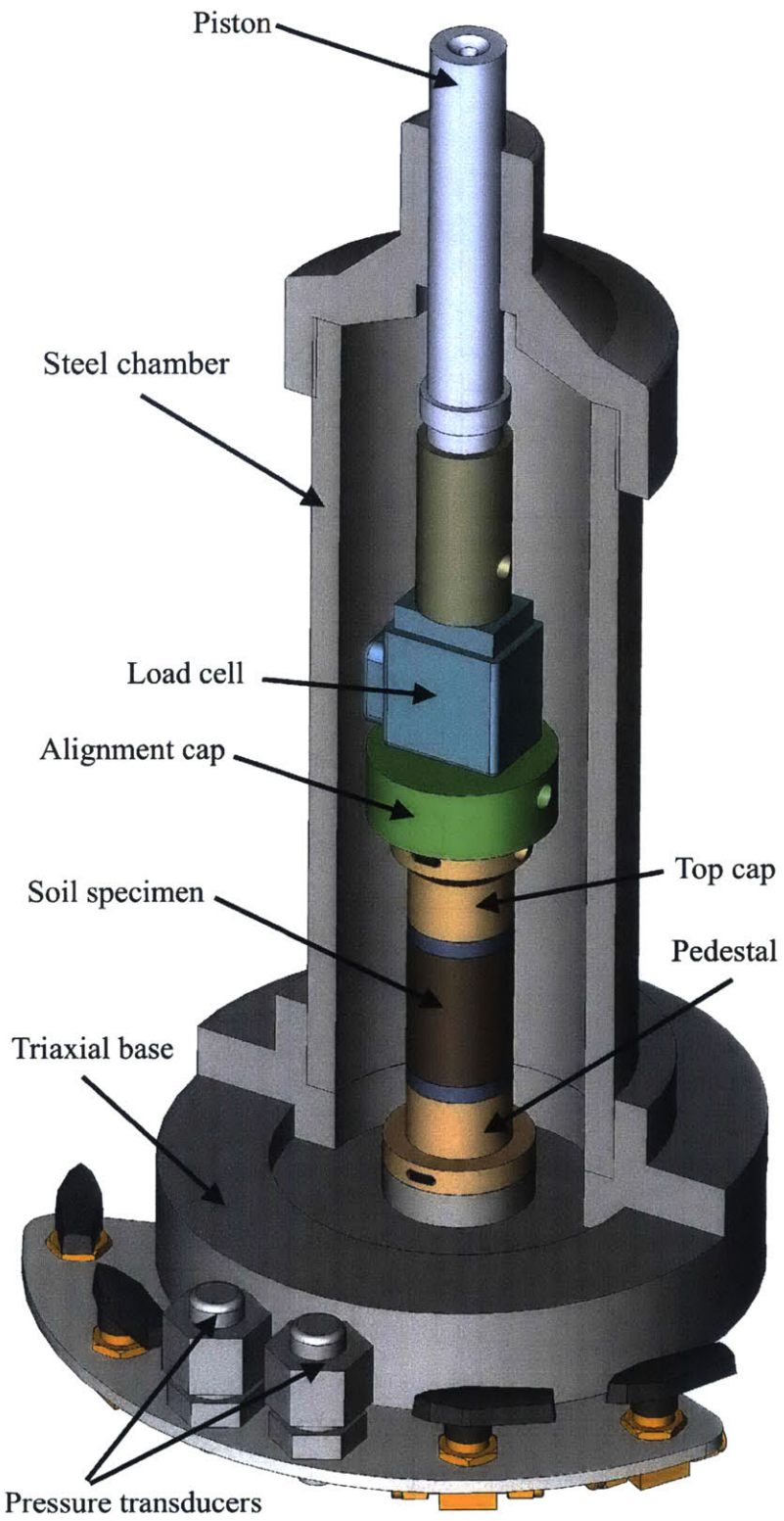

Figure 3-17: Schematic of medium stress triaxial cell

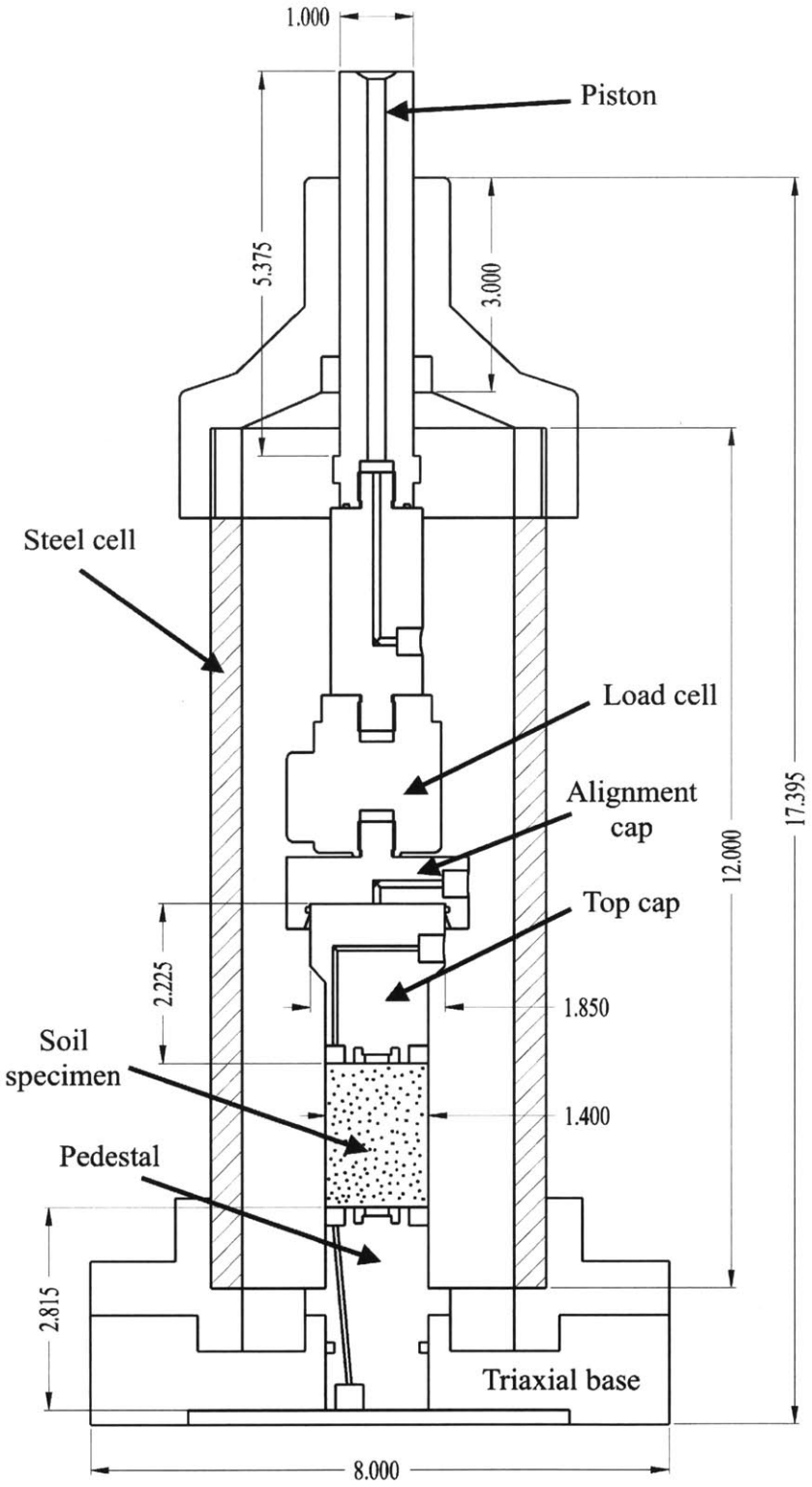

Figure 3-18: Section view of medium stress triaxial cell. Dimensions are in inches

Figure 3-19: The piston, attached to a spacer, then the load cell, and finally the alignment cap that fits with and aligns the top endcap. The alignment cap seen here has the ability to connect to the piston to enable suction; however, this was not used in this research. The standard top cap used in this research did not rigidly connect to the piston

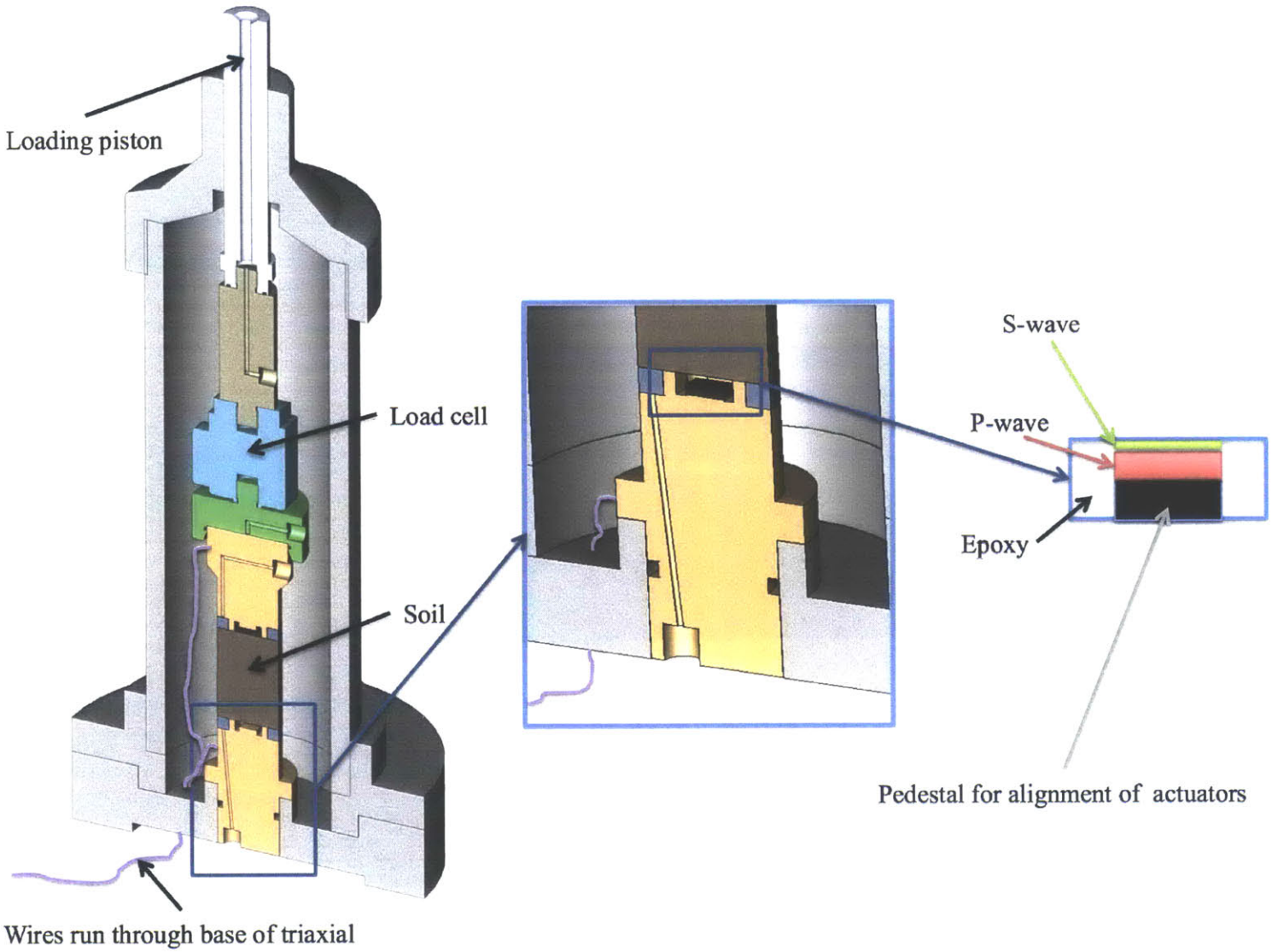

Figure 3-20: This schematic shows the assembled triaxial cell, and a more zoomed rendering of the endcap and the inside of the cavity that holds the piezoceramic actuators

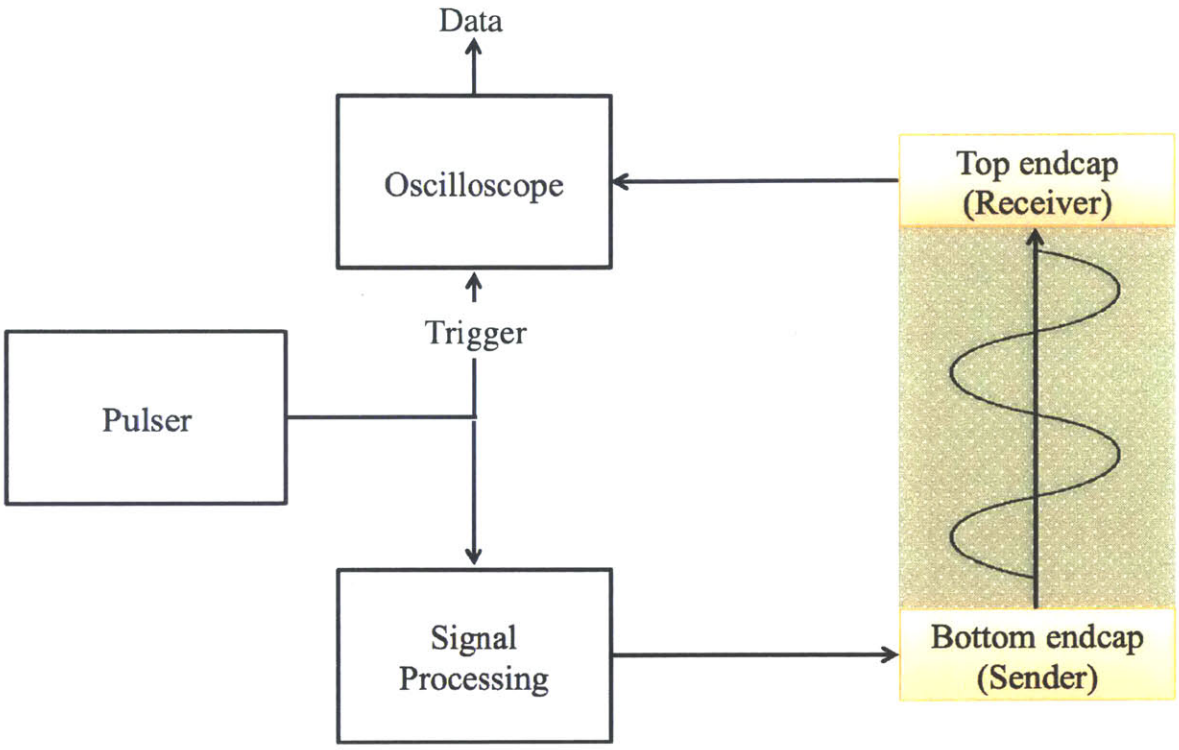

Figure 3-21: Schematic drawing of the components of the wave propagation system

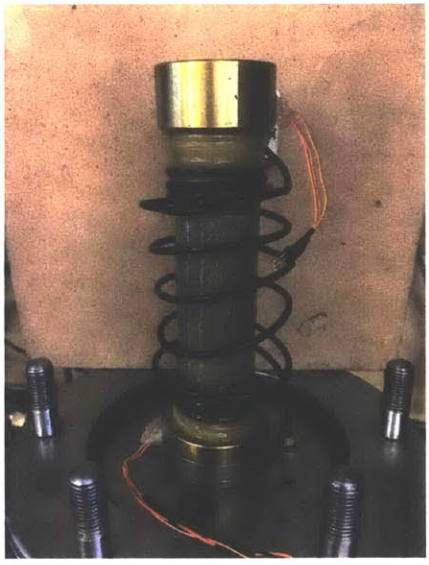

Figure 3-22: The setup with a clay specimen confined with 2 thin membranes. The drainage line is connected, but the wiring for the velocity measurements is unconnected here. The wires would typically be connected together and passed through the 9-pin amphenol connection seen in the foreground

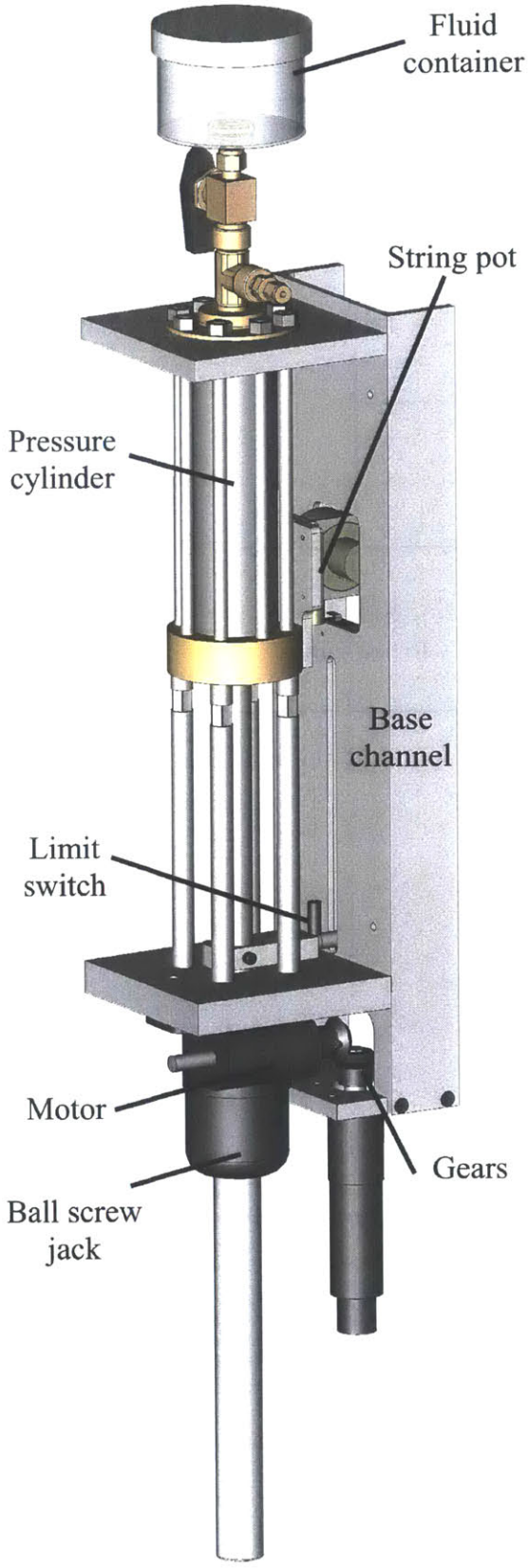

Figure 3-23: Schematic of PVA

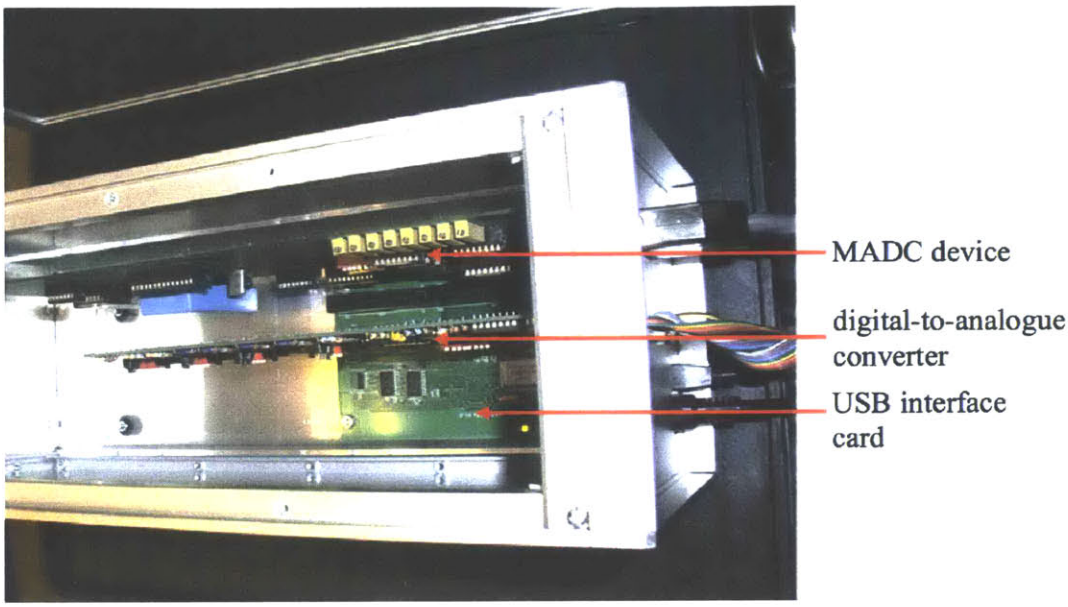

Figure 3-24: The MADC box houses the components needed to take an analog signal and feed it into a computer (Casey, 2014)

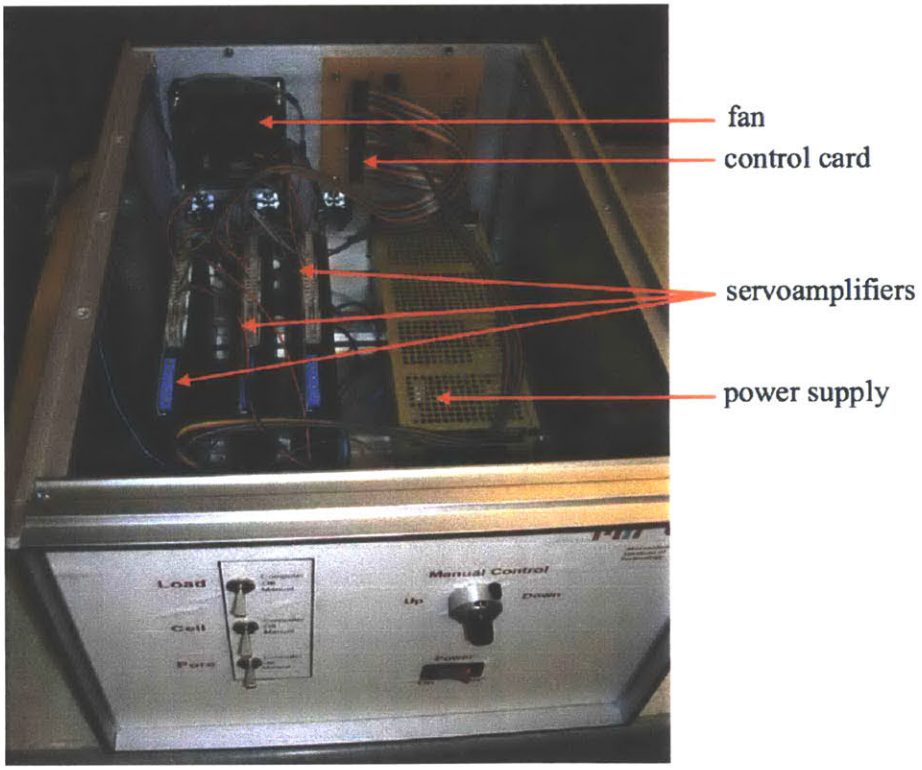

Figure 3-25: The control box receives signals from the computer and controls the motors on the PVAs. It can also be switched to manual control so that the user can dictate which direction and how fast the motors move (Casey, 2014)

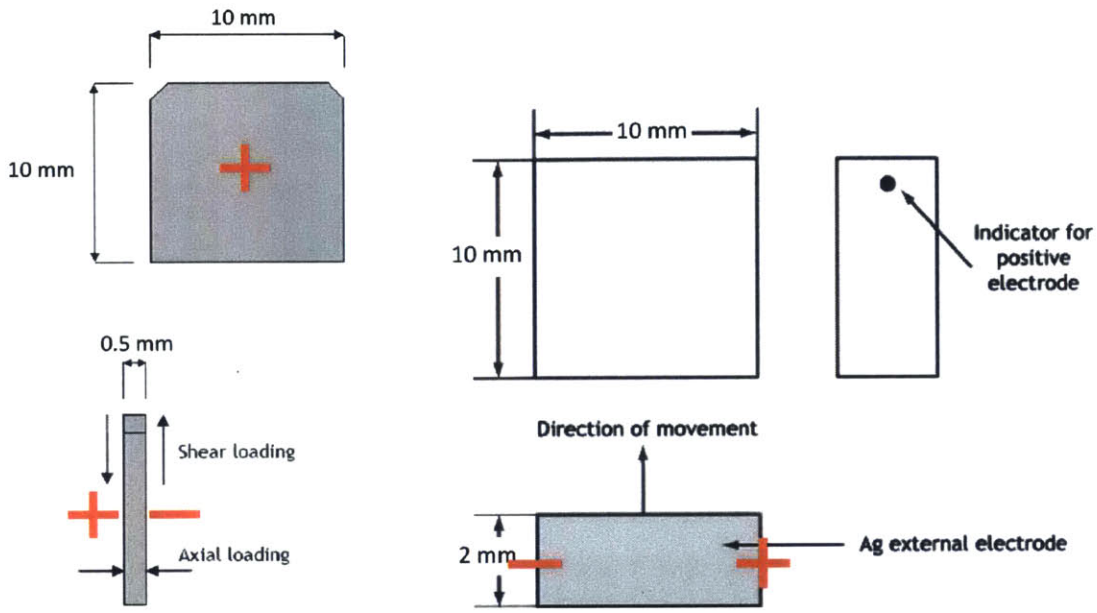

(a) S-wave piezoceramic

(b) P-wave piezoceramic

Figure 3-26: Schematics of the Noliac S-wave (CSAP03) and P-wave (NAC2015) piezoceramics obtained from the Mictromechatronics, Inc. website

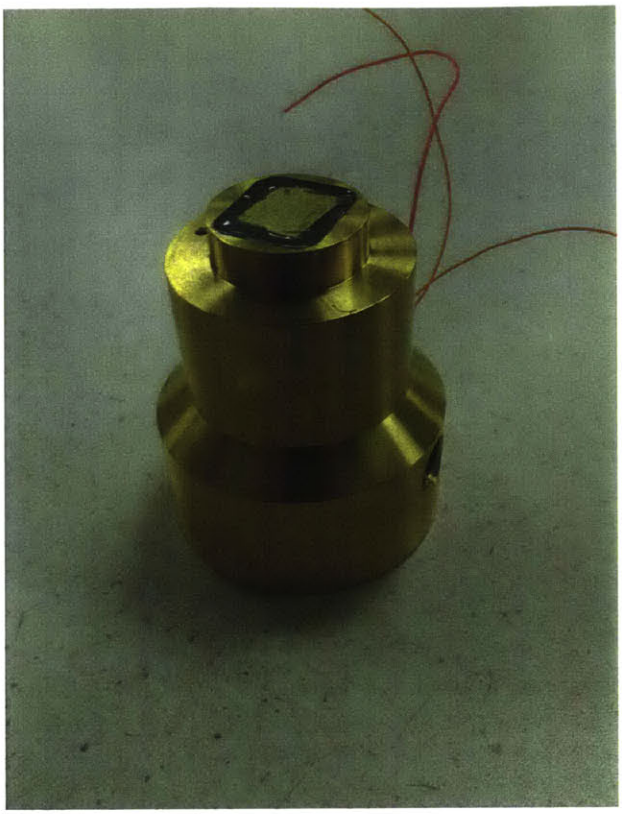

Figure 3-27: The brass endcap is hollowed out and fitted with P and S-wave actuators. The square brass area is the shim stock that is adhered to the S-wave actuator. It is surrounded by a grey epoxy

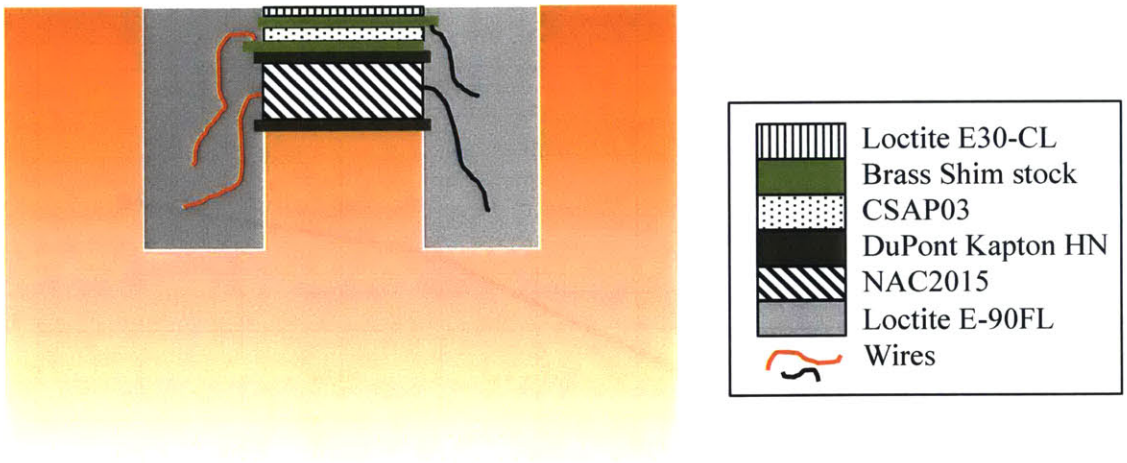

Figure 3-28: The brass endcap is shown here with the hollowed-out area and pedestal that is subsequently filled with the actuators and epoxy. The grey epoxy (E-90FL) is relatively soft and allows the elements to deform, while the surface epoxy (E30-CL) was chosen to be very hard to promote signal transfer. CSAP03 is the S-wave actuator, and NAC2015 is the P-wave actuator

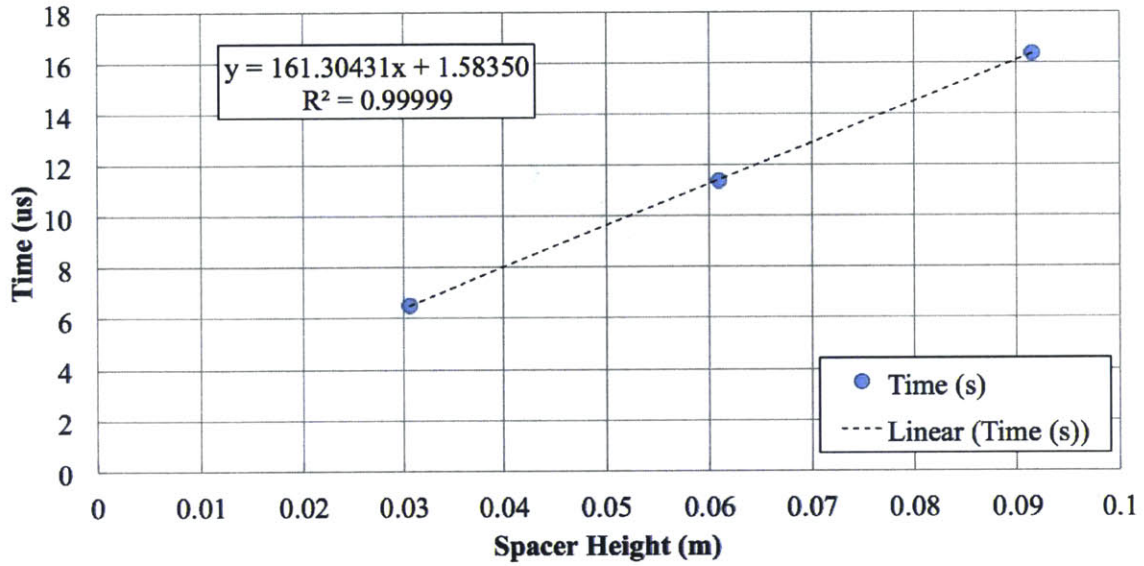

Figure 3-29: The arrival times for a P-wave sent through aluminum spacers at different lengths is plotted. The y-intercept crossing corresponds with the lag time present in the system

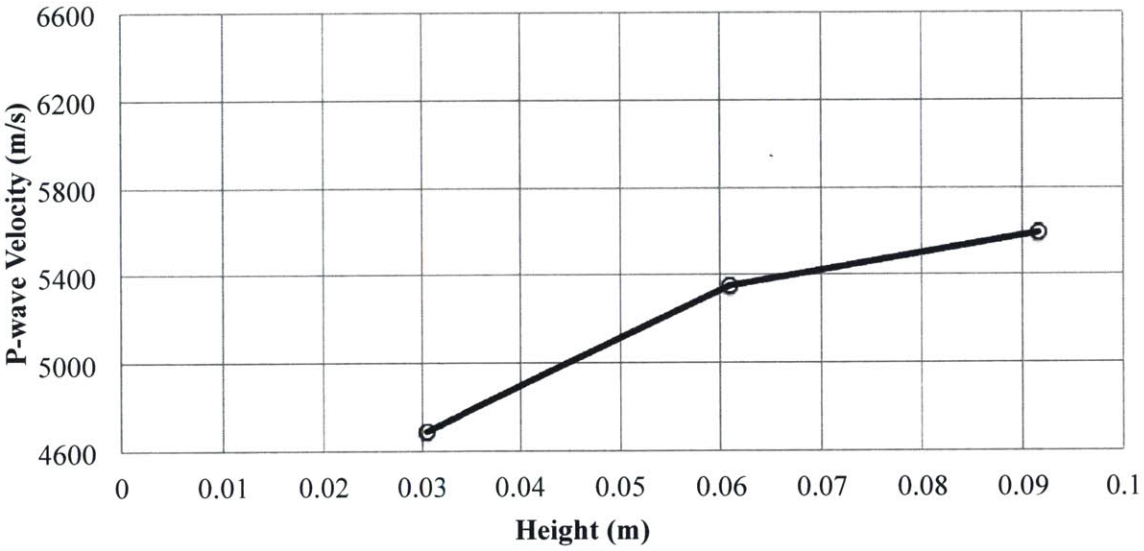

Figure 3-30: This is the raw velocity through aluminum spacers without taking into account lag time. It is clear that for different lengths of aluminum, the velocity varies, which should not be the case

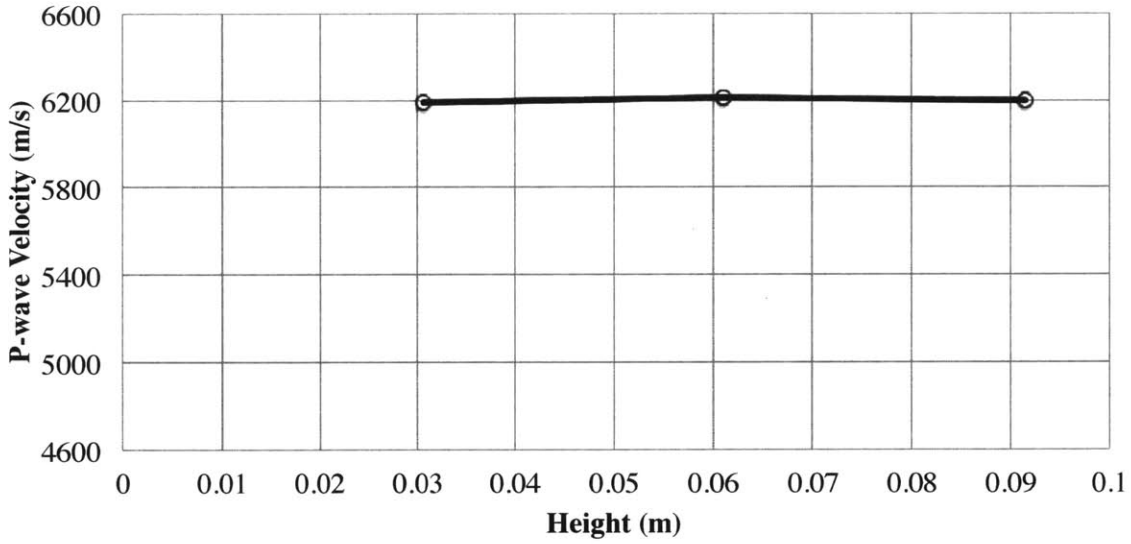

Figure 3-31: This is the velocity through aluminum spacers after taking into account the lag time. Once the lag time is taken into account, the resulting velocity profile is constant as a function of spacer height, which is expected

Chapter 4

Electronics and Instrumentation Development

4.1 Pulser requirements

As seen in the schematic in Figure 3-21, the piezoelectric actuators are excited by a pulser (also called pulse generator). The pulser, an Agilent 214A Pulse Generator, sends continuous square pulses at a set frequency and repetition rate. The settings on the dial of the pulser are as follows:

1. Trigger Mode Internal Repetition Rate: 0.01-0.1 KC
2. Pulse Position: 10-100 μ sec
3. Pulse Width: 1K-10K μ sec
4. Pulse Amplitude: 10V

See Figure 4-1 for the entire settings configuration. All of the settings above are controlled by two dials: one that controls the range such as specified above, and another that fine-tunes the setting within that range (labeled "vernier"). The settings of the pulser is set to send a square pulse with a frequency of 115 Hz, and the repetition of these square waves is set at the minimum possible frequency, f = 6.76 Hz (or 148 ms), as shown in Figure 4-2. Attached at the output BNC connection is a 50

Ohm terminal, as specified by the pulse generator manual. The function generator is designed with a 50Ω impedance since many Radio Frequency (RF) cable connections have 50Ω impedances as well. The output voltage specified by the dial setting on the pulse generator is only correct in the presence of a 50Ω terminal resistor. If the pulse is fed through to a high impedance oscilloscope (1 MΩ), then the voltage output on the oscilloscope versus that of the pulse generator will not match up. Furthermore, when leading into a high impedance oscilloscope, adding a 50Ω resistor at the oscilloscope input will reduce ringing.

Upon using the pulser to excite the P and S-wave actuators, it became evident that, while the S-wave signal worked, the P-wave signal did not. The reason for this was due to the mismatch in the capacitance of the two actuators. The capacitance of the P-wave actuator (NAC2015), as provided by Noliac Inc., is $C_p = 760nF$, while the capacitance of the S-wave actuator (CSAP03) is $C_s = 3.32nF$. The measured values using a multimeter were $622nF$ and $3.67nF$, respectively. This meant that the current needed for each of these actuators was very different, as can be calculated using the equation

$$I_{ave} = f \times C \times V_{pp} \tag{4.1}$$

where f is the frequency, C is the capacitance, and V_{pp} is the peak-to-peak voltage. The current values obtained for the P and S-wave actuators were 15.2 and 0.066 Amps respectively. This was calculated using a frequency of $f = 1MHz$ and a voltage of $V_{pp} = 20V$. These values of frequency and voltage are typical values seen in rock testing and the oil industry, thus these were the design criteria for any operational system. The amount of current that was being sent to the piezoceramics with just the pulse generator can be measured using the following equation:

$$I = C_p \times \frac{dV}{dt}. \tag{4.2}$$

C_p is the capacitance of the actuator, while $\frac{dV}{dt}$ is the slope of the initial ascent of the step function that excites the actuator. $\frac{dV}{dt}$ was measured on the oscilloscope as being $\frac{8V}{11\mu s}$ with an input voltage of $V = 20$, while the capacitance used was $C_p = 760nF$.

This resulted in a current of $I = 0.553A$, which is well below the previously quoted $I = 15.2A$ for the P-wave actuator.

Before attempting to use any components in a circuit that would condition our signal, the Resistor Capacitor (RC) delay behavior needed to be clarified. The equation for the RC delay is as follows:

$$\tau = RC = \frac{1}{2\pi f_c} \tag{4.3}$$

where τ is the delay time in seconds, R is the resistance, C is the capacitance, and f_c is the characteristic frequency. In the case of the P-wave actuator, which has a capacitance of approximately 760nF, and assuming a typical frequency of 100kHz, the resistance would be about 2.1Ω. Thus the starting point for the circuitry was close to this resistance. Equation 4.3 can also be used to calculate the delay time to ensure the delay time does not exceed the expected arrival time of the response output signal. Based on the parameters listed above, the delay time would be $\tau = 1.59\mu s$, which is well before the arrival time of any P or S-wave signal in this research, thus would not disrupt the signal in any way.

To resolve the different capacitances of the actuators, an electrical circuit that included a MOSFET (Metal-Oxide-Semiconductor Field-Effect Transistor), a few capacitors, and a few resistors was built on a breadboard. The schematic of the system can be seen in Figure 4-3. The part numbers and properties of the various parts are as follows:

Ultrafast MOSFET driver: IXDD614PI

Capacitor 1 (C1): 10 nF

Capacitor 2 (C2): 4700 μF, 25 V rating

Capacitor 3 (C3): 4700 μF, 50 V rating

Resistor 1 (R1): 75 Ω

Resistor 2 (R2): 80 Ω

Resistor 3 (R3): 95 $k\Omega$

Resistor 4 (R4): 10 $k\Omega$

Capacitors were used to increase the stability of the signal and provide more driving current. The resistors (R2, R3, R4) were used as a voltage divider to feed the input signal from the pulse generator into the oscilloscope. The system was powered by a DC Power Supply at $20V$. The MOSFET transistor is used since the actuators are current-limited. A MOSFET passes high current while running on a small current itself.

4.2 Noise Reduction

Electrical noise was seen to be a prominent problem for the quality of the signals. Even the use of one power outlet for the power supply, oscilloscope, and pulser seemed to have a marked effect on the signal noise. In addition, the large amount of radiative noise originating from other sources in the room, such as the motors running the PVA's or the computer, increased the level of noise in the system. Through an iteration of the various configurations of plugging the components into different electrical outlets and using a ferrite choke on all the possible wires in the system, an optimal signal was achieved. The ferrite choke did not seem to affect the quality of the signal; however, plugging the oscilloscope and pulser into one power strip, while plugging the power supply for the MOSFET into another outlet in the room seemed to minimize noise.

4.2.1 Op Amp

An operational amplifier can be used as a tool to reduce the noise and create a clearer signal. A TLC2262AI rail-to-rail Operational Amplifier (Op Amp) was used, with a series of resistors to select the gain level of the amplifier. Depending on the resistance of the two resistors used, the gain can be controlled using the following equation

$$G = \frac{R_1}{R_2} + 1 \tag{4.4}$$

where G is the gain, and R_1 and R_2 are the two resisters placed in the configuration seen in Figure 4-4. The Op Amp was set to have a gain of 1, 10 and 20 with different resistors. The resulting signal can be seen in Figure 4-5. The legend indicates the raw output signal, as well as the different gains used on the signal. A zoomed-in version of the graph can be seen in Figure 4-6. It is clear that using an Op Amp with a gain of one (G=1) results in a shift of the signal, as marked with the arrow. Figure 4-7 even further clarifies that as a higher gain is used, there is a greater shift in the signal. While the use of an Op Amp does reduce the noise in the signal and creates a smoother arrival, the shift that is present in the G=1 case is also present in the other gain cases, thus is not an adequate form of noise reduction.

4.2.2 Connections

The type of clips used for the connections have a significant effect on the quality of the signals. To connect from the oscilloscope to the received signal, as well as the input signal, BNC-alligator clip connections were used. To connect from the output signal sent from the MOSFET to the actuators in the endcaps, plain double-ended alligator clips were used. Using these connections and the electrical sources specified in the previous paragraph, a signal named "Alligator clips" can be seen in Figure 4-8. The substitution of minigrabbers (also called mini hooks) for the alligator clips were surprisingly detrimental to the signal, as seen in Figure 4-8. Finally, if the power sources, oscilloscope, and pulse generator was taken were connected to a single power strip, the resulting signal can be seen, labelled "Minigrabber/Mini hook, new setup".

4.2.3 Wires

The wiring scheme between the transducers and the peripheral electronics was investigated as a possible major source of noise. To isolate the noise problem specifically in the wires connecting the components, a 100 kHz signal at 15 V was sent through a 1 μ F capacitor, since a capacitor essentially mimics the behavior of the piezoceramic elements. This research investigated whether the top and bottom endcap (receiver

and sender, respectively) can be connected in a single bundle of wires or whether they should be separated to reduce the noise. The type of wire used was an audio communication and instrumentation cable (22 AWG, each pair beldfoil shielded, part # 8723 080), containing five separate wires and a single multi-wire ground wire, all wrapped together with foil and then nonconductive plastic tubing. The five wires allowed for a P and S-wave power line for both the bottom and top endcaps, as well as a combined ground wire, as seen in Figure 4-9a. This configuration was compared to a setup where the top and bottom endcaps had their own wire bundle, with separate grounds (Figure 4-9b). The results for an S-wave signal can be seen in Figure 4-10. The isolated configuration, where the top and bottom endcaps are wired separately coming out of the 9-pin amphenol connector in the base of the triaxial cell (Figure 4-9b), was seen to have significantly less ringing and noise than the scenario with the two endcaps running through the same wire (Figure 4-9a). This is likely due to the proclivity for wires in parallel to be influenced by external magnetic fields, thus increasing the presence of noise.

In addition to different wiring configurations, the length and type of wire used is addressed. The input was directly taken from the pulse generator, seen as a black dashed line in Figure 4-11. The use of long wires caused the worst signals since long wires tend to act as antennas and invite noise. The use of coaxial cables, usually known for minimizing some noise due to the shielding of the wires, had better quality signals than the use of long wires; however, not quite as much as the "No wire" option. The absence of wires (i.e. directly connecting through the breadboard) seemed to have the best signals, with the least amount of ringing and distortion of the input wave. Although it would be ideal to have this configuration, it is impractical for connection purposes, thus a system with very short wires (5-12") and alligator clips was used to connect from the bottom of the triaxial cell to the peripheral electronics.

4.2.4 Grounding

Another measure used to reduce the noise was combining the grounds of the transducers. The top and bottom endcaps each had a P-wave power, S-wave power, and

ground wire. The ground wire for the P-wave and S-wave was combined in the end-cap. An attempt at combining the ground wires for the top and bottom endcaps did not show any improvement in the quality of the signal. Furthermore, the wires coming out of the endcaps were braided. Although Figure 4-9b shows the wires inside and outside the triaxial cell as parallel wires, they are actually braided. The P, S, and ground wires were braided both inside the triaxial cell, as well as coming out of the triaxial cell. The wires coming out of the bottom of the cell (attached using a 9-pin amphenol connector) were attached to the peripheral devices using a combination of double-ended alligator clips and BNC-alligator clip connectors.

Ground loops were found to be an exacerbating problem in the setup scheme. It was discovered that the oscilloscope being used had its own ground, and the input and output being channeled into the oscilloscope had the same earth – the housing of the BNC ports were electrically connected. Having too many sources of ground increases the noise in the signal. Allowing a few of the ground sources to "float" while trying to maintain one definite "earth" would minimize the noise caused by ground loops.

Finally, mains hum was a ubiquitous problem in the signals. Mains hum is caused by the electrical fields emanating from the outlets in the room, usually running at about $60Hz$. The degradation to the signal caused by mains hum was not significant, and any means of eradicating this problem seemed too difficult for the slight benefit it would provide.

4.3 Input Frequency Selection

The frequency of the input signal is generally believed to affect both the arrival time and the quality of the output signal. To further investigate the frequency effect, a series of tests were conducted in the triaxial cell to help aid in the selection of an appropriate input frequency.

One of the first preliminary tests done to evaluate whether the frequency had a marked effect on the arrival time was an experiment done on saturated Ticino Sand,

isotropically confined at 10 MPa. The input frequency of the square step was set at a high enough frequency so that the input is both excited and grounded before the arrival of the output signal. An appropriate frequency for this condition was 100 kHz. Alternatively, the converse scenario was to have a square pulse with a low enough frequency so that it entirely encompasses the arrival signal of the P-wave. In this case, the frequency was lower than 11 kHz. The corresponding graph can be seen in Figure 4-12. The figure shows that there is no effect on the arrival time (taken at the zero-crossing) or the frequency response of the output signal. The difference in the two signals only occurs at a time q after the first zero-crossing arrival, where q is the period of the input signal. The spike that occurs at time q after t=0 in the high frequency case is the cross-talk that occurs in the output signal. The cross-talk conveniently allows us to see the signature of the input signal in the output signal. Whether the frequency of the output signal is affected when using a frequency much higher than the resonant frequency of the soil is difficult to validate since the quality of the signal significantly deteriorates when using higher frequencies.

The down-step of a step function causes significant disturbance in the signal if it arrives before the received signal. Figure 4-12 is manipulated to highlight the magnitude of disturbance. A signal obtained using a large step function is superimposed with a delayed, inverted version of the same original signal. The delay time is equivalent to 100 kHz. The superposition of these two signals results in a signal *identical* to the signal produced by the 100 kHz square step. As seen in Figure 4-13, the 100 kHz signal and the superimposed signal overlap each other exactly. Since the 100 kHz signal is noisier than the low frequency step function signal, the author suggests using a low frequency step function.

The previous paragraph looks at a dry sand specimen. While the sand sample showed very similar signal quality for the different frequencies, this was not the case for a clay specimen. A specimen of intact Presumpscot clay was tested in the triaxial cell, where it was consolidated under K_0 conditions while fully saturated. At 0.1 MPa, the P-wave signal was recorded when the frequency of the input square pulse was very low and very high, similar to the sand conditions. As can be seen in Figure 4-

14, the quality of the signal greatly deteriorates when using high frequencies, where the up-dip and down-dip of the square pulse occur entirely before the arrival of the P-wave signal. While it does not expressly change the arrival time, it does affect the interpretation of the arrival time, thus leading to potential erroneous velocity values due to the ambiguity of the arrival selection. When looking at an example of an S-wave signal at 2.1 MPa, seen in Figure 4-15, the same ambiguity when using a high frequency input can be seen. The quality of the signal using a high frequency input is difficult to interpret. A black dot was added where the arrival was interpreted. The inability to make a selection for the high frequency input is clear. For clarity, the two signals were offset by an arbitrary amount in the amplitude.

Finally, a frequency sweep was conducted on dry Ticino sand under vacuum to see what the effect of changing the input frequency has on the output signal, starting with $0.4kHz$ and stepping to $400kHz$ by a factor of ten each time. The P and S-wave responses can be seen in Figure 4-16 and 4-17, respectively. The black dotted lines are input step functions while the solid colored lines are the received signal responses. The input step functions have been normalized in order to fit on the graph, while the output signals are shown in actual amplitude (in volts), with an offset between the data sets for clarity. It becomes clear that the cross-talk occurs during the beginning of the input signal. In the case that the arrival of the received signal should occur around the same time as the down-dip of the input signal, it becomes difficult to distinguish where the arrival is. If the frequency of the input is very high (higher than the resonant frequency of the soil), the amplitude of the response diminishes greatly. When a low frequency is used, resulting in the largest step function, then the signal appears to have some amount of noise that may make the interpretation harder; however, by having the down-dip occur long after the arrival of the response, this eliminates the possibility of masking the arrival with the crosstalk of the down-dip. In the case of the 4 kHz signal, the down-dip almost exactly coincides with the arrival of the signal, thus skewing the interpretation.

The frequency sweep was done on dry Ticino sand. The response for wet sand or clay can be quite different. It especially becomes a concern when the P-wave is

traveling through a saturated medium, in which case the arrival time would occur much earlier than in the case of a dry specimen. With the arrival time occurring earlier, the down-dip of a mid-range frequency step function (10 - 100 kHz) can interfere with the arrival time and interpretation.

The selection of an appropriate input frequency at which to excite the actuators is a sensitive process. This should not be confused with the frequency effect that causes dispersion and attenuation in the specimen, but rather simply an input signal that yields the strongest, clearest return signal. If the goal is to select a frequency that has an up and down-dip occur before the arrival time, an entire test at a range of stress levels might be necessary in order to ensure that the arrival time is never going to coincide with the down-dip of the input. The safest selection that is least prone to error and has satisfactory quality of signals is a very low frequency so that the down-dip of the input occurs after the arrival of the received signal. In the case of Figures 4-16 and 4-17, there was no load applied on the specimen, thus the response was so weak that the arrival was not interpretable in the response signal. At higher stresses, such as seen in Figure 4-12, Figure 4-14 and Figure 4-15, it is evident that the larger step function (higher wavelength) is a more appropriate choice for clarity. Thus this research used a large step function for all the subsequent velocity results.

4.4 Post-processing Filters

Post-processing filters are useful tools in noise reduction. While they have the ability to diminish ringing and noise, they sometimes have the converse effect and actually include more ringing and artifacts that can obscure the arrival time. To investigate which type of post-processing tool to use, many signals were analyzed, including the relatively clear signals as well as the extremely unclear signals.

An attempt at using a boxcar filter can be seen in Figure 4-18. In order to apply a boxcar filter, the data is converted to the frequency domain using FFT. A range of desirable frequencies is selected, which the boxcar filter allows to pass, while eliminating any activity outside of this range. Thus the boxcar filter of [10 kHz-

1 MHz] only keeps the frequencies of the signal between 10 kHz to 1 MHz, while zeroing the rest of the signal. Post-processing filters have been known to cause shifts in the arrival time, so when the arrival time was measured in Figure 4-18, the error in the arrival time was calculated to be 0.25%.

To further investigate the effect of filters on the signal, a Gaussian cutoff FFT and a Butterworth filter were compared to the boxcar filter and the untouched original signal. The average response frequency of the original P-wave signal was calculated to be about 20 kHz, thus the boundaries of 8 kHz and 120 kHz were used for the boxcar and Butterworth filters. The difference between the boxcar and Butterworth is that the boxcar simply cuts out the non-desired frequencies with a sharp box function in the frequency domain. The Butterworth filter does not have quite so sharp of a cutoff and rather accepts some of the undesired frequencies to reduce the ripples. Finally the Gaussian filter with a 20 kHz central frequency and a +/-3 kHz span is a Gaussian distribution applied in the frequency domain with the 20 kHz maximum peak, and a standard deviation of 3 kHz. Thus the 20 kHz signal has the highest intensity while frequencies diminish in intensity the further away they are. When looking at Figure 4-19, it is clear that these different filters have very different effects on the signal. All of them seem to be shifted to a degree from the original signal. This can likely be adjusted if a zero phase filter is applied, where the filter is applied once forward and once reversed; however, this was not used at the time of the analysis. Furthermore, some of the peaks in the original signal seem to be lost once the filter has been applied, most prominently in the Gaussian filter case.

An example of a relatively unclear signal with a filter applied to it can be seen in Figure 4-20. The original signal has a response frequency of approximately 14 kHz, thus the boundary conditions for the filters reflect the optimal bounds around this frequency. A boxcar filter was applied to the original signal with cutoff frequencies of 10 kHz and 18 kHz, while the Gaussian filter was applied at the dominant 14 kHz with a standard deviation of 4 kHz. The crosstalk occurring early in the output signal is avoided since it significantly alters the results with a strong edge effect. The use of filters in the case of a poor signal do not clarify the arrival time, but rather mask

the signal to a point where an interpretation of any arrival time is impossible.

Another processing technique was applied to the signal to observe whether it was possible to avoid the shift in time caused by an FFT filter. The same signal as in Figure 4-18 was now smoothed with a 5-point moving average, which can be seen in Figure 4-21. The error in the arrival time calculated in this case was 0.08%. This small error could be caused by the scatter in the arrival time selection and is essentially negligible. Due to the convenience of the 5-point smooth (MATLAB has built in "smooth" command) and the reduction in arrival time error, this processing method was used for the arrival selection.

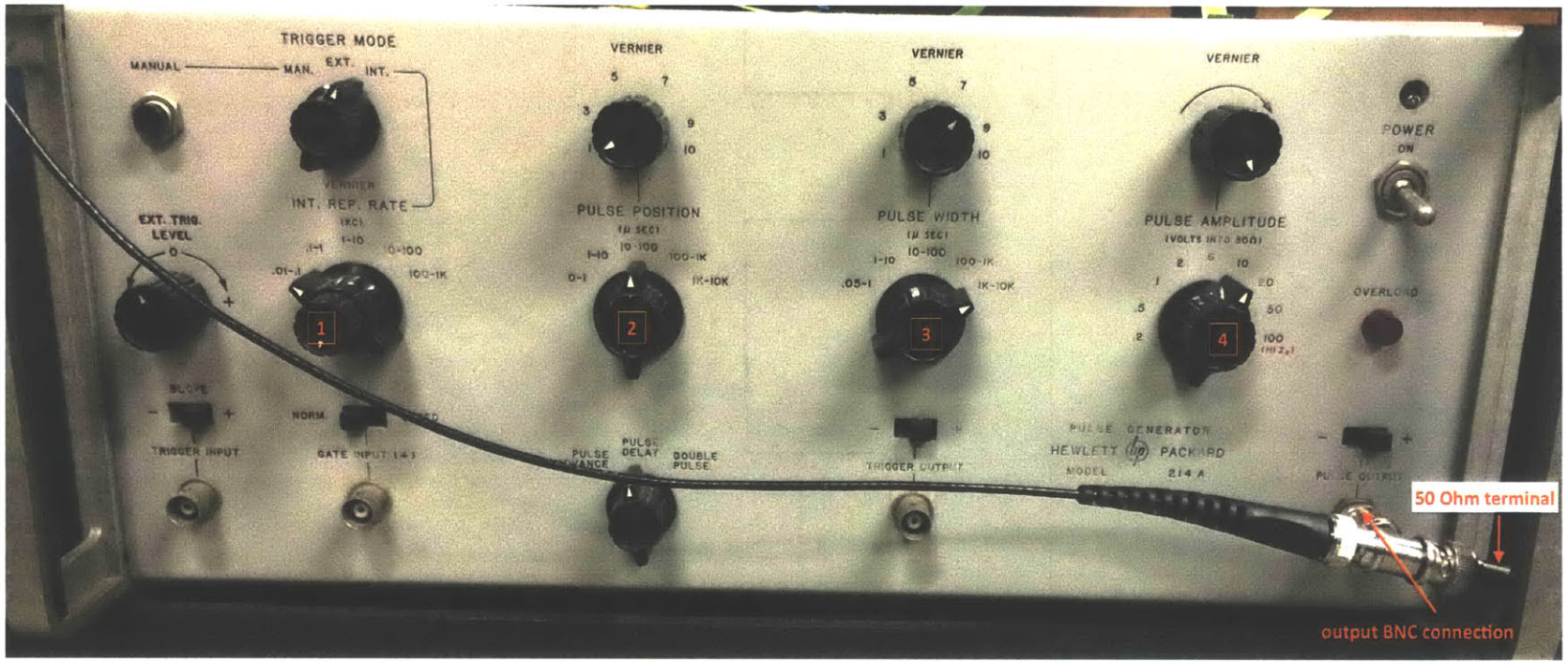

Figure 4-1: The pulser settings for the Agilent 214A Pulser Generator can be seen above

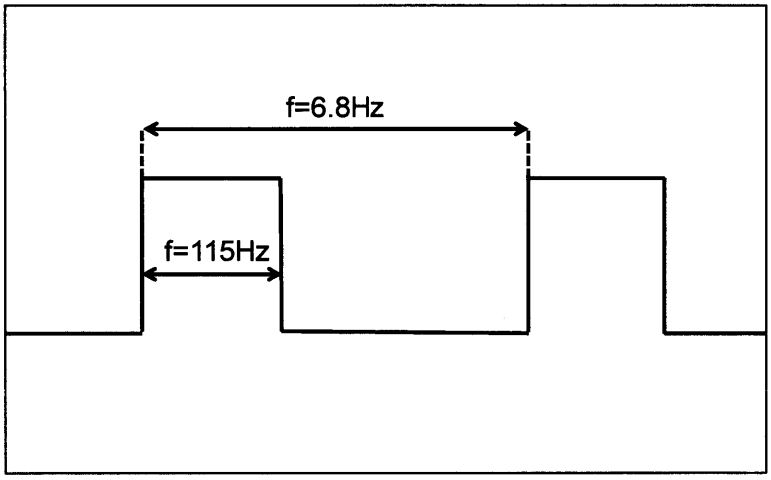

Figure 4-2: A schematic of the output the pulser produces, repeating square waves with a set width and repetition rate

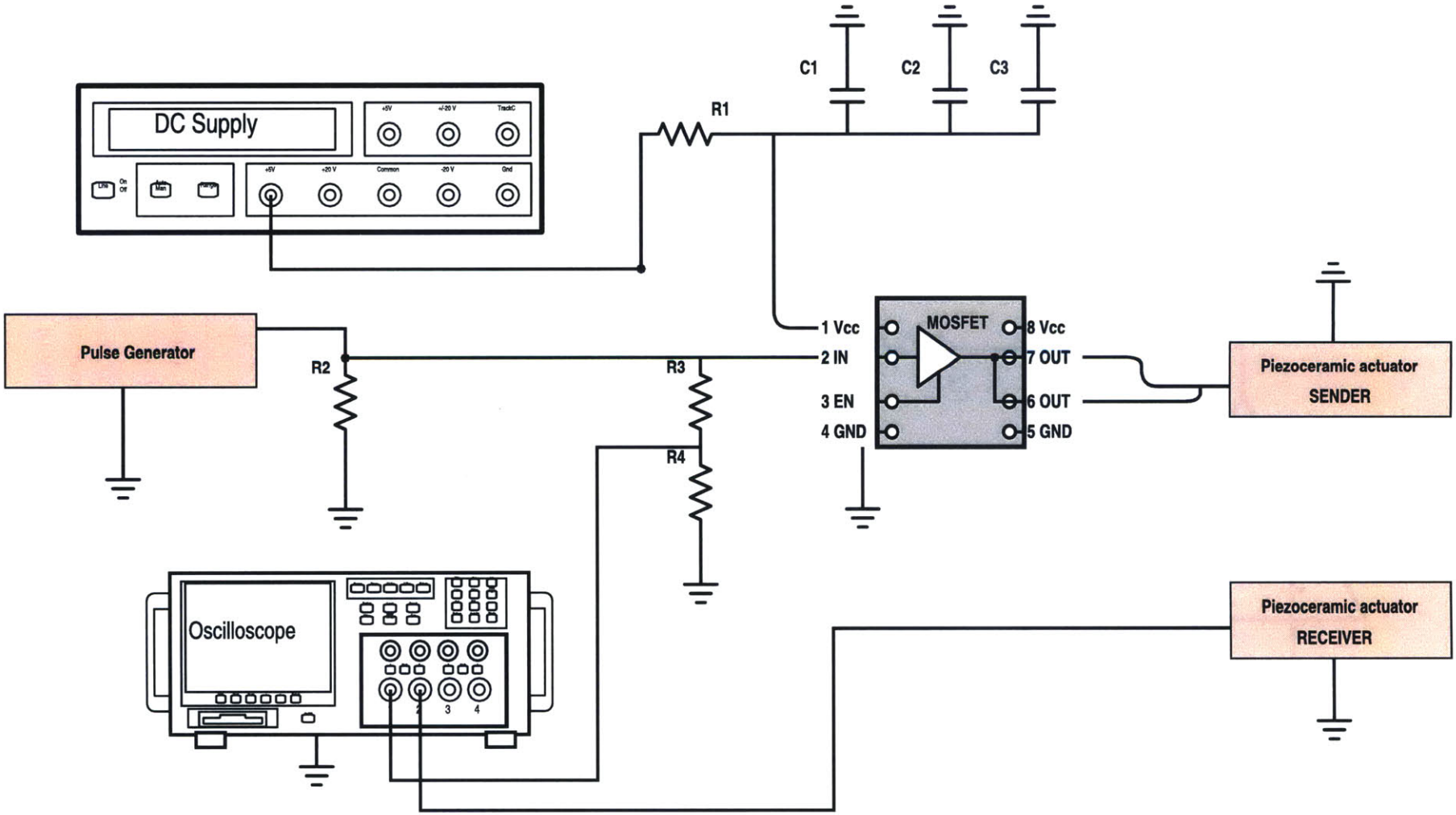

Figure 4-3: The schematic shows the peripheral components used to send and receive the signal. Additionally a MOSFET was used to increase the current going to the piezoceramic actuators, while capacitors and resistors were used to stabilize the signals

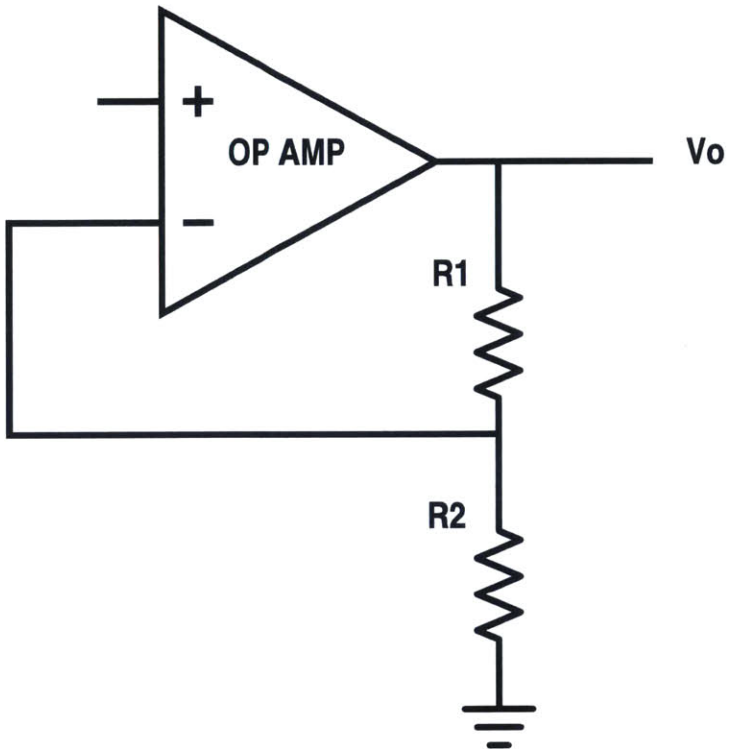

Figure 4-4: The Operational Amplifier (Op Amp) used here is the TLC 2262AI, with R_1 and R_2 signifying the two resistors used to control the amount of gain for the Op Amp

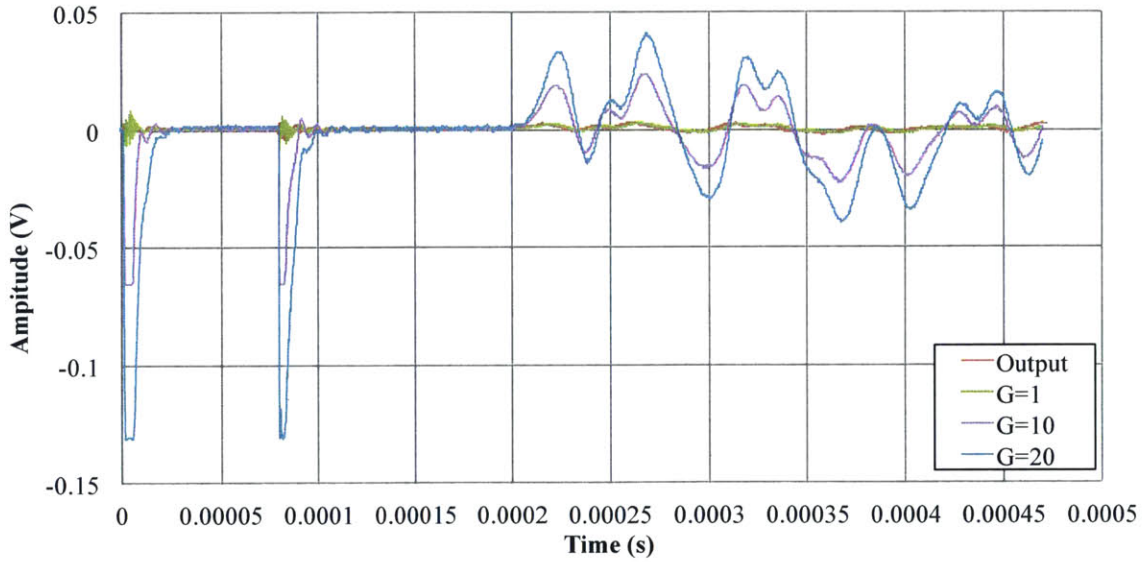

Figure 4-5: The use of an Op Amp with different gain settings of 1, 10 and 20 are compared to the original output signal of a P-wave through dry Ticino sand (under vacuum) at a driving voltage of 25V and frequency of 12kHz. The Op Amp provides a stronger, cleaner signal

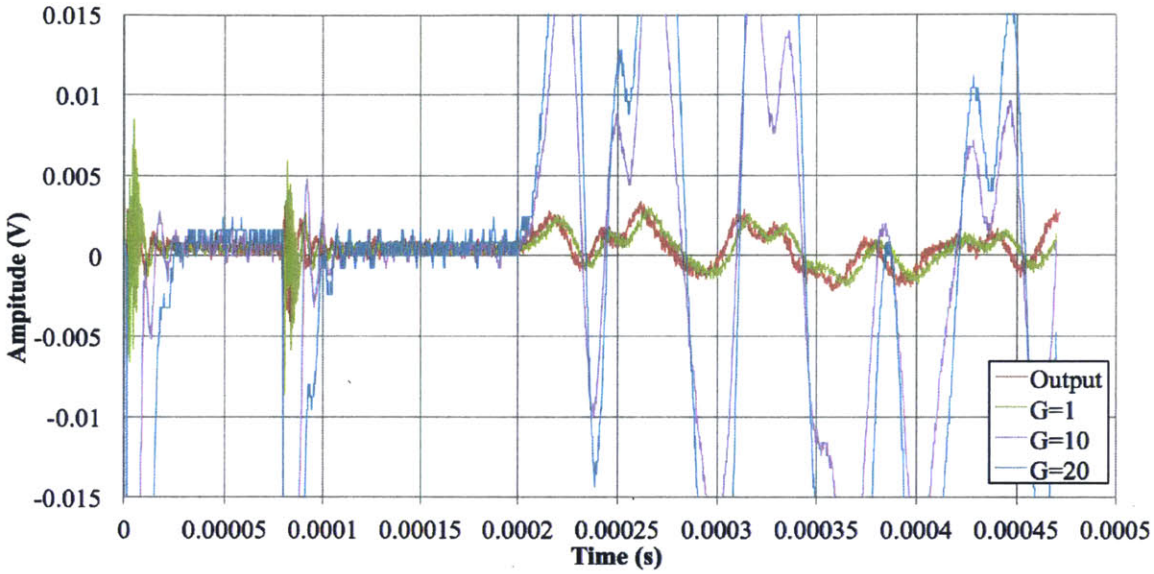

Figure 4-6: The same as Figure 4-5 is shown here with a zoomed-in perspective. It becomes apparent that the use of an Op Amp shifts the signal, thus causing an error in the travel time

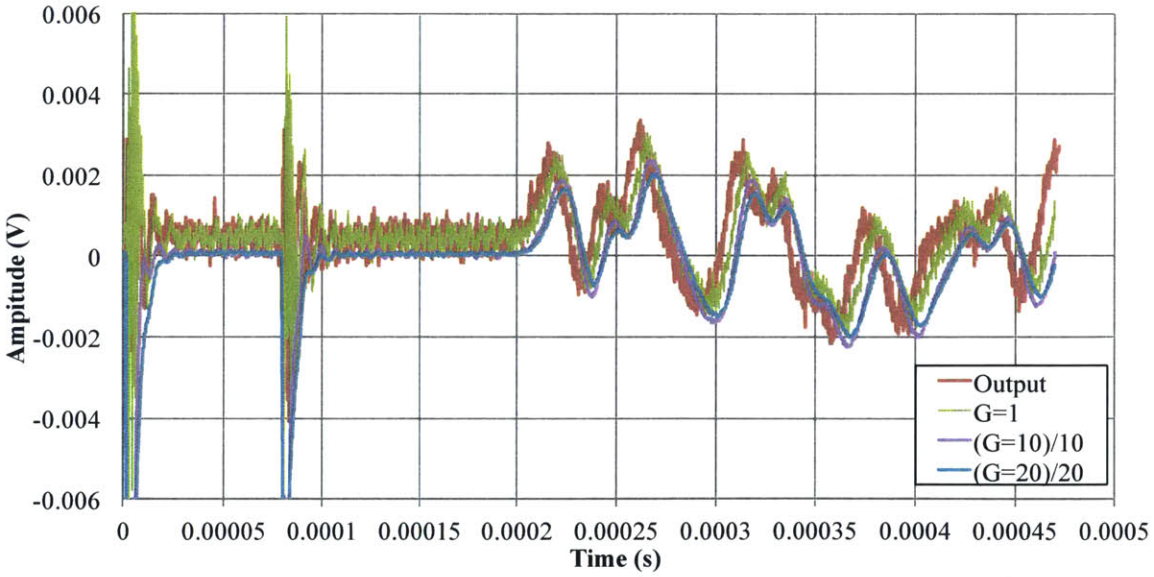

Figure 4-7: The same as Figure 4-5 is shown here with a zoomed-in perspective and with the gained signals normalized by the gain amount. Higher gains cause more shifting in the signals, with the gain of 1 having the smallest shift, and the gain of 20 signal having the greatest shift

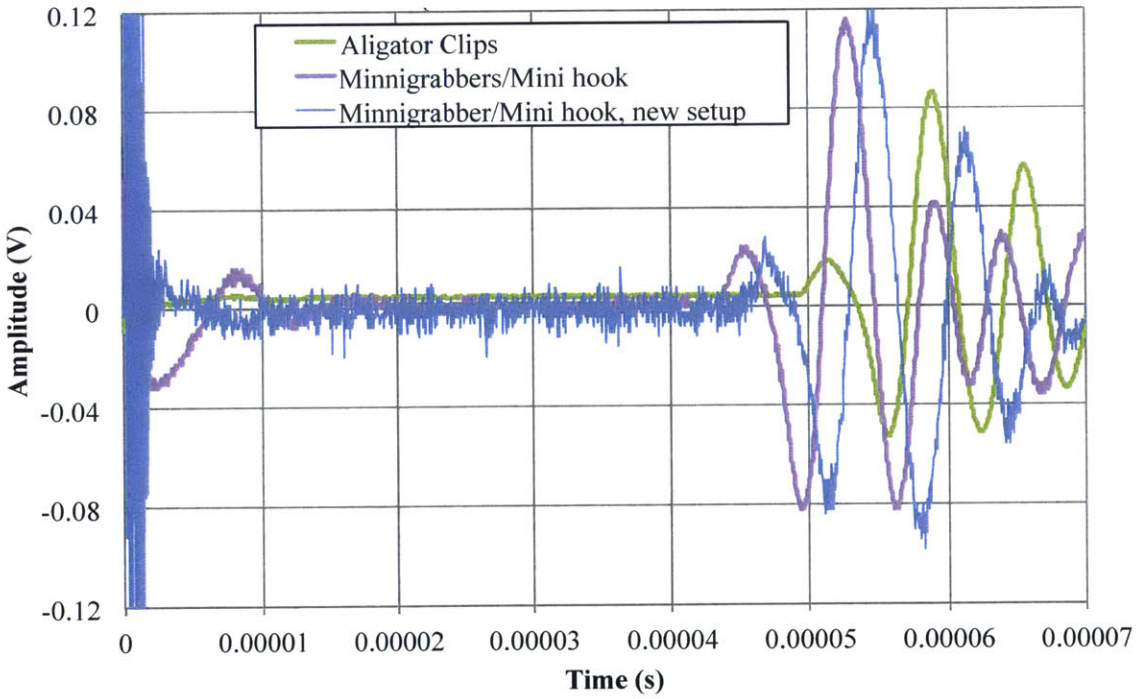

Figure 4-8: The best signal quality was achieved using alligator clips, as opposed to minigrabber/mini hook connectors. Furthermore, using a "new setup" of connecting all the peripheral devices into one power strip increased the noise significantly. The time shift is different since each scenario corresponds to a different test in the following order: TX1229 (RGOM-EI), TX1231 (RGOM Upper), and TX1232 (RGOM-EI), at 0.6 MPa, 1.6 MPa, 1.3 MPa respectively. Travel-distances also vary for each test

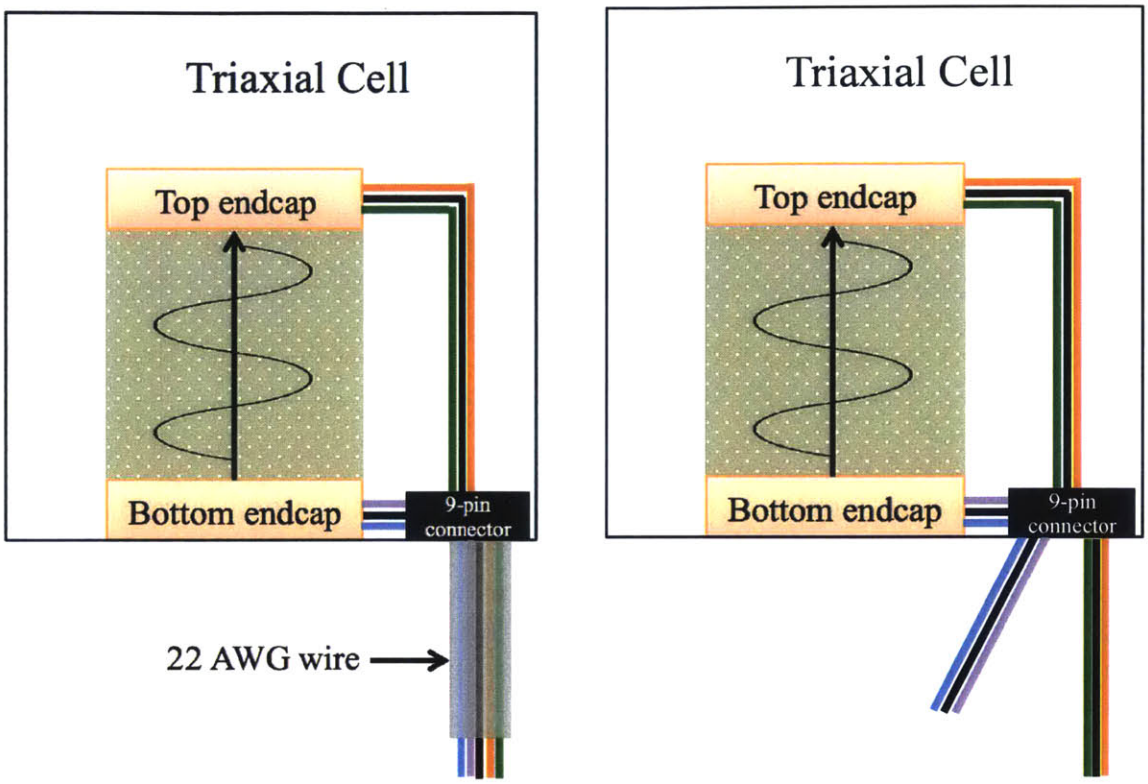

(a) Wiring configuration with a single wire

(b) Wiring configuration with separate wires

Figure 4-9: Schematic of two scenarios of wires used. Figure a) combines the top and bottom endcap wiring outside the triaxial cell, while b) keeps them separate. A black wire always represents ground, while the colored wires indicate P (orange & purple) or S (green & blue) waves. Results comparing the two scenarios are seen in the next figure

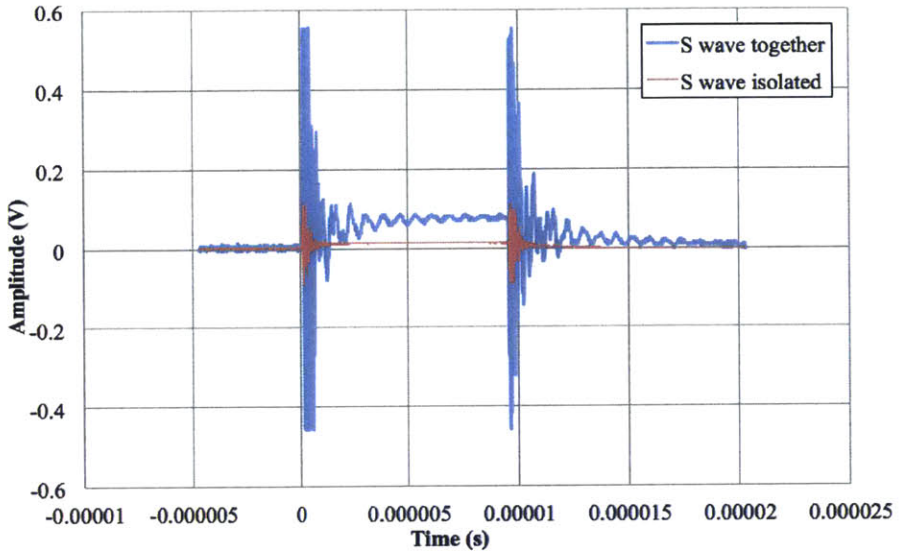

Figure 4-10: The top and bottom endcap wires were combined in a single bundled tube wiring, shown by the blue line. This was then compared to a scenario where the top and bottom endcaps used the same type of wire but have two separate wires for the top and bottom endcap

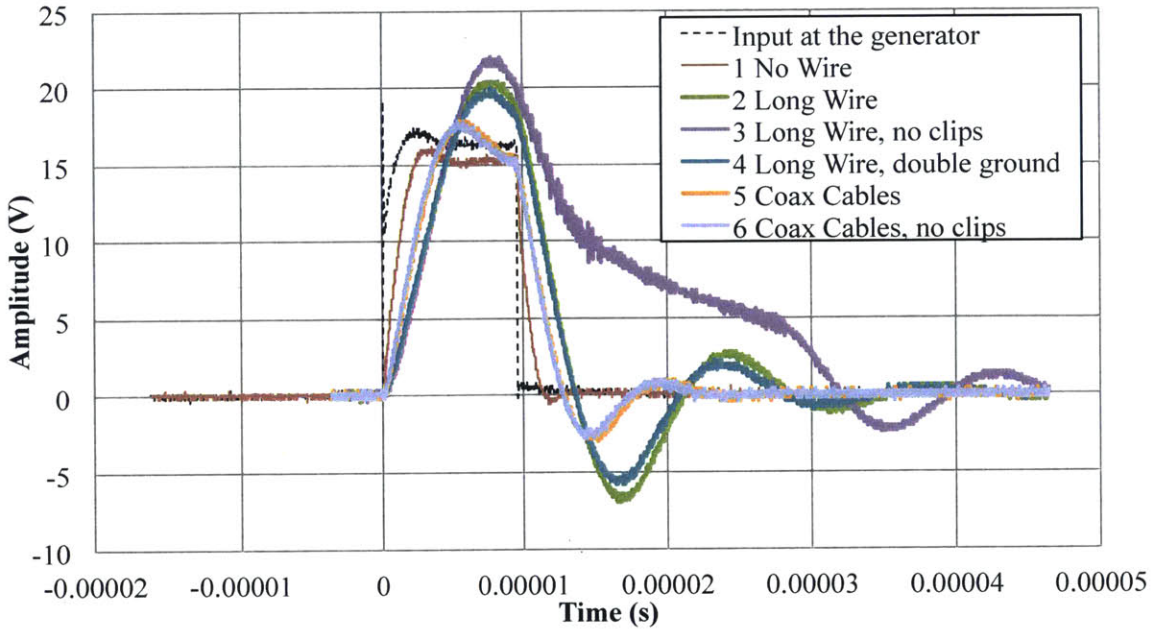

Figure 4-11: The direct input from the pulse generator is collected and compared to a signal going through a 1 μF capacitor at 100kHz and 15V. The baseline configuration is with a BNC cable connecting the pulse generator to a breadboard containing the capacitor, followed by a BNC cable connecting the output from the capacitor to an oscilloscope. Different ways of connecting the capacitor to the oscilloscope are tested. The long wires with no clips causes the worst signals (with severe damping), while the absence of wires has the best signals

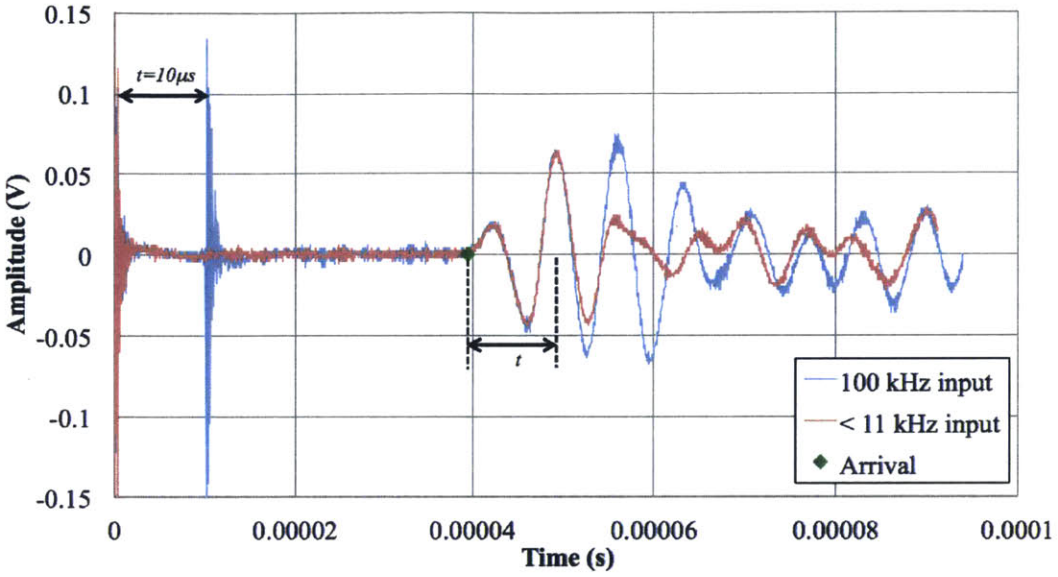

Figure 4-12: A specimen of saturated Ticino Sand is isotropically loaded by 10 MPa. The input frequency of the square wave is changed to be both high enough to occur before the arrival of the P-wave (freq = 100 kHz or t = 10μ s), as well as low enough to entirely encompass the arrival (q< 11 kHz). The two output signals are shown. The arrival time is unaffected by the frequency, as the two output signals overlap each other until the down dip of the square wave for the high frequency case

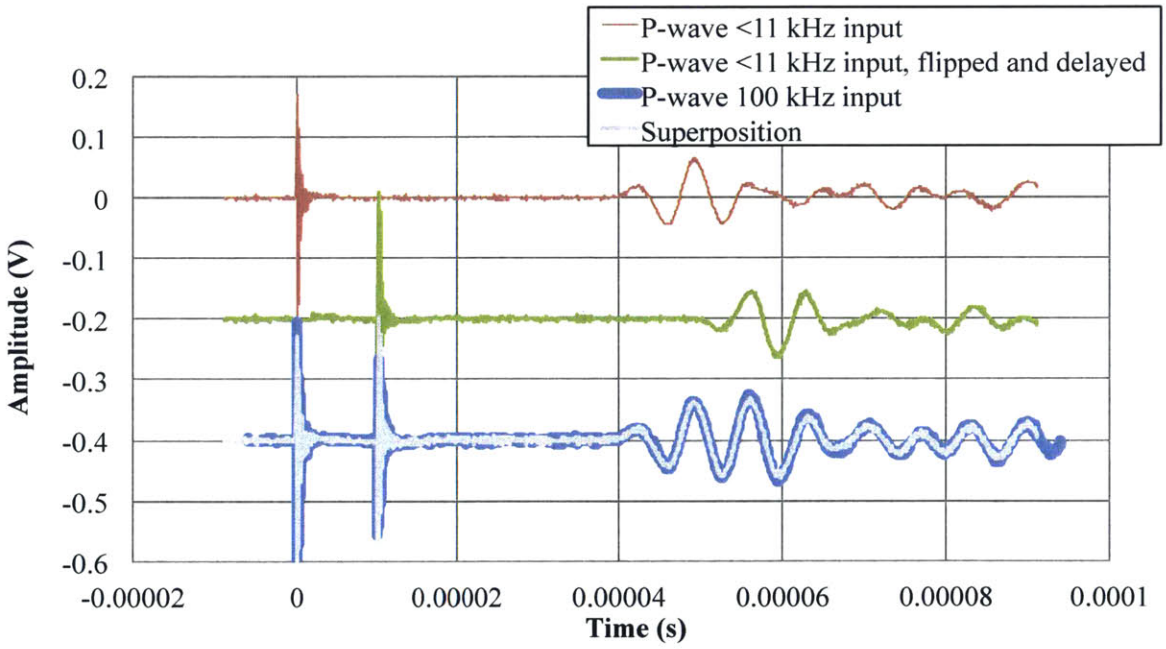

Figure 4-13: The output signal obtained from a low frequency input signal (<11 kHz) is delayed by q=100 kHz and inverted. The original superimposed with the inverted, delayed signal overlaps exactly with the signal obtained from a square step function caused by a 100 kHz input

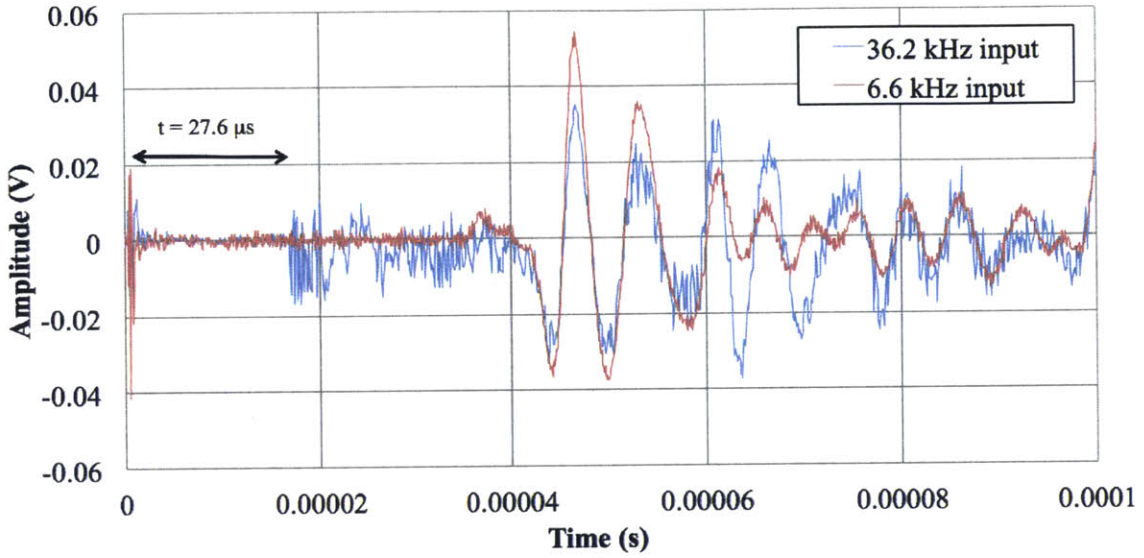

Figure 4-14: A specimen of Presumpscot clay is saturated and confined by 0.1 MPa. The input frequency of the square wave is changed to be both high enough to occur before the arrival of the P-wave (36.2 kHz), as well as low enough to entirely encompass the arrival (6.6 kHz). The quality of the signal is much better for the low-frequency step input. The high frequency input makes the arrival time of the P-wave signal very ambiguous

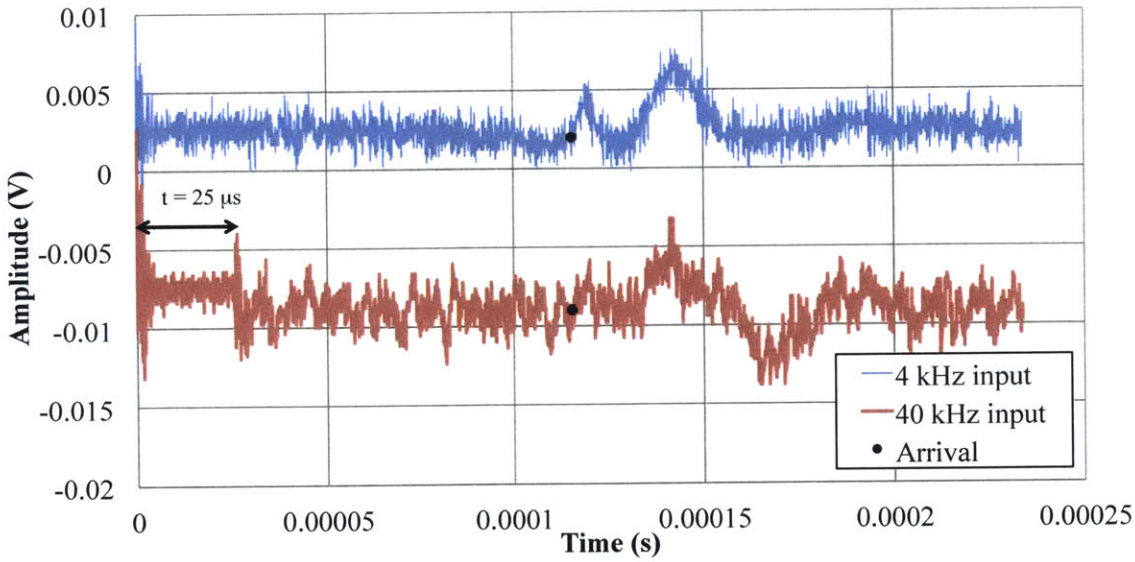

Figure 4-15: A specimen of Presumpscot clay is saturated and confined by 2.1 MPa. The input frequency of the square wave is changed to be both high enough to occur before the arrival of the S-wave (40 kHz) , as well as low enough to entirely encompass the arrival (4 kHz). The quality of the signal is much better for the low-frequency step input. The high frequency input makes the arrival time of the S-wave signal very ambiguous. The black dots are the arrival time obtained from the low frequency input arrival.

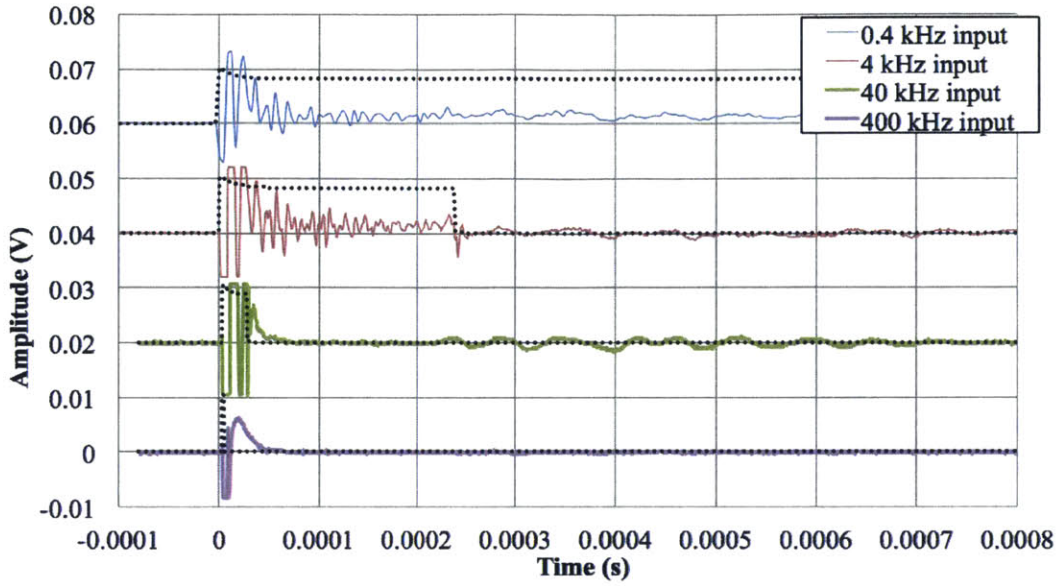

Figure 4-16: A specimen of dry Ticino sand under vacuum is excited by a series of different excitation frequencies, with the received P-wave signal responses shown in solid lines. The input pulse is shown with a black dotted line for each case. The signals have arbitrary offsets in the amplitude to space them apart for clarity. The amplitude of the input signals (shown with dotted lines) is divided by 600 to fit on the graph

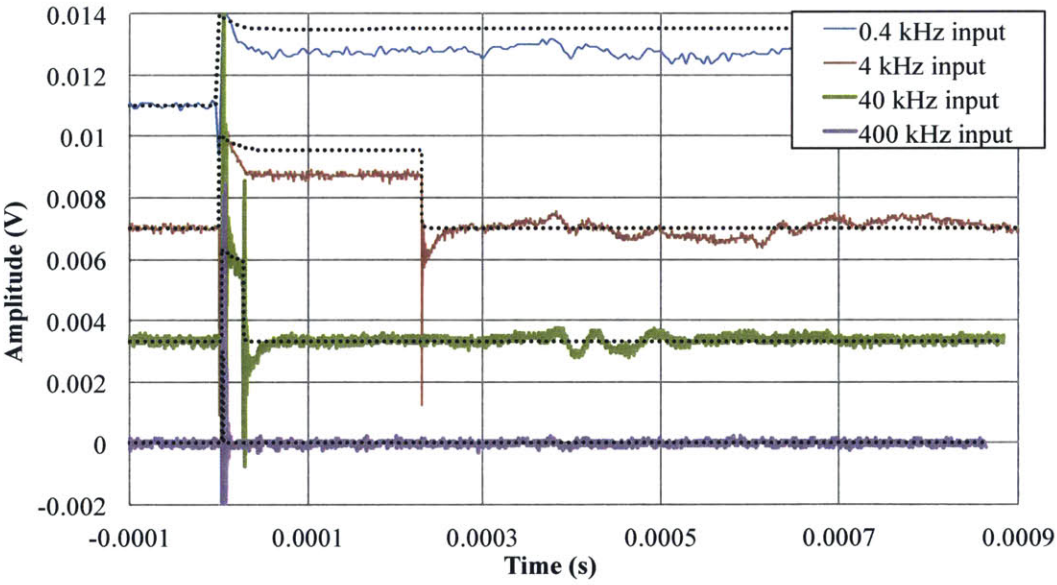

Figure 4-17: A specimen of dry Ticino sand with no load applied was excited by a series of different excitation frequencies, with the received S-wave signal responses shown in solid lines. The input pulse is shown with a black dotted line for each case. The signals have arbitrary offsets in the amplitude to space them apart for clarity. The amplitude of the input signals (shown with dotted lines) is divided by 2000 to fit on the graph

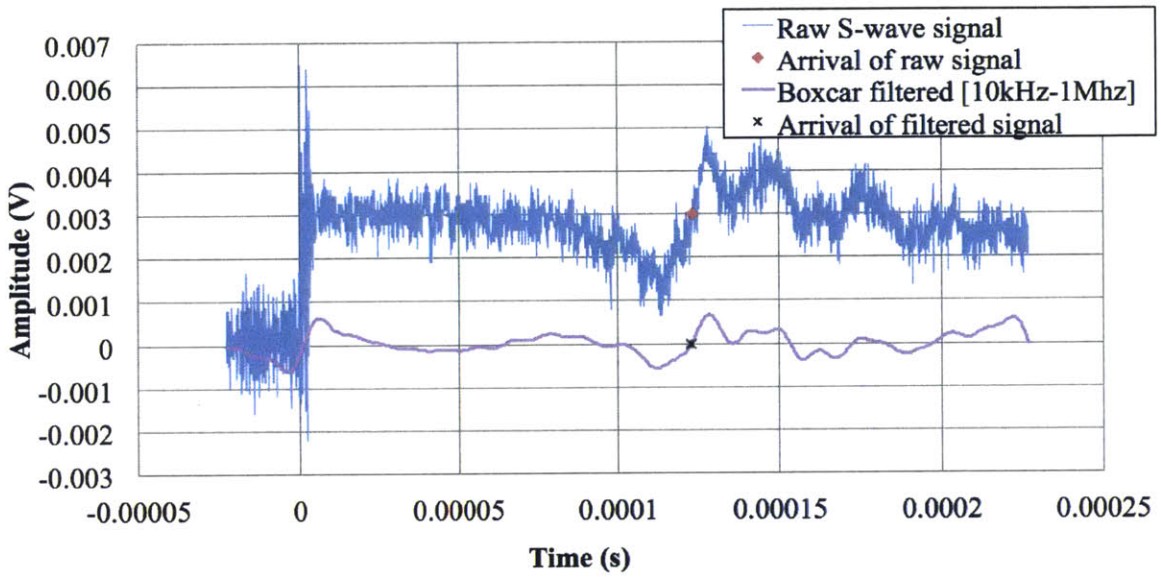

Figure 4-18: S-wave signal through RBBC at 4.9 MPa is shown in the raw form and its respective arrival, as well as the post-processed signal that was filtered by a boxcar filter with the limits being 10kHz and 1MHz and its arrival. Everything outside this frequency range was eliminated. The arrival times were 123.0 and 122.7 μ s, resulting in a 0.25% error

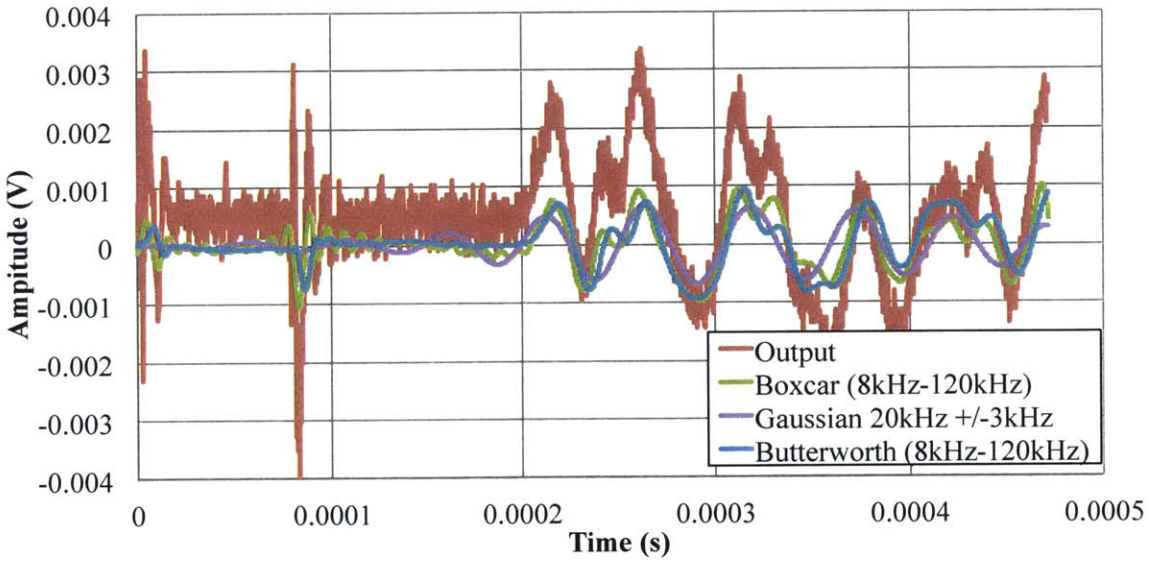

Figure 4-19: The output P-wave signal through Ticino sand is shown in the raw form, as well as the signals after some post-processing filters are applied. A boxcar, Gaussian, and Butterworth filter are applied to the signals, and it becomes apparent that the arrival time is affected by the filter used

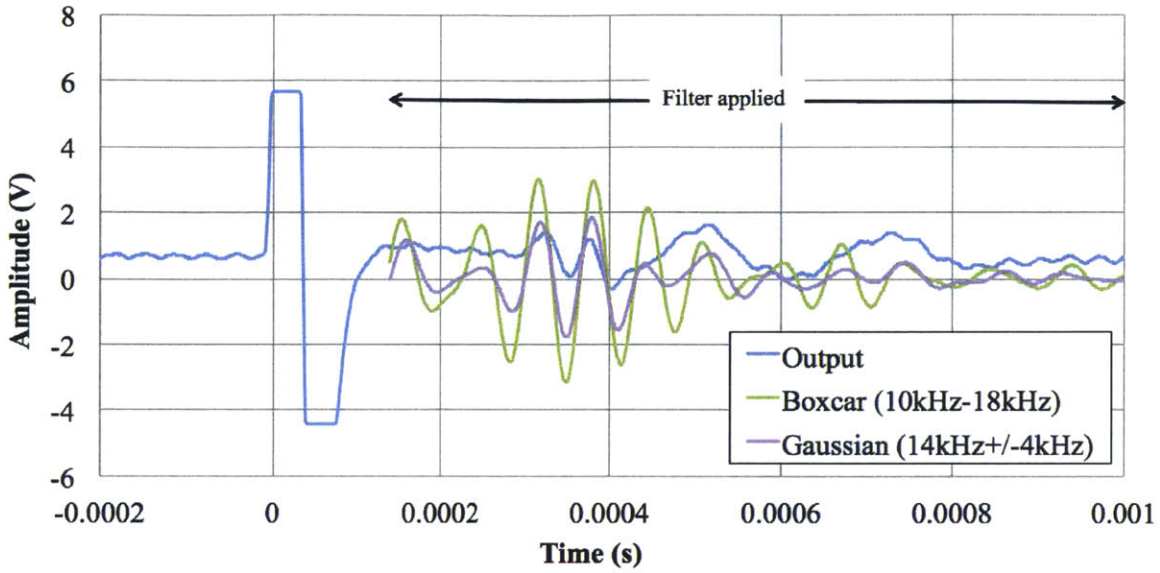

Figure 4-20: A poor-quality S-wave signal through RBBC at very low stress (0.05 MPa) is shown in its original state as well as filtered using a boxcar and Gaussian filter. The dominant frequency of the response is approximately 14kHz. In this case, the application of a filter does not improve the signal quality, but rather masks the arrival

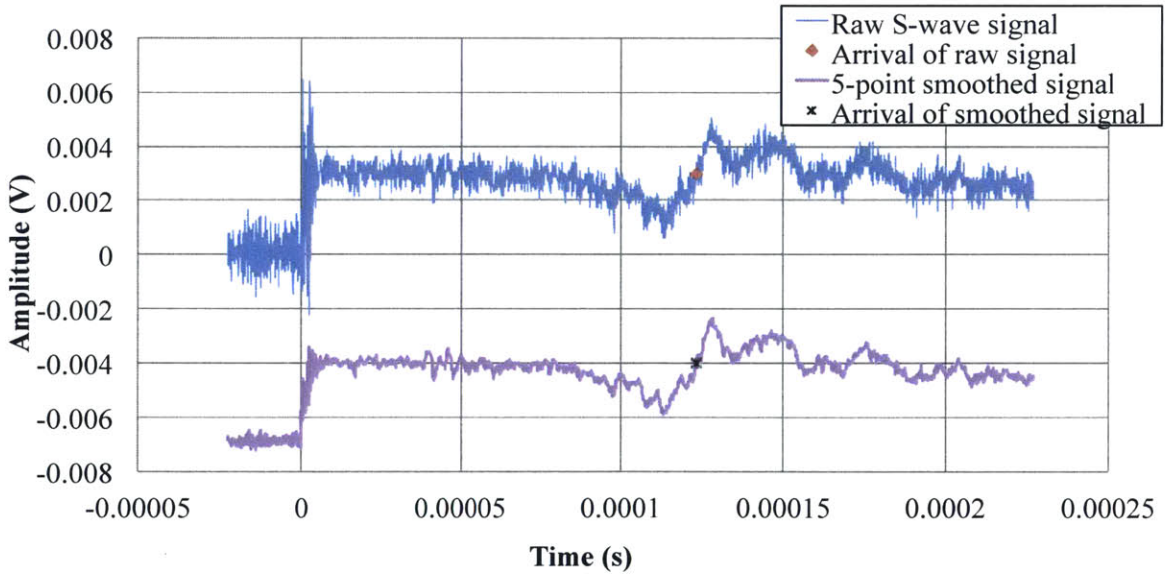

Figure 4-21: S-wave signal through RBBC at 4.9 MPa is shown in the raw form and its respective arrival, as well as the 5-point smoothed signal and its arrival. The arrival times were 123.0 and 123.1 μs, resulting in a 0.08% error. The 5-point smoothed signal was arbitrarily shifted for clarity in the y-direction

Chapter 5

Experimental Results

5.1 Introduction

This chapter serves the purpose to present data acquired during the medium stress triaxial tests. First, Section 5.2 briefly discusses how the velocity signals are processed in order to obtain the velocities through the materials, followed by an analysis of the error band present in the interpretation in Section 5.3. Section 5.4 presents the compression behavior of the materials, followed by Section 5.5, where the velocity results during the loading portion are discussed. The high stress velocity results are presented in Section 5.6. Section 5.7 discusses the frequency response of the signals as a function of stress and type of material. After the initial introduction of all the raw data, Section 5.8 presents the data in different forms, including velocity as a function of porosity, stress, and density, as well as the modulus curves and Poisson's ratio calculations. Next, the effect of creep on the velocity results is presented in Section 5.9, which then leads into the unloading portion of the compression curves and how the velocity behaves during the unloading part (Section 5.10).

A compilation of all the medium stress triaxial tests are presented in Table 5.1, including the resedimentation numbers or bore tubes, as well as the initial and final phase relations and the level of unloading performed during the test.

5.2 Signal Interpretation

First, the signal waveform is introduced before signal acquisition and processing are described. Figure 5-1 shows a typical P-wave signal through RBBC, as well as the input signal directly obtained from the pulser. These signals from the oscilloscope are averaged 128 times by the oscilloscope. The upwards step of the input signal begins before the zero time marker because of the trigger selection. The oscilloscope is set to trigger the data acquisition when the input signal reaches an amplitude of approximately 2/3 of the maximum peak. This avoids any false triggering. In the received signal, there is evidence of crosstalk, which can be seen as a burst of energy in the received signal appearing close to the beginning of the step input function. Crosstalk can be caused by inadequate shielding and conductive coupling between the pore fluid and the sending and receiving transducers (Montoya et al., 2012).

Each time the output signal (in blue) is collected, the corresponding input signal is always taken. Although common practice assumes the crosstalk observed in the output signal corresponds exactly with the input signal, this research finds that there is sometimes a slight delay between the crosstalk and the actual input step pulse. Therefore the travel time measurement is always taken by analyzing both the direct input signal and the output signal. The travel time is the time difference between the first evidence of increased voltage in the input signal and the zero-crossing of the first major peak in the output signal, marked by a red dot in Figure 5-1.

During the course of the triaxial test, velocity measurements are taken both during the loading and unloading portion of the compression curve. The measurements are manually taken with an oscilloscope that averages the readings 128 times and has a sampling rate of 500 MS/s. Due to an electrical communication between the pulser and the triaxial computer controls, which causes a disruption in the stress-strain controls, the computers are momentarily stopped while the signal is acquired. The signals are saved onto a flash drive and transferred to a computer. A MATLAB code written by the author collects the individual files taken for both the P and S-waves for each stress level and processes them, makes a first approximation of

the arrival time, and exports it into an excel file. Furthermore, the MATLAB code smooths the signal by applying a 5-pt average smoothing. The P-wave signals are smoothed and normalized to the maximum peak in the signal, as shown in Figure 5-2. The author goes through the signals and generated arrival times for quality control, making adjustments if needed. The signals are incrementally offset in the vertical direction for clarity. The stress level of each signal is shown in the legend, and only the loading signals were selected. The arrival of the P-wave is represented with a black asterisk.

In the case of the S-wave, there is an offset observed in the amplitude of the signal if the arrival occurs during the input step function (which is the case for all the signals in general, as specified in Chapter 4). The code shifts the voltage so that the signal is crossing the x-axis, which facilitates zero-crossing picking performed by the MATLAB code. Finally, the S-wave signals sometimes exhibit a declining major axis (the axis of symmetry is not parallel to the x-axis), resembling a capacitative discharge during the signal. The signal is straightened out so that it can be appropriately shifted for the arrival time interpretations. The resulting S-wave signals are presented in Figure 5-3. The arrival time of the S-wave is shown with a red asterisk, while the peak is shown with a blue dot. Additionally, the P-wave arrival obtained from Figure 5-2 is superimposed onto the S-wave signals, again marked by a black asterisk. The black asterisk clearly coincides with a packet of activity seen in the signal, which indicates the presence of a weak P-wave signal in the S-wave signal. A zoomed-in version of Figure 5-3 can be seen in Figure 5-4. The location of the red asterisks signifying the S-wave arrival becomes more apparent. As mentioned previously, the zero-crossing of the signal is selected for the arrival time, as shown by the dashed line. For the shear wave, there appears to be a down-dip that precedes the zero-crossing. This is a peculiarity of the clays tested in this research, and is not present in the other materials tested, such as sand and the calibration spacers. It closely coincides with a reflection of the P-wave arrival, which is dependent on both the geometry of the specimen and the P-to-S wave ratio. Furthermore, the endcaps were carefully calibrated and the orientation for the S-wave transducers was validated before any testing on soils was

performed, thus a positive peak is expected, rather than a negative peak. The down-dip is believed to be P-wave energy that arrives before the S-wave and is regarded as an artifact in the signals.

5.3 Errors

The primary sources of error found in this research are attributed to electronics limitations and noise, rather than the repeatability of the experiments themselves. The scatter seen in geotechnical laboratory measurements is quite common for many reasons, including the variability in the specimens used, sensitivity of the soil type, and procedural difference due to human error. Although there has been a great effort to standardize testing procedures, such as with ASTM, the unfortunate stereotype of geo-materials testing having a high variability due to the inherent materials being tested has also allowed for relaxed expectations of repeatability. Despite the low precision that is common in geotechnical testing, the use of resedimented materials has greatly improved this research's ability to have high precision while maintaining low bias. The data in this research is evaluated based on two methods – assess the precision based on the signal quality and interpretation methods, and look at the repeatability of the tests.

Precision of the data is determined by analyzing the digital velocity signals and the possible error in the height measurements of the specimen, since these two factors are fundamental to the subsequent velocity measurement. The aim of this error analysis is to procure the most extreme cases of velocity interpretations, thus creating the largest possible error band. The arrival time interpretation is conducted on a single test (TX1235) to obtain a representative example of the quality of the velocity signals. The upper and lower bounds are taken around the actual arrival time selected at the time of the original interpretation. The upper bound is taken to be approximately the amplitude at 10% of the peak of the signal. For example, if the maximum amplitude of the first peak is about 0.03V (as is typical for a P-wave), the upper bound is taken as the time index closest to an amplitude of 0.003V, after the correct arrival

time. Since a discrete signal is analyzed (rather than a continuous best-fit curve), the amplitude is sometimes slightly less than 10% of the maximum peak. The lower bound is either taken as the index where -10% of the maximum amplitude occurs before the arrival time in the case of a precursory downdip (as seen in S-wave signals), or taken to be the point at which the signal definitively tapers off or has an amplitude of zero. Sometimes precursory activity in the signal occurs, usually marked by an exaggerated amount of noise, in which case the lower bound is taken right before this additional noise. In addition to the signal analysis, height measurements of the specimen are considered. The maximum variability in the height is taken as the difference between the calculated final measurements based on LVDT displacement during the test and the initial height measurement, and the height based on the final specimen measurements. After these two factors are considered, an error band around the actual measurement is produced. The fastest travel time and tallest specimen height is used to calculate the fastest upper bound (UB) velocity, while the slowest arrival time and shortest specimen height is used for the slowest lower bound (LB) velocity. The difference between the actual velocity and the UB and LB velocities is calculated as a percentage, plotted as a function of stress in Figures 5-5 and 5-6, for P and S-wave respectively. It's evident that the errors for the UB and LB is approximately the same, indicating that there isn't a significant bias to higher or lower velocities.

While Figures 5-5 and 5-6 provide the values for a specific test (TX1235), the error bands are taken as a representative amount of expected error in any given test based on the velocity interpretations and height measurements. These errors are fit by a linear regression, which produces upper and lower bound errors as a function of stress for both the P and S-wave velocity. These upper and lower bounds are applied to the average velocity profile for all RBBC experiments performed in this research. The resulting curves are seen in Figure 5-7. The yellow shaded region encompasses the possible spread of velocity results around the average line based on the most extreme possible cases. This band should *not* be confused with the error present in this research, but rather as the maximum possible error due to poor interpretation

and measurement practices.

The level of repeatability is a measure of how repeatable the results are when tests are conducted on the same specimens by the same person using the same equipment and procedures. While the general sense of repeatability can be observed in the previous velocity figures in this chapter, an attempt at quantifying these values for the P-wave can be seen in Figure 5-7. There are four tests conducted on RBBC and three tests conducted on RGOM-EI. These velocity curves facilitate a standard deviation calculation around the average velocity as a function of stress. The vertical bands on the RBBC and RGOM-EI symbols indicate one standard deviation away from the average value. Figure 5-7 shows a wider spread in the RBBC results than for RGOM-EI. This might be partly due to the sequence of the tests. The RBBC tests are performed earlier in the experimental sequence, thus are more prone to error due to the learning curve of the experimentalist. It is clear, however, that the variability in the experimental results is significantly less than the possible errors due to electronics, indicating that interpretation errors are quite low in this research.

The same analysis is performed on the S-wave signals, with the results shown in Figure 5-8. When observing the differences in error for the P and S-wave signals, the S-wave signal clearly shows a much lower sensitivity than the P-wave signal, supported by a much smaller error band caused by electronics for the S-wave error. On the other hand, the error band on the repeatability of the S-wave velocity results is much closer to that of the error band caused by electronics, thus indicating that the resolution of the signal and the human interpretation are approximately of the same order of magnitude. While it may seem to imply that S-wave arrival picking is less ambiguous than P-wave arrivals, this is mostly dictated by the resolution of the signal. Due to the scaling of the oscilloscope and the high speed at which the P-wave travels, we are more bit-limited in the P-wave signal, thus introducing a higher amount of possible electronics error.

This analysis assumes that there is no ambiguity in picking the arrival of the S-wave, despite the downdip precursory effect seen in Figure 5-4. The method of picking the S-wave arrival is consistently taken as the point where the signal sees

the zero-crossing, indicated by a red asterisk in the figure. If the S-wave error band calculation were taken as the very beginning of the downdip, the error values would be significantly higher, on the order of over 50%, which is unrealistically high.

In addition to the possible error in velocity measurements, the errors in stress and void ratio are calculated. The stress calculation is based on a force measured by a load cell and a cross-sectional area of the specimen. The cross-sectional area is prone to error, thus the difference between the computer-calculated area and the measured area at the end of the test is taken as the maximum error in area, much like the previous analysis of height. In Figure 5-9, the error bars for both the velocity and stress are presented for TX1235, showing that the error in stress is very small. There is a slight increase in error for the stress because the load applied by the axial load frame is proportionally increasing as compared to the cell pressure. The error is only shown on a graph with P-wave velocity since it is the same amount of error for the S-wave velocity curve.

Similar to the stress error calculation, the error in void ratio is calculated, shown in Figure 5-10. Void ratio is the fraction of volume of voids to volume of solids. Both the area and height are used to derive the void ratio, thus an extreme difference in area and height are used to calculate the void ratio error. The final computer-calculated dimension based on initial dimensions and changes registered by LVDT's and string pots is compared to the final measured dimensions of the specimen using a caliper. The void ratio is highly sensitive to the height and area dimensions, exemplified by the large error possible in the void ratio calculation in Figure 5-10. The amount of error possible in the void ratio is equivalent or larger than the error present in the velocity measurements. Once again, it is worth mentioning that these are the extreme errors possible from inaccurate dimensional measurements rather than errors present in the measurements themselves.

5.4 Compression Behavior

5.4.1 Compression Curve Results

The K_0-consolidation compression curves are presented in Figure 5-11. The curves are plotted in log-linear space, where the void ratio is a function of vertical effective stress in logarithmic scale. The lines are color coordinated so that clusters of the same material are different shades of the same color. The unloading portions of the curves have been omitted for clarity and will be discussed later in Section 5.10. It should be noted that although the unloading portion is left out, the creep that occurs before the unloading portion is present. Creep, or secondary compression, occurs when the specimen is held at a specific stress state for a prolonged amount of time after experiencing virgin compression. Depending on the material, the amount of deformation during secondary compression can be significant. Creep is further discussed in Section 5.9.

Based on the compression curves in Figure 5-11, and further supported by the strain curves in Figure 5-12, the high smectite clays (RGOM-EI, Upper and Lower) begin with a higher void ratio at low stresses. As consolidation occurs, the high smectite clays experience greater amounts of deformation, indicated by a greater drop in void ratio. The exception to this is RGOM Lower, whose compression curve is much lower, partly due to its low specific gravity. The Presumpscot clay is intact and overconsolidated, with a negligible smectite content, rendering it very stiff and not as compressible. Overall, the different soils tend to converge at higher stresses. Furthermore, the high plasticity clays have a decreasing compression index (C_c), marked by a slightly concave-up curve. C_c is the slope of the virgin compression line in void ratio - log effective stress space. These results are consistent with Casey (2014).

The stability of the stress controls is also a distinguishable feature in the compression curve graphs. Some of the tests early in the experimental sequence, including TX1222, have more instability until the correct sensitivity parameters are used in the PID control code. Additionally, the high smectite clays have more instability

due to the system's difficulty in maintaining K_0-consolidation with low permeability samples.

5.4.2 K_0 Results

During the course of the triaxial tests, K_0-consolidation is followed using a PID algorithm that ensures zero lateral strain. The algorithm applies a constant axial rate of strain while monitoring the axial and volumetric strain exhibited in the specimen. The axial strain multiplied by the initial specimen area needs to be equal to the volumetric strain of fluid expelled from the specimen via drainage lines in order for the K_0 criterion to be fulfilled. The lateral stress ratio (K_0) of the material is measured based on the applied axial and radial stresses. Figure 5-13 shows all the K_0 values for the different tests. The different starting points indicates differences in the preconsolidation pressures. The unloading portions are omitted again for clarity and will be revisited in Section 5.10. All of the tests begin at K_0=1 since the specimen is hydrostatically loaded during back pressure saturation. As K_0-consolidation commences, more axial load is applied and the K_0 value plummets briefly as it is stabilizing. Next the K_0 value rebounds a little to a stable condition and maintains a relatively constant K_0 value. In the case of the high smectite clays like the RGOM's, there is a clear trend of increasing K_0 as a function of stress, while the low smectite clays exhibit a very constant K_0.

From Figure 5-13, it can be seen that the RGOM's K_0 generally falls between 0.6 - 0.8 over the span from 1 to 10 MPa. RBBC typically has a K_0 value between 0.55 - 0.6. Finally, the Presumpscot clay varies between 0.43 - 0.5, with the wide range attributed to the natural variability of intact samples. All of the materials seem to follow a narrow range of K_0 with the exception of TX1228, which seems to be anomalously low for RBBC. This low value could be due to a small error in the area calculation in the computer algorithm, which is henceforth propagated throughout the rest of the test.

5.5 Loading (K_0) Velocity Behavior

When looking at the velocity behavior through clays, the compressional velocity and shear velocity need to be viewed as two separate entities before they can be compared with each other. The P-wave is significantly affected by the presence of water and travels through both the matrix and fluid, while the shear wave only travels through the matrix but is slightly altered by the density effect of water[1]. This statement alone leads the reader to come to the conclusion that the S-wave velocity is dependent on either the mineralogy or clay particle interaction. On the other hand, the P-wave is affected by the pore fluid chemistry and mineralogy.

Before analyzing the influence of mineralogy on the velocity behaviors, it is warranted to briefly describe the clay mineralogy itself. Clay particles are flat, platy structures surrounded by a diffuse double layer of water. The size and geometry of the platy structures varies greatly, depending on the type of material. Kaolinite, which is considered a "large" particle, has a thickness of 30-1000 nm and a diameter-to-thickness ratio of 3-10. Illite has a thickness of 10-200 nm with a diameter-to-thickness ratio of about 10. Finally smectite, which is considered a "small" particle, has a thickness of 1-10 nm and a diameter-to-thickness ratio greater than 100 (Lambe and Whitman, 1969). The diffuse double layers, which are commonly referenced in geotechnical literature, are layers of water electrostatically attached to the clay faces. The thickness of the double layer depends on the type of material and the pore fluid. The specific surface area (surface area per mass) of a clay particle directly relates to the magnitude of the electrical charge of the particle. The Specific Surface Area (SSA) of smectite is around 50 times larger than that of kaolinite (Lambe and Whitman, 1969), thus smectite has a larger amount of exchangeable ions in order to neutralize its net charge. The Cation Exchange Capacity (CEC) is a measure of the exchangeable ions present on a clay particle, thus it is expected that smectite has a much higher CEC than kaolinite for the same mass quantity[2]. In the presence of

[1]There are some frictional effects introduced by water, as well as possible Poiseuille type movement of the fluid within the pores (Biot, 1956)

[2]Kaolinite has a CEC of 5 meq/100g while smectite has a CEC of 100 meq/100g

water, the exchangeable ions and mineral surfaces attract water. Since smectite has more surface area and exchangeable ions, a larger double layer forms. Furthermore, a high pore fluid salinity can decrease the thickness of the double layer, shown by Horan (2012). The effect of this diffuse double layer on the velocity measurements is not well-understood. There are two schools of thought about how the double layer behaves (Ladd, 1996):

1. The double layer contributes to the cohesive strength of the material since it has a very high viscosity, which is responsible for the creep effect

2. The double layer behaves like a 2D liquid, highly resisting movement away from the clay surface, but is easily moved along the surface, thus not contributing to strength

Regardless of which theory is true, it is generally accepted that the double layer reduces the amount of mineral to mineral contacts. Since kaolinite has the smallest double layer, it has the most grain contacts, while smectite has the least, with illite falling between the two. Furthermore, with such large double layers, the overlapping of double layers in smectite causes a more parallel plate orientation. This explanation is supported by the sedimentation tests performed by Horan (2012) and Fahy (2014) for leached BBC and leached GOM-EI respectively. The images seen in Figures 5-14 and 5-15 show that for BBC, salinity ranging from 1 g/L to 256 g/L has virtually no impact on the sedimentation height (or flocculation of the structure), whereas GOM-EI has a marked decrease in sedimentation height as a function of increasing salinity. As the salinity increases, the double layer decreases, allowing for more face to edge contacts that form floccs. As the amount of flocculation increases, there are more void spaces through which sedimentation occurs, thus expediting the sedimentation. BBC is insensitive to salinity differences from 1 to 256 g/L whereas the double layer thickness of GOM-EI is quite sensitive to changes in salinity from 1 to 256 g/L.

Investigating the effects the double layer has on permeability sheds some light into the effects it would have on the velocity. Mesri and Olson (1971) report that permeability is most affected by the flocculation of clay particles, which subsequently

influences the size and shapes of the void spaces. With the application of stress, the particles become more aligned orthogonal to the axis of principle stress, thus increasing the tortuous flow paths in the principle axis, decreasing the permeability. The mean particle orientation obtained by analyzing SEM images by Adams (2014) can be seen in Figure 5-16. This effect is larger for particles with large diameter-to-thickness ratios (i.e. smectite). In addition to the tortuosity, the size of the double layers affects the permeability – larger double layers obstruct the flow path (Mesri and Olson, 1971).

One can look to the factors influencing permeability to explain the velocity behavior:

- Flocculation during deposition determines void shapes and sizes
- Extent of particle rotation/alignment is determined by particle geometry
- Thickness of double layer encroaches into void space

While the magnitude at which each of these factors influences the velocity values is not quantified, the wide range of materials tested at different salinities can be used to highlight which factors are at play, when the results are discussed in the next chapter. In general, it is useful to recall that the dominant mechanisms controlling the behavior of the different soils is different. Sridharan and Prakash (1998) note that even the liquid limit of kaolinitic and montmorillonitic soils are controlled by different things – kaolinite is controlled by the mode of particle arrangement as governed by the inter-particle forces, montmorillonite is controlled by the double layer thickness.

5.5.1 P-wave Velocities

Figure 5-17 plots the P-wave velocity using piezoceramic actuators in the direction orthogonal to bedding (and parallel to the major principle stress σ_1'). This figure includes the dry and wet Ticino sand. Since the dry Ticino sand velocity has a significantly lower V_p than the saturated velocities, a graph with only the saturated

materials is presented in Figure 5-18. From the graph, it is apparent that RGOM-EI and saturated Ticino sand have the highest V_p, while RBBC has the lowest V_p.

Many velocity relations, such as the Wyllie time average equation (WTA) (Wyllie et al., 1956) and the Raymer-Hunt-Gardner (RHG) equation (Raymer et al., 1980), as mentioned in Section 2.9, assume that the P-wave velocity of the composite is a combination of the V_p in the fluid and the solid matrix. For the WTA, it is a volume-weighted sum of the two, while the RHG is a combination of the two P-wave velocities with transitional intervals between the high and low end of the porosity scale. If we extend this line of thought to the results seen in Figure 5-17, the P-wave velocity of the fluid likely has a non-negligible effect on the measured P-wave velocity through the composite. Table 3.7 indicates the salinity of each of the resedimented clays. Figure 5-19 shows the P-wave velocity through different saline mixtures. A salinity of 4 g/L was assumed to be representative of Presumpscot clay; however, it was not directly measured. The dashed lines representing the velocity through saline mixtures serve to give the reader an approximate sense of how salinity affects P-wave velocity. The P-wave velocity at σ'_v= 5 MPa for each soil is plotted againts the actual soil salinity, as listed in Table 3.7. Presumpscot clay is an outlier, with the actual salinity unknown, but estimated to be around 4 g/L. The data point for RGOM Upper is also an outlier that doesn't follow the salinity trend. This may indicate that either one or both are true: 1) there is another mineralogical component that strongly affects the P-wave (for the Presumpscot), or 2) there is scatter in the salinity measurement (for RGOM Upper).

If the pore fluid were the driving factor affecting the P-wave velocity, then the curves in Figure 5-17 would follow the trend of salinity; however, since this is not the case, there are clearly other factors at play that affect the P-wave velocity, most likely linked to the mineralogy. In particular the Presumpscot clay does not follow the ordering of the salinity. This could be due to the fact that it is an intact sample obtained from the field, and could contain heterogeneities, including larger granular material that would have a higher stiffness, increasing the P-wave velocity. Since its fabric and pore fluid is not controlled like that of the resedimented materials, it is

more difficult to understand which parameters are at play. This highlights the benefits of resedimented materials – even the two specimens of Presumpscot clay have quite a large discrepancy in P-wave velocity. Presumpscot clay has a considerable amount of quartz (38%), which could be shifting its P-wave velocity curve higher. In addition, the depositional history can have an effect on the stiffness of the soil, as Mitchell (1993) noted that intact clays have more edge-to-edge and edge-to-face contacts. It should also be pointed out that the P-wave seems to be quite sensitive to small differences in the mineralogy and pore fluid, while in the next section, the S-wave velocity is not as such. Furthermore, both WTA and RHG are mostly for consolidated mature clastics and carbonate, and they are known to be inaccurate when applying them to soft, unconsolidated clastics Dvorkin (2008).

5.5.2 S-wave Velocities

Figure 5-21 plots the S-wave velocity in the direction orthogonal to bedding (and parallel to the major principle stress σ'_1). Both dry and wet Ticino sand are included. A zoomed in version of the S-wave velocity results are seen in Figure 5-22.

First, it should be noted that there is a slight difference between the dry and saturated S-wave velocity in Ticino sand. This is attributed to the saturation effect: since $G_{sat} = G_{dry}$, as the bulk density increases due to saturation, the velocity decreases. The addition of water is also known to have a minor effect on grain interactions, however it is usually negligible and $G_{sat} = G_{dry}$ is still assumed to be true.

From Figure 5-22, it is firstly clear that there is excellent repeatability between the tests on the same materials. The largest difference is between the two Presumpscot clay experiments. This is in part caused by the heterogeneities present in intact samples, as well as the sequence in which the tests were run, TX1222 being one of the very first tests, thus making it more prone to error. The difference between the Presumpscot clay S-wave velocity is about the same as the difference seen in the P-wave, in absolute velocity change, with the V_p having a slightly higher difference. This implies that the S-wave is slightly less sensitive. The trend for P and S wave is reversed in terms of TX1222 and TX1243, with TX1222 having a lower P wave but a

higher S-wave than TX1243. The P-wave is in particular likely to be affected by the pore fluid and the mineralogy, while the S-wave is more dependent on grain contacts and mechanical behavior.

There is a clear trend in the S-wave as a function of mineralogy. The lowest plasticity clay, Presumpscot clay, has the highest V_s, while the high plasticity RGOM-EI and RGOM Upper have the lowest V_s.

Finally, TX1228 (RBBC) is an outlier when compared to the other RBBC tests. When looking at the P-wave velocity, although there is more scatter in general in the RBBC results than seen in the S-wave results, TX1228 agrees very well with the rest of the P-wave results. On the other hand, for the S-wave results, all the RBBC results are so tightly in agreement except for the TX1228. TX1228 is identical in composition as the other RBBC tests, but the stress path followed during the experiment is slightly different, as seen in both the compression curve (Figure 5-11) and the K_0 (Figure 5-13), highlighting the dependence of the V_s on grain contacts and mechanical behavior.

5.5.3 Stiffness Moduli

The velocity results from Sections 5.5.1 and 5.5.2 are used to calculate the constrained and shear moduli, in Figure 5-23 and 5-24. The modulus curves include the density effect, and when comparing the V_p to M, the trends are almost identical, with the exception of the Presumpscot clay. It appears that the Presumpscot clay intact samples, although taken from the same bore hole, have differences in densities, which rectifies the gap between their P-wave velocity results. Overall, the scatter in the P-wave velocity is reduced when looking at the M curves, which indicates that the density has a strong correcting effect on the modulus – it would have been more likely that the differences increase since M takes the velocity-squared term, which would amplify the differences; however, this is not the case. The differences between the V_s and G values is approximately the same.

Using the velocity-derived M and G values, the bulk modulus is calculated with Equation 2.3. The results, in Figure 5-25, are showing the trend of increasing modulus

with increasing plasticity, with the exception of Presumpscot clay. This trend is virtually the same as the M trend, indicating a stronger dependence of K on the M than G.

5.6 High Stress Measurements

Measurements at high stresses using ultrasonic transducers were performed at Shell E&P on RBBC. The material tested at Shell is identical to the material tested at the MIT Geotechnical Laboratory. The same procedures were followed, whenever possible. Rather than following a continuous compression curve, maintaining K_0-consolidation, the test was manually stepped up to the desired stress, in increments of 10 MPa. The approximate time needed for end of primary consolidation (EOP) was pre-calculated. Each stress increment was performed over a duration of about 30% of the time needed for EOP, plus the specimen was left at that stress for the pre-calculated time needed for EOP. This ensured EOP had definitely been reached. The steps can be seen in the compression curve in Figure 5-26. Since some of the steps were held longer (such as those held overnight), the author would suggest taking an average line through the data points as a rough approximation of the corresponding compression curve. At a constant stress, the void ratio decreases as the specimen consolidates. The figure also contains the compression curves for the RBBC tests the author ran using the medium stress triaxial equipment. Unfortunately, experimental errors precluded the use of the TXSHELL01 data before 20 MPa, primarily due to the difficulties in maintaining the appropriate lateral stress ratio using the automated radial strain technique. Even though the two sets of data do not overlap, the compression curve at high stress agrees quite well with an extrapolation of the medium stress results.

During the course of the test at Shell, both the P and S-wave velocities were measured, shown in Figures 5-27 and 5-28, respectively. The P-wave velocity for the high stress range agrees well with the medium stress range. There is potentially a small difference between the two data sets, with the high stress results having slightly lower

V_p values than the extrapolated medium stress results. Considering the different experimental setups, different calibrations, and different loading progressions (one being constant strain rate loading, the other a step-wise incremental loading), the agreement is encouraging. An average line with the least amount of errors should be taken as the average trend through the high stress data. In Figure 5-28, the low stress velocity results obtained using bender elements by this author is added, represented by a single best-fit line. The low stress bender element results agree well with the medium stress piezoelectric transducer results, with the bender elements slightly underestimating the V_s after 1 MPa. This is likely due to the reduced quality of signals after 1 MPa for the bender elements, causing ambiguity in the interpretations. The medium stress V_s matches nearly perfectly with the high stress V_s results. Evidence of the step-wise stress increments is seen in the high stress P and S-wave results. Velocity measurements were taken at both the end of stress application, as well as after equilibration had occurred, immediately before the next stress was applied.

These results are the first reported measurements of V_s in a soft clay from 0.1 to 70 MPa. The P-wave results, from 0.5 MPa to 70 MPa, are also a considerable accomplishment for a soft clay. The difficulties of testing a single specimen of clay over such a wide stress range include the significant amount of strain that the test experiences, as well as the sensitivity mismatch (with respect to the equipment) between different stress regimes. For these reasons, as well as the fact that very few labs exist that have the ability to test such a wide stress range, the results presented here are quite novel in both the geotechnical and geophysics fields.

5.7 Frequency Response

The input frequency used to excite the piezoelectric transducers is a square wave with a period much larger than the arrival time of the first signal. When a square wave is used, a packet of frequencies is sent through the soil, with the dominant resonant frequency arriving at the receiver. For each of the signals measured, the peak of the first signal is measured in addition to the zero-crossing arrival time. The

time difference between the zero-crossing time and the peak is multiplied by four to calculate the period of the wave, and subsequently the frequency of the wave. The frequency is measured as a function of vertical effective stress for both the P-wave and S-wave. The compiled results are presented in Figures 5-29 and 5-30. The figures include the data points for all the tests, as well as a best fit line and equation for each of the materials. The P-wave frequency response clearly behaves differently from the S-wave frequency response. In Figure 5-29, the different materials do not follow any apparent trend, but rather overlap each other arbitrarily. In fact the trend lines for the RGOM-EI and the RGOM Upper & Lower overlap each other exactly. The only discernible difference appears between the dry Ticino sand and the rest of the wet materials. The dry Ticino sand has a frequency response around 40 - 55 kHz, while the wet materials (including the wet Ticino sand) have a frequency response between 100 - 180 kHz.

The shear wave frequency response behaves differently from the compressional wave frequency response. Rather than appearing randomly like the P-wave response, the S-wave response increases linearly as a function of vertical effective stress over the stress range tested. Much like the P-wave response, the dry Ticino sand differentiates itself from the rest of the saturated materials. The dry Ticino sand has the highest range of frequency response. Furthermore, the rest of the material frequency responses follow a pattern based on the plasticity of the material. The highest plasticity material (RGOM - EI) has the lowest frequency response, while the lowest plasticity clay (Presumpscot clay) has the highest frequency response, followed by the saturated Ticino sand that effectively has zero plasticity. A graph of the S-wave frequency response at 8 MPa as a function of liquid limit is shown in Figure 5-31 for clarity.

The frequency response can effectively be translated to which frequencies are transmitted versus attenuated as a function of stress. For example, the fact that the frequency response of the S-wave signal increases as a function of stress implies that the high frequency content is no longer attenuated at higher stresses, but remains in the signal. The apparent link between the plasticity of the material and the frequency response indicates that the high plasticity particles have an attenuative effect on the

high frequencies. Further discussion is included in Section 6.1.4.

5.8 Summary and Comparison of Results

5.8.1 Stress Behavior

Putting the velocity results in terms of mean effective stress can be more insightful in certain situations, and can ameliorate some of the scatter present in the data. For example, Figures 5-32 and 5-33 show the P and S-wave velocities, respectively, as a function of both vertical and mean effective stress. The P-wave velocity scatter seems to be about the same, or even worse (when looking at, for example, all the data on RBBC) when put in terms of σ'_m. It does not significantly impact the relative placement of the velocities for different materials; therefore, it can be hypothesized that the lateral stress ratio does not have a significant impact on the P-wave velocity results at this stress range. On the other hand, however, when comparing the S-wave velocity, this is not the case. The V_s in terms of σ'_m is less scattered than the data in terms of σ'_v. In particular, the TX1228 (RBBC) matches much better with the rest of the RBBC data when put in terms of mean effective stress. This test experienced an anomalously low K_0, which is seen in the difference in the S-wave velocity data, and is subsequently accounted for when put in terms of mean effective stress. The same can be said about the TX1237 (RGOM Lower) test results. These observations lead to the conclusion that the S-wave velocity is more sensitive to the lateral stress ratio. This is consistent with the fact that the P-wave has a vertical propagation and *vertical* motion, whereas the S-wave has a vertical propagation and a *horizontal* motion, thus the S-wave feels the effects of the horizontally-applied stress.

5.8.2 Porosity Behavior

Based on Figure 2-2b, it is clear that the compression behavior of clays can greatly dffer, with both the curvature and placement of the compression curves. For example, in $e - log\sigma'_v$ space, RBBC follows a straight line while RGOM-EI curves upward. At

high stresses, for the most part the compression curves tend to converge.

Previous to this research, it was commonly accepted that the P-wave velocity for illitic clays are higher than smectitic clays (Heppard and Ebrom, 2010). The results in terms of stress shown in Figure 5-18 contradict this preconceived notion; however, the porosity behavior is an essential factor in the velocity behavior that should not be disregarded. An example of this is presented in Figures 2-12 and 2-13, where kaolinite V_p is faster than smectite V_p when put in terms of vertical effective stress, but the trend is reversed in terms of porosity. Similarly, when the velocity values from Figure 5-18 are put in terms of porosity (see Figure 5-34), the high smectite RGOM-EI has the highest V_p at a given porosity. If a single velocity value is selected, the corresponding porosity for RGOM-EI is much higher than RBBC. The large amount of clay-bound water in RGOM-EI contributes to the void ratio without significantly reducing the stiffness of the soil.

In addition to the P-wave velocity, the V_s, M, G, and K are plotted as a function of porosity in Figures 5-35 through 5-38. Once again, the porosity-velocity behavior is insightful when looking at the S-wave velocity. The curves for RGOM-EI and RBBC converge and intersect each other, indicating a strong resemblance to the compression behavior. The S-wave velocity is much more closely linked to the mechanical behavior of the soil than the P-wave velocity, which is dominated by the mineralogy and pore chemistry. The anomalous behavior of RGOM Lower is likely attributed to its exceedingly low specific gravity.

When considering the velocity behavior of soils, both the porosity and stress conditions are necessary. As quoted by Lohani et al. (2001), "the effect of aging, especially chemical hardening or cementation makes the soil fabric stable even in the relatively loose state without letting it reduce the void ratio."

5.8.3 Density Behavior

Density-velocity crossplots are often used in industry. They are generally thought to be good indicators of clay type (Alberty et al., 2003) and unloading (Chopra and Huffman, 2006). Using a $V - \rho$ crossplot to recognize unloading is shown to be

successful with low-smectite clays only, as discussed in Section 5.10. Whether a $V-\rho$ crossplot is a good indicator of clay type can be easily tested by plotting the velocity data presented earlier in terms of density. Figure 5-39 and 5-40 show the P and S-wave crossplots, respectively. While the P-wave crossplot roughly seems to follow the plasticity trend, with the exception of Presumpscot clay, the S-wave velocity does not. There may be a trend, but it has poor correlation with liquid limit. In fact, the S-wave curves intersect each other as a function of density. This suggests that $V_s-\rho$ crossplots cannot be used to clearly identify clay type. The corresponding modulus values are also put in terms of density for reference in Figures 5-41 through 5-43, but show no improvement with respect to trends.

Although the P-wave velocity for smectite-dominated versus illite-dominated soil in terms of stress does not agree with the conventional trends seen in industry[3], the $V_p-\rho$ crossplot does agree with the general trends, such as in Alberty et al. (2003).

5.8.4 Poisson's Ratio

Poisson's ratio can be calculated based on the velocities measured through a medium with the following equation:

$$\nu = \frac{(V_p/V_s)^2 - 2}{2[(V_p/V_s)^2 - 1]}. \tag{5.1}$$

This is the dynamic ν and should not be confused with the static ν. The static ν is determined by uniaxially loading a specimen and measuring the ratio of radial strain to axial strain. Differences between the static and dynamic parameters (including Poisson's ratio, elastic moduli, etc.) are well-recognized and explicitly measured. Zimmer (2003) showed an overall trend of higher dynamic than static bulk modulus in dry sands, including much higher scatter in the static moduli measurements due to the difficulty in measurement method. Vucetic (1994) showed a decreasing stiffness trend with increasing strain (dynamic measurements usually have lower strains than static measurements), and also as the plasticity of a soil increased, he saw an increase

[3]That illite has faster P-wave velocity than smectite, as seen in Figure 2-15

in the cutoff strain needed for elastic behavior. Furthermore, low plasticity clays had steeper stiffness reduction with strain than high plasticity clays (Vucetic and Dobry, 1991). Although this trend was not explicitly explained besides generally being linked to the size of soil particles, it sets the tone for strong plasticity effects in elastic behaviors in soils, as is discussed in this section.

The dynamic Poisson's ratios measured in this thesis for all the clays are for saturated materials. The stiffness parameters for wet materials are significantly higher than for dry materials due to the contribution of the water component. Figure 5-44 shows the calculated Poisson's ratios, including dry Ticino sand. The large difference between the dry and saturated ν is the water-dependent V_p. In theory, as the specimens are further consolidated at higher pressures, the calculated ν continues with a decreasing trend. As the stress goes up, the grain contact stiffness goes up, so the water component of V_p is less significant.

Figure 5-45 shows a zoomed-in image of Figure 5-44. The origin of the curves at $\sigma'_v = 0$ corresponds to $\nu = 0.5$, which is the theoretical undrained Poisson's ratio. The curves in Figure 5-45 follow a strong plasticity trend, where the highest plasticity clay (RGOM-EI) forms the upper boundary, while the lowest plasticity clay (Presumpscot Clay), forms the lower boundary. Ticino sand technically does not have a plasticity since sands are not categorized in this fashion, but it is included as a convenient reference zero plasticity. The plasticity trend can be described in many ways, including the plasticity index, liquid limit, CEC, or SSA; however, the liquid limit is selected for a few reasons. The liquid limit is generally a much stronger indicator of clay composition than the plastic limit, whose values can be more scattered and inconsistent. Although CEC and SSA are viable options, the absence of these values for Presumpscot clay precluded their use. Additionally, the liquid limit is the parameter used in the UT Geofluids Consortium for correlations with permeability, strength, and compressibility, thus there is a unified attempt to standardize the use of this parameter. Finally, liquid limit is a very cheap, quick test that can be done without extensive expertise, deeming it a convenient parameter.

The liquid limit is strongly correlated with mineralogy – liquid limit increases with

smectite content. An increase in clay particles, especially smectite, is associated with generally smaller particles, and thus smaller pore sizes. The double layer effect, which is most dominant in high smectite materials, increases with liquid limit. The aspect ratio of the platy clay particles, combined with the double layer effect, significantly impacts the depositional microstructure, and furthermore the eventual behavior with the evolution of stress. Finally, liquid limit is shown to be a useful predictor of permeability, compressibility, and strength by Casey (2014).

The plasticity trend in Figure 5-45 for normally consolidated samples as a function of stress is not present in all the different spaces. For example in Figure 5-46, the ν is presented as a function of porosity; however, the curves do not follow a consistent plasticity trend as is the case for σ'_v. The selection of σ'_v and w_L is deliberate.

Since the curves in Figure 5-45 follow a trend of plasticity, a quick evaluation of what kind of trend they follow is performed by selecting one particular stress level, and selecting the corresponding Poisson's ratios at that stress for each material. In Figure 5-47, these ν values are plotted against the corresponding liquid limit of each material at a stress of $\sigma'_v = 2MPa$. The data points can fit with a rational equation of the functional form $y = (p1 * x + p2)/(x + q1)$, with $p1$, $p2$, and $q1$ as constants. Since there is an upper limit of 0.5 for the Poisson's ratio, and this type of equation can account for that, it is a good fit, however does not preclude the use of other possible fits. For the data points in Figure 5-47, this equation is able to fit the data points very accurately, resulting in an $R^2 = 0.980$. Figure 5-48 plots the data for many different stress levels in addition to $\sigma'_v = 2MPa$. With increasing stress, the curves shift lower and take on a slightly different curvature, supported by the observation that at $w_L = 0$, the points for different stresses are more spread apart than at $w_L = 87$. With increasing plasticity, stress has a smaller effect on the Poisson's ratio. Finally, rational fits are performed for all the stresses listed in Figure 5-48, with the coefficients plotted as a function of stress in Figure 5-49. If the liquid limit and stress are known, Figures 5-49 can be used to roughly predict the Poisson's ratio. Although this is a useful tool to perform a quick calcuation, it is not robust enough for rigorous use due the the subjectivity of the fitting methods.

Since the Poisson's ratio is simply a function of the V_p/V_s ratio, a robust predictive model is applied in the next section on the V_p/V_s ratio, with the intention that ν can be seamlessly calculated from this model.

5.8.5 P and S-wave relationships

The V_p/V_s ratio has liberally been used to predict stress state, lithology, and saturation. Prasad (2002) notes that the V_p/V_s ratio increases with overpressure and decreases with gas saturation. V_p decreases in the presence of overpressure and saturation (when partially saturated), while V_s decreases in the presence of overpressure but is unaffected by saturation, moving the V_p/V_s ratio in different directions. Gregory (1976) also suggests that the V_p/V_s ratio is an indicator of whether the formation is consolidated or unconsolidated, and if gas or oil is present, publishing extensive experimental data to support this. The V_p/V_s ratio has been rather well-documented for sands and rocks, with Gardner et al. (1968) reporting ratios of greater than 2 for water-saturated unconsolidated sands, and less than 2 for consolidated rocks or gas-saturated sands. Zimmer (2003) also reports the V_p/V_s ratio as a function of stress for differently-sorted sands. Fawad et al. (2011) showed that for eight different dry sands, the V_p/V_s ratio converges to 1.7 - 1.85 at 50 MPa. The controlling behavior of the V_p/V_s ratio is still not entirely understood. It is often used as a lithology predictor, thus lithology is clearly a dominating factor in the V_p/V_s ratio (Pickett et al., 1963). Tatham (1982) claims the pore geometry has a stronger effect on the V_p/V_s ratio than the mineral elastic constants, and that the inferred link with lithology is rather controlled by the dominant pore sizes and distributions in those respective lithologies. This thesis contributes to the knowledge of V_p/V_s ratios in clays with different plasticities.

The V_p/V_s ratios as a function of σ'_v are presented in Figure 5-50. The plot includes both dry and saturated Ticino sand. At the very low stress regime, the ratio is very high, following an exponential increase with decreasing stress. It appears as though the ratio for clays converges with increasing stress. It is difficult to tell which extrapolated ratio it converges to; however, if the ratios and stresses are put

in log-log space, it becomes clear that the lines follow a straight trend, shown in Figure 5-51. In log-log space, the different clays are ordered and inclined roughly in order of plasticity. The trends are quantified by fitting a logarithmic equation to the data, seen in Figure 5-52. The equation is in the form of

$$log(V_p/V_s) = \alpha log(\sigma'_v) + \beta \tag{5.2}$$

where α and β are the slope and intercept, respectively. The equation is in log_{10}, and σ'_v is in MPa. The α and β terms follow a trend of plasticity, thus they are plotted as a function of liquid limit (w_L in %) in Figures 5-53 and 5-54. Both of these graphs are fitted with a best fit line with encouragingly high R^2 values. The best fit equations are as follows:

$$\alpha = \frac{-0.4981 w_L - 10.67}{w_L + 82.78} \tag{5.3}$$

$$\beta = \frac{1.459 w_L + 79.75}{w_L + 144.6} \tag{5.4}$$

A model has been developed with the set of equations presented here (Eqns 5.2-5.4). Given the liquid limit of the material, a V_p/V_s ratio can be predicted, and furthermore the dynamic Poisson's ratio using Equation 5.1, which is simply a function of the V_p/V_s ratio.

Returning back to the question of whether the V_p/V_s ratio is dominated by lithology (or mineralogy) or pore size remains unanswered. Work done by Deirieh (2015) analyzed the pore size distribution for RGOM-EI and RBBC as a function of stress for pores larger than 35 nm (wiich represents 30-50% of the total porosity). He found that at low stress (0.2 MPa), the median pore size for RGOM is 350 nm while for RBBC is 500 nm. However at high stress (20 MPa) the pore size for RGOM is 310 nm while RBBC is 180 nm. There is a significant reduction in pore size as a function of stress for RBBC, but RGOM pore size insignificantly changes with stress. The trends in Figure 5-52 are not explained by the pore size observations made by Deirieh (2015), thus this research suggests that the V_p/V_s ratio is dominated by lithology.

Finally, a crossplot of the V_p to V_s ratio in Figure 5-55 shows data for all the resedimented materials following a plasticity trend; however, the intact Presumpscot clay is violating this trend. Since the Presumpscot clay could have possible oxidation and cementation effects, the P-S wave velocity crossplot could be a tool used to indicate the presence of heterogeneities in the material.

5.9 Creep Behavior

Secondary compression, also called creep, is a time-depenedent continued rearrangement of particles at a constant stress. When a material experiences creep, it effectively becomes overconsolidated. In other words, its yield surface is higher than the active stress. When a clay is actively being consolidated, it lies on the Virgin Compression Line (VCL); however, when creep occurs, the material moves away from the VCL. Ladd (1996) describes how general clays, σ'_p increases by about 10% per log cycle of secondary compression. Soils go through a hardening process by two means: first is the soil mass formation, and second is the creep caused by overburden, occurring after soil formation (Lohani et al., 2001). Both are termed 'aging', since this means the general stiffening of soil. The creep effect on the shear modulus has been described as follows by Shibuya et al. (1995):

$$\frac{G_{max}(t)}{G_{max}(t_p)} = [\frac{t}{t_p}]^{N_G} \tag{5.5}$$

t is the current time, and t_p is the time to EOP. N_G is the constant representing the magnitude of creep in an experiment. Results reported by Lohani et al. (2001) indicated about 30% increase in G_{max} in very high plasticity clays (higher than RGOM-EI, with I_P=78%) when stress was held up to 10 days after EOP (approx. one log cycle). This study also tested Kaolin (I_P=23%), allowing three log cycles of creep, which resulted in less than 5% change in G_{max}, highlighting the stark difference in creep behavior between different plasticity clays. Finally, a simple relation between the N_G

term and the coefficient of secondary compression (C_α) is found to be

$$N_G = C_\alpha^{0.5} \tag{5.6}$$

based on test results from many different plasticity clays.

5.9.1 Equilibration

Creep not only affects the stress that the specimen has effectively experienced, but also the velocity measurements. The velocity values, as well as the amount of strain that occurs, depends on the type of clay. High smectite clays creep significantly more than low smectite clays, as is evident in Figure 5-12 and the large strain drop in TX1240 RGOM-EI .The extreme strain in TX1229 was caused by some experimental setbacks, where the test had to be taken down and reassembled, and left at a stress for a prolonged amount of time, thus is not typical.

Although it would be more convenient to avoid creep entirely by loading continuously, this is not possible if unloading cycles are performed. In order to obtain accurate unloading behavior, the test must equilibrate first. The consolidation strain rate needs to reduce to about an order of magnitude lower than the loading strain rate before it is unloaded, otherwise the specimen does not have time for particle rearrangement due to secondary compression, thus obscuring the true unloading trend. In the case of RBBC, the loading strain rate is 0.15%/hr, so for the strain rate to reduce to 0.015%, it takes about 15 hours, after which point unloading can be performed at the same strain rate as the loading had been done (0.15%/hr).

5.9.2 Stress Extrapolation Due to Creep

As mentioned above, the specimen effectively becomes overconsolidated as creep occurs. At a constant stress, continued strain is exhibited, as shown in Figure 5-56, where a compression curve of RBBC and a zoomed-in section is presented, with the creep pointed out. The black dashed line in the figure is the VCL, while the hollow dots are where velocity measurements are taken. In the figure, it can be seen that

velocity measurements are taken at three points for 5 MPa: the end of loading, after creep has occurred and the specimen has equilibrated, and after the specimen has been reloaded to 5 MPa. None of the velocity measurements at 5 MPa lie on the VCL, thus it must be corrected. Either the points can be considered as overconsolidated and the points have an OCR, or considered normally consolidated (NC) by calculating the extrapolated stress that corresponds to the VCL. The latter is selected for this thesis.

The first step of correcting the stress of the points is to fit a line to the VCL, as is done by the dashed black line in Figure 5-57. Next a curved line that follows the curvature of the unloading and reloading portion of the curve is drawn. The unloading curve is used to adjust the points before unloading, while the reloading curve is used to adjust the points after the reloading. These curves are represented by a dashed red line. This red line is moved such that it intersects both the velocity measurement point, as well as the VCL. The point at where the dashed red line intersects the dashed black line is the new state of stress for the velocity measurement, represented by a square. Thus the three velocity measurements taken at 5 MPa have three new stresses after the adjustment, all of which are higher than 5 MPa due to creep. The new stresses for this particular case are 5.1 MPa, 5.3 MPa , and 5.8 MPa, respectively.

5.10 Unloading Behavior

Understanding the behavior of soil when it is unloaded (or overconsolidated) is critical in predicting its behavior in the field, particularly during excavations and for pressure prediction methods. Recently the use of velocity values to predict pressures in the field is a concern, since clay-rich formations have a small reduction in velocity during unloading, which is contrary to the behavior of the more familiar rock formations. A single velocity reading can correspond to many different stresses, depending on whether the soil is NC, overconsolidated (OC), or if OC, then which unloading cycle. Since velocity is often used as a proxy for predicting porosity and stress, if the wrong prediction is used, well-bore drilling failure can be a serious issue, especially

when it comes to shallow locations prone to erosion. Techniques have been proposed to deal with this problem, most notably by Bowers (1995); however, characterizing these "unloading limbs" warrants an experienced user (Alberty et al., 2003), and the unloading limbs transform as a function of stress, thus a new interpretation is needed for each depth examined.

Earlier in this chapter, the compression curves, strain curves, and lateral stress ratio curves were presented for the loading portions of the experiments. the unloading portions are included in addition to the loading portion for void ratio (e), strain (ε), and K_0 are included in the Appendix in Figures A-1 - A-4, Figures A-5 - A-8, and Figures A-9 - A-12, respectively. The corresponding P and S-wave velocity curves as a function stress are presented in Figures 5-59 and 5-58, respectively. The same results are seen in Figures 5-60 through 5-63 in terms of density and porosity. The experimental protocol is to have at least two unloading loops when possible, at 5 MPa and 10 MPa. Before each unloading loop is performed, it is necessary to allow the specimen to equilibrate and enter secondary compression, otherwise the clay particles do not have enough time to rearrange appropriately.

In Figure 5-58 and Figures 5-59, the velocity unloading portion as a function of stress behaves differently based on the type of material. The low plasticity Presumpscot clay has significant decrease in the velocity during the unloading portion, while the high plasticity RGOMs maintain their high velocity values during unloading. RBBC falls somewhere between the two in terms of trends. The same can be said for both P and S-wave velocity. Figures 5-60 and 5-61 show velocity-density crossplots. These crossplots are commonly used in the oil industry (Bowers, 1995, Alberty et al., 2003) as an indicator of clay type and unloading. The unloading portion is clear in the RBBC and especially in the Presumpscot clay results, marked by a small drop in density but a large drop in velocity. The crossplots for RGOM-EI and RGOM Upper and Lower are not nearly as clear. In fact, the unloading portion is virtually indistinguishable from the loading portion, indicating the inability to use these crossplots as a predictor of the unloading portion. The benefit is that they are a good predictor of density. Furthermore, the same can be said with the velocity-porosity

curves in Figure 5-62 and 5-63. The velocity-density and velocity-porosity crossplots for RGOM-EI appear as though they are a single, normally consolidated trend.

5.10.1 Unloading behavior for compression versus velocity

The change in velocity or stiffness relative to the change in density or porosity, as mentioned above, is a topic of interest, especially since many velocity-porosity relationships have been devised and implemented in the field. Rather than exhaustively analyze all the tests and clay types, this section looks at a couple RBBC, Presumpscot, and RGOM-EI tests, comparing the unloading portion of the compression curve and velocity curve. The RGOM Upper and Lower tests encountered some instability during unloading, thus are left out in this analysis. Table A.1 lists the slopes of the unload/reload cycles of the compression curve (in log-space), familiarly known as the swelling index, C_s. The C_s does not change between the different loading cycles, despite the increment in stress. For example, TX1235 has an unloading cycle at 5 MPa, 7.5 MPa, and 10 MPa, but the slopes of the compression curve does not change as a function of maximum past stress.

Since the swelling index is in terms of semi-log space, the velocity curves during unloading are put in terms of log space and a best-fit line is applied to obtain the slope. Figure 5-64 contains the resulting slopes as a function of maximum past stress. The P and S-wave slopes are relatively similar, on the same order of magnitude. Since the slope is in terms of the difference in velocity relative to the difference in stress rather than the change in velocity relative to the absolute value, the P and S-wave results are comparable. Although there is considerable scatter, the trend of increasing slope with decreasing plasticity prevails. Furthermore, the slope increases as a function of maximum past stress, σ'_{vmax}, with the exception of TX1229 for V_s, which encountered some difficulty during the unloading portion at 5 MPa. All of the data points within each test were taken to the same OCR, thus eliminating any OCR effect. These graphs indicate a dependence of unloading behavior on the maximum past stress. Both the maximum past stress σ'_{vmax} as well as the OCR are needed to characterize the unloading behavior.

5.10.2 Normalized unloading behavior

The previous section points out that the unloading behavior depends on both the maximum past stress as well as the OCR. To isolate these effects, the unloading velocities need to be normalized by the maximum past stress and plotted as a function of OCR. Figure 5-65 through Figure 5-68 plot the normalized unloading sections for each clay. All reasonable unloading data are included in these graphs. Usually about two unloading cycles are performed during a test, at 5 and 10 MPa (as listed in the legend), however a couple tests have one or three unloading cycles.

The normalization method is not entirely straightforward, due to the creep that occurs when a constant stress is held. As mentioned in Section 5.9, a correction is performed where a higher stress is extrapolated to account for the creep. The new stress is then used as a basis for the OCR calculation. For example, if a test is taken to 5 MPa, and due to creep, the apparent maximum stress is 5.2 MPa, then the original OCR = 2 becomes OCR = 2.08.

The vertical scale for the normalized P and S-waves is kept the same for each of the clay types to highlight the difference in magnitude of the P and S-wave unloading behavior. The P-wave velocity changes less during unloading than the S-wave velocity. For the P-wave, the velocity during unloading on average changes by a maximum of 4%, while the S-wave changes between 6-27%, depending on the clay type. Although the absolute change in velocity (in m/s) is quite similar for the P and S-waves, the water-dominated P-wave velocity is so high that the change looks relatively small. A power-fit is used to obtain a single line describing the unloading behavior for each soil. These lines facilitate the comparison of general unloading behavior for the different soils for the P and S-waves in Figures 5-69 and 5-70. The change in normalized P-wave velocity does not follow a strict plasticity trend; however, the low plasticity clays (RBBC and Presumpscot clay) tend to have a larger change in velocity during the unloading portion than high plasticity clays. Similarly, the normalized S-wave velocity decreases much more for RBBC and Presumpscot clay than it does for the RGOM's (Figure 5-70). This unloading behavior reinforces the results presented

earlier in Figures 5-60 through 5-63, where the unloading portion is unidentifiable for the high plasticity clays. Finally, the P and S-wave unloading behaviors differ dramatically. The P-wave velocity has a relatively uniform reduction across all soils, while the S-wave behavior is more soil-dominated, supported by the large difference between the high and low smectite clays in Figure 5-70. At this time, there does not appear to be a definitive trend in unloading behavior based on the maximum past stress. Although Figure 5-66 does support a trend of increasing velocity reduction as a function of the maximum past stress, this trend is not consistent in all the materials.

Table 5.1: Summary of triaxial tests performed

Test #	Sample #	Soil Type	Initial wc (%)	Final wc (%)	Initial e ()	Final e ()	Preconsol-idation Pressure, σ'_p (MPa)	Maximum Measured Axial Effective Stress, σ'_{vmax} (MPa)	Unloading cycles performed at these stresses, σ'_v (MPa)
TX1217	F10 R-B T-1	Presumpscot Clay	22.7	18.0	0.649	0.531	2	5.4	-
TX1220	-	Ticino Sand	-	-	-	-	-	10.0	10
TX1222	F10 R-B T-1	Presumpscot Clay	23.9	20.4	0.694	0.479	1.5	4.4	-
TX1223	RS394	RBBC	34.8	18.9	0.971	0.478	0.63	10.1	5, 10.1
TX1226	RS390	RBBC	34.3	18.5	0.960	0.419	0.67	10.0	5, 10
TX1228	RS389	RBBC	34.4	18.6	0.964	0.364	0.66	10.2	5, 9.9
TX1229	RS396	RGOM-EI	36.1	17.2	1.058	0.474	0.63	10.2	5, 10.2
TX1230	RS329	RBBC	30.0	18.4	0.843	0.531	1	10.2	5, 10.2
TX1231	RS406	RGOM Upper	32.2	17.4	0.970	0.434	1	9.0	5, 9
TX1232	RS395	RGOM-EI	34.0	17.3	0.999	0.462	0.65	10.2	5, 9.3, 10
TX1235	RS440	RBBC	36.5	19.0	1.014	0.500	0.6	10.0	5, 7.5, 10
TX1237	RS398	RGOM Lower	25.8	12.6	0.750	0.319	1	10.2	5.3, 7.5, 10.2
TX1240	RS449	RGOM-EI	39.8	31.3	1.163	0.511	0.5	7.4	5
TX1243	F10 R-B T-1	Presumpscot Clay	22.3	15.5	0.652	0.419	1.5	10.0	5, 10

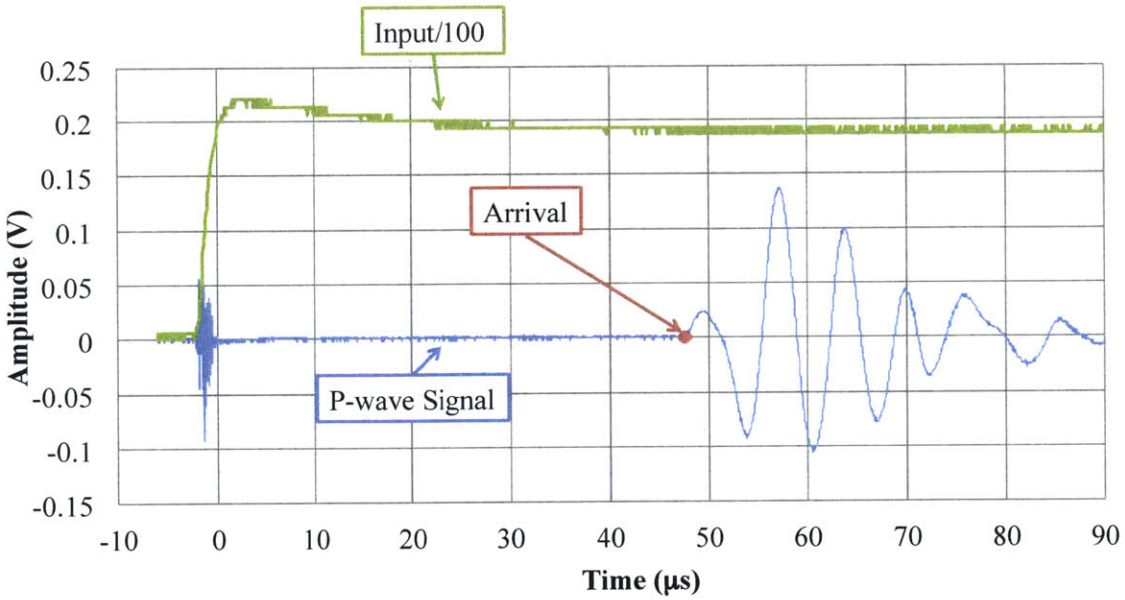

Figure 5-1: Arrival time selection for a representative P-wave signal through RBBC at 1 MPa

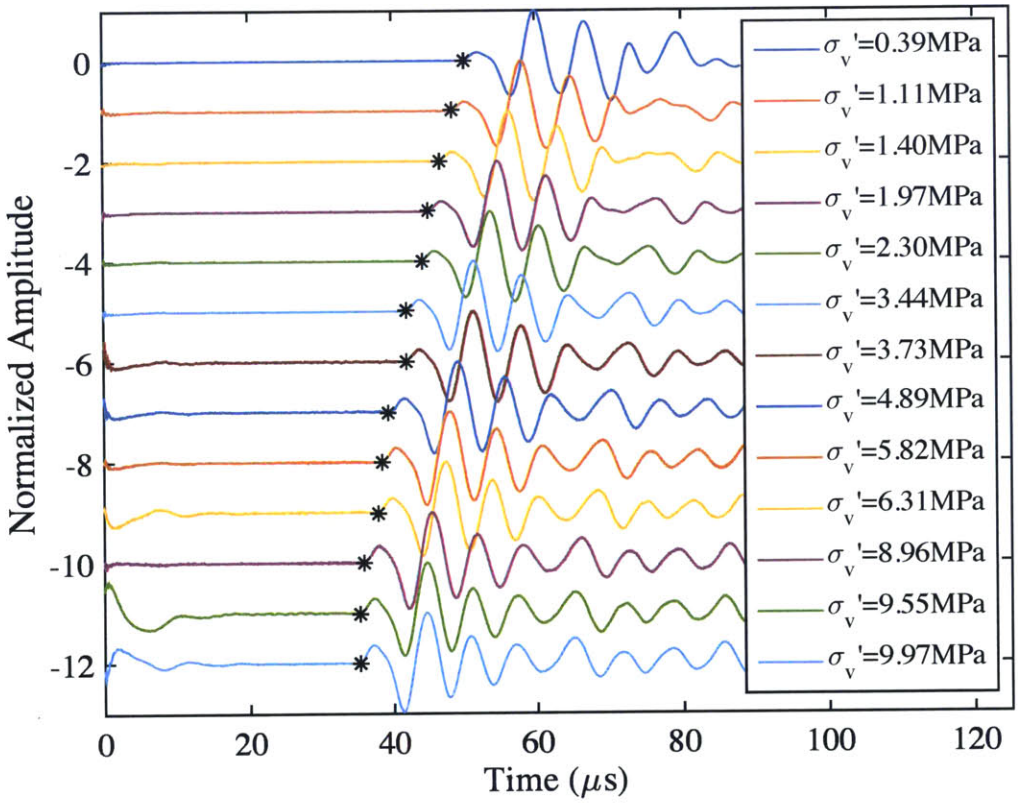

Figure 5-2: P-wave signals through an RBBC specimen (TX1230) for the entire span of the loading stage. The arrival is marked by a black asterisk. The unloading signals have been omitted for clarity. The signals are shifted vertically by an arbitrary fixed value for clarity. The amplitude of each signal is normalized to the maximum value in the signal

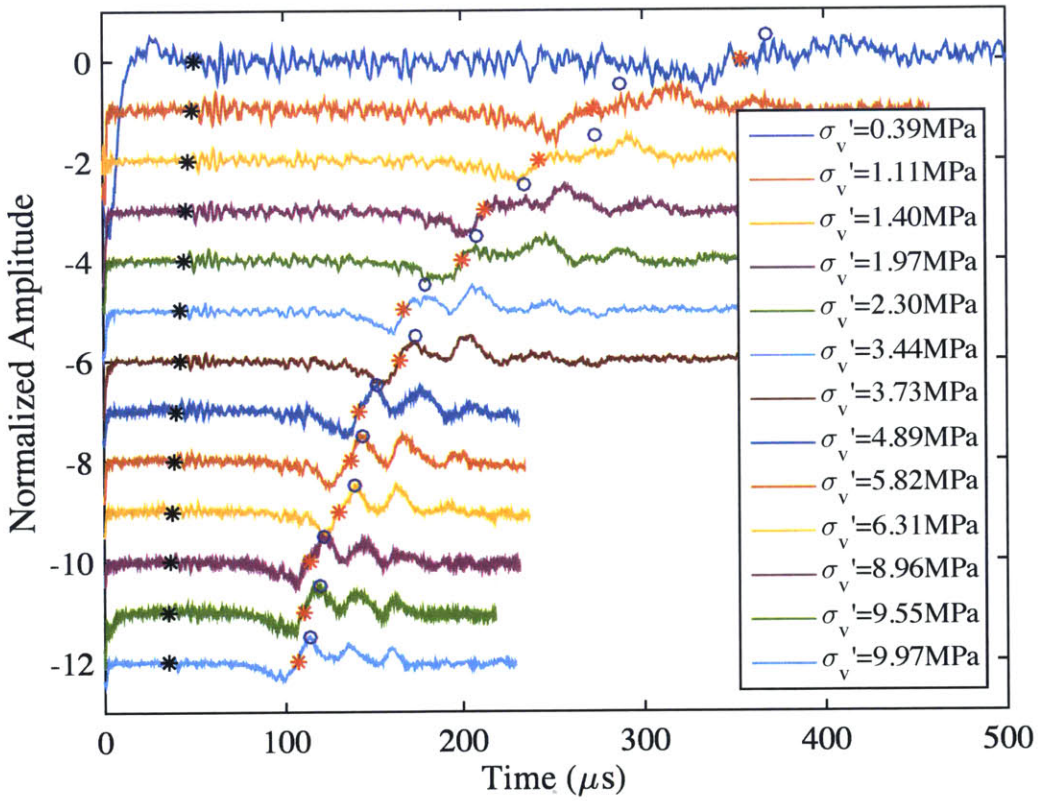

Figure 5-3: S-wave signals through an RBBC specimen (TX1230) for the entire span of the loading stage. The S-wave arrival is marked by a red asterisk, the first peak is marked by the blue circle, and the black asterisk represents the P-wave arrival obtained from Figure 5-2. The unloading signals have been omitted for clarity. The signals are shifted vertically by an arbitrary fixed value for clarity. The amplitude of each signal is normalized to the maximum value in the signal

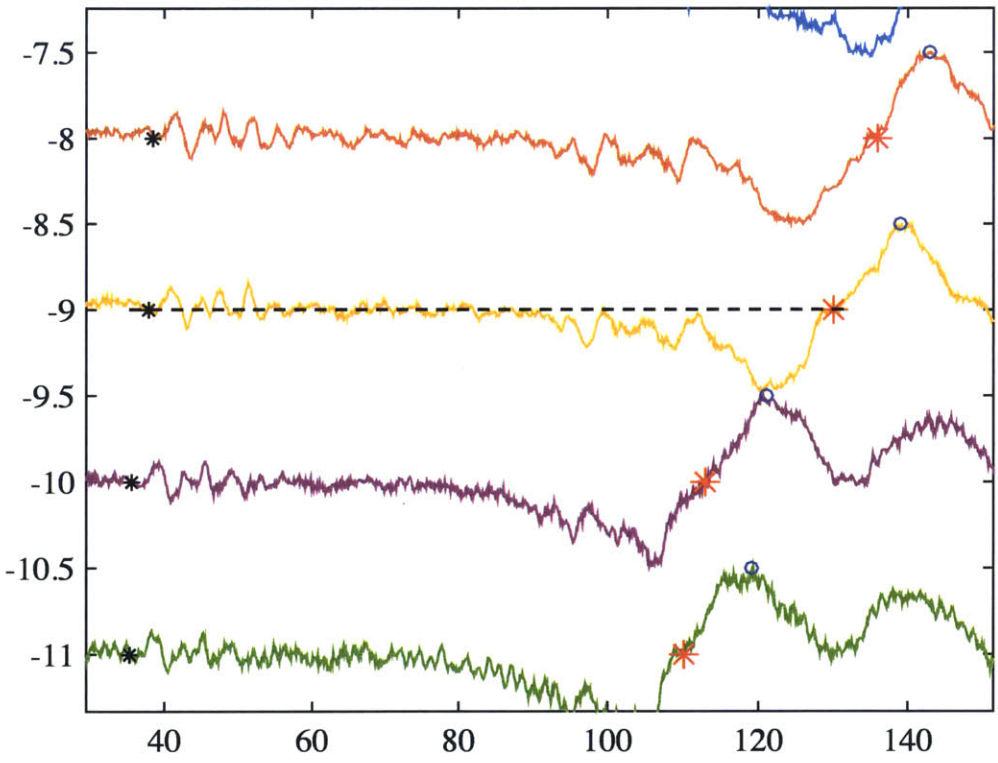

Figure 5-4: A zoomed-in image of Figure 5-3. The zero crossing after the precursory downdip is selected as the arrival time, marked by a red asterisk. The dashed line highlights the zero-crossing

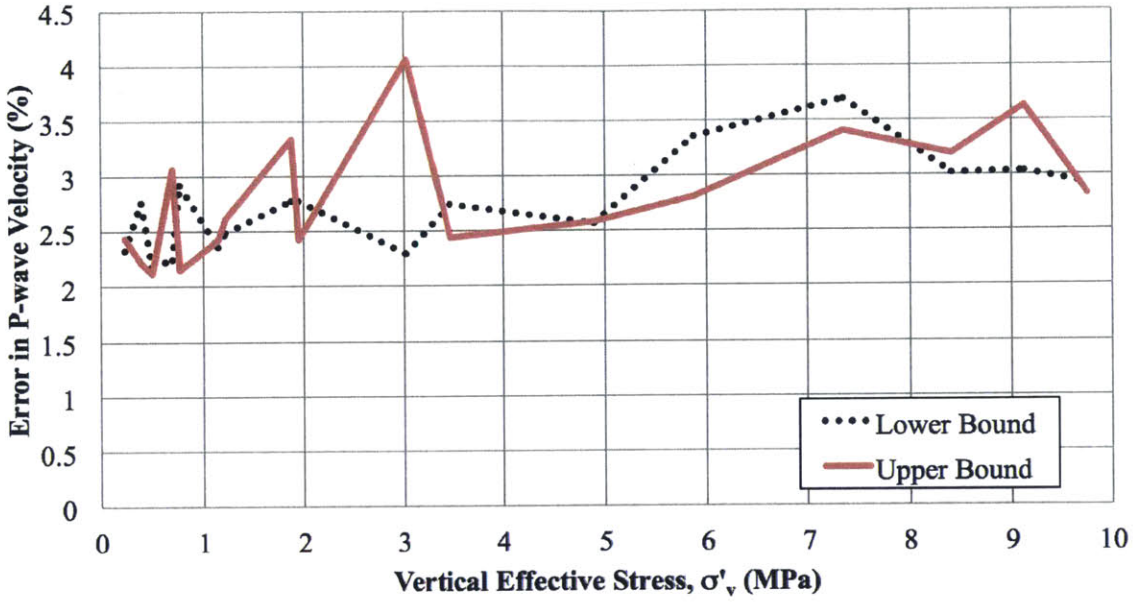

Figure 5-5: The percent error in the P-wave velocity caused by the arrival time interpretations and the height measurements are calculated here, as a function of stress

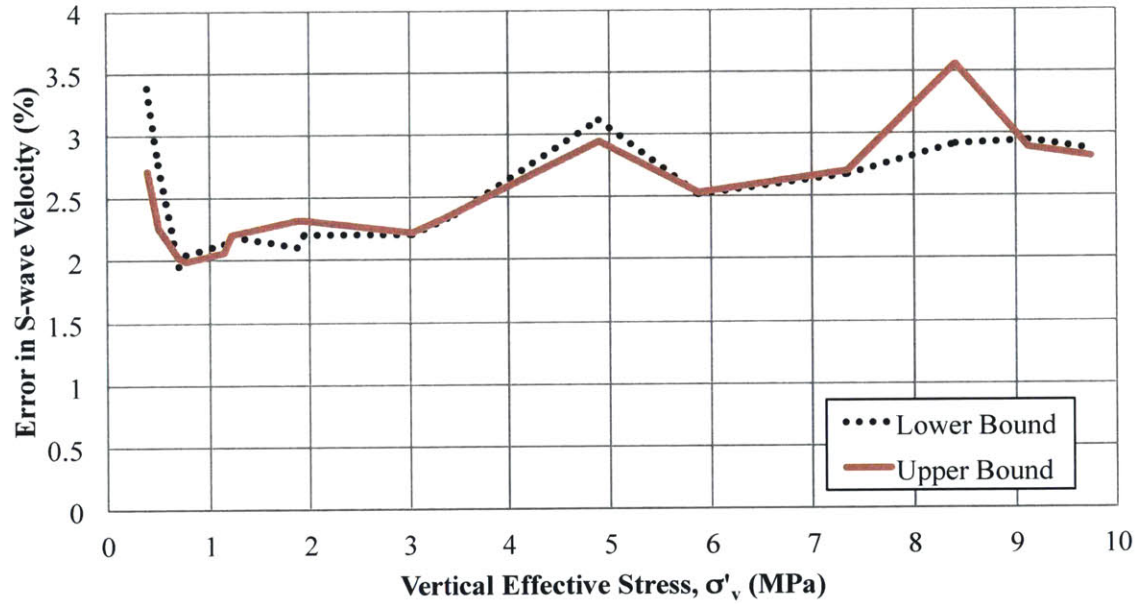

Figure 5-6: The percent error in the S-wave velocity caused by the arrival time interpretations and the height measurements are calculated here, as a function of stress

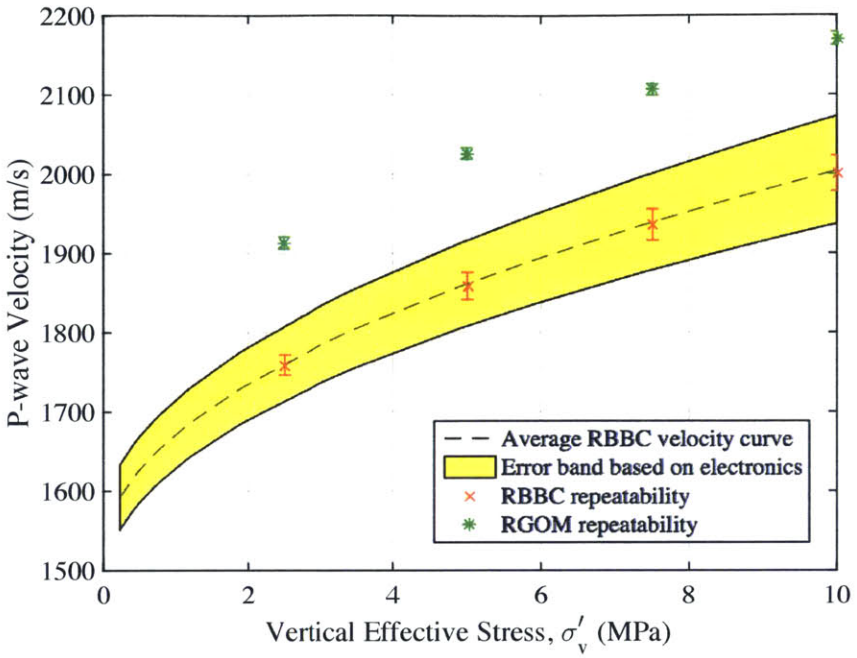

Figure 5-7: The average P-wave velocity for RBBC can be seen with a dashed line, surrounded by a yellow band that represents the error present based on the interpretations of the signals. This error band is showing the maximum and minimum possible errors based on extreme interpretations of the velocity arrivals. Furthermore the repeatability of the tests conducted on RBBC and RGOM-EI are shown with the markers that have vertical error bars showing one standard deviation. The standard deviation is based on the population data

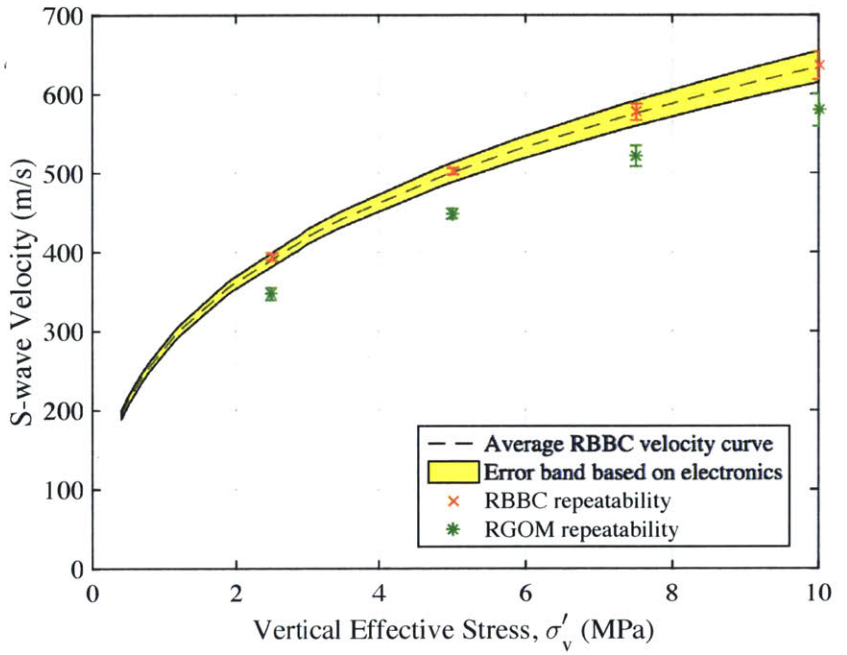

Figure 5-8: The same description applies as the previous figure

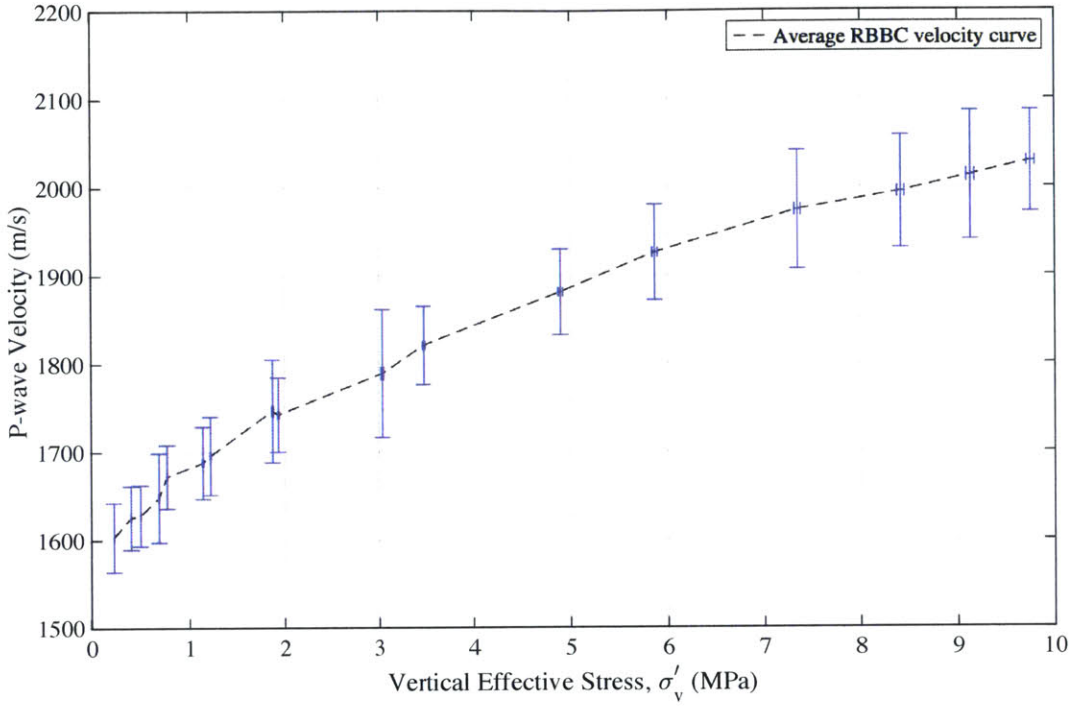

Figure 5-9: The average P-wave velocity for TX1235 (RBBC) with error bands on the velocity and stress measurements are shown in blue

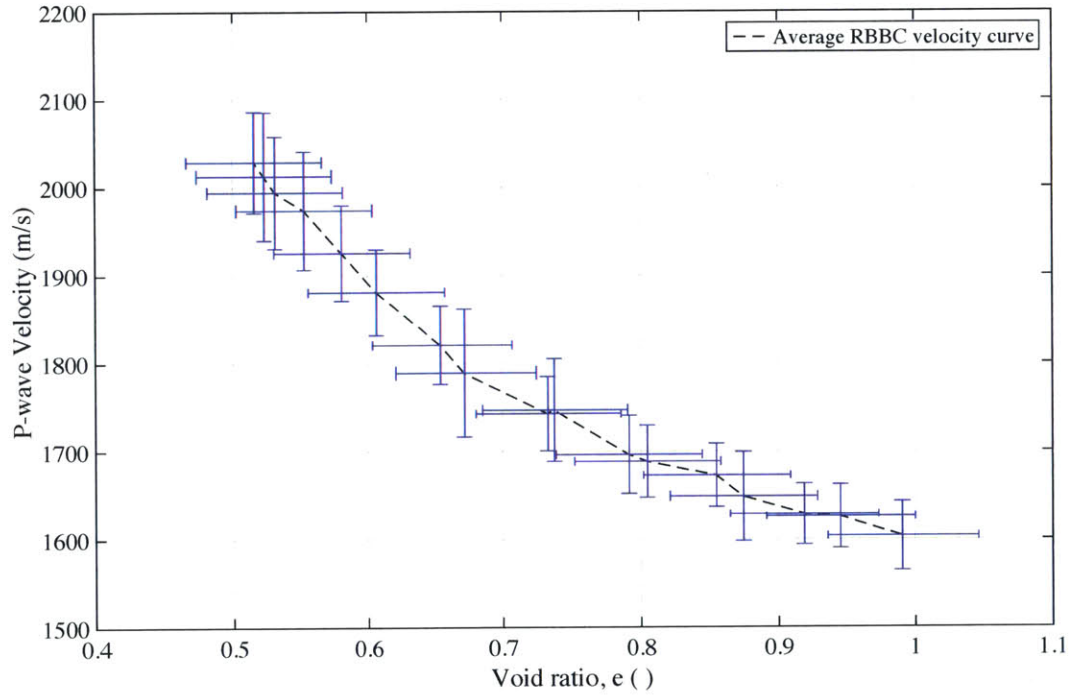

Figure 5-10: The average P-wave velocity for TX1235 (RBBC) with error bands on the velocity and void ratio measurements are shown in blue. The possible error in void ratio is equal or greater than the error in velocity measurement

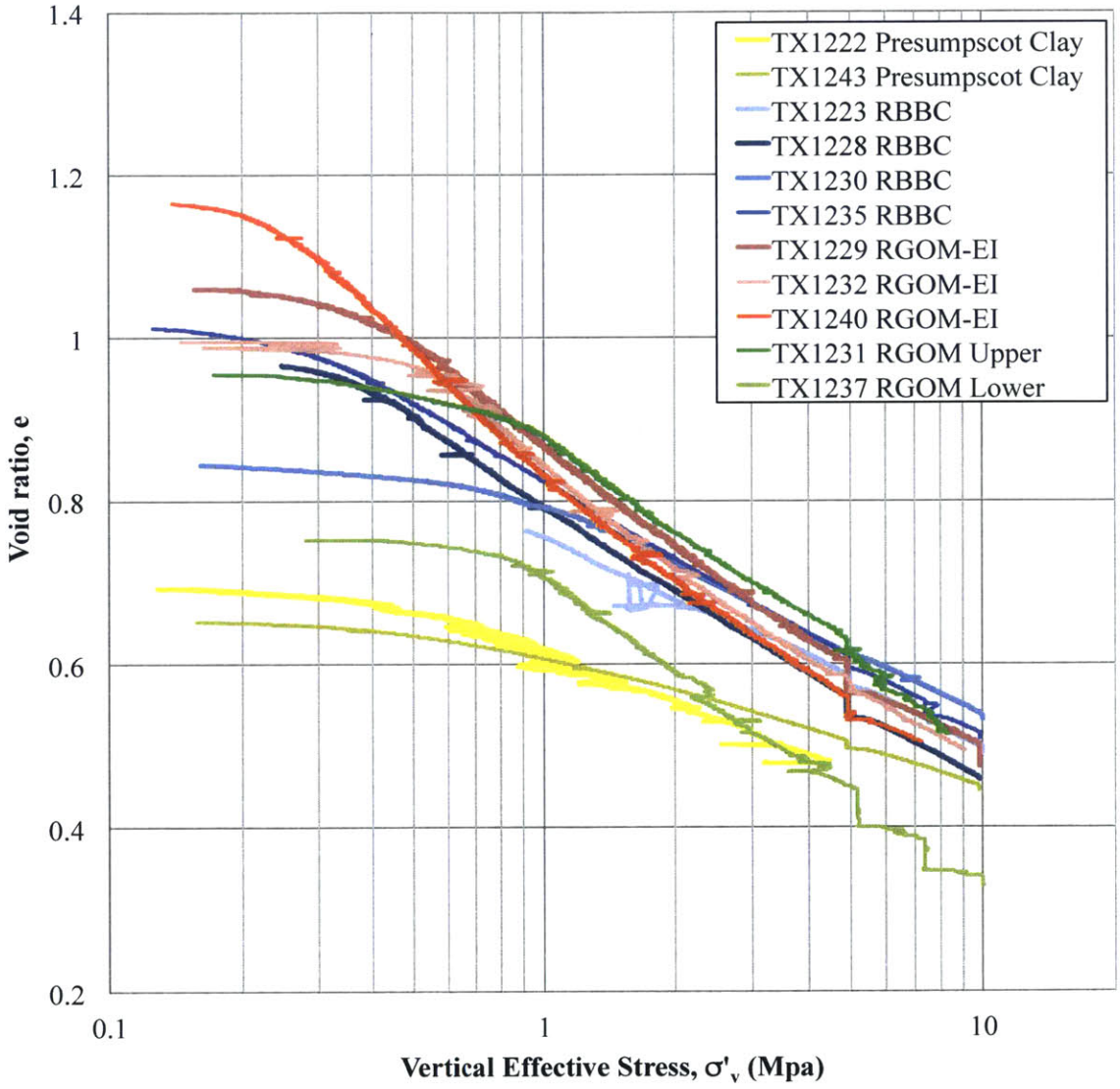

Figure 5-11: Loading compression curves for all clays tested in this research (unloading cycles removed)

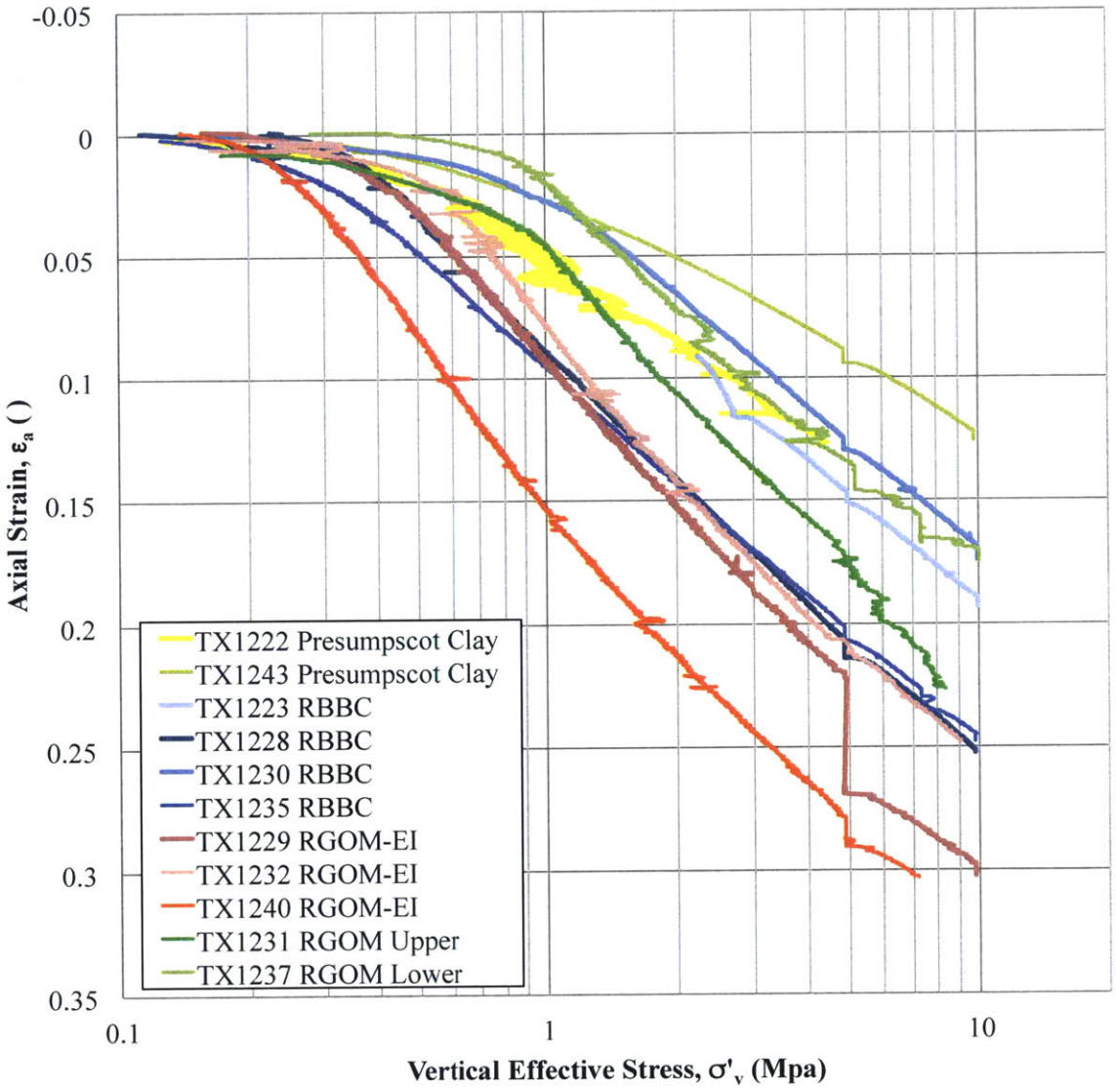

Figure 5-12: Loading axial strain curves for all clays tested in this research (unloading cycles removed). TX1299 was unloaded, taken down, and reloaded, explaining the large increase in axial strain at 5 MPa

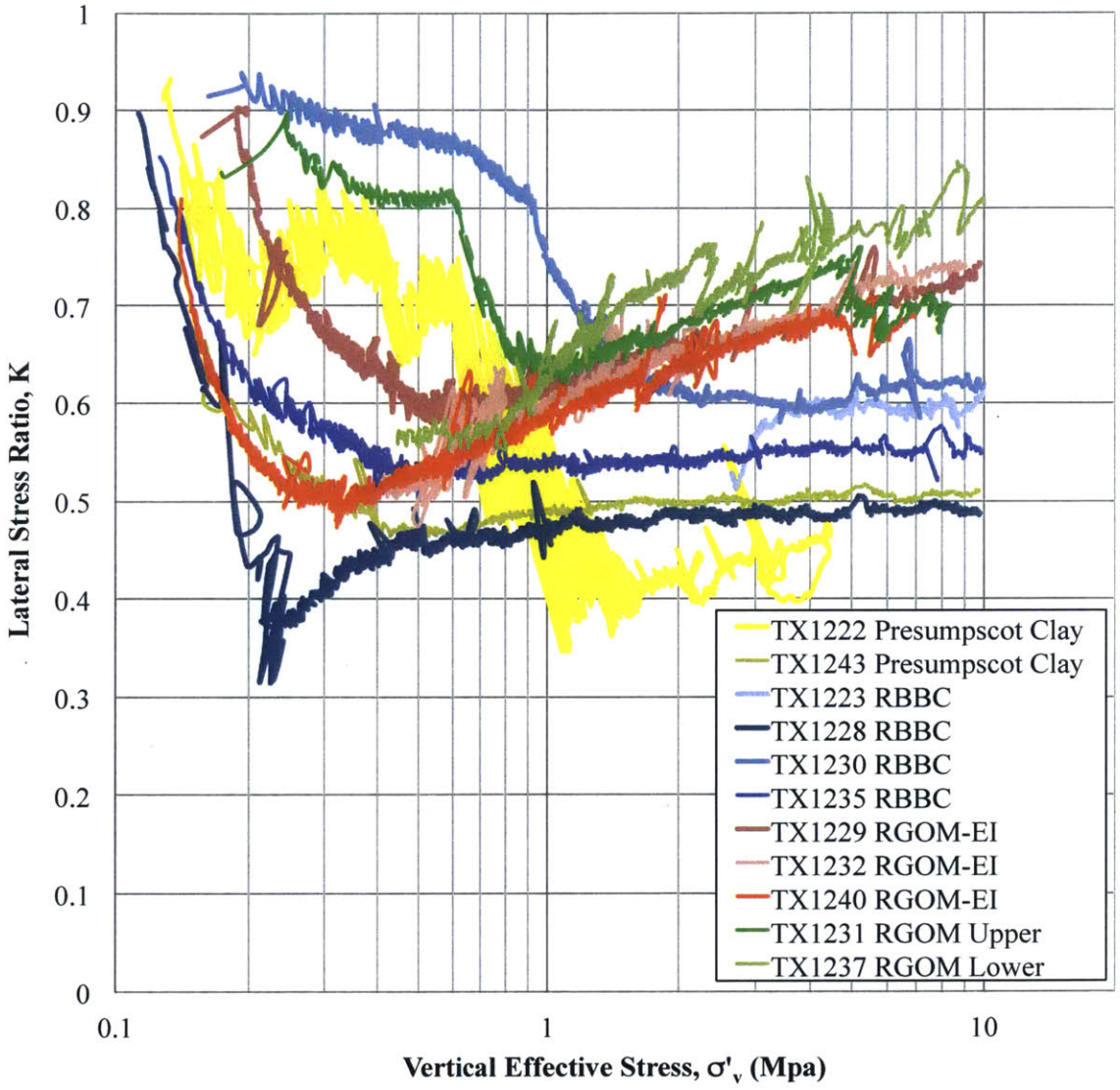

Figure 5-13: Loading K_0 curves for all clays tested in this research

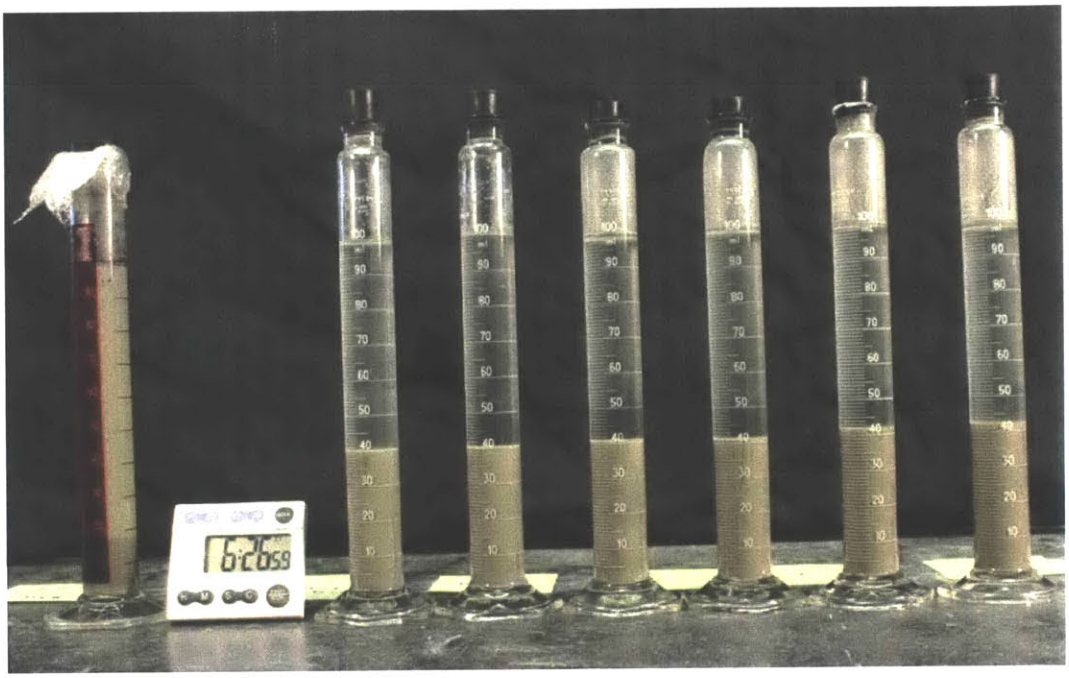

Figure 5-14: Sedimentation columns of leached BBC, with salinities of (left to right) 1, 4, 16, 64, 128, and 256 g/L NaCl, using 5 g of soil (Horan, 2012)

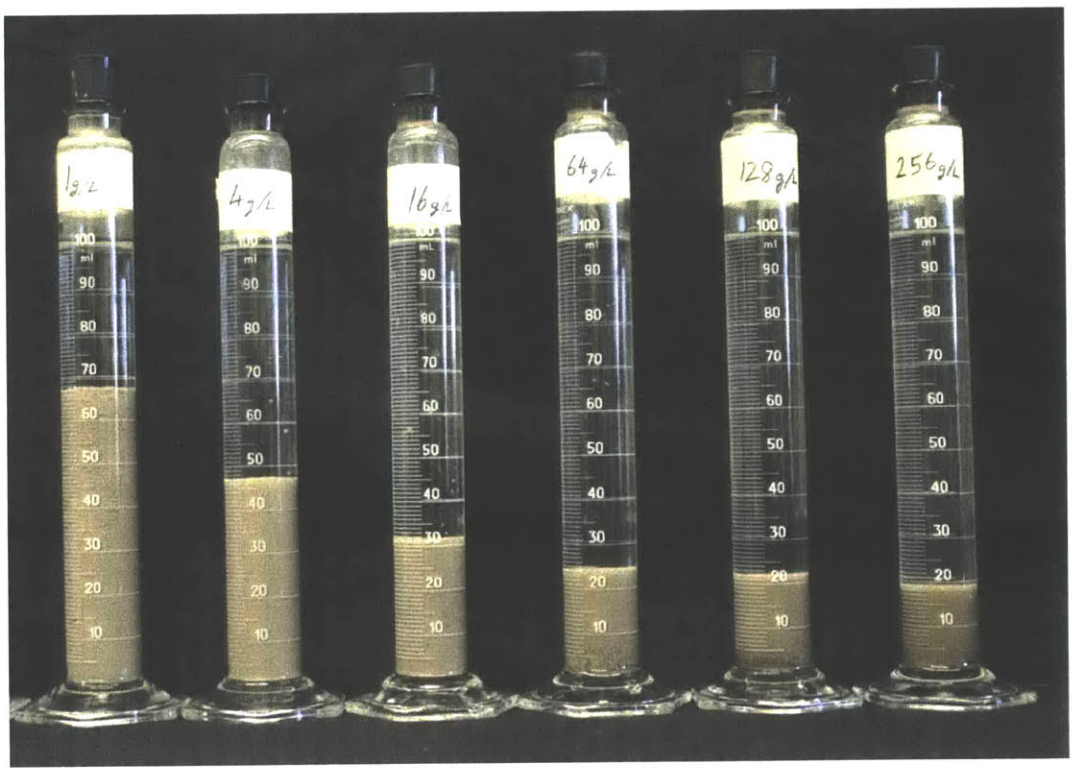

Figure 5-15: Sedimentation columns of leached GOM-EI, with salinities of (left to right) 1, 4, 16, 64, 128, and 256 g/L NaCl, using 5 g of soil (Fahy, 2014)

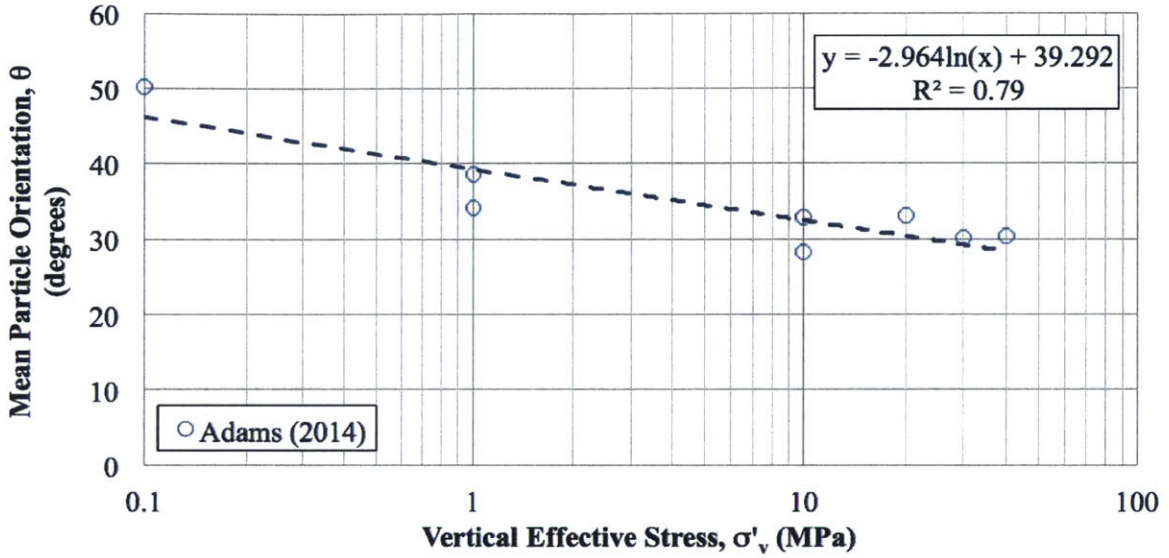

Figure 5-16: The mean particle orientation of RBBC obtained by analyzing SEM images (Adams, 2014). Figure adapted from Adams (2014)

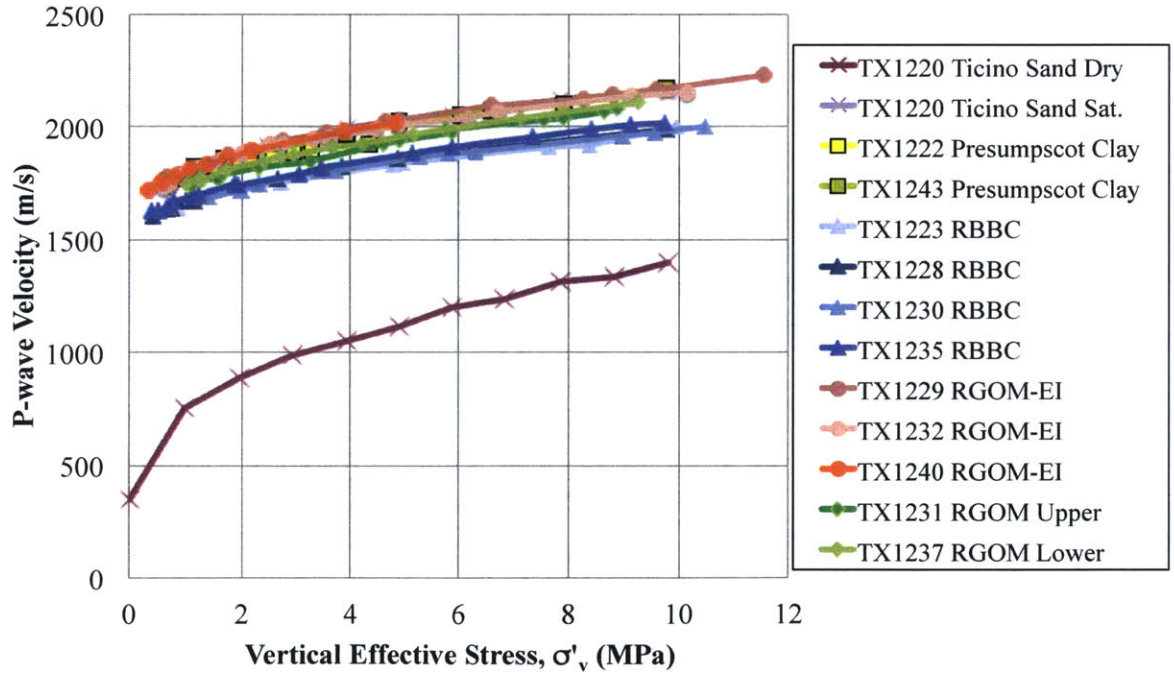

Figure 5-17: P-wave velocity results as a function of vertical effective stress for all materials tested, including the dry and wet Ticino sand

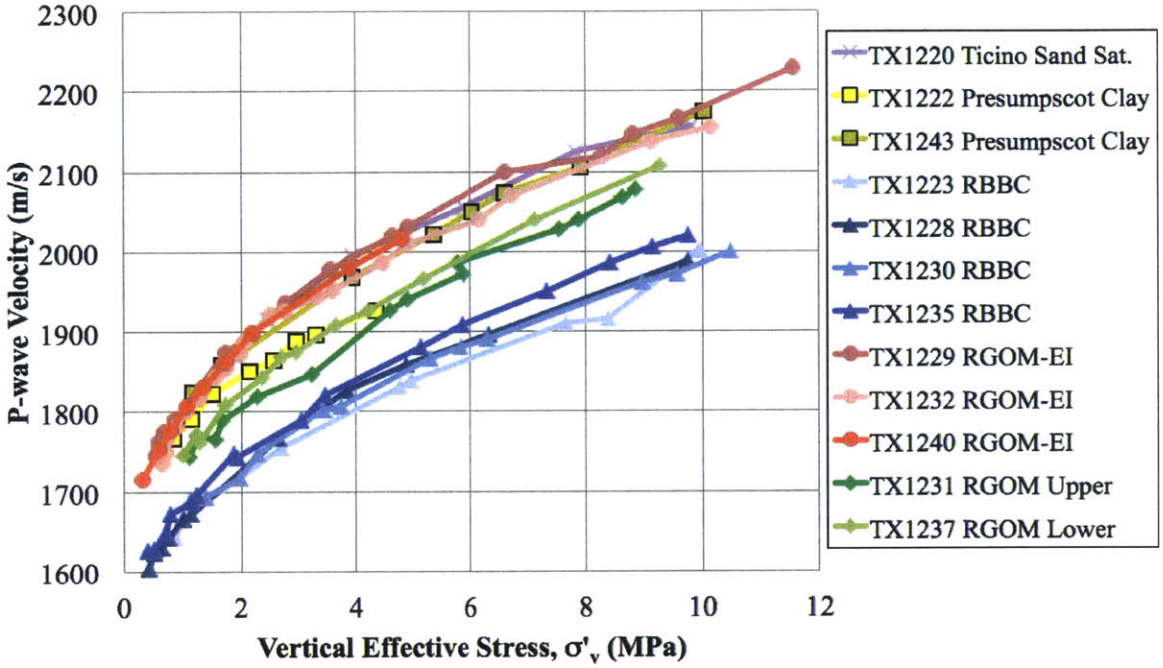

Figure 5-18: P-wave velocity results as a function of vertical effective stress for all saturated materials tested

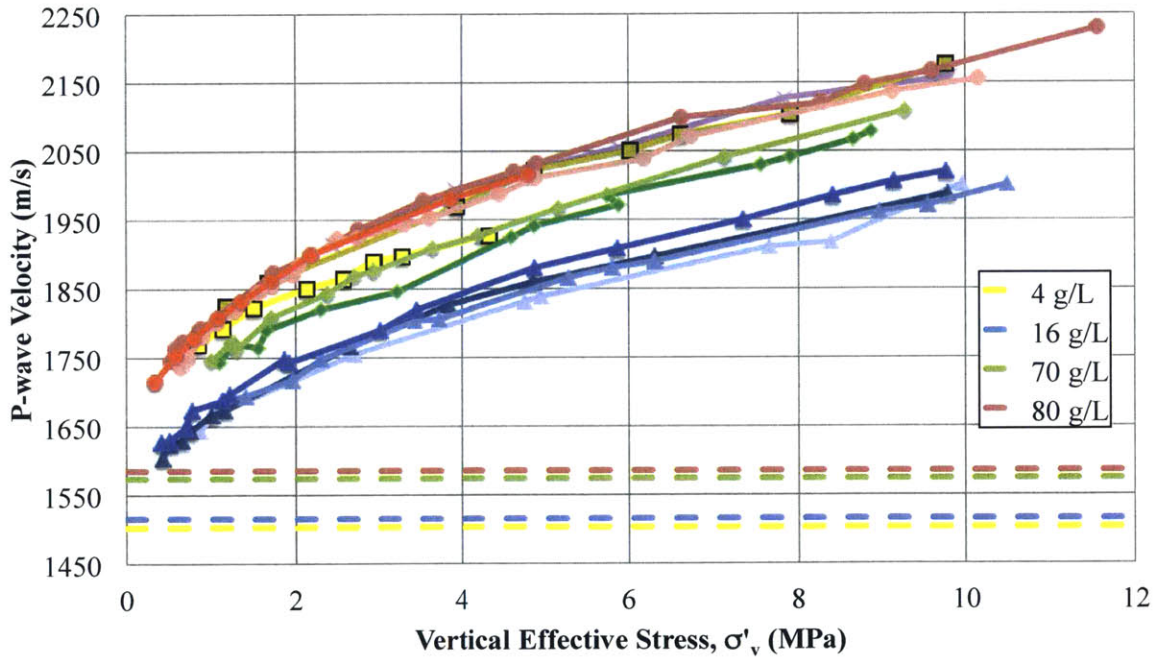

Figure 5-19: P-wave velocity, using the same legend as Figure 5-18, with dashed lines showing the velocity through saline water at various salinities, based on Del Grosso (1974). Interactive GUI at http://resource.npl.co.uk/acoustics/techguides/soundseawater/content.html

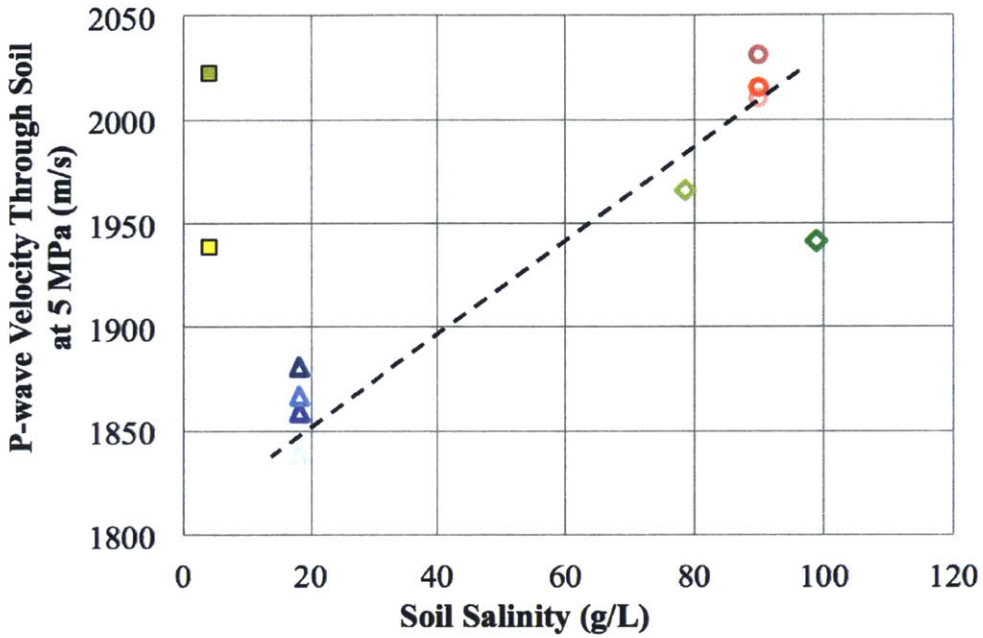

Figure 5-20: P-wave velocity as a function of salinity for a stress of σ'_v= 5 MPa. The dashed lines shows a general trend of increasing P-wave velocity through soils with higher salinity. The sample salinity is listed in Table 3.7 in the column "Actual Salinity". Colors match up with TX numbers in Figure 5-18

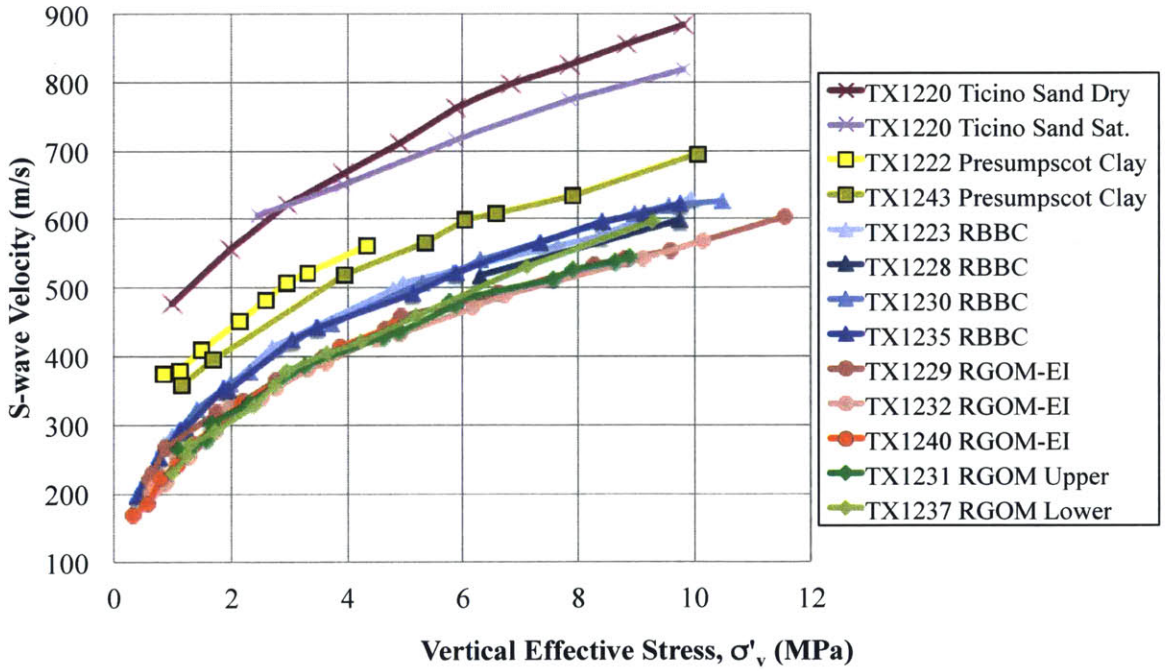

Figure 5-21: S-wave velocity results as a function of vertical effective stress for all materials tested, including the dry and wet Ticino sand

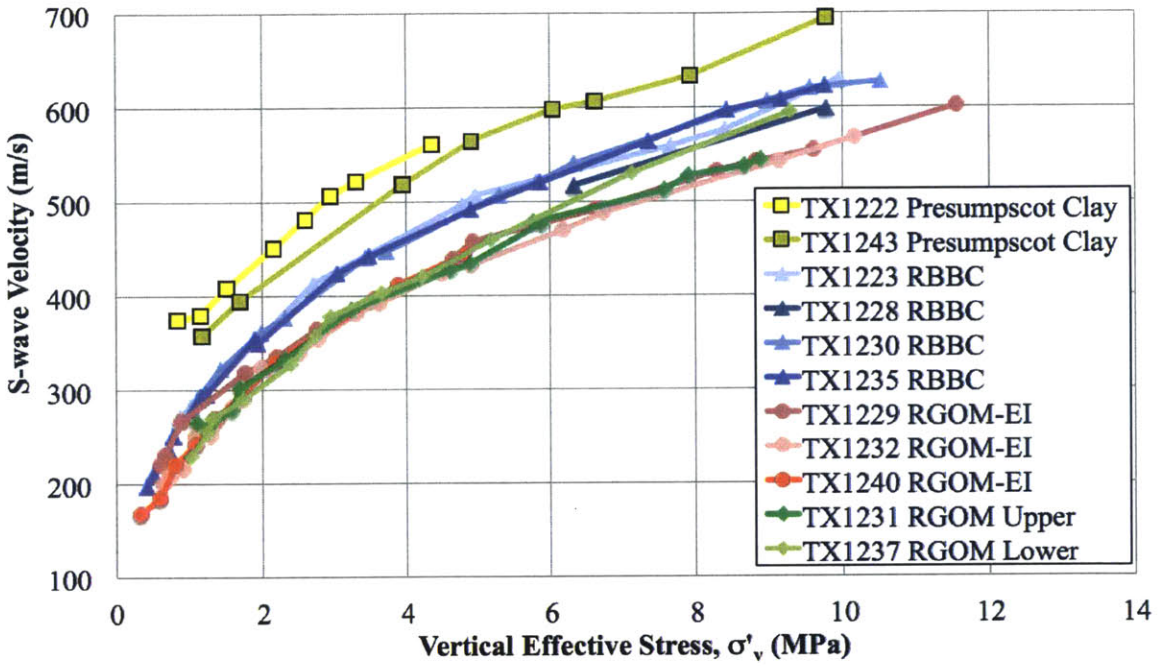

Figure 5-22: S-wave velocity results as a function of vertical effective stress for all saturated materials tested

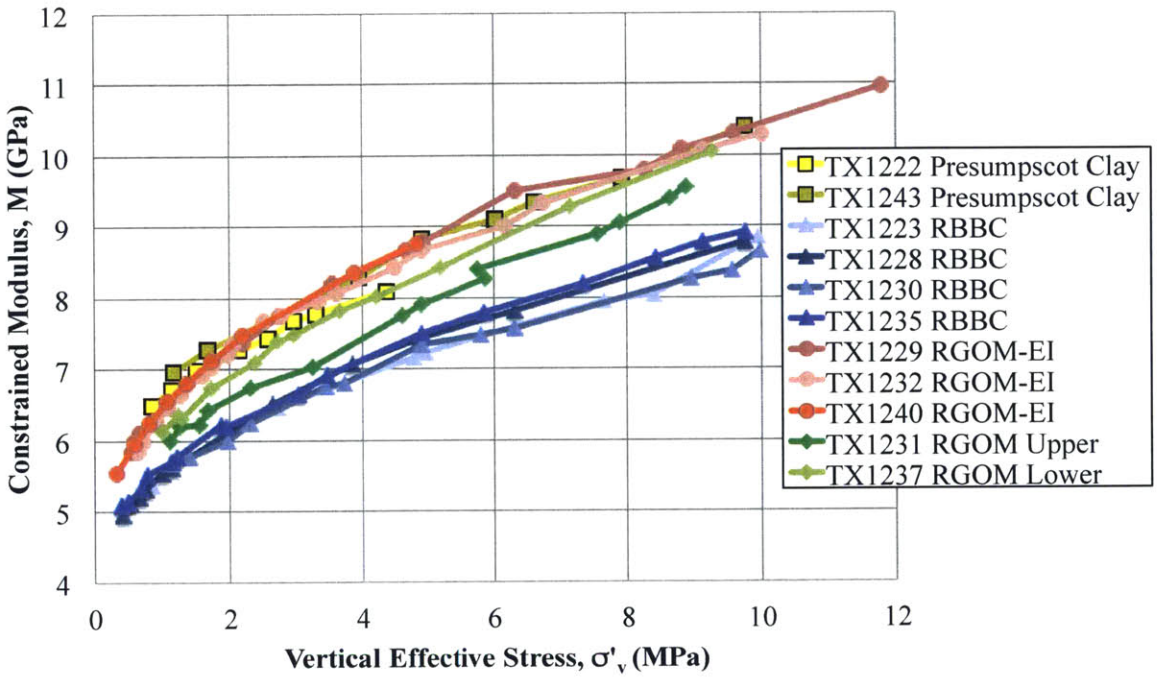

Figure 5-23: Constrained modulus results as a function of stress

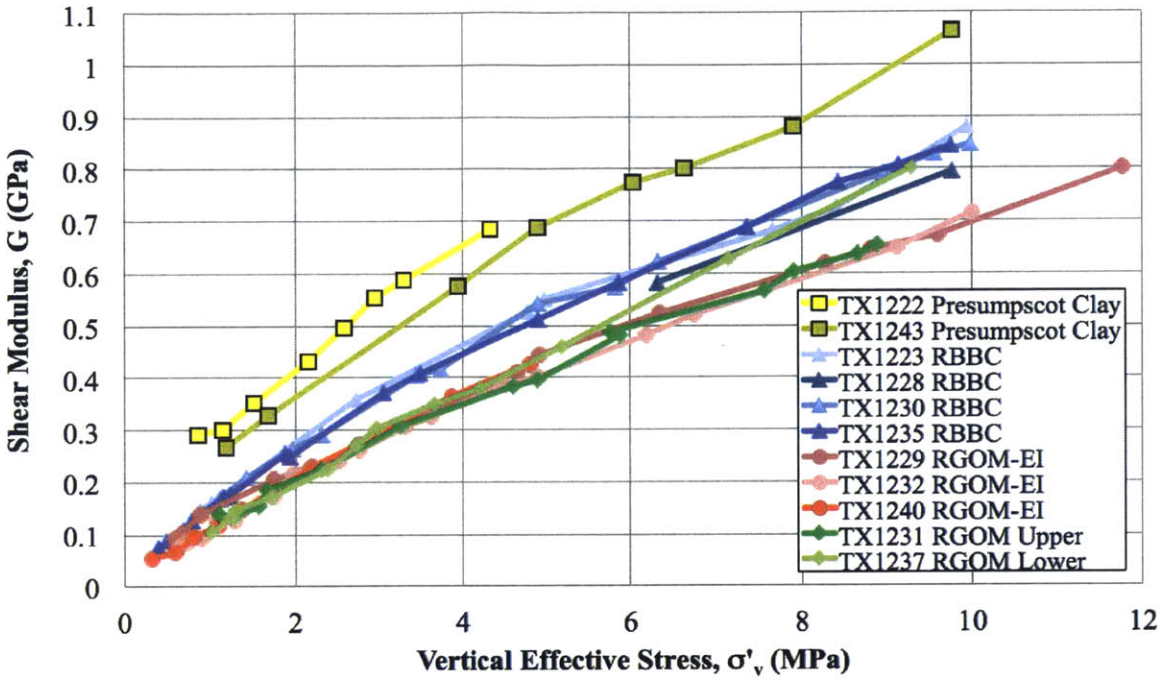

Figure 5-24: Shear modulus results as a function of stress

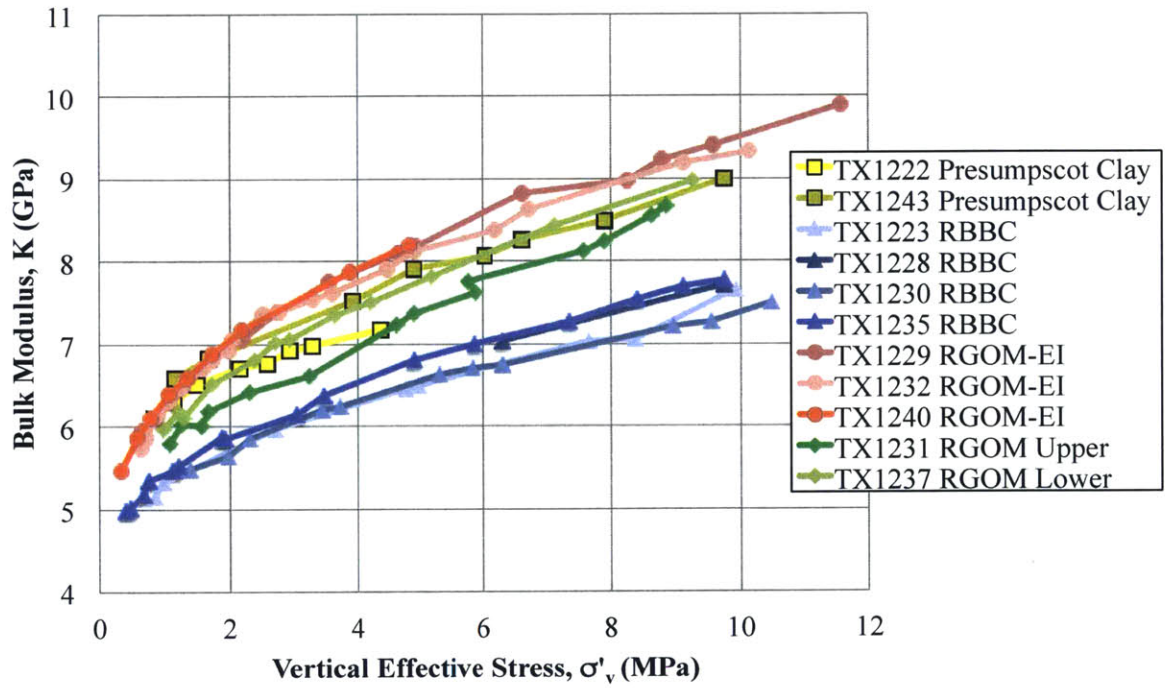

Figure 5-25: Bulk modulus results as a function of stress

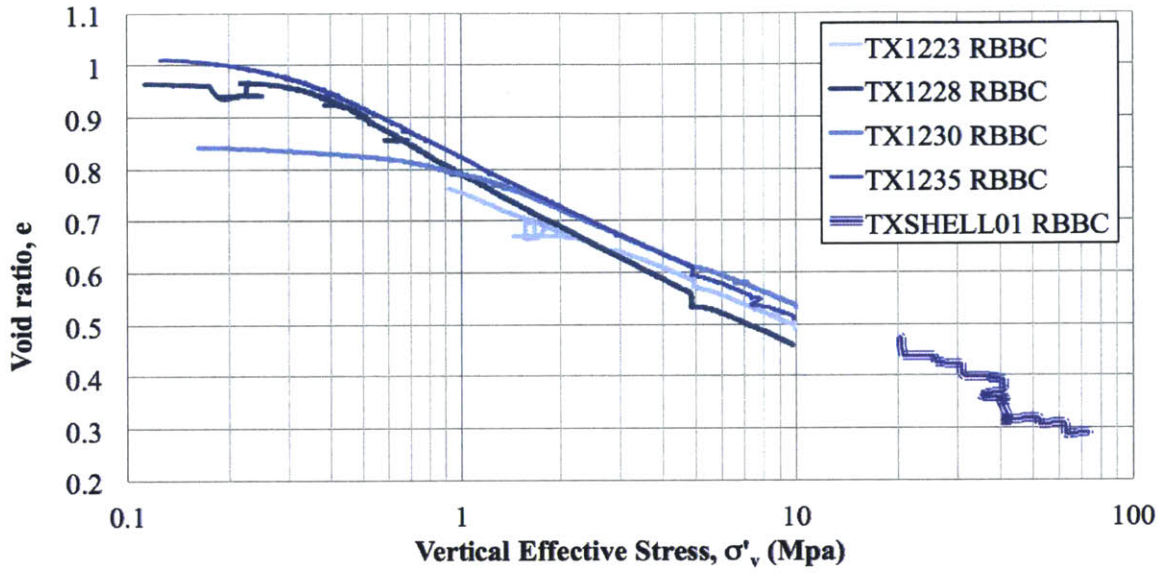

Figure 5-26: A high stress compression curve obtained from testing at Shell E&P is compared to the medium stress triaxial results for RBBC

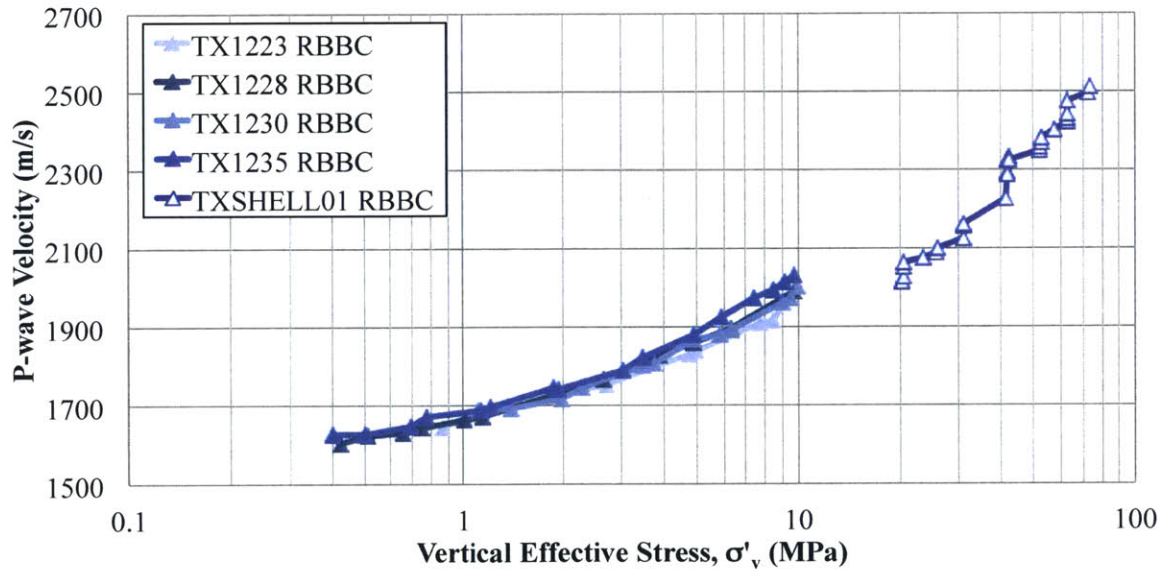

Figure 5-27: High stress P-wave velocity results obtained from testing at Shell E&P are compared to the medium stress triaxial results

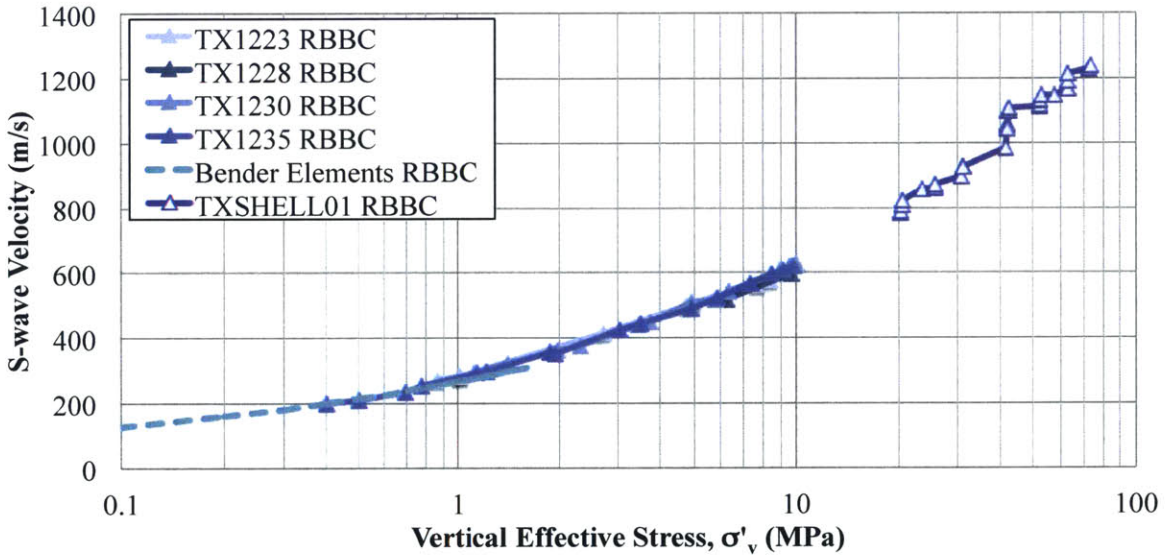

Figure 5-28: High stress S-wave velocity results obtained from testing at Shell E&P are compared to the medium stress triaxial results. Furthermore, the results from the low stress triaxial cell fitted with bender elements is presented here

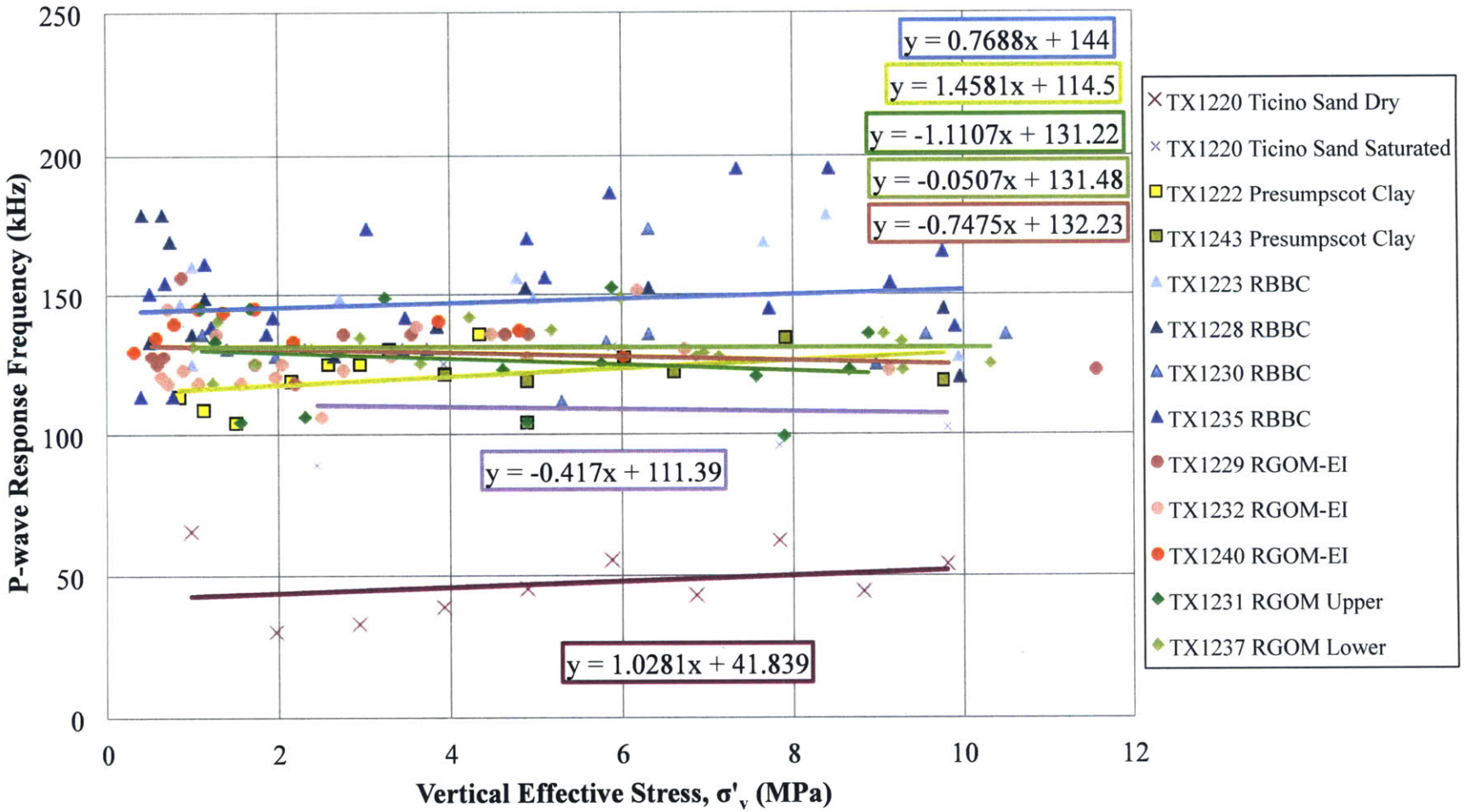

Figure 5-29: Frequency response of P-wave signals. A best fit line is shown for each material, with the corresponding equation boxed next to the line

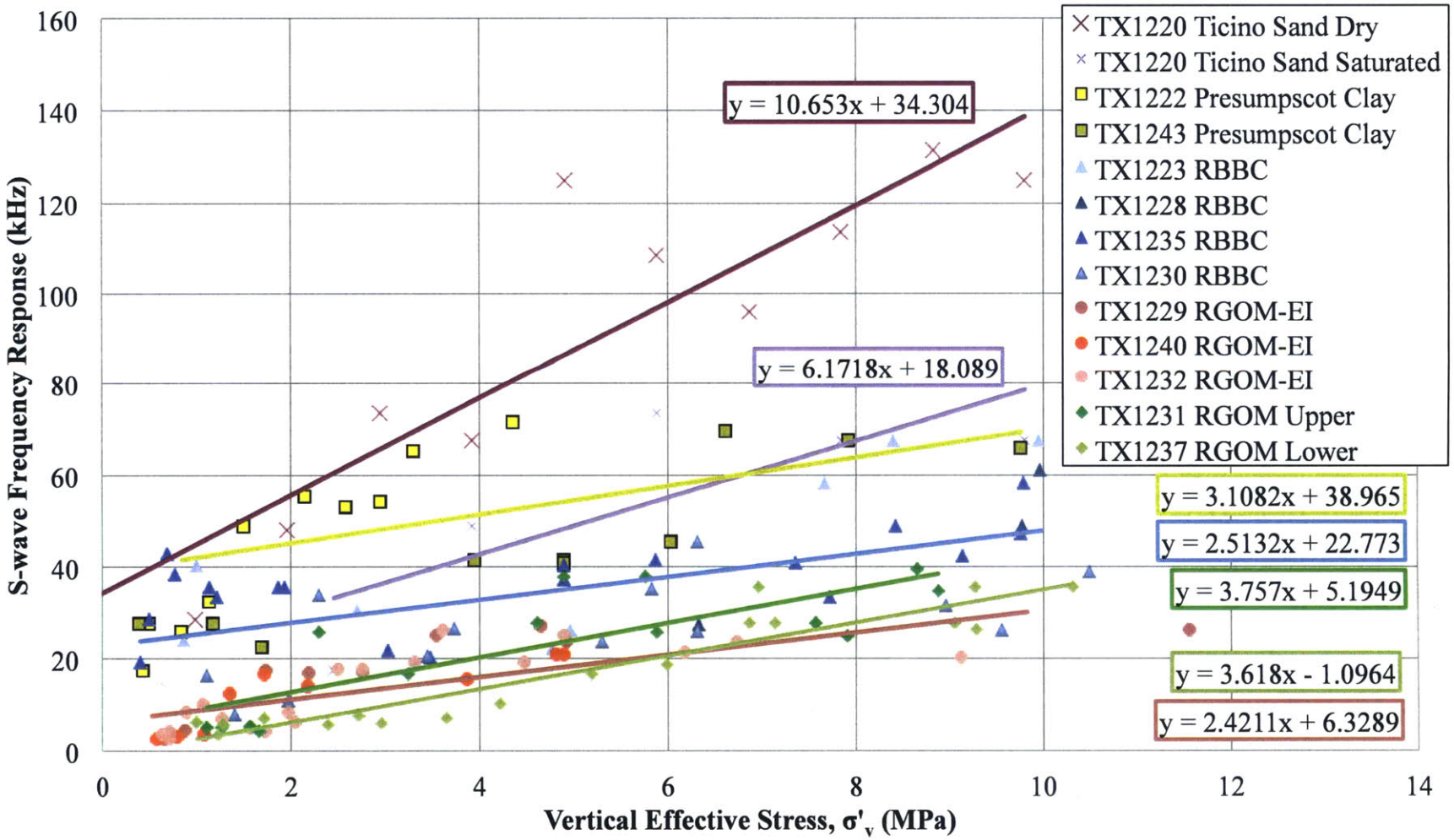

Figure 5-30: Frequency response of S-wave signals. A best fit line is shown for each material, with the corresponding equation boxed next to the line

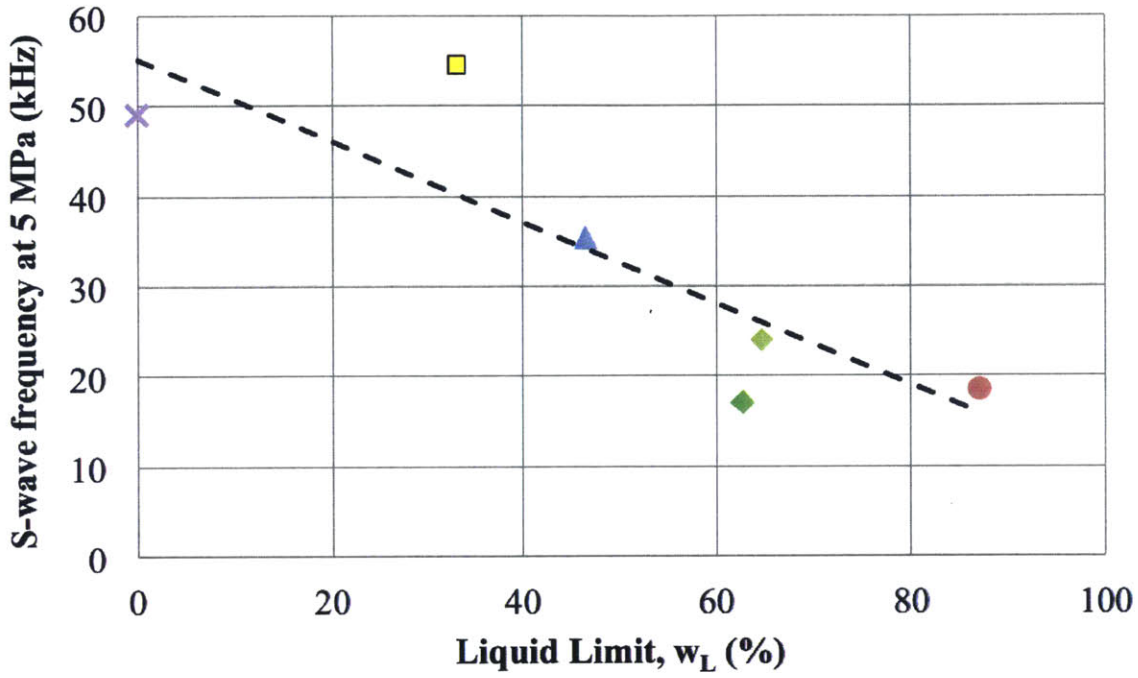

Figure 5-31: The S-wave frequency response for a single stress level from the previous figure (σ'_v= 5 MPa) as a function of liquid limit, showing a trend in plasticity. Dashed line is simply to show a trend

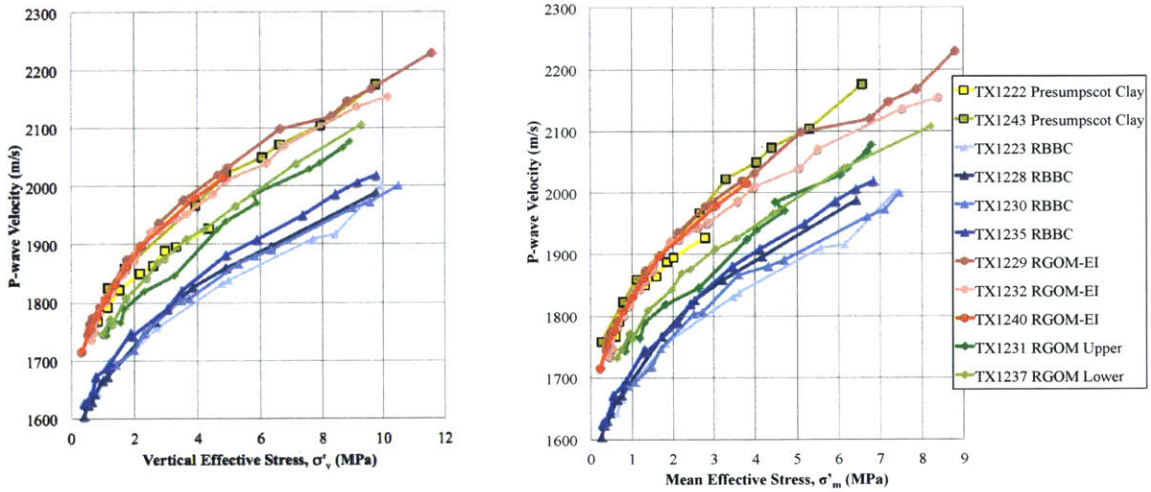

(a) V_p as a function of vertical effective stress

(b) V_p as a function of mean effective stress

Figure 5-32: V_p as a function of vertical and mean effective stress for all clays

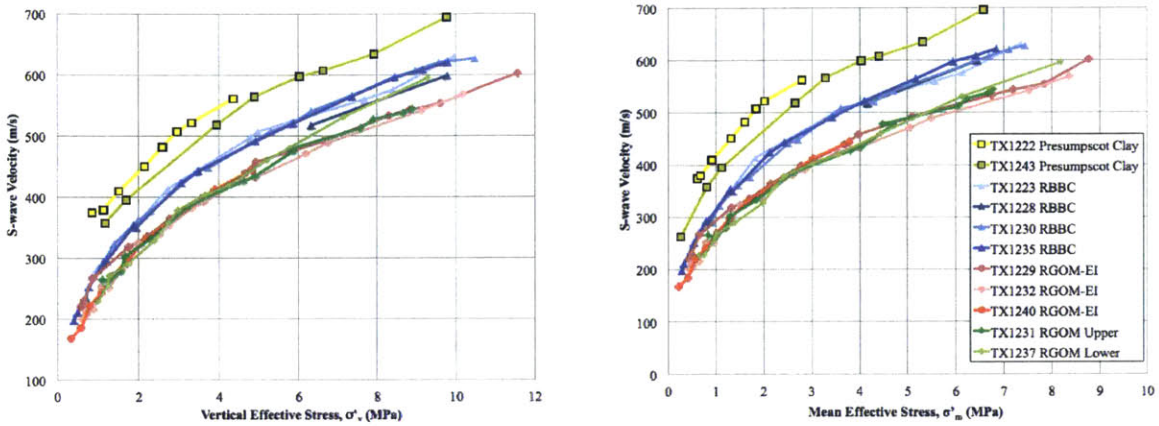

(a) V_s as a function of vertical effective stress

(b) V_s as a function of mean effective stress

Figure 5-33: V_s as a function of vertical and mean effective stress for all clays

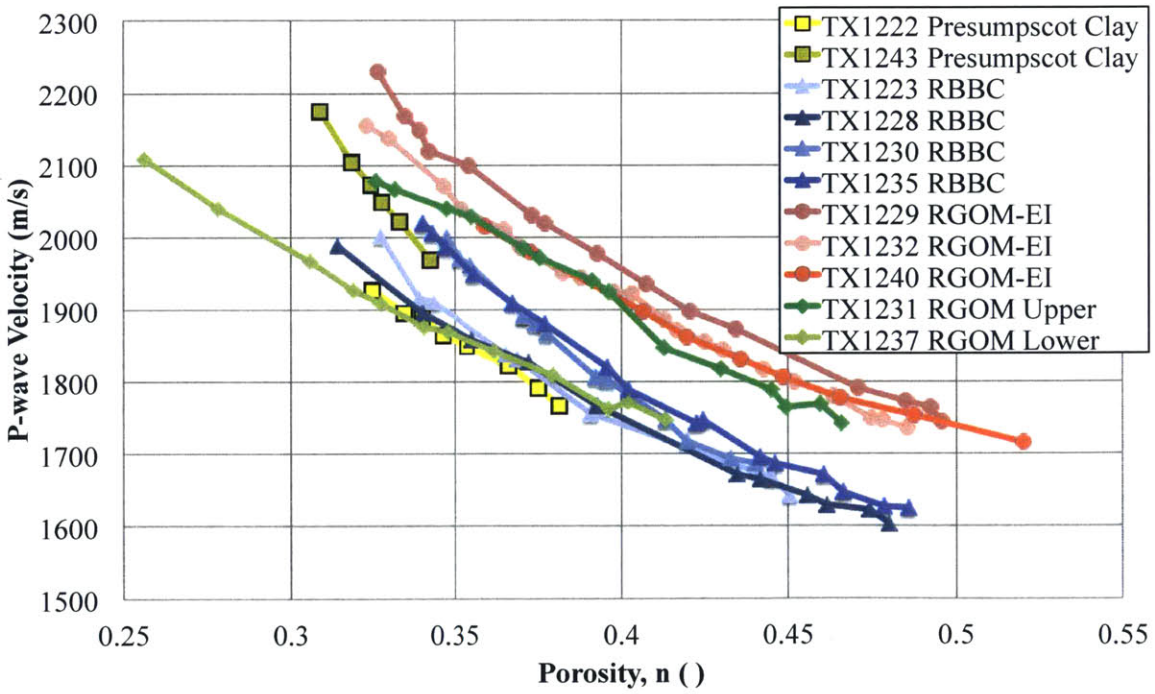

Figure 5-34: V_p as a function of porosity

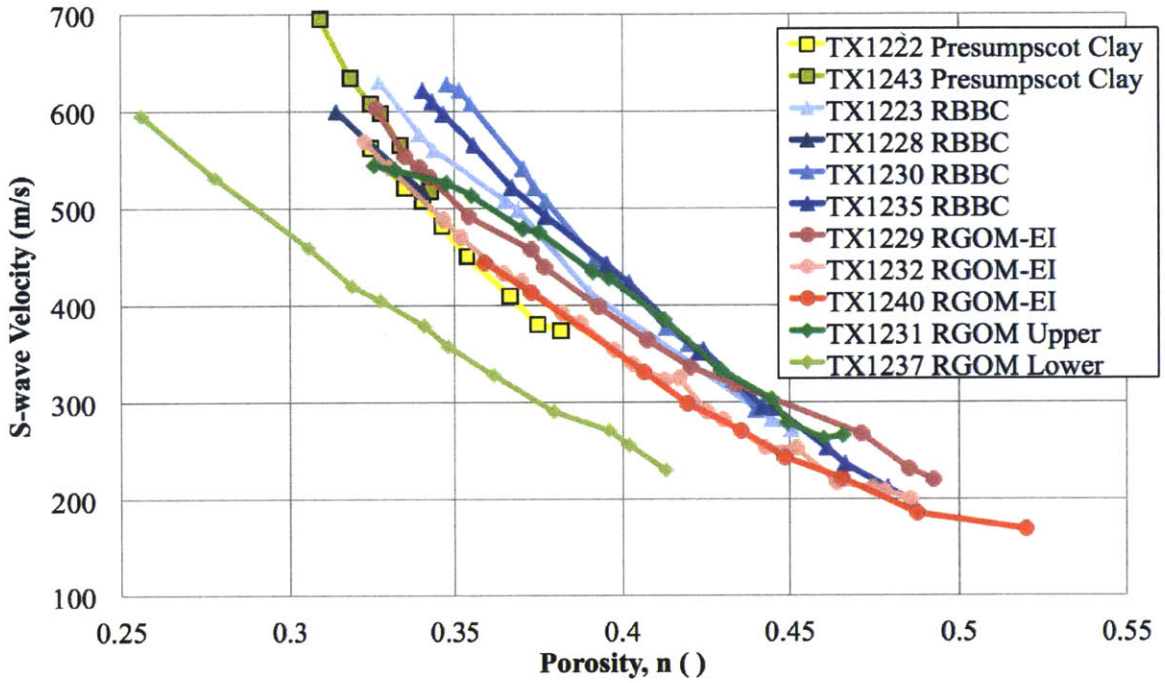

Figure 5-35: V_s as a function of porosity

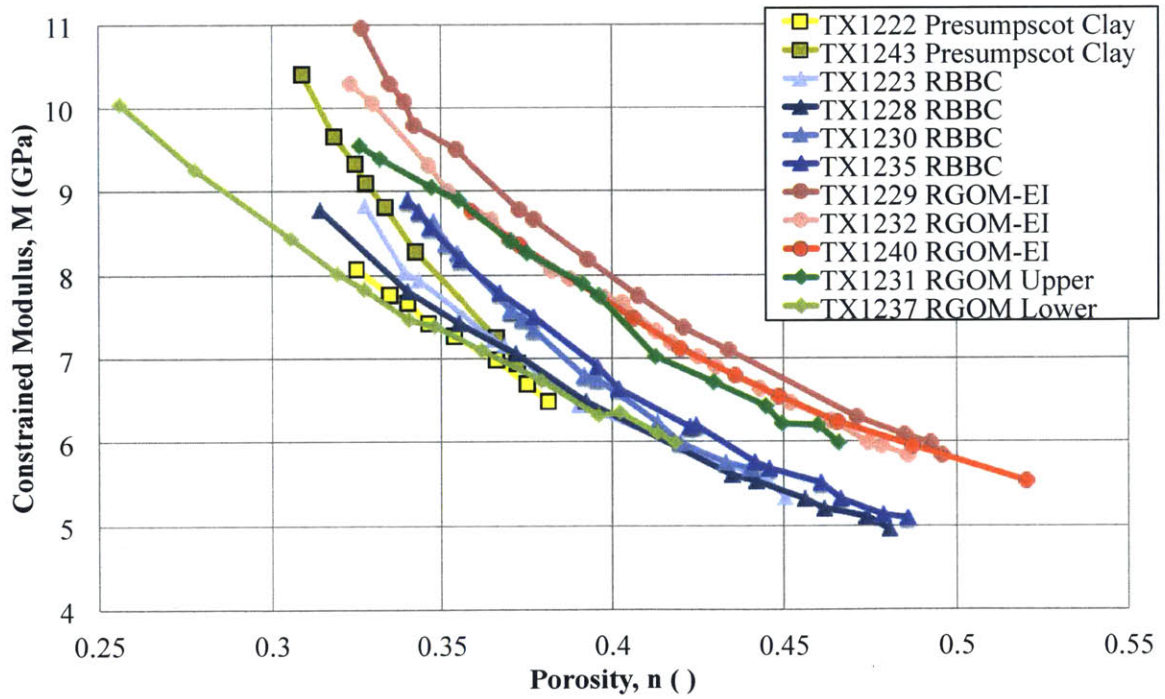

Figure 5-36: M as a function of porosity

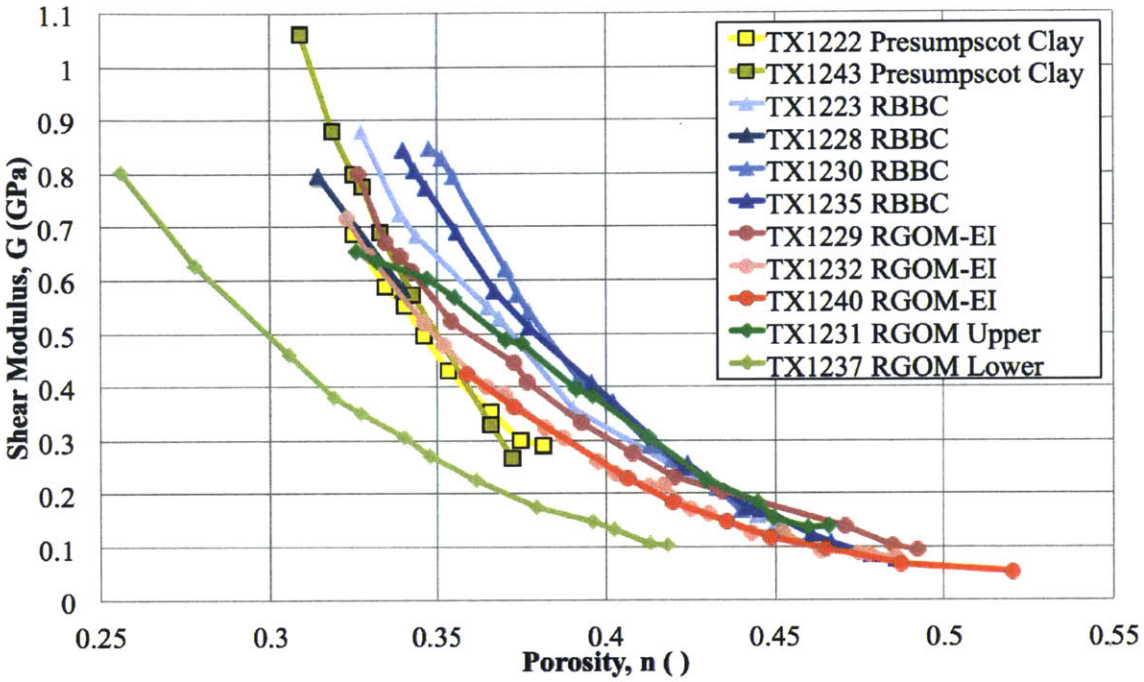

Figure 5-37: G as a function of porosity

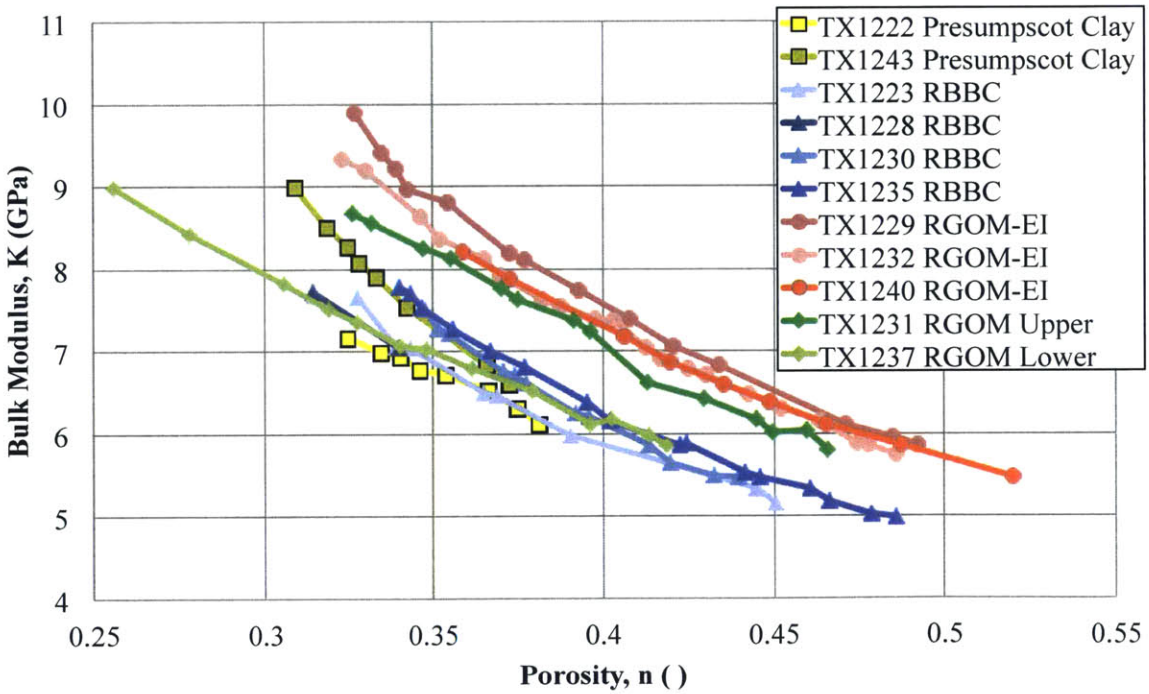

Figure 5-38: K as a function of porosity

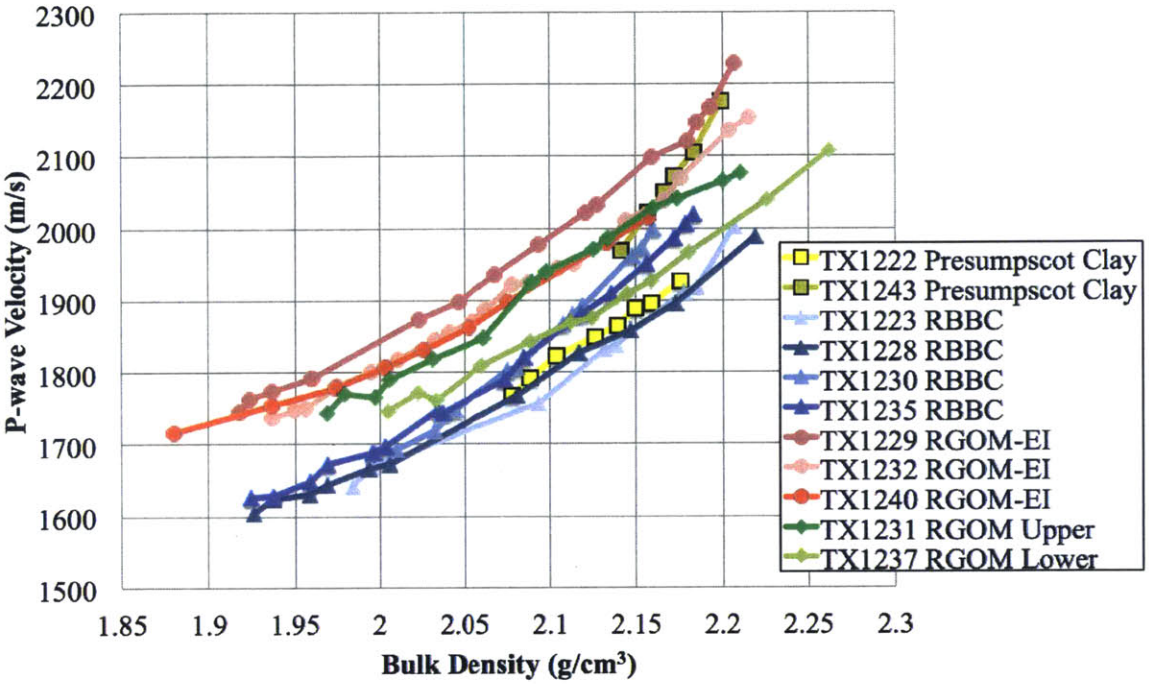

Figure 5-39: V_p as a function of density

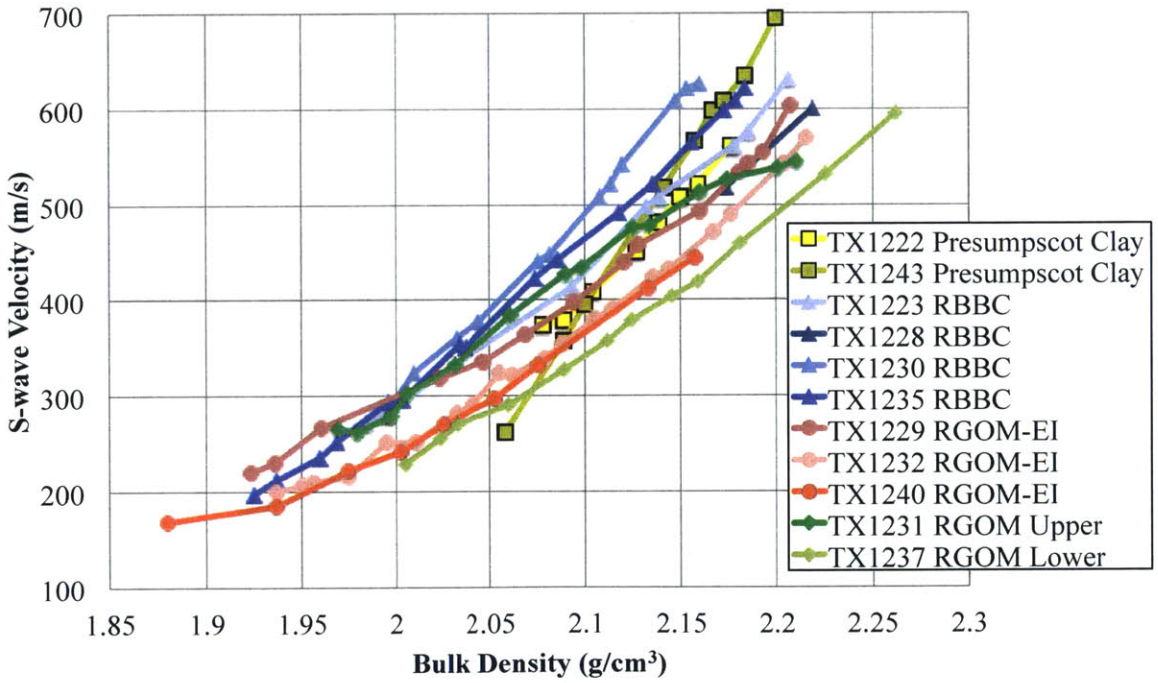

Figure 5-40: V_s as a function of density

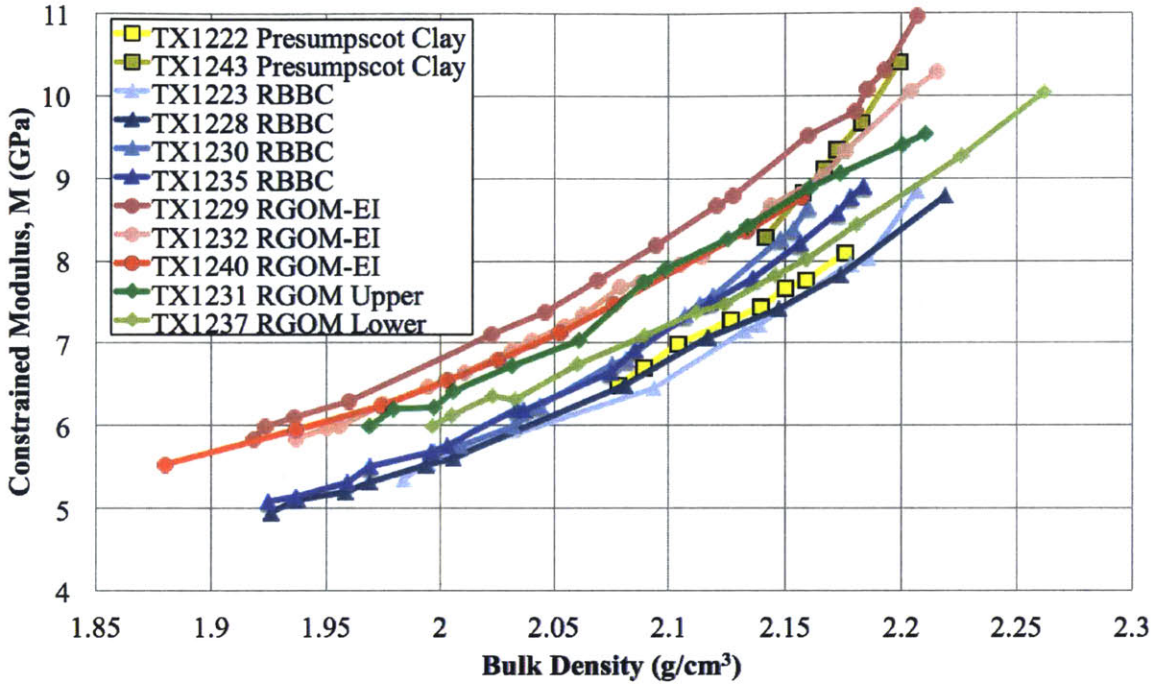

Figure 5-41: M as a function of density

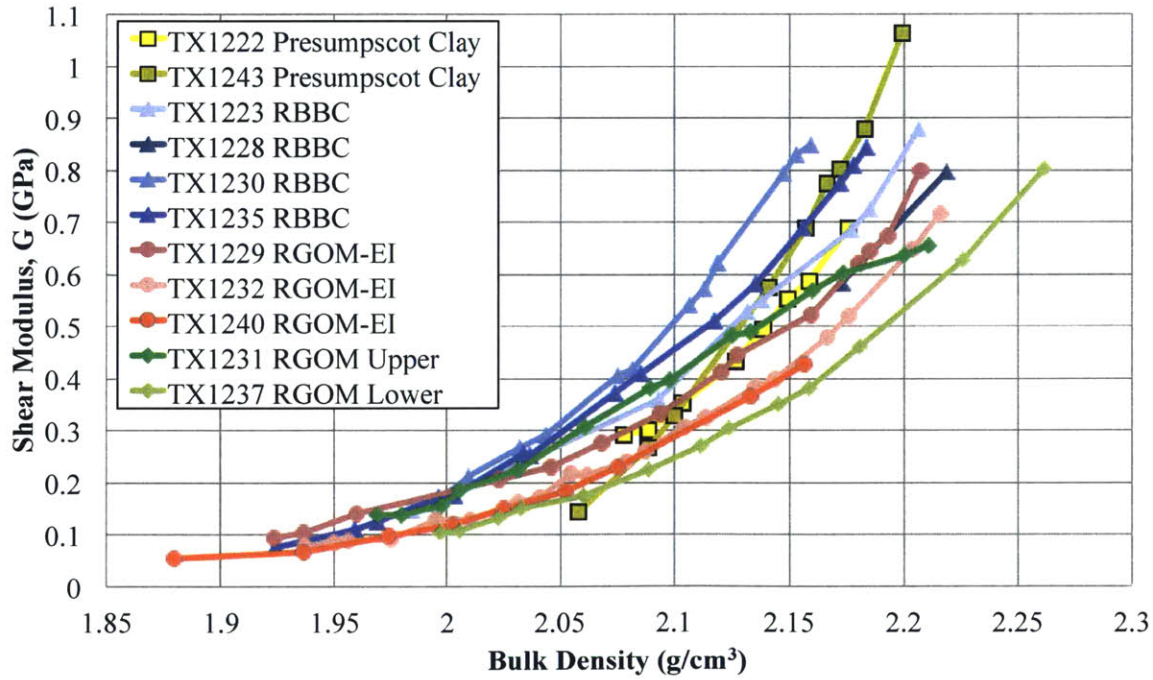

Figure 5-42: G as a function of density

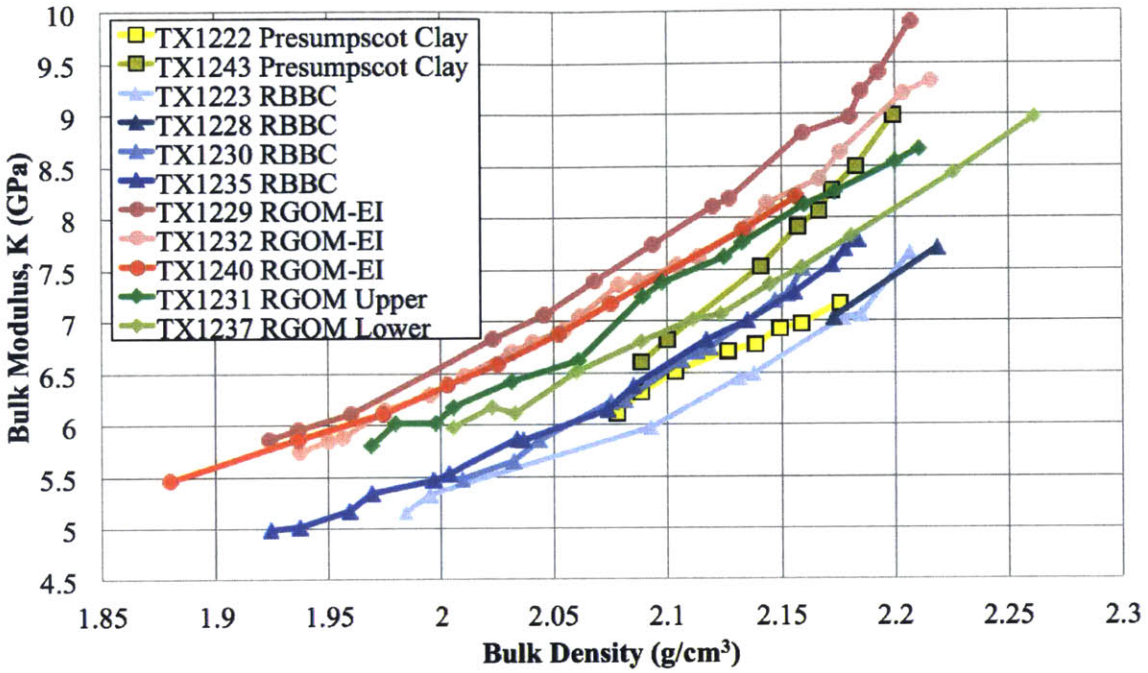

Figure 5-43: K as a function of density

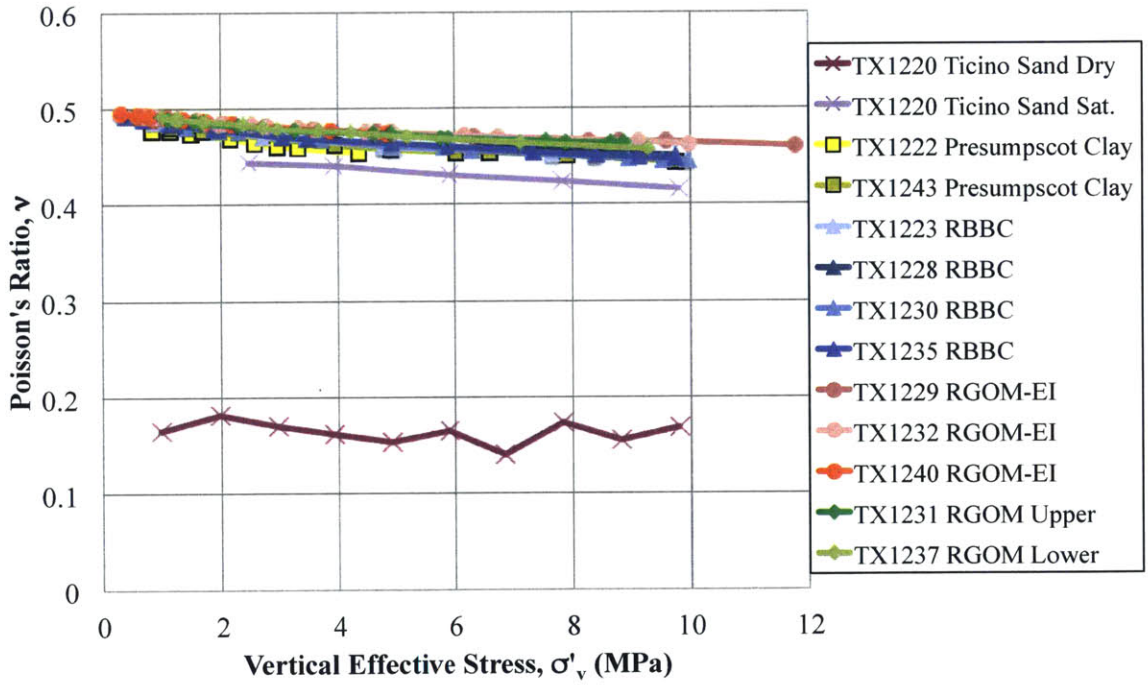

Figure 5-44: Velocity-derived Poisson's ratio for NC material as a function of stress, including the dry Ticino sand

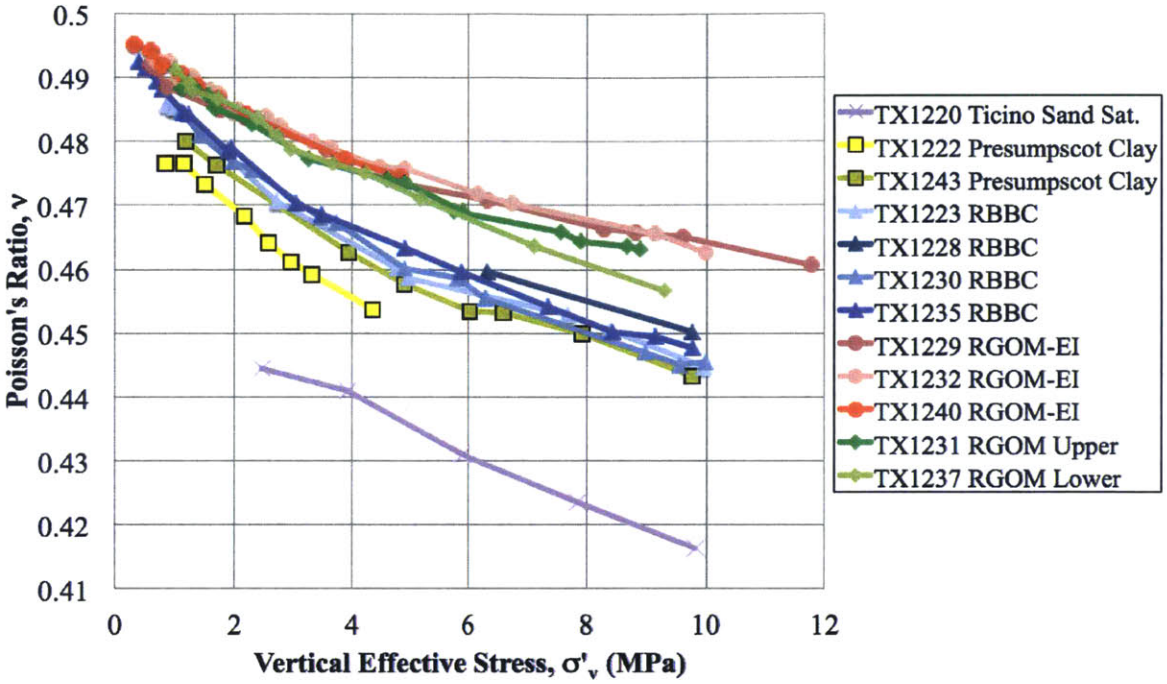

Figure 5-45: Velocity-derived Poisson's ratio for NC material as a function of stress

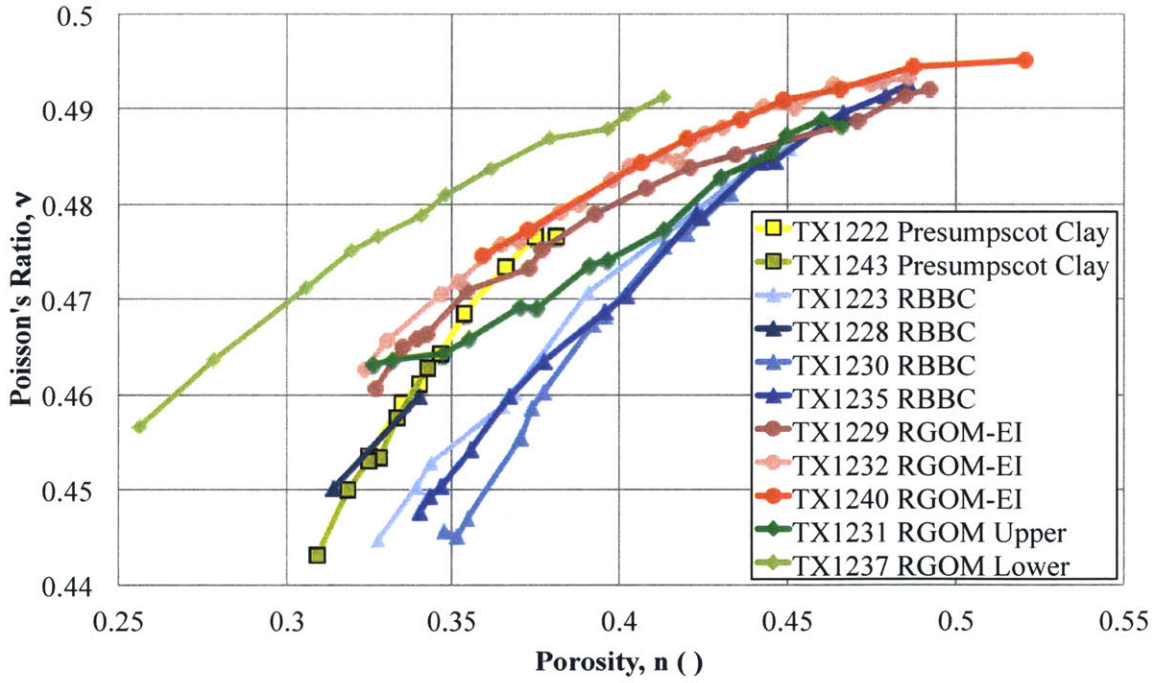

Figure 5-46: Velocity-derived Poisson's ratio as a function of porosity

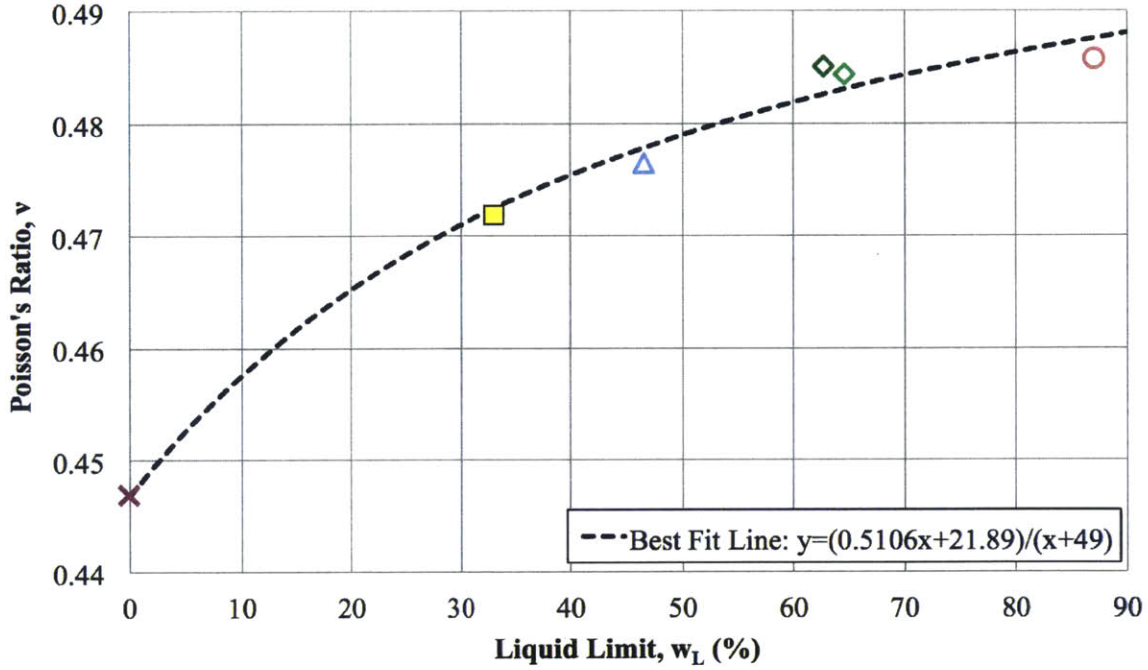

Figure 5-47: Velocity-derived Poisson's ratio as a function of liquid limit at $\sigma'_v = 2MPa$. R^2 value of 0.980

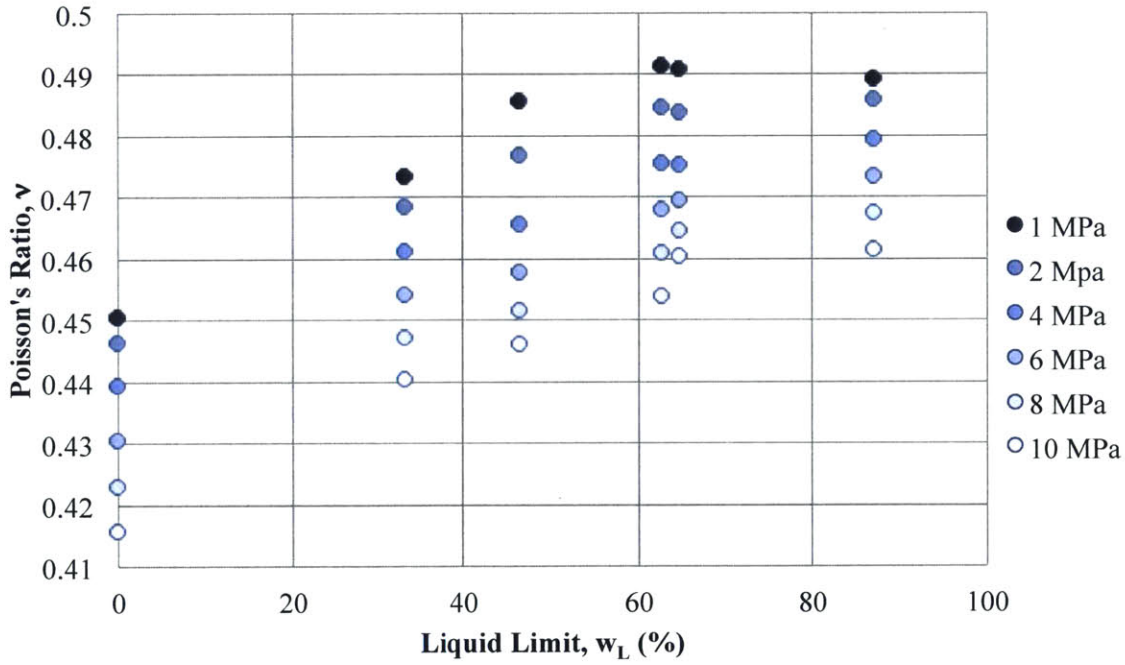

Figure 5-48: Velocity-derived Poisson's ratio as a function of liquid limit at $\sigma'_v = 1 - 10MPa$

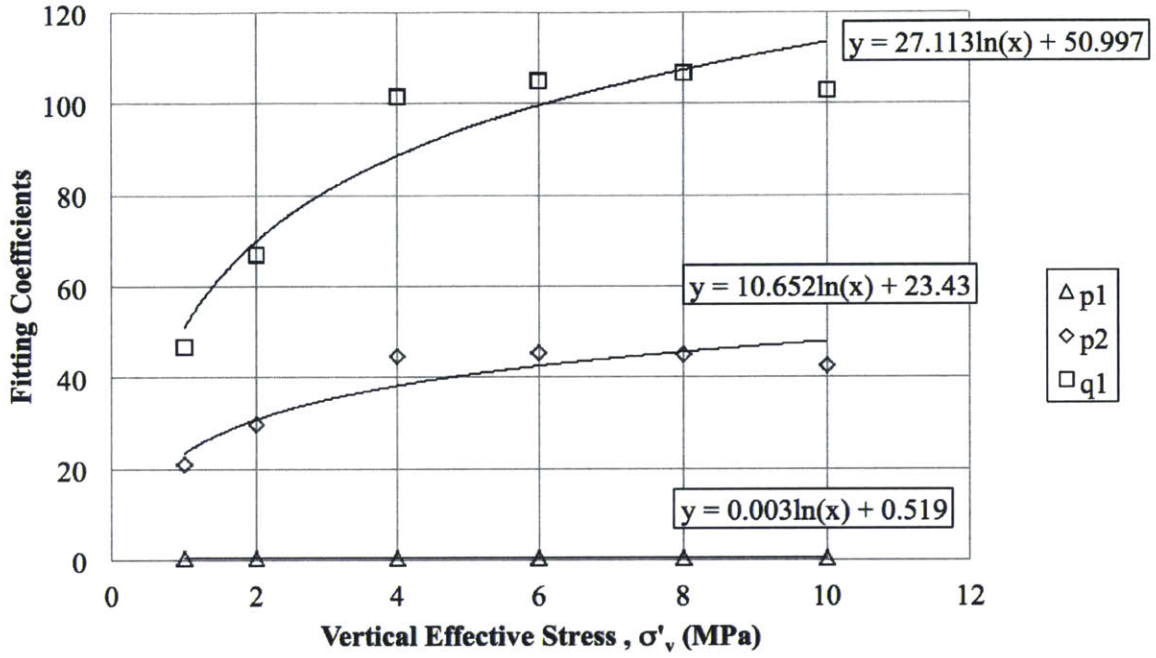

Figure 5-49: Using the best-ft curve in Figure 5-47, and applying that fit to all the stresses in Figure 5-48, an equation of the form $\nu = (p1 * w_L + p2)/(w_L + q1)$ can be used with this p1, p2, and q1 parameters. If a stress and liquid limit is known, the Poisson's ratio can be predicted

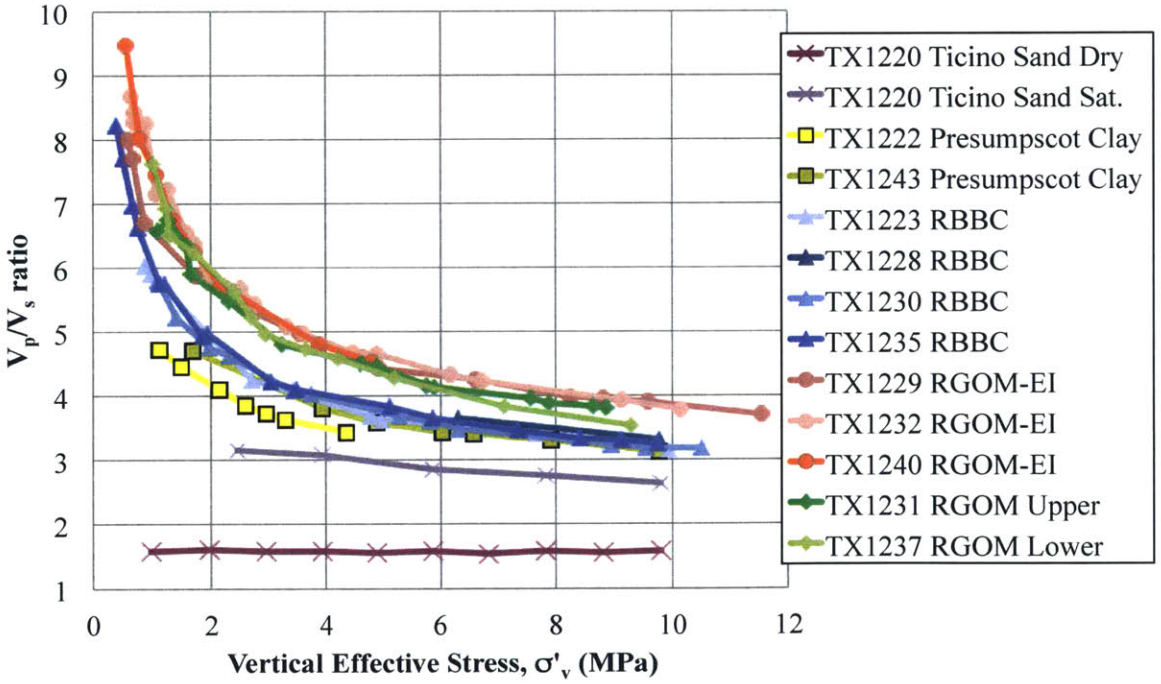

Figure 5-50: The ratio of P-wave to S-wave velocity is shown as a function of vertical effective stress

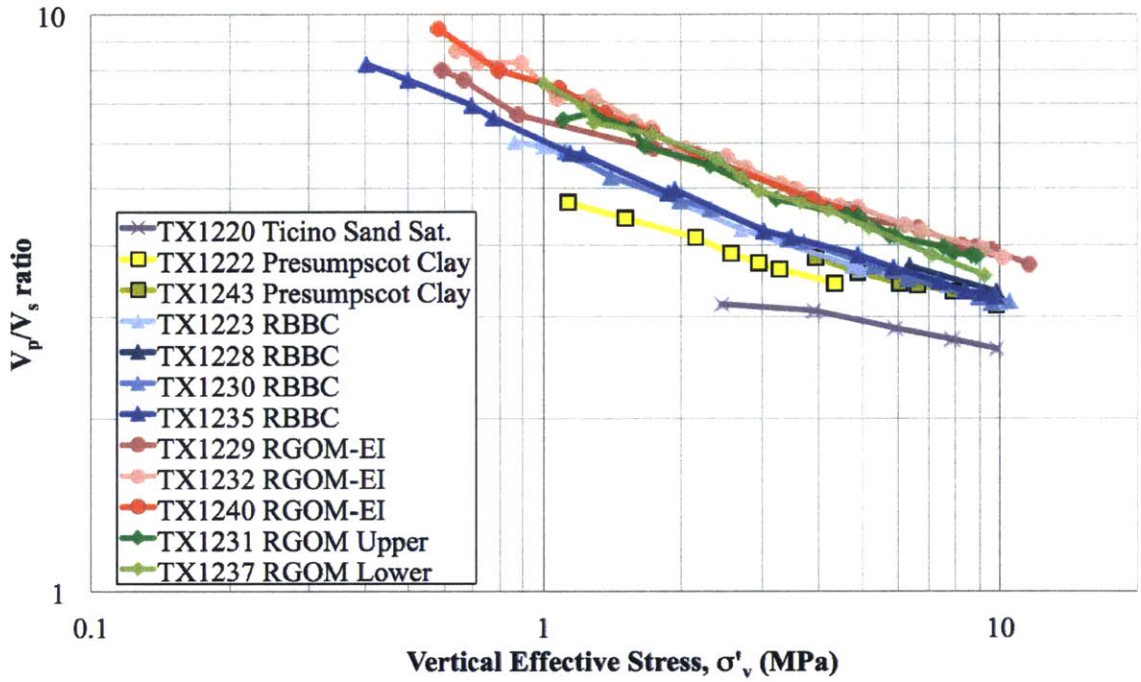

Figure 5-51: The ratio of P-wave to S-wave velocity is shown as a function of vertical effective stress

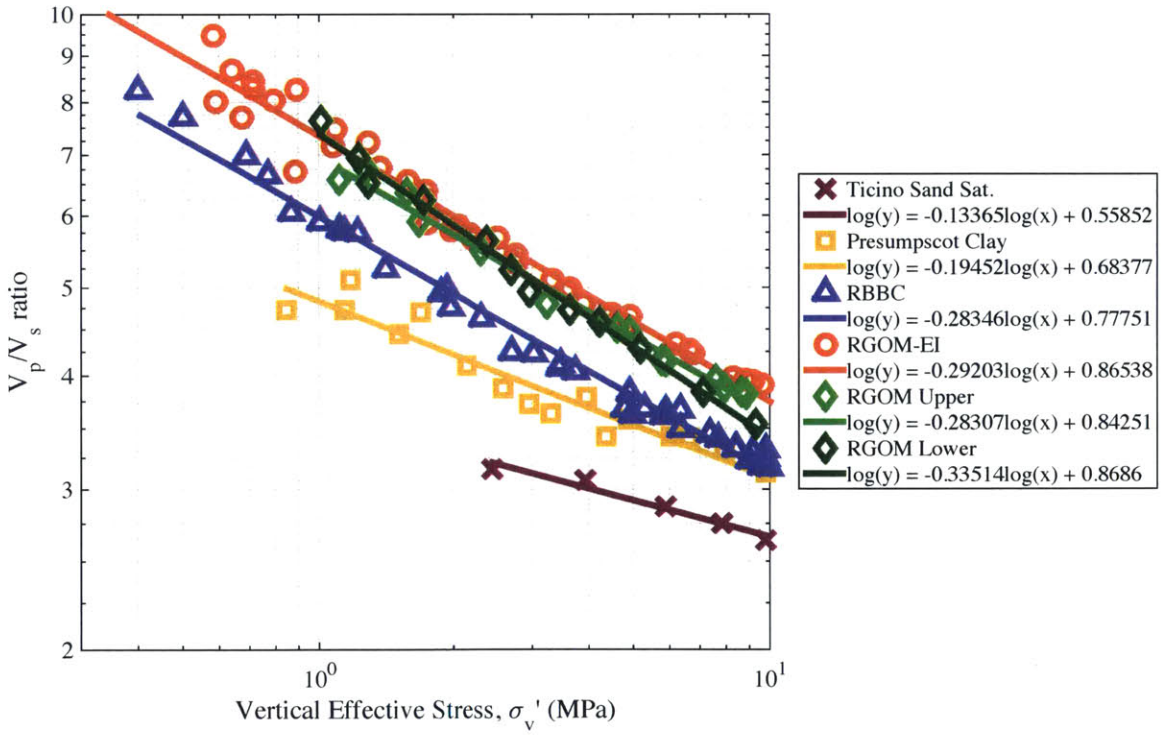

Figure 5-52: The ratio of P-wave to S-wave velocity is shown as a function of vertical effective stress, with best fit lines

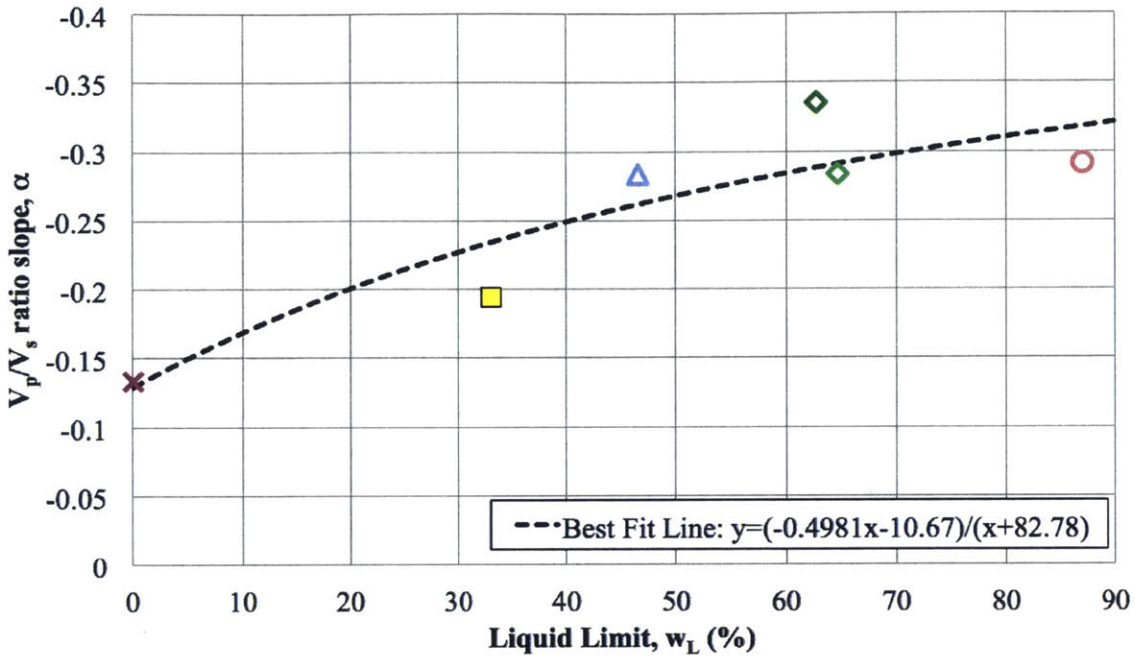

Figure 5-53: The slope of the P-wave to S-wave velocity ratio is shown as a function of liquid limit for each material. The colors correspond to the legend above. R^2 value of 0.697

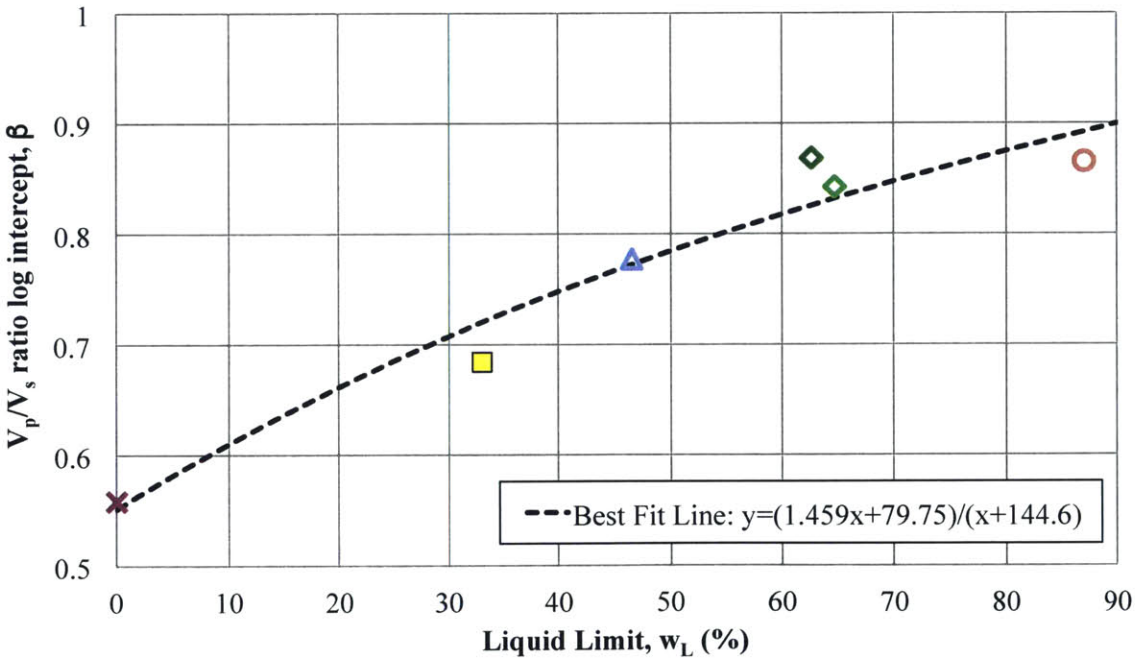

Figure 5-54: The intercept of the P-wave to S-wave velocity ratio line is shown as a function of liquid limit for each material. The colors correspond to the legend above. R^2 value of 0.911

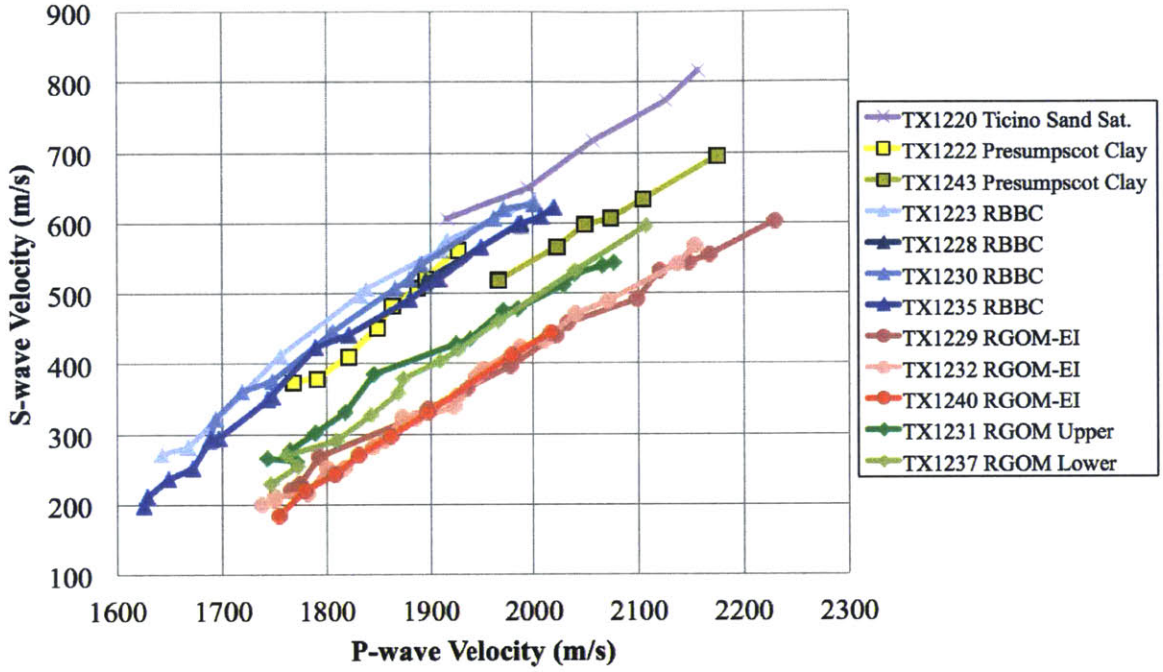

Figure 5-55: Crossplot of P-wave velocity to S-wave velocity as a function of vertical effective stress. Legend same as previous figure

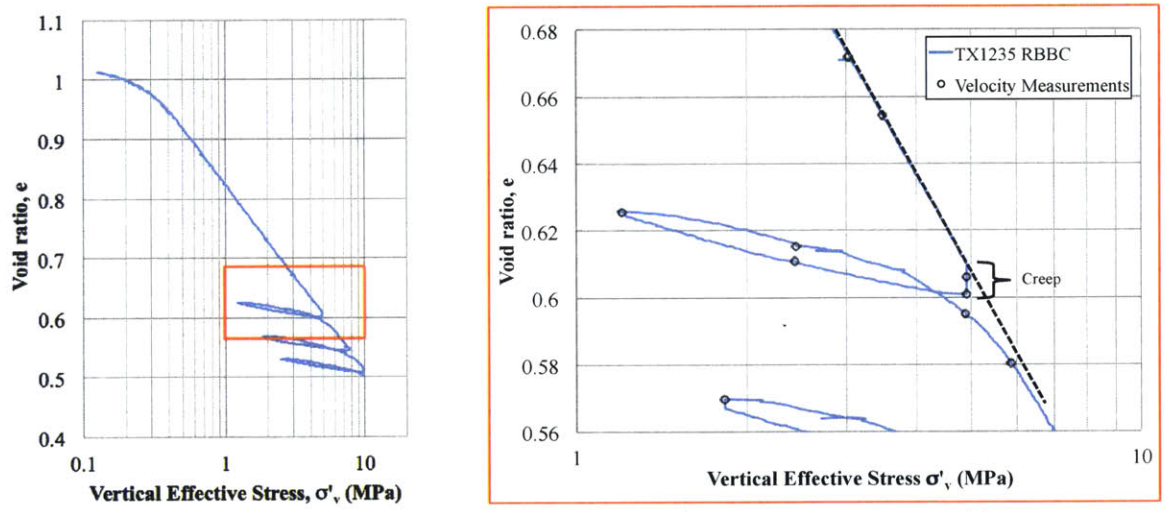

(a) Creep in compression curve

(b) Zoomed-in version of (a)

Figure 5-56: Zoomed-out and zoomed-in image of an RBBC compression curve. The dashed line is the Virgin Compression Line (VCL), and the creep is pointed out, occurring when a constant stress is held while the void ratio is changing

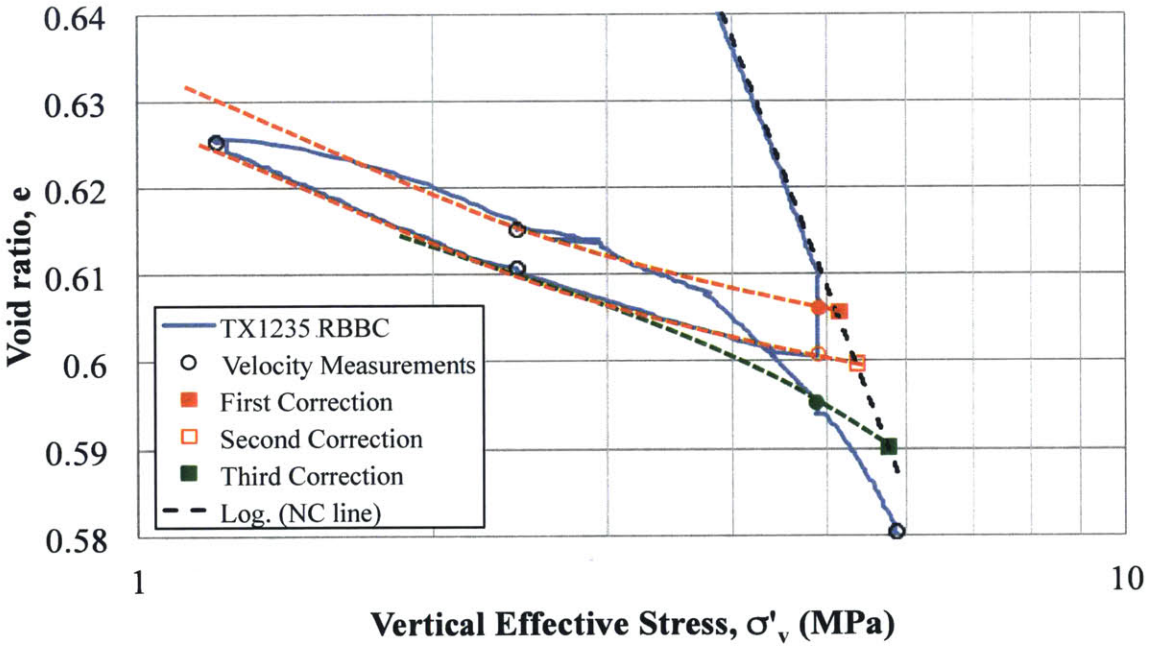

Figure 5-57: A stress adjustment is performed on the velocity measurements. The red and green dashed lines follow the curvature of the unload and loading portion, respectively. The colored circle lying on the dashed line is extrapolated to the corresponding square with the same color

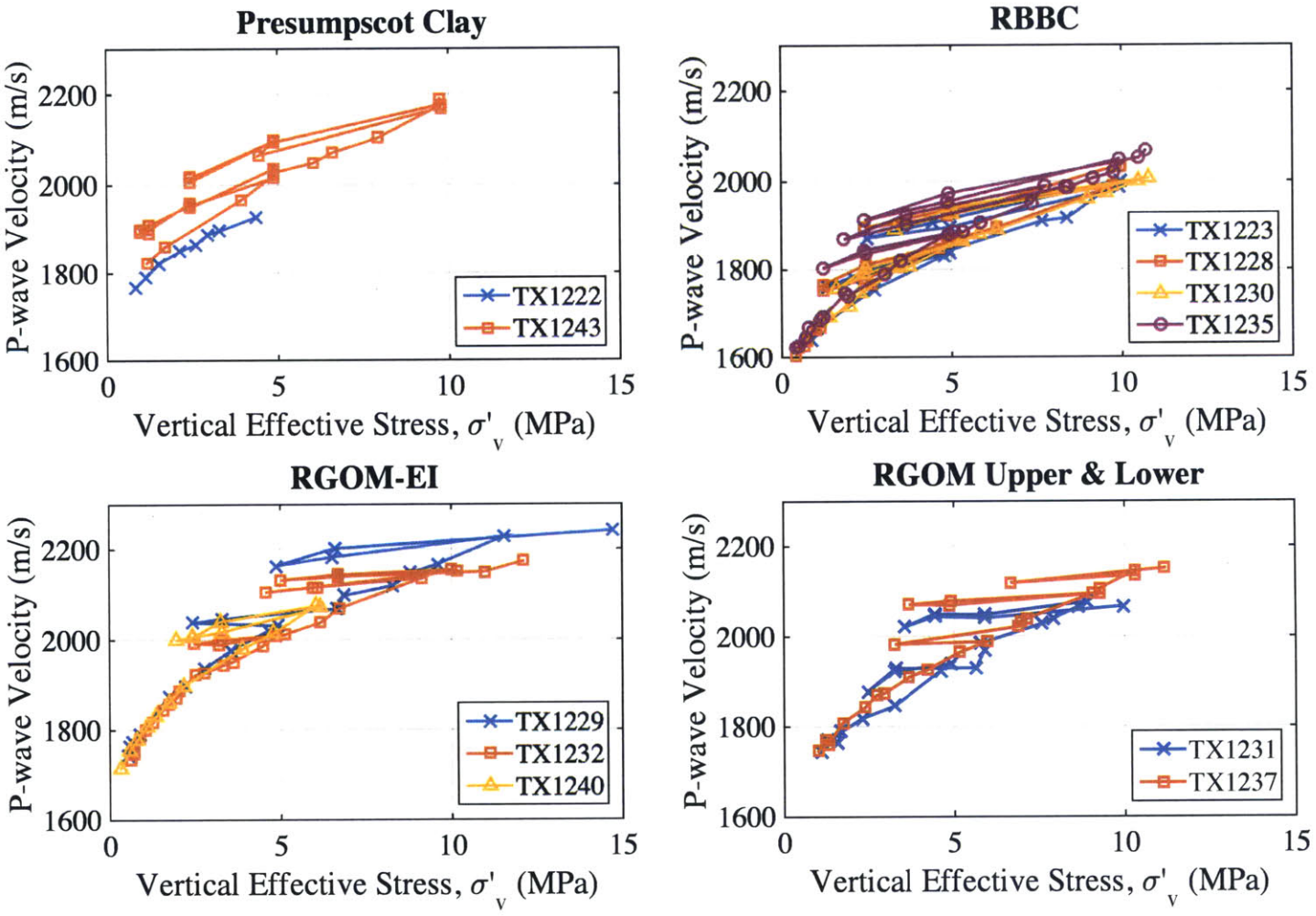

Figure 5-58: The loading and unloading portions of the P-wave velocity curves for all materials tested. No unloading portion in TX1222 Presumpscot clay

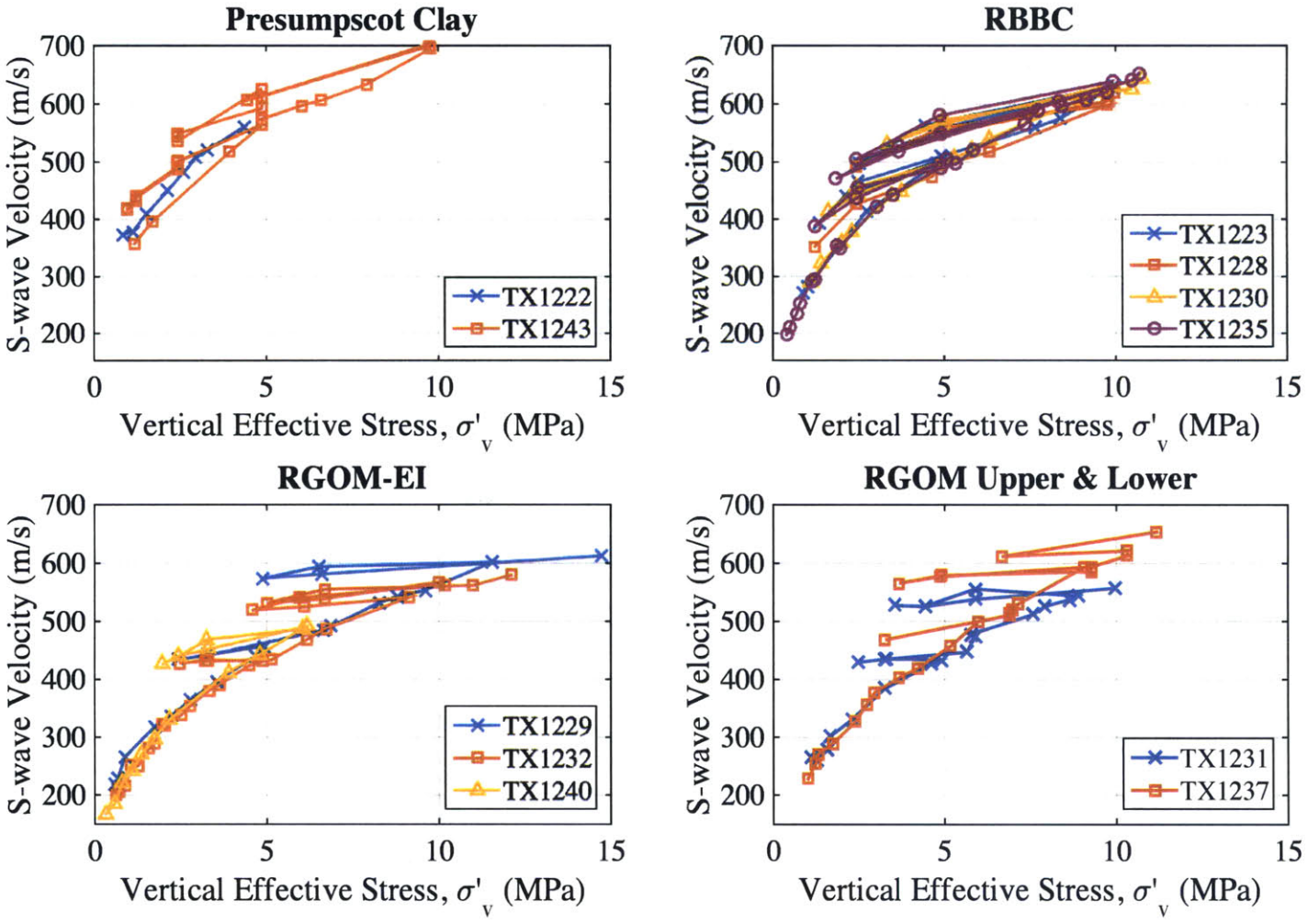

Figure 5-59: The loading and unloading portions of the S-wave velocity curves for all materials tested. No unloading portion in TX1222 Presumpscot clay

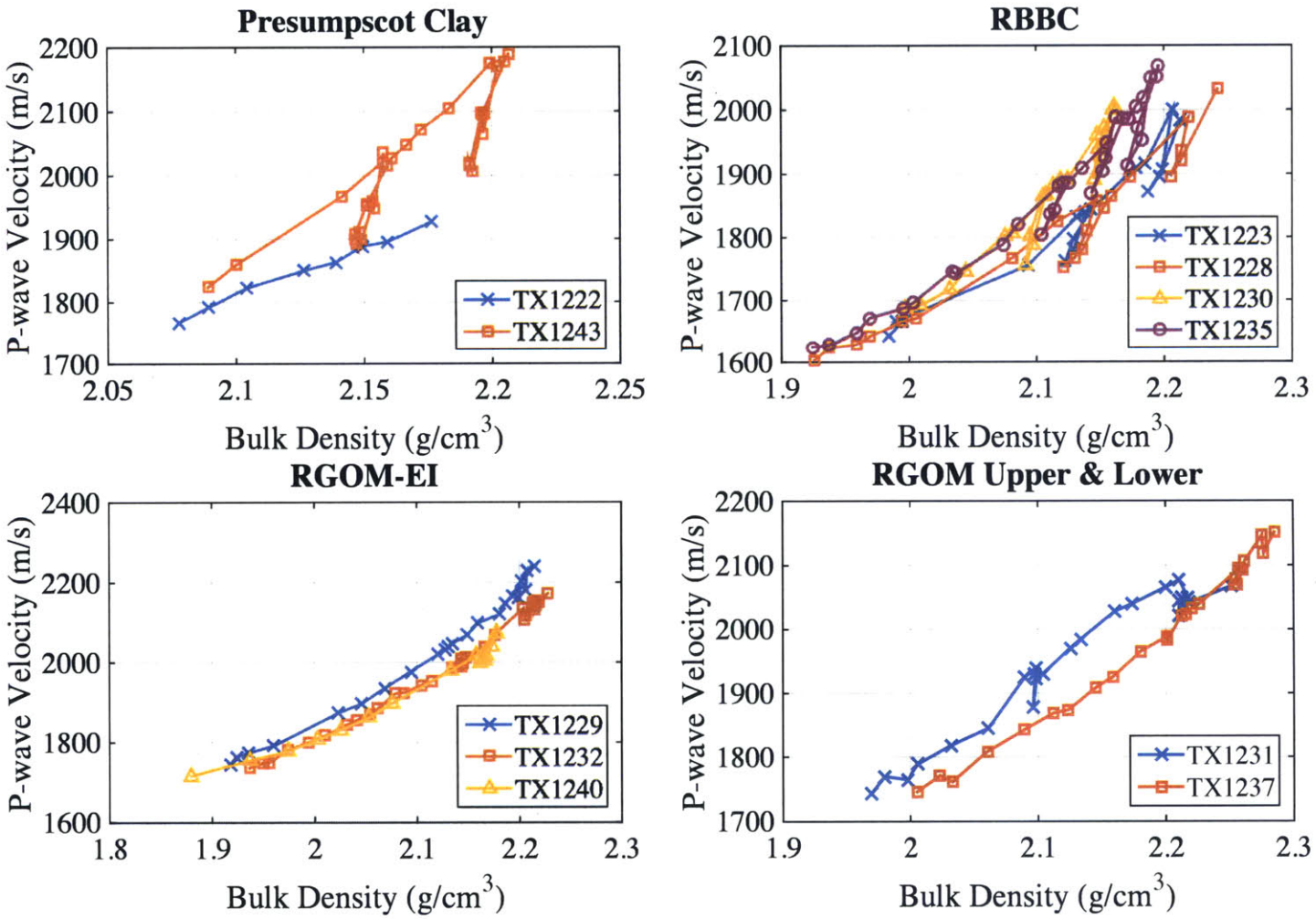

Figure 5-60: The loading and unloading portions of the P-wave velocity-density crossplots for all materials tested. No unloading portion in TX1222 Presumpscot clay

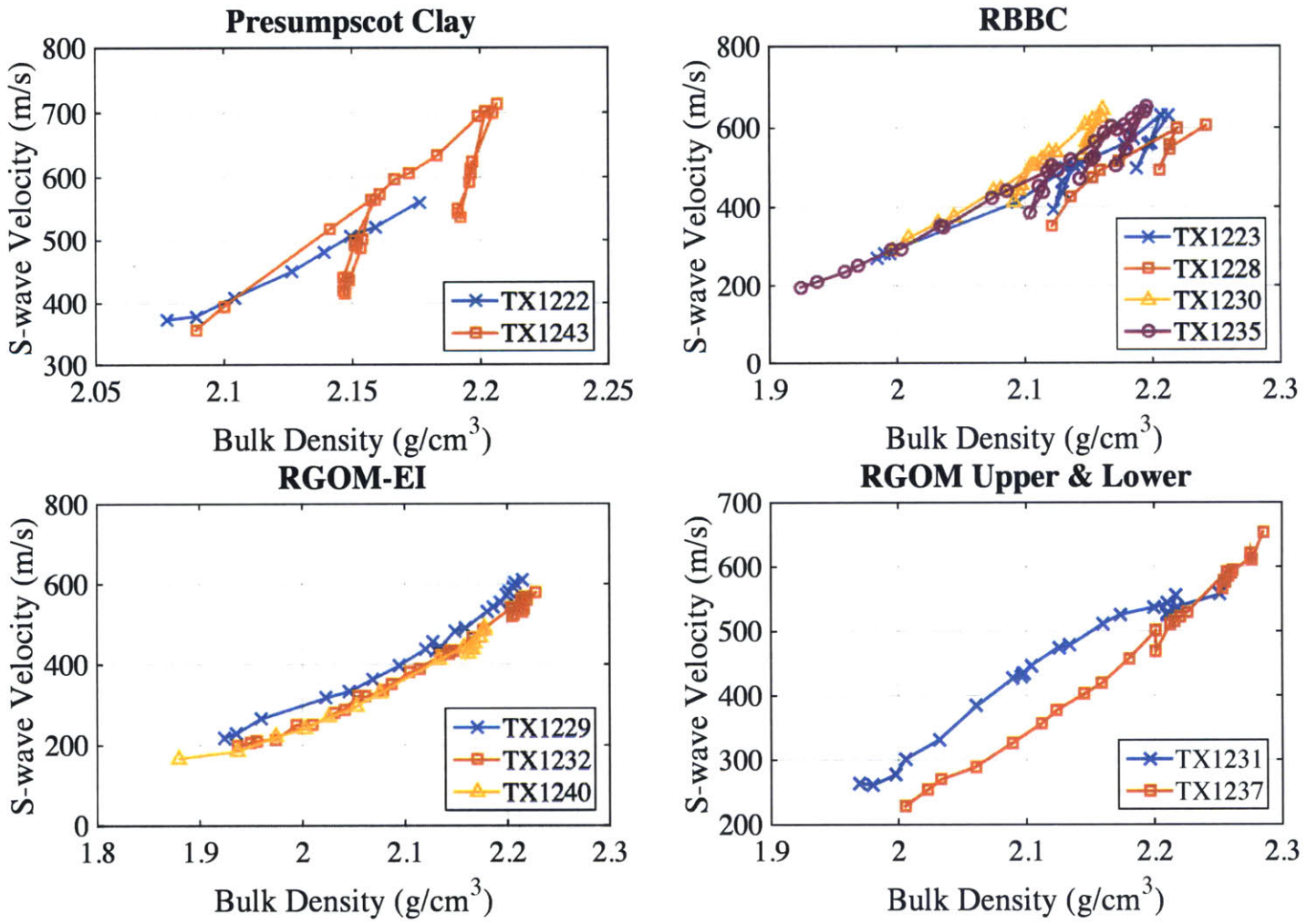

Figure 5-61: The loading and unloading portions of the S-wave velocity-density crossplot curves for all materials tested. No unloading portion in TX1222 Presumpscot clay

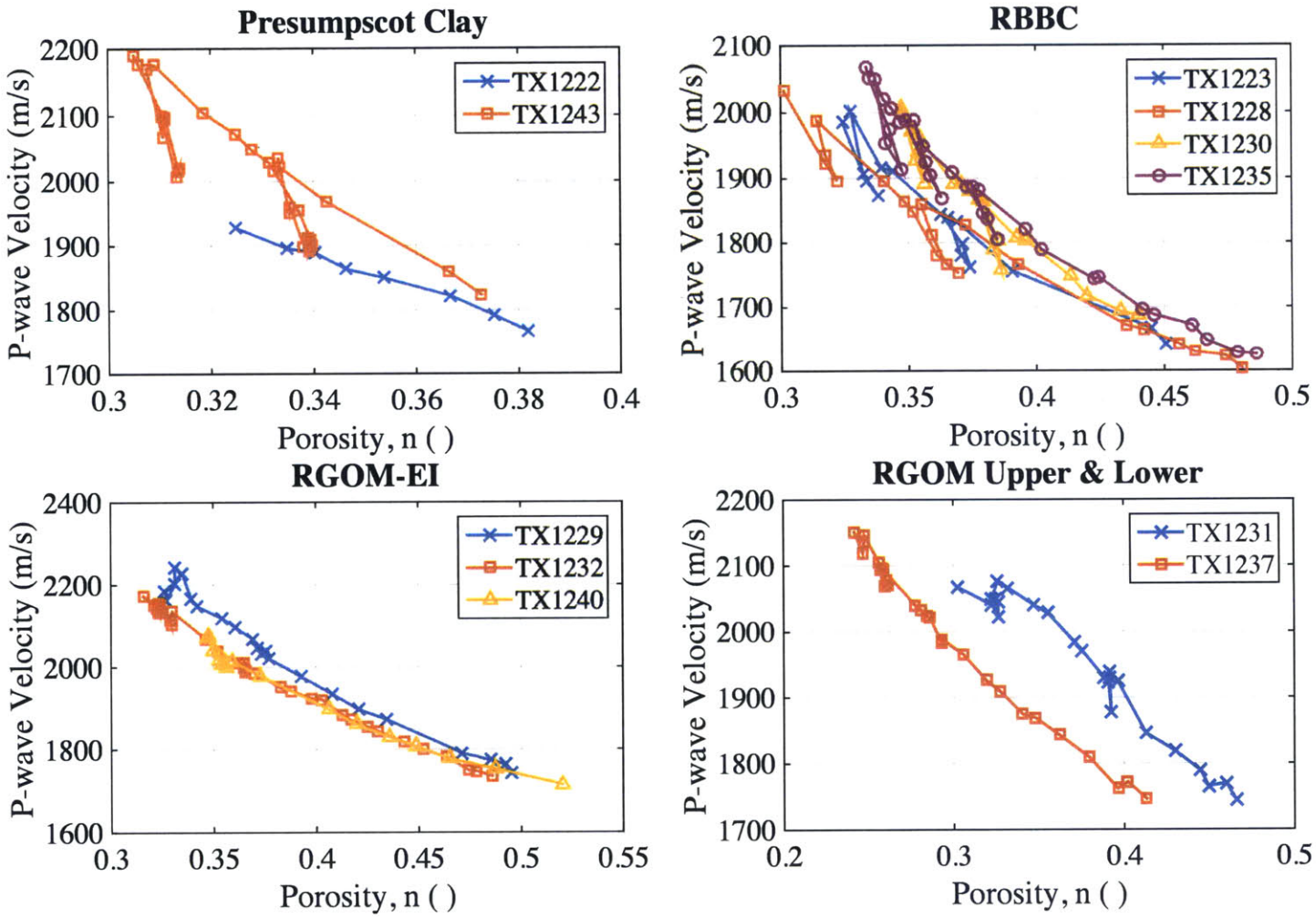

Figure 5-62: The loading and unloading portions of the P-wave velocity-porosity curves for all materials tested. No unloading portion in TX1222 Presumpscot clay

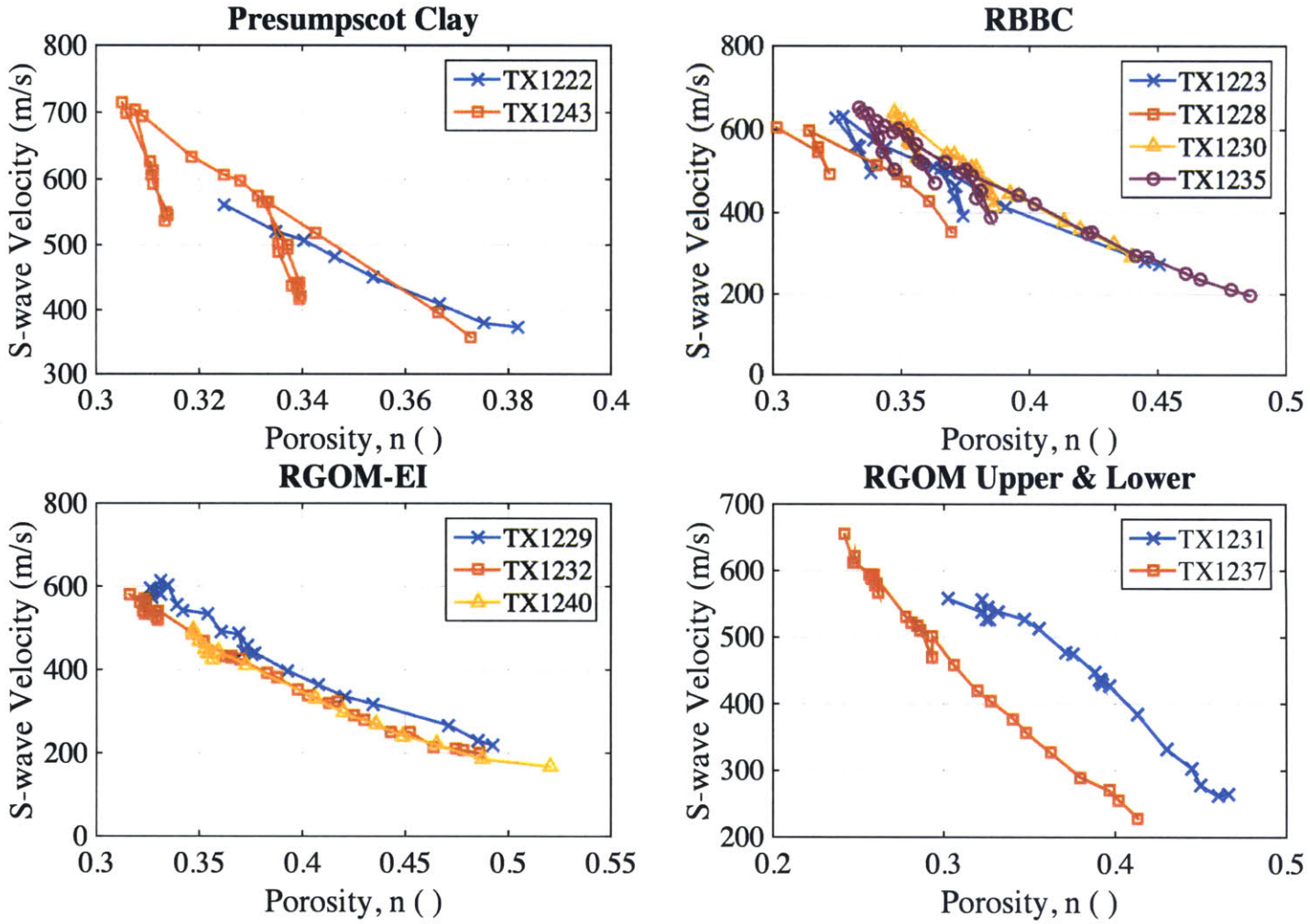

Figure 5-63: The loading and unloading portions of the S-wave velocity-porosity curves for all materials tested. No unloading portion in TX1222 Presumpscot clay

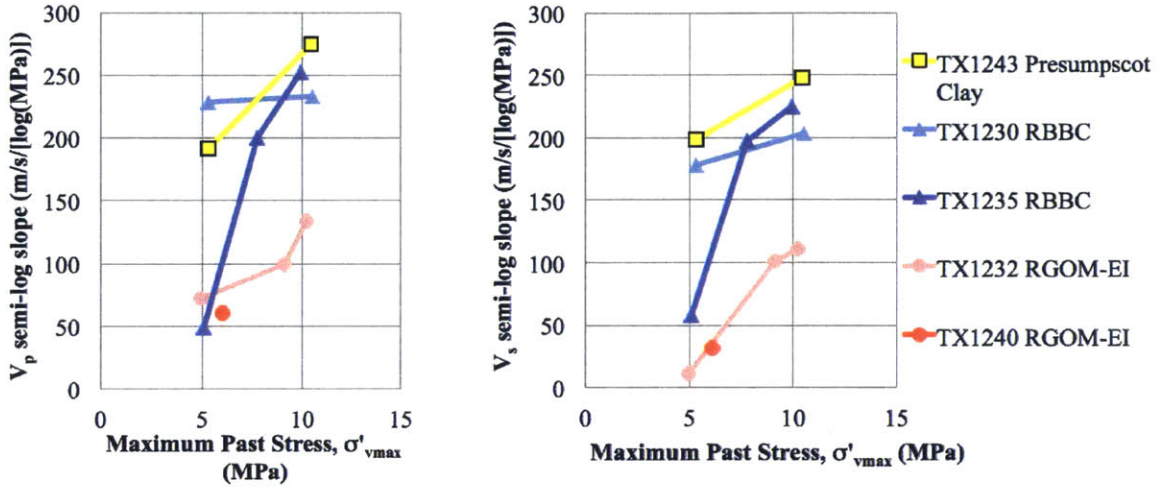

(a) Semi-log slope of V_p

(b) Semi-log slope of V_s

Figure 5-64: The semi-log slope of the unloading curve as a function of the maximum past stress of that unloading cycle

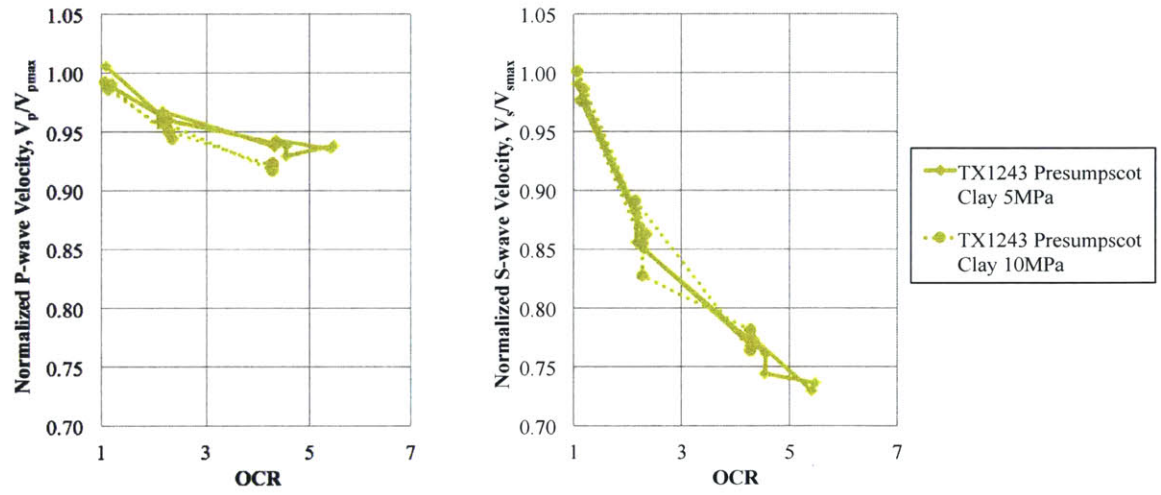

(a) Normalized V_p

(b) Normalized V_s

Figure 5-65: Normalized velocities as a function of OCR for Presumpscot clay. The OCR's and maximum velocity used for normalization is adjusted to account for creep

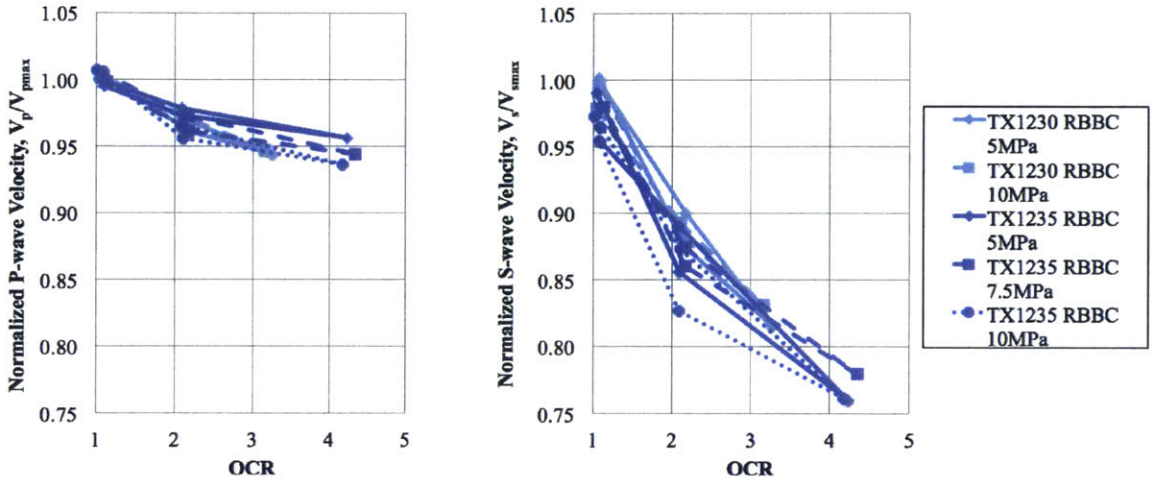

(a) Normalized V_p (b) Normalized V_s

Figure 5-66: Normalized velocities as a function of OCR for RBBC. The OCR's and maximum velocity used for normalization is adjusted to account for creep

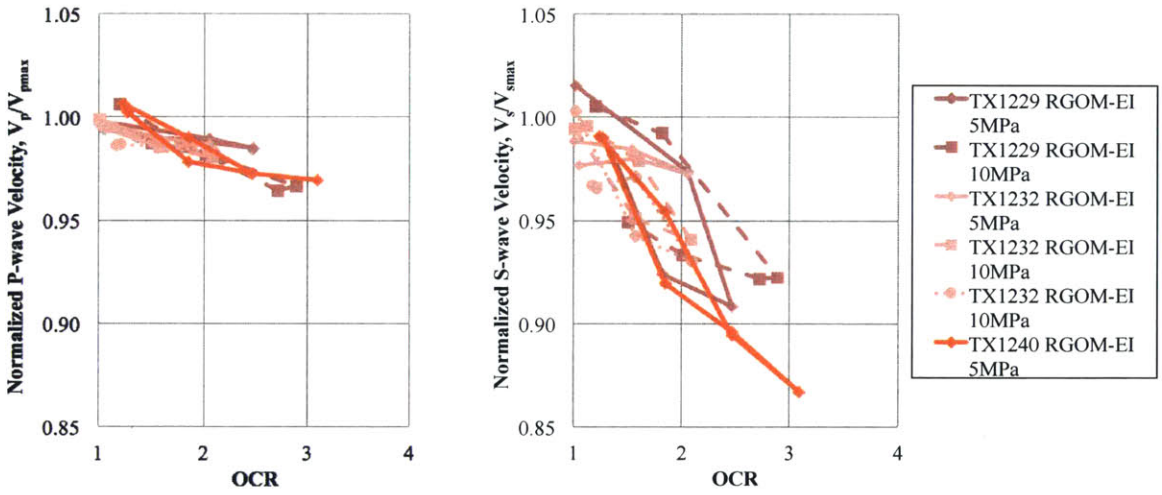

(a) Normalized V_p (b) Normalized V_s

Figure 5-67: Normalized velocities as a function of OCR for RGOM-EI. The OCR's and maximum velocity used for normalization is adjusted to account for creep

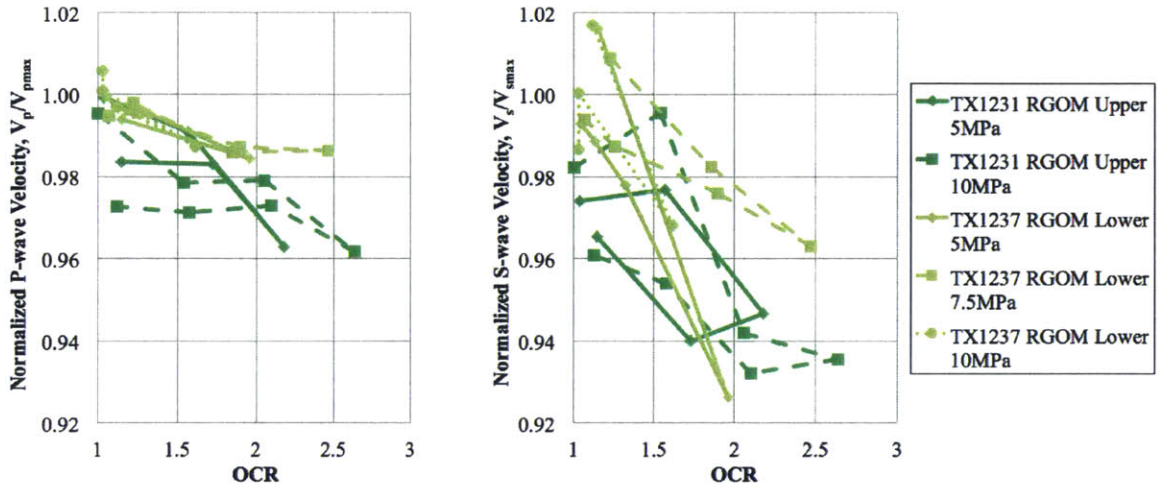

(a) Normalized V_p (b) Normalized V_s

Figure 5-68: Normalized velocities as a function of OCR for RGOM Upper & Lower. The OCR's and maximum velocity used for normalization is adjusted to account for creep

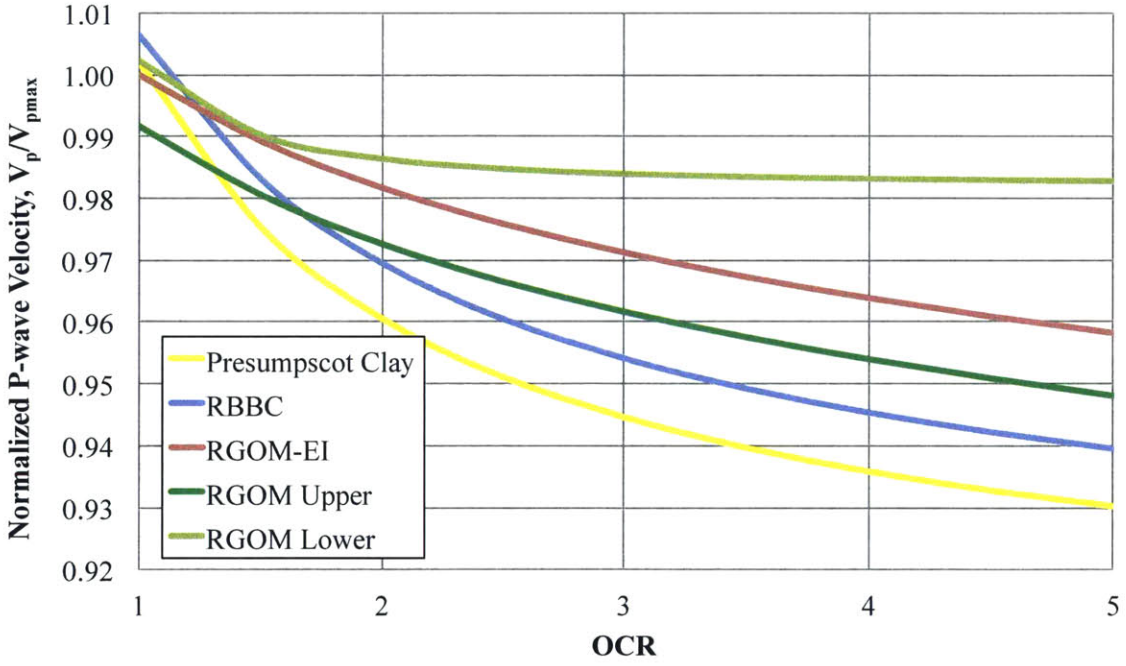

Figure 5-69: The normalized unloading P-wave velocity curves are shown for all the clays. These are best-fit lines intended to describe the general behavior

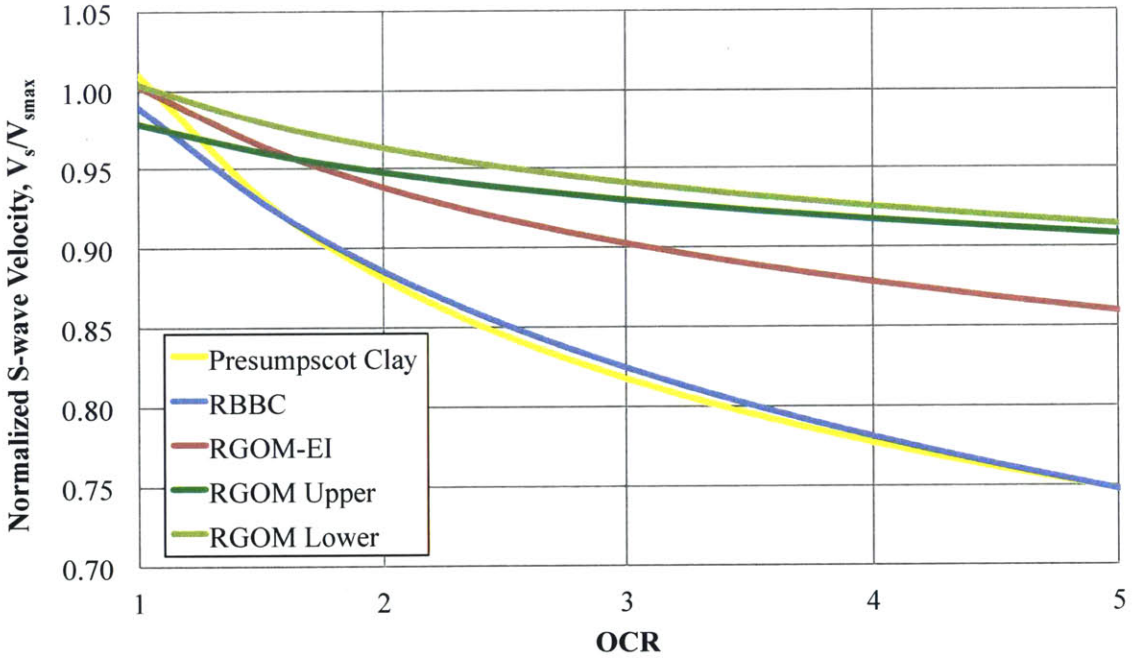

Figure 5-70: The normalized unloading S-wave velocity curves are shown for all the clays. These are best-fit lines intended to describe the general behavior

Chapter 6

Interpretations

6.1 Variables Affecting Velocity Trends

6.1.1 Comparison of Different Technologies

High stress velocity results are presented in Section 5.6. This marks the first effort of collecting a comprehensive stiffness characterization for a single soil over such a wide stress range. The majority of the velocity testing performed on clays is in the low-stress regime (<1.5 MPa) using bender elements, such as ?Flores et al. (2010), ?), ? to name a few. Figure 5-28 presents the low stress regime bender element experiments performed by the author, combined with the medium and high stress piezoelectric measurements. Even the medium and high stress triaxial experiments used completely different setups and transducers, both of which were home-made in their respective labs. Assuming the specimens are taken to be identical since they were all resedimented RBBC samples made at the MIT Geotechnical Lab, the difference in technology has an insignificant impact on the S-wave velocity. The curves for all three experimental setups show impeccable agreement, despite the TXSHELL01 following a stepped incremental loading path. The agreement in the S-wave velocity results is better than the P-wave velocity results, signifying that the S-wave is less sensitive to small differences in experimental setups and stress paths than the P-wave. This is generally seen in this research as well, where the V_p in Figure 5-18 shows more scatter

in the RBBC results than V_s in Figure 5-22. This sensitivity, which is also pointed out in Section 5.3, implies that the S-wave is generally a safer velocity to chose in order to minimize error. One of the explanations could be that a small change in travel time for the P-wave has a much larger impact on the velocity than on the S-wave due to the magnitude of the velocity. Another explanation is that slight differences in pore chemistry (or possible partial saturation) can affect the P-wave velocity, while the S-wave velocity is almost insensitive to this.

6.1.2 Intact versus Resedimented Samples

Although using all resedimented samples would definitively establish a trend of velocity as a function of mineralogy without any unknown factors, having the intact Presumpscot clay introduces some discussions about which kind of predictive method is appropriate for the field. Presumpscot clay seems to be the outlier when looking at the P-wave velocity, in terms of plasticity trend.

Firstly, there is a large discrepancy between the two Presumpscot clay tests, especially when comparing to the consistency of the RBBC and RGOM-EI tests, which overlap each other almost exactly. The inherent heterogeneity between intact field samples is expected, and perfectly exemplified here. The difference in S-wave velocity is almost the same as the P-wave velocity; however, the sample with higher velocity is reversed between the P and S-wave velocity. TX1222 has a lower P-wave but a higher S-wave than TX1243. While the S-wave velocity in terms of porosity corrects the discrepancy between the two Presumpscot clay samples, the P-wave velocity as a function of porosity is not rectified, implying that the S-wave velocity is more dependent on density behavior, while the P-wave velocity is sensitive to some difference in the two samples beyond just the density differences. An explanation could be the mineralogy and pore content. The variability of salinity could account for the difference in V_p. The texture of TX1243 was more granular to the touch, possibly having a higher amount of sand-sized particles, increasing the V_p. Finally, since the source of these samples is above the groundwater table, possible aging effects have occurred, structurally differentiating the two samples.

Another advantage of having the Presumpscot clay samples is the obvious lack of plasticity trend in the P-wave velocity. Although the V_s follows a plasticity trend, the V_p only follows a plasticity trend for the resedimented materials, with the Presumpscot clay being the outlier. If all of the soils were to follow a trend for both P-wave and S-wave, one could have drawn the conclusion that both of these can be used as predictors of mineralogy or clay type. However, the fact the V_p does not follow a plasticity trend, whereas the V_p/V_s ratio and the Poisson's ratio follow a plasticity trend points out that these ratios are a better predictor of clay type than the individual velocity values. Despite the sensitivity of P-wave velocity on small heterogeneities in structure of pore fluid, these differences are diminished when put in terms of V_p/V_s ratio or ν, which validate these parameters as a better representation of the material properties or clay type in the field, and V_s is controlling the V_p/V_s ratio.

6.1.3 Velocity and Plasticity Trend

The trend in S-wave velocity varies consistently with the mineralogy of each soil. The lowest V_s is in the RGOM-EI and RGOM Upper materials, which have the highest smectite content, and the smallest grain size distribution. The highest V_s is found in the Presumpscot clay, which has the largest sized grains, as well as largest amount of quartz, muscovite, and plagiclase content (with low fraction of illite-smectite). Any cementation that may have occurred in Presumpscot clay, although unlikely since the material is compressed to the normally consolidated range, may have increased its V_s, without disturbing the plasticity trend. Ticino sand is even higher than the Presumpscot clay, with the sand having a significantly higher mean grain size, and no clay content. The high smectite materials have the largest double layers, causing a reduction in the mineral to mineral contacts, thus the V_s is expected to be the lowest in these materials for a given stress, since shear stiffness is dominated by grain contact interaction. It seems as though the S-wave signal is more sensitive to K_0 than the P-wave, shown by TX1228 in Figures 5-32 and 5-33, which has an anomolously low K_0. This low K_0 results in a lower S-wave velocity at the same σ'_v. This implies a strong dependence of the V_s on the grain contact stress.

There is no clear trend in the P-wave velocity based on mineralogy. Although the resedimented materials follow a plasticity trend, Presumpscot clay is an outlier. Observing only the resedimented materials, one can conclude that there is a dependence on salinity. It could either be directly proportional to the difference in stiffness associated in different salinity water, or it could be explained by the structural formation of the material during deposition due to the salt content. Higher salinity is conducive to flocculation. As more floccs are formed via van der Waals forces, better transfer of the P-wave is possible, or in other words, floccs have a higher bulk modulus than the individual particles surrounded by water. Since patchiness in water distribution was shown to affect P-wave velocity (Knight et al., 1998), it is reasonable to assume clustering of particles could also have an effect.

Large double layers in smectite minerals create a more parallel plate orientation, as supported by the March model (Figure 2-25). Section 5.5 mentions that the salinity effect on the RGOM-EI double layer is large, over the span of 1 - 256 g/L. The actual salinity of RGOM-EI is approximately 90 g/L, which means that although the salinity has decreased the size of the double layer, it is still large enough to impact the microstructure, falling in the lower side of the affected salinity range. The flocculated state of the slurry eventually corresponds to a more tight packing of the particles.

The relative location of the Presumpscot clay samples might be related to the depositional history of the material, or merely the content of the intact samples. A higher sand content in the Presumpscot clay would explain its shift in V_p, moving it much closer to the Ticino sand P-wave results.

Pore size distribution can also be a driving factor. At low stress (0.2 MPa), RGOM-EI has a smaller pore size than RBBC (350 v. 550 nm, respectively) for the pores larger than 35 nm, i.e. the macro-scale pores. As stress increases, the macro-scale pore size in RGOM-EI slightly decreases while RBBC pore size significantly decreases. This analysis does not account for the behavior in the micro-scale intra-particle pore size (< 35 nm), which comprises over 50% of the porosity. It is currently inconclusive how the pore size evolution contributes to velocity measurements as a function of stress, since there does not seem to be a significant shift in the curvature

of RBBC versus RGOM-EI as a function of stress.

In general, it appears that the S-wave is more dependent on particle contacts (easily explained by the mineralogy and double layer interaction), while the P-wave velocity is more sensitive to the pore fluid composition and structural deposition during formation. Some individual factors, such as in-situ heterogeneities or salinity, can affect the trends seen in the individual P and S-wave velocities; however, when the results are observed in terms of V_p/V_s ratio, there is a distinct plasticity trend that corrects for these extraneous factors. Therefore a model is developed that predicts V_p/V_s as a function of stress for different liquid limit inputs. Liquid limit is shown to correlate well with the results, however plasticity index could equivalently be used for this analysis. Much like the compression behavior, the V_p/V_s seems to converge at high stresses, indicating all clays exhibit similar behavior at high stress regardless of their composition.

6.1.4 Frequency Behavior

Figures 5-29 and 5-30 showed that the P-wave frequency response is consistent over the stress range tested, while the S-wave frequency response is both stress and plasticity dependent. There are two ways in which one can interpret these results. Either the frequency results are indicative of the dispersion qualities of the soil, altering the frequency of the propogating signal based on soil properties, *or* the frequency response is simply a function of the charging and dissipation of the piezoceramic elements that behave like capacitors. In the author's opinion, the later is a more reasonable explanation to the frequency response.

The increase in frequency response with stress is an artifact of increasing stiffness of the soil. As higher stresses are applied on the specimen, a higher stress is also directly applied to the peizeoceramic element. As the stress on the piezoceramic increases, the capacitance decreases (Cho and Mandai, 1995). The charge time required to activate the piezo material decreases as the stress increases, and frequency increases. This behavior can be seen in the rise time of the input signal for different stress levels, as seen in Figure 6-1. The rise time generally decreases as stress

increases, although the P-wave response does not necessarily follow this trend, much like the P-wave frequency response in Figure 5-29. The piezoceramic charges up (like a capacitor) at a faster rate when higher stress is applied, explaining the increase in frequency as a function of stress.

The frequency response increases until it reaches a critical limit, dictated by the material properties, applied voltage, and geometry of the piezo material. This is believed to have happened in Figure 5-29, where all the clay values have plateaued and occupy a band between 100 - 180 kHz. The increasing trend of frequency with stress seen for the dry Ticino sand P-wave is due to the fact that the upper limit has not been reached. Once it reaches that maximum value, it will likely behave like the other materials. On the other hand, the S-wave frequency response increases with stress for all the soils since the upper boundary for the reaction of the piezoceramic has not been reached. A different plateau would be expected for the P and S-wave frequency response since they are different elements with different capacitances. The relative ordering of the frequency trend in the S-wave response is directly proportional to the stiffness of the materials. The different stiffnesses affect the charging and discharging rate of the piezeceramic.

Additionally, the author's experience with bender elements indicates that if a lower frequency pulse is used to excite the bender element piezeoceramic, the received signal (after it has passed through the soil), has the same characteristic frequency as the input pulse. However once the maximum operable frequency of the bender element is reached, which occurred around 10-14 kHz, the response would be at the resonant frequency of the bender element (10-14 kHz), even if >20 kHz input pulse is sent to the bender element. Once the critical frequency is reached, the bender element cannot physically respond any faster. The velocity is shown to be independent of input frequency.

Finally, in order to validate this theory, the frequency response of the tests ran at Shell are inspected. The experimental setup at Shell is entirely different from that MIT. The Shell transducers are different geometries, capacitances, and slightly different types of piezoceramics. Even the input frequency was different – MIT used a

low frequency (<10 kHz) step function with the down-step of the function occurring much later than the arrival of the signal, while Shell used a high frequency input pulse (1MHz). If the frequency response were material-dependent, the high stress Shell frequency response would follow the same trend as the medium stress frequency results in Figure 5-29 and 5-30; however, this is not the case, as shown in Figure 6-2 and 6-3. The P-wave frequency response for the high stress test (TXSHELL01) are higher than the band of frequencies seen in the medium stress triaxial results (beyond 180kHz), and they seem to be decreasing. This implies that the Shell piezoceramic element has a different plateau than the MIT peizocermaics, and that once the plateau has been surpassed, the response time might even begin to diminish, indicated by the decreasing slope. It is not certain, however, whether this decreasing slope is a valid frequency behavior or merely scatter in the data. Similarly for the S-wave frequency response, the TXSHELL01 results still show a trend of increasing frequency with stress (due to the increasing stiffness), however it is completely different, in both slope and intercept, from the RBBC results measured by the equipment at MIT. This difference implies that the frequency response is dependent on the piezoceramic transducer rather than the material being tested. Furthermore, the velocity results agree with each other perfectly between the medium and high stress setups, validating that the velocity is independent of frequency.

6.1.5 Creep Behavior

When unloading is desired, equilibration is needed at a single stress state, incurring creep. Allowing creep or secondary compression to occur and accounting for its effects on the stress state are crucial to the velocity interpretation. Few studies have looked at the unloading behavior of cohesive soils in depth. The challenge with unloading is derived from the need to equilibrate the sample, allowing the creep rate to decay significantly. A few studies, including Lohani et al. (2001) and Shibuya (2000) have measured creep, however, their scope is limited. They measured the shear modulus using bender elements, and their tests were performed in an oedometer cell, where side-wall friction can affect the distribution of stresses within the specimen. Their

research presented the creep effects in low and high smectite clays, and Shibuya (2000) accounted for creep in the S term (a material constant) in a Hardin-type equation similar to Equation 2.15, while Lohani et al. (2001) came up with an N_G term, as described in Section 5.9.

Creep is associated with particle reorientation, densification, and an outward shift of the yield surface. There are two ways in which creep can be accounted for. The first is by extrapolating the compression curve to a new stress, as described in Section 5.9. The velocity data point is then presumed to be at that new stress level. The other method by taking the new extrapolated stress, and calculating an OCR for the velocity data point, effectively regarding it as an overconsolidated state. The first method is selected for this research.

Another complication lies in the characterization of the OCR for the unloading points. Since the specimen has effectively experienced a higher stress due to creep, the unloading points need to be referenced to the new maximum stress based on the extrapolation, referred to as apparent preconsolidation, rather than the actual applied stress. This step is crucial in describing the stress state and the ability to fit an equation to the unloading data, as is done in Section 6.2.

6.1.6 Unloading Behavior

The unloading cycles performed in this research disproved the feasibility of using velocity-density or velocity-porosity crossplots to identify overpressure and lithology for high plasticity clays; however, distinction for low plasticity clays may still be possible. For high plasticity clays, the reduction in stiffness is very small compared to the low plasticity clays. Although some experimental issues were experienced during the unloading cycles, the results are sufficient to determine that the amount of stiffness change during unloading for a constant maximum past stress and OCR varies dramatically. The compression behavior during unloading, when looking in semilog-space, is the same irrespective of maximum past stress, supported by the consistent value of C_s for different unloading cycles (Reference Table A.1). The equivalent slope of velocity in terms of log-σ'_v is clearly affected by the maximum past stress, shown

by the increasing slope as a function of stress in Figure 5-64, and seems to follow a plasticity trend. The compression behavior versus velocity behavior is unlinked by some other factor. The exact nature of this unlinking factor is not currently known, but it could include pore structure or the evolution of particle contact stress.

Although this research has commenced the population of unloading velocity behavior in clays, the scope of unloading presented is very limited. Some of the experiments (in particular the RGOM Upper and Lower) experienced instability during the unloading portion. The equilibration time for these tests was likely insufficient. The importance of allowing equilibration is clear from the difference in C_s between TX1232 and TX1240, where TX1240 was given more time for equilibration. Low smectite, high permeability materials like RBBC and Presumpscot are far less sensitive to the equilibration time. Despite this shortcoming, there is still a clear plasticity trend in the unloading behavior, with high plasticity clays having minimal stiffness change during unloading while low plasticity clays have significant change.

6.2 Methods of Fitting Trends to Data

Many attempts at fitting equations to experimental data have been attempted by various authors, some of which are described in Section 2.9. Rampello et al. (1997) noted that when describing the shear stiffness of a soil under isotropic stress conditions, one term out of OCR, e and σ'_m can be neglected, due to redundancy. When it comes to the behavior under K_0-consolidation, this is not the case. The following sections discuss the experimental results in Chapter 5, and which parameters seem to be dominating the velocity behavior. Rather than exhaustively attempt to apply all types of equations to this research, a select few are used in the following sections, primarily focusing on those that account for the unloading portion.

6.2.1 Hardin & Blandford equation

Hardin and Blandford (1989) created an equation that describes the shear modulus as a function of void ratio, OCR, and stress (Equation 2.16). This form of equation

is discussed in Section 2.9 and will not be repeated here. Using the same form of equation as Santagata (1998) in Equations 2.11 and 2.12, the following equations for shear modulus are fitted for all the soils tested in order to obtain the fitting parameters a, b, and c:

$$G = a \times e^b \times \sigma_v'^c \quad (MPa) \tag{6.1}$$

$$G = a \times OCR^b \times \sigma_m'^c \quad (MPa) \tag{6.2}$$

where e is the void ratio, OCR is overconsolidation ratio, σ_v' is vertical effective stress, and σ_m' is mean effective stress. The same equations with different fitting parameters are used for bulk modulus (K). The fitting parameters needed for each soil tested for G and K are listed in Tables 6.1 through 6.4. These tables provide a modulus value in GPa rather than MPa. In general the R^2 value is better when using Equation 6.2, which uses OCR and mean effective stress. To investigate how well the fitting parameters predict modulus values, three tests are selected: Presumpscot clay (which has about equal R^2 values for the two methods), RBBC (which has better R^2 values Equation 6.2), and RGOM Lower (which has better R^2 values Equation 6.1). Plotting the data and prediction in Figure 6-4 for Presumpscot clay shows that both have exceptional agreement with the measured data points. Figure 6-5 shows that Equation 6.2 agrees better with the experimental data, and finally Figure 6-6 shows Equation 6.1 has better agreement, as expected by the R^2 values. Overall, the suggestion is to use Equation 6.2 to capture the loading and unloading behavior of the soils tested, since it captures the K_0 effect in the mean effective stress term, and includes both the maximum past stress and present stress effects. The void ratio term in Equation 6.1 cannot effectively capture the stiffness behavior of the soil, indicating once again an unlinking between the compression curve unloading behavior and the velocity unloading behavior.

6.2.2 Bowers Method

Bowers (1995) suggested an equation of the following form to describe the P-wave velocity in overpressured rocks:

$$V_p = C + A(\sigma'_{max}(\frac{\sigma'}{\sigma'_{max}})^{\frac{1}{U}})^B \tag{6.3}$$

where A, B, and C are fitting parameters, and Bowers (1995) assumes $C = 5000ft/s$ in all cases. U is a fitting parameter for the unloading portion. σ'_{max} is the maximum past stress, and σ' is the current effective stress. U is referenced by Bowers (1995) as typically being between 3 - 8, with $U = 1$ being a perfectly elastic unloading, and $U = \infty$ being a perfectly plastic unloading. Using Equation 6.3, the A, B, and C parameters obtained for an optimal fit are listed in Table 6.5. Different U's are fitted for the different unloading cycles, as signified by the subscript. The curves based on Table 6.5 are compared to a set of measured data points in Figure 6-7. Since the fitting parameters for RBBC and RGOM-EI are based on multiple tests, the fit does not exactly match the solid data points in Figure 6-7, while Presumpscot clay, RGOM Upper, and RGOM Lower are based on a single test.

The fitting parameters in Table 6.5 are indicative of a few shortcomings of this fitting type. Although the normally consolidated portion is fit nicely by the equation of the form $V_p = C + A\sigma_v'^B$, the unloading portion is dependent on a U parameter that changes as a function of stress. Small changes in U can significantly impact the unloading portion, thus using a single U is not appropriate. Furthermore, the typical range for U suggested by Bowers (1995) does not encompass the U's used to fit some of the clays in this research. The equation, although can be used to describe the velocity behavior if all the parameters are known, cannot be used as a predictive equation. Even the A, B, and C parameters vary greatly between the clay types, thus generalizing these constants would create unacceptable fits.

6.2.3 Summary

The list of different types of fits to the data is exhaustive. The two methods above are chosen for their ability to characterize the unloading portion of the velocity trend. Among all the other possible methods available, work done by Kawaguchi and Tanaka (2008) should be mentioned due to its use of the liquid limit, which has shown to be a determining factor in the velocity trends in this thesis. Their work used a permutation of Equation 6.2, and rather than have a single a term as a material coefficient, they incorporated the liquid limit (w_L) in the equation, which is a logical improvement to the ambiguous a parameter. Their equations do not accurately predict the behavior of the soils tested in this research, but rather over-predicted the shear modulus by over 20% for RGOM-EI and over 50% for RBBC.

Based on the equations used to describe the velocity data, the author recommends using a form closer to the Hardin-type equation that incorporates σ'_m (Equation 6.2). Overall, it is shown to have better agreement with the data, and accounts for the K_0 behavior. Since the scatter in void ratio tends to be relatively high compared to stress, it introduces further error. Although it is an important parameter, it generally has less success in describing the velocity behavior. Incorporating the liquid limit is also a feasible improvement to the current state of the equation.

6.3 Results Compared to Hashin-Schtrickman Bounds

One of the most famous effective media models is the Hashin-Shtrikman bounds (HS bounds), which predicts an elastic modulus based on the volume fractions and elastic moduli of the two constituents. The equations are as follows:

$$K^{HS\pm} = K_1 + \frac{f_2}{\frac{1}{(K_2-K_1)} + \frac{f_1}{(K_1+\frac{4}{3}G_1)}} \tag{6.4}$$

$$G^{HS\pm} = G_1 + \frac{f_2}{\frac{1}{(G_2-G_1)} + \frac{2f_1(K_1+2G_1)}{5G_1(K_1+\frac{4}{3}G_1)}} \tag{6.5}$$

where K is the bulk modulus, G is the shear modulus, and f is the volume fraction of each constituent (i.e. the porosity). The subscripts 1 and 2 indicate the constituents. Assigning the stiffer material as 1 produces the upper bound, while using the softer material for the terms with subscript 1 produces the lower bound. The HS bounds are applied to the materials tested in this research by assuming the soft constituent is the pore water, while the hard constituent is the aggregate modulus of the mineral composition of the clays, based on the XRD analysis[1]. The resulting aggregate elastic modulus values for each soil are listed in Table 3.3[2]. These values are effectively the Voigt upper bound without water. The effect of salinity on the modulus values is considered. Figure 6-8 and 6-9 show the bulk modulus upper and lower bounds (dashed lines), as well as one representative test for each material. The HS upper bound for K is the largest for Presumpscot clay, dominated by almost 40% quartz fraction and large portion of plagiclase and muscovite. On the other hand, RGOM-EI with the lowest HS upper bound. Furthermore, based on the HS bounds, RBBC has the widest bounds, while RGOM-EI has the narrowest bounds for K. The measured velocity-derived K lies much closer to the lower bound than the upper bound. Although the lower bound dashed lines in Figure 6-9 do not follow the same trend that the experimental data does, as far as position of the modulus curves relative to each other, the measured K is always higher than the calculated lower bound K.

Figure 6-10 shows the shear modulus measured values and the HS upper bound. The lower bound is zero since the soft constituent (salt water) is assumed to have $G = 0$. The measured G values are much lower than the HS upper bound. For comparison, Figure 5-24 can be referenced for a zoomed in version of the measured shear modulus curves. Once again, much like the HS K upper bound, Presumpscot clay has the highest upper bound for G. The trend of the HS upper bounds more closely follows the trend of the measured data, with Presumpscot having the highest measured G and RGOM-EI/RGOM Upper with the lowest measured G.

In summary, the HS upper bounds severely overestimate the measured elastic

[1]The XRD provides a bulk mineralogy (weight %) by RIR (Reference intensity Ratio) Method
[2]Modulus values for each mineral component is taken from Mavko et al. (2003), Wei (2009), and Zhou et al. (2011)

modulus values in this research. The lower bound is a better method of predicting the bulk modulus; however, it does not provide an accurate trend of modulus curves as a function of plasticity. The assumption of computing a grain K and G based on the XRD data might be affecting the success of the HS bounds. Additionally, the HS bounds are intended for isotropic, linear elastic materials, and although they have had success in rocks, applying it to clays is inappropriate. Especially since the HS bounds were derived for spherical particles rather than platey and flat clay particles. Although HS method is unsuccessful in predicting K and G, it is chosen since it has a narrower range than the Voigt Upper Bound and Reuss Lower Bound. The Voigt-Reuss-Hill average is also unable to accurately predict the elastic moduli of clay, tending to overestimate it by 70 - 120%.

6.4 Results Compared to Other Published Data

6.4.1 Comparing Lab to Field Data

As previously described in Chapter 3, the material used to make RGOM-EI specimens is a mixture of the material extracted from two wells (A-12 and A-20ST2) in the Gulf of Mexico. After the core was extracted from these two wells, a wireline logging tool took velocity measurement inside well A-20ST2. While the wireline velocity measurements are interesting to compare to this research's laboratory data, there are a number of differences between the measurement techniques that could cause differences in the results. When velocity measurements are taken in the field, the sonic logging tools typically have a depth of investigation of 0.8 ft and a vertical resolution of 6 ft. The depth of investigation is the increment of reading, while the vertical resolution is the distance over which the reading is averaged. The logging tool reports an average reading over the depth specified by the vertical resolution, thus depending on which index point the average velocity value was taken, a shift in the data could be present. Furthermore, the coring process can disturb the soil near the borehole, thus it is unclear how much the velocity measurements could be compromised with

both mechanical and chemical (i.e. drilling fluid fingering) disturbances. Despite these possible differences, the results from the wireline log in well A-20ST2 are plotted next to the laboratory-obtained velocity results from this research (TX1229) in Figure 6-11. While the slopes seem to be different, the results are generally in the same range, which is very encouraging. The largest differences between the two occurs at low stresses; however, the data below 2 MPa for the log data is usually prone to error and would normally be disregarded, as it is dominated by the drilling fluid effects. Moreover, there is possible lithification and other chemical weathering that may have occurred in the well, not to mention that the resedimentation powder is a heterogeneous mix of both wells rather than just the well in which the wireline log is taken. When this is taken into account, the two results match up extremely well.

Fortunately, in addition to the logging data, the two cores were sectioned off and some of the intact material was tested, while the rest of it was ground and processed into material to be used for resedimentation. The location of these two samples is marked by hollow circles in Figure 3-10. The intact core from both wells was processed and tested by Stump and Flemings (2002). The velocity testing on the cores was performed over a wide stress range, but only the data points above the preconsolidation stress (thus entering the normally-consolidated region) are presented in Figure 6-11. The measured K_0 values for these two tests are 0.86 and 0.85 for well A-12 and A-20ST2, respectively. The velocity results from this research, whose RGOM material is a mixture of wells A-12 and A-20ST2, falls between the laboratory tests on the intact samples from the two different wells. Furthermore, when comparing the log data for well A-20ST2 and the core data for well A-20ST2 obtained from Stump and Flemings (2002), the two profiles do not align. In fact, the profile of the laboratory-tested intact core matches up better with the results from this research (TX1229). This could indicate one of two possibilities – 1) the log data has been disturbed and is much more prone to error caused by the resolution, disturbance, etc. or 2) the curvature of the laboratory tests match up better because they are in the normally consolidated region, whereas the in-situ measurements are of overconsolidated material. Finally, it should be noted that the density affect is neglected in this comparison, which could

also be causing differences in velocity results.

6.4.2 Clay

As mentioned in Section 2.6, there are two primary means of obtaining stiffness moduli of soils using a triaxial apparatus. The first is directly measuring the stress-strain behavior based on a specimen-mounted yolk system such as Santagata (1998). The second is a typical undrained compression test (CK_0UC) where the strains are externally measured.

The method used by Santagata (1998) is explained in Section 2.6. She tested RBBC and developed an empirical equation to describe the behavior in Equation 2.12. The equation for the Young's modulus is compared to the experimental velocity results in this research – the V_p and V_s can be used to calculate E. The results presented are in Figure 6-12, with a zoomed-in version to accentuate the low stress behavior in Figure 6-13. The second method, undrained shear via external strain measurements, was performed by Casey (2014) and Abdulhadi (2009) for Presumpscot clay and RBBC, respectively. The data points from Casey (2014) and Abdulhadi (2009) are discrete experimental data points at particular stress levels. Two strain levels are included for the results obtained by Casey (2014); however, the lower strain level (0.005%), is below the usual resolution of the test and can be unstable. The two strain levels presented by Casey's (2014) data show the stiffness reduction attributed to increased strain.

Overall the trends seem to tell a consistent story. The velocity-derived Young's modulus is expected to yield the highest stiffness parameters, since this test method exhibits the smallest strain levels and is elastic behavior. The Presumpscot clay results from Casey (2014) underestimate E relative to the velocity-derived E. The RBBC results measured by Abdulhadi (2009) also underestimate E, as is expected by the large strains encountered. The results from Santagata (1998) match the velocity-derived E very well at low stresses; however, the dashed line at high stresses (which is extrapolated beyond the scope of her research) overestimates the Young's modulus. The agreement between Santagata (1998) and velocity-derived E is encouraging and

validates that Santagata's results are in the small-strain linear region that yields the elastic response. The large discrepancy in strain levels between Abdulhadi (2009) and Santagata (1998)can explain the relative position of their results, as strain softening occurs, even though the same experiment is performed. Furthermore, Santagata's strain measurement techniques are far more precise, with higher resolution. Since all the triaxial measurements are undrained, they compare much better to the velocity-derived results than the drained CRS tests discussed in the following section.

6.4.3 Sand

Chapter 2 discusses some velocity measurements on sand. Most notably Prasad (2002) and Zimmer (2003) looked at the V_p/V_s ratio as a function of stress for sands of different grain sizes. Both of them found that sorting had a negligible effect on velocity. Zimmer (2003) did not provide a best fit line for his data; however, the approximate mean V_p/V_s ratio is taken from his graphs and plotted onto the V_p/V_s ratio log-log graph from Chapter 5, and is presented in Figure 6-14. Additionally, Prasad (2002) came up with a best-fit equation to describe her sand results ($V_p/V_s = 5.6014\sigma_v'^{0.2742}$), which is also plotted on the figure. While Zimmer's data matches closely with the Ticino sand results, Prasad's data is higher and overlaps with the clay results.

6.5 Mechanical- versus Velocity-Derived Modulus

6.5.1 CRS consolidation results

A Constant Rate of Strain (CRS) Test is a common geotechnical experiment that measures permeability by applying a vertical stress to a specimen confined in a metal cylinder, thus only vertical strain occurs. The constrained modulus (M) can be calculated from the CRS results by dividing the change in stress by the change in strain (Wissa et al., 1971, Janbu, 1965). Thus the slopes of the curves in Figure 6-15 can

be used to calculate the constrained modulus,

$$M_{soil} = \frac{\Delta\sigma'_v}{\Delta\varepsilon_v} \tag{6.6}$$

were $\Delta\varepsilon_v$ is the axial strain during a CRS test. The constrained modulus values are seen in Figure 6-16 and 6-17. The M values of all the soils are increasing with a concave upward shape, except for the Presumpscot clay, which is following the converse trend. At first glance, it becomes clear that the M values obtained from the CRS tests are *much* lower than those obtained from measured velocity data (Figure 5-23), by almost a factor of 50. The immediate answer that accounts for the difference is that the P-wave velocity is predominantly controlled by the water, thus is measuring the "wet" constrained modulus, rather than the "dry" constrained modulus of the soil skeleton that the CRS test is measuring. This may account for most of the discrepancy between the two methods; however, whether this is the only factor needs further analysis. A Gassmann fluid substitution is performed to investigate whether using the "dry" CRS modulus can be used to infer a "wet" constrained modulus in the following section.

6.5.2 Use of Gassmann Equation for Dry Clay Interpretations

To use the Gassmann fluid substitution (Equation 2.32), the shear and bulk modulus of both the solid and liquid phase is needed. The XRD analysis was used to calculate the stiffness parameters of the "grains" of each of the soils. The XRD provides a bulk mineralogy (weight %) by RIR (Reference intensity Ratio) Method. Using the percentages listed in Table 3.3, and commonly accepted bulk and shear modulus values for each component, a weighted-average K, M, and G were calculated in Table 6.6. Equation 2.3 was used to obtain the M. These values would be the theoretical value of a zero-porosity material, thus is expected to be much higher than anything that could be measured. It is convenient to compare these values to the measured composite moduli based on the velocity measurements, even though the composite moduli include fluid, while the calculated values in Table 6.6 do not.

For calculating the "wet" bulk modulus based on the CRS test results, the following steps are taken:

- The dry M calculated from the CRS test is converted to a dry K using Equation 2.3. Since in theory, $G_{dry} = G_{sat}$ (Gassmann, 1951a), the G based on velocity measurements is used in the equation
- The grain bulk densities are calculated for each soil as prescribed in the previous paragraph
- The Gassmann equation is applied using the bulk modulus of salt water and the grain bulk modulus listed in Table 6.6

Even with the fluid substitution, the saturated K based on the CRS results is significantly lower than the measured velocity-derived K, and is even lower than the calculated Hashin-Schtrickman lower bound. The reasoning for this large difference can be explained by examining the type of constrained modulus, M, obtained from the CRS test. It is commonly understood that the stiffness during the loading portion of a compression curve is much softer than the stiffness during the unloading portion (Miller et al., 2013). The unloading portion is a quasi-elastic behavior, while the loading portion is a plastic behavior. Hence when the CRS constrained modulus was taken from the slope of the loading portion, this provided the "plastic" modulus rather than the "elastic" modulus, which is obtained from the velocity values. Therefore to have more reasonable values of K based on the CRS test results, the *unloading* portion of the stress-strain curve should be taken. Zimmer (2003) notes that "upon unloading, the static modulus values approach or exceed the dynamic modulus on the first unloading step, and then drop back down below the dynamic modulus with continued unloading". Unfortunately, there are insufficient CRS tests that contain an unloading portion in order to perform this analysis for the unloading portion, thus another approach is taken. Since the unloading portion is unavailable, we use the M from the loading portion, and multiply it by a factor X, assuming the X factor is the multiplier between the loading and unloading stiffness. Although it is

understood that the X factor would not be a constant value over the entire stress range, a single value is taken for now, in an attempt to see whether reasonable X factors can be back-calculate to produce good agreement between the CRS-derived K and the velocity-derived K. The X factors used to achieve the best fit are listed in Table 6.7, and the respective curves are shown in Figure 6-18. As can be seen based on the Figure, the X factor underestimates the CRS-obtained K at the low stresses, and overestimates at the high stresses. This would correspond to higher values of X factors at low stress, and lower values at high stress.

To evaluate whether this inferred X factor is reasonable, an analysis is performed on four CRS tests performed by Adams (2011) on RBBC. Each of the CRS tests have at least one unloading cycle, up to a max of three unloading cycles. The X factor (the ratio of unloading to loading M) is presented in Figure 6-19. Although there is considerable scatter, a trend line is fitted to the data. This varying X factor is used in lieu of the constant inferred X factor that was presented in Table 6.7. Using the varying X factor on the CRS-derived Gassmann fluid substitution, the new result is seen in Figure 6-20. This figure includes the original velocity-derived K, the line for the inferred constant X factor that achieved the best fit, and finally the new K calculated with the varying X factor. The varying X factor creates a line that fits exceptionally well with the velocity-derived data. Based on this figure, the inferred X factor seems to yield a line that fits reasonably well with the velocity-derived K curve. Although the single inferred X factor should not be ubiquitously used for any test, it seems to provide a reasonably accurate prediction of the bulk modulus in the 1 - 10 MPa stress range, as verified by the RBBC curves in Figure 6-20. Finally, the X factor trend in the RBBC is a subjective trend. The exponential fit is selected since it provides with the best fit to the velocity-derived K; however, it has not been rigorously proven that such a trend is expected.

Table 6.1: The fitting parameters for the Hardin-type equation (Equation 6.1) for shear modulus (G). The average values are taken for multiple tests. R^2 values are provided. NOTE: input stresses are in MPa, but resulting G is in GPa

	Presumpscot Clay	RBBC	RGOM-EI	RGOM Upper	RGOM Lower
a	0.102	0.184	0.084	0.151	0.063
b	-2.01	-0.80	-2.56	-1.58	-2.26
c	0.31	0.42	0.12	0.16	0.06
R^2	0.994	0.929	0.969	0.941	0.994

Table 6.2: The fitting parameters for the Hardin-type equation (Equation 6.1) for bulk modulus (K). The average values are taken for multiple tests. R^2 values are provided. NOTE: input stresses are in MPa, but resulting K is in GPa

	Presumpscot Clay	RBBC	RGOM-EI	RGOM Upper	RGOM Lower
a	4.457	4.913	5.676	5.446	4.993
b	-0.71	-0.41	-0.57	-0.47	-0.50
c	0.05	0.07	0.04	0.05	0.02
R^2	0.981	0.920	0.978	0.977	0.997

Table 6.3: The fitting parameters for the Hardin-type equation (Equation 6.2) for shear modulus (G). The average values are taken for multiple tests. R^2 values are provided. NOTE: input stresses are in MPa, but resulting G is in GPa

	Presumpscot Clay	RBBC	RGOM-EI	RGOM Upper	RGOM Lower
a	0.300	0.208	0.157	0.131	0.134
b	0.16	0.24	0.44	0.55	0.60
c	0.67	0.73	0.72	0.84	0.87
R^2	0.993	0.985	0.987	0.989	0.985

Table 6.4: The fitting parameters for the Hardin-type equation (Equation 6.2) for bulk modulus (K). The average values are taken for multiple tests. R^2 values are provided. NOTE: input stresses are in MPa, but resulting K is in GPa

	Presumpscot Clay	RBBC	RGOM-EI	RGOM Upper	RGOM Lower
a	6.361	5.564	6.574	5.714	6.064
b	0.07	0.06	0.10	0.12	0.12
c	0.18	0.16	0.17	0.20	0.19
R^2	0.980	0.887	0.985	0.933	0.986

Table 6.5: The fitting parameters for the Bowers-type equation (Equation 6.3). The average values are taken for multiple tests

	Presumpscot Clay	RBBC	RGOM-EI	RGOM Upper	RGOM Lower
A (m/s)	130.6	160.2	272.2	65.9	176.2
B	0.5761	0.483	0.3746	0.8231	0.4985
C (m/s)	1680	1510	1527	1689	1571
U_{5MPa}	1.9	2.355	4.03	3.3	8
$U_{7.5MPa}$		2.95	4.39		7.45
U_{10MPa}	2	2.45	4.64	4.46	9

Table 6.6: Calculated moduli values based on a weighted-average of each component of the soil, based on the XRD data in Table 3.3

	Bulk Modulus, K (GPa)	Constrained Modulus, M (GPa)	Shear Modulus, G (GPa)
RPC	65.5	115.7	37.6
RBBC	59.4	101.6	31.7
RGOM-EI	37.6	71.5	25.5
RGOM Upper	41.8	76.1	25.7
RGOM Lower	43.5	83.4	29.9

Table 6.7: X factor used to account for different in the velocity-derived wet modulus and dry CRS modulus

	X factor
RPC	21.0
RBBC	14.6
RGOM-EI	27.8
RGOM Upper	22.3
RGOM Lower	11.0

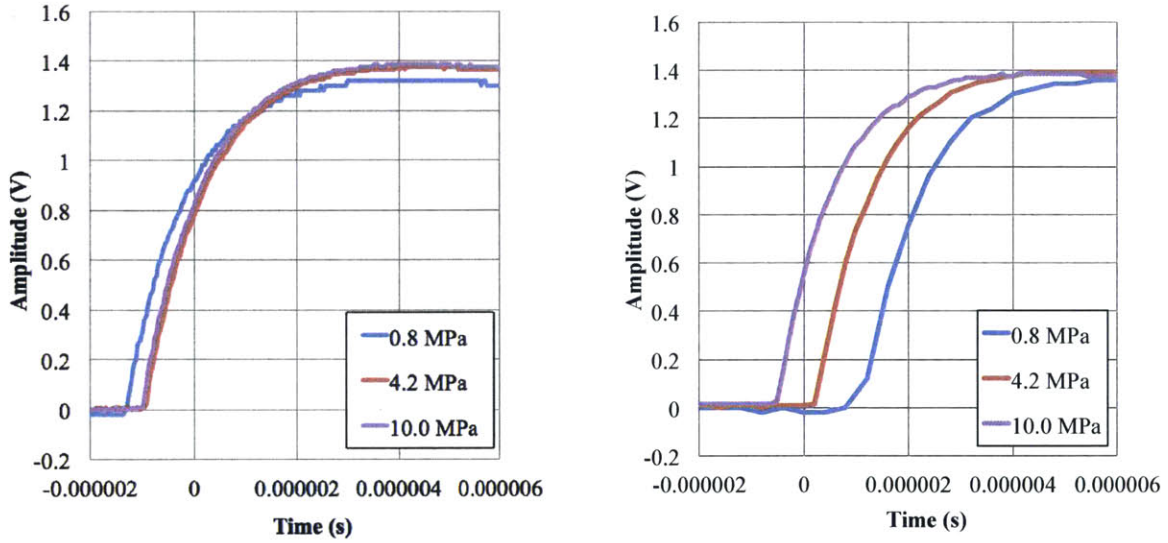

(a) P-wave

(b) S-wave

Figure 6-1: The input pulse signal is connect to the *Sender* P and S-wave transducers during test TX1237. The rise time for the pulse decreases as stress increases

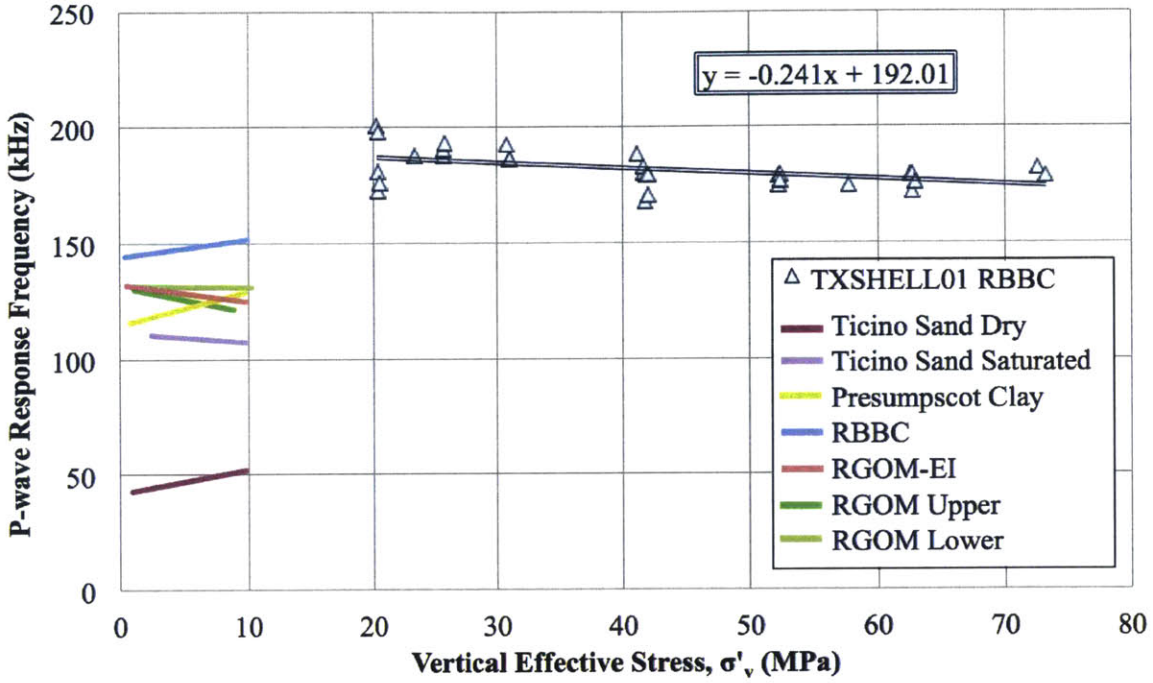

Figure 6-2: P-wave frequency response for all the materials, as shown in Figure 5-29, including the high stress triaxial test run at Shell using different equipment

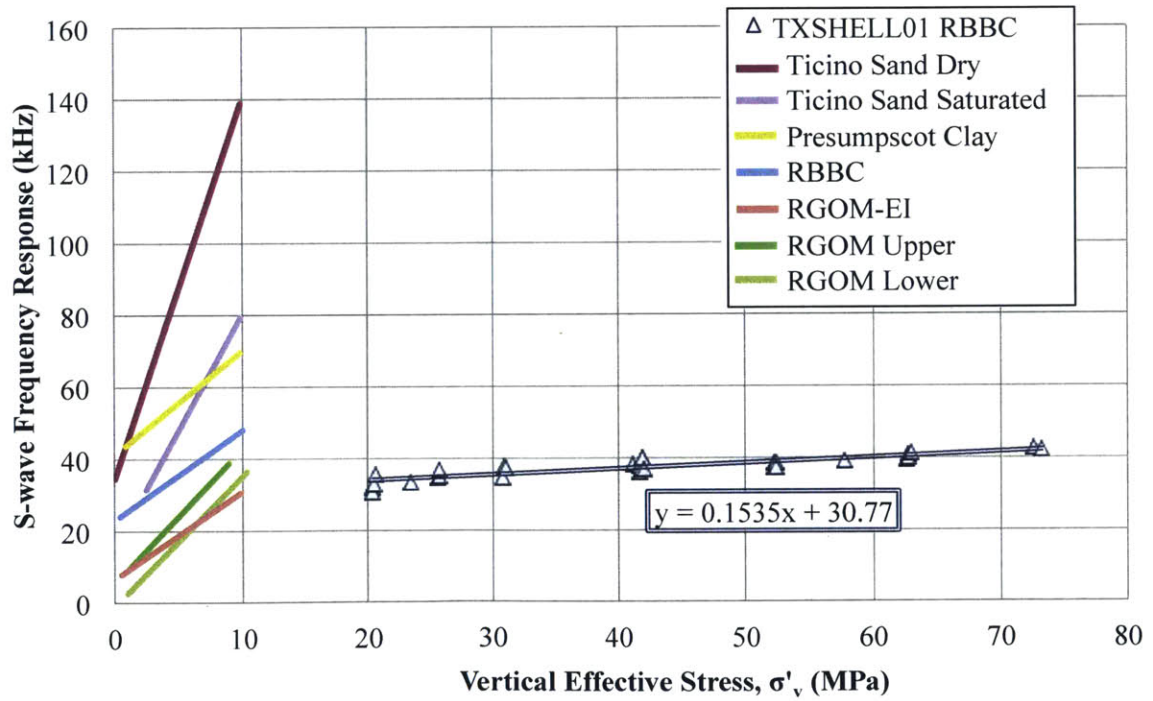

Figure 6-3: S-wave frequency response for all the materials, as shown in Figure 5-30, including the high stress triaxial test run at Shell using different equipment

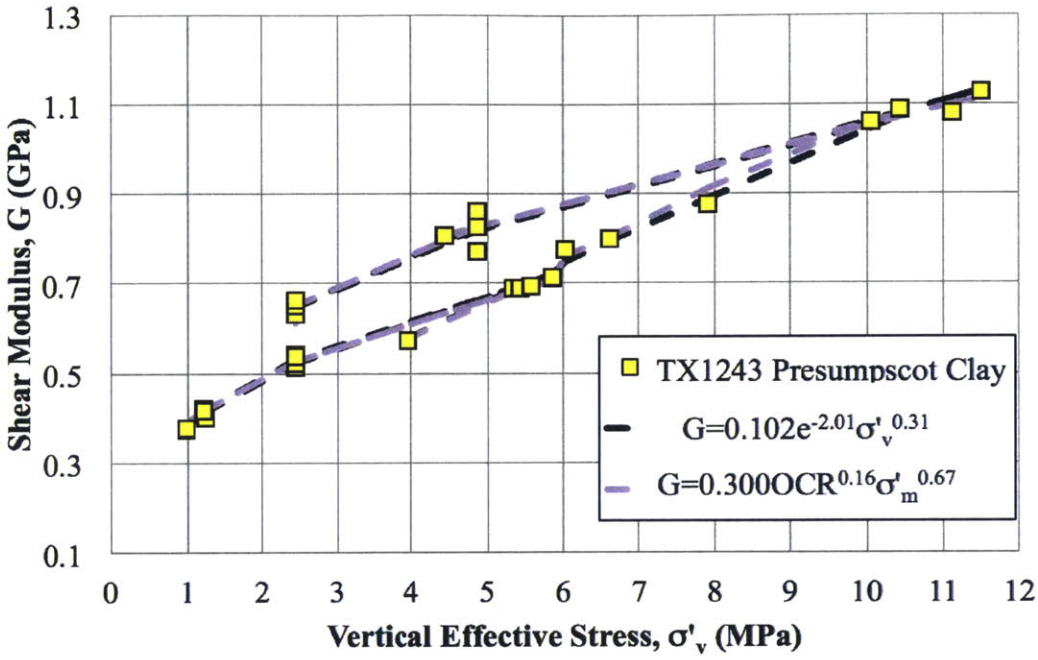

Figure 6-4: The two forms of the Hardin-type equation are used on Presumpscot clay – both with good success, as expected by the R^2 values for the fitting parameters in Tables 6.1 and 6.3

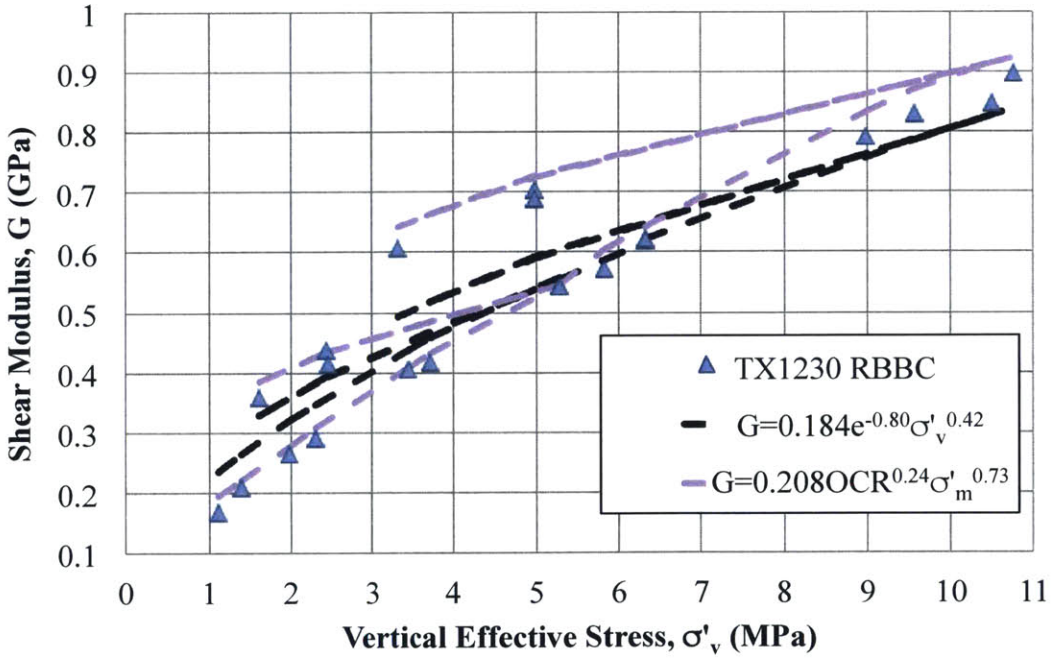

Figure 6-5: The two forms of the Hardin-type equation are used on RBBC – $G = a{*}OCR^{b}{*}\sigma_v^{'c}$ has better success, as expected by the R^2 values for the fitting parameters in Tables 6.1 and 6.3

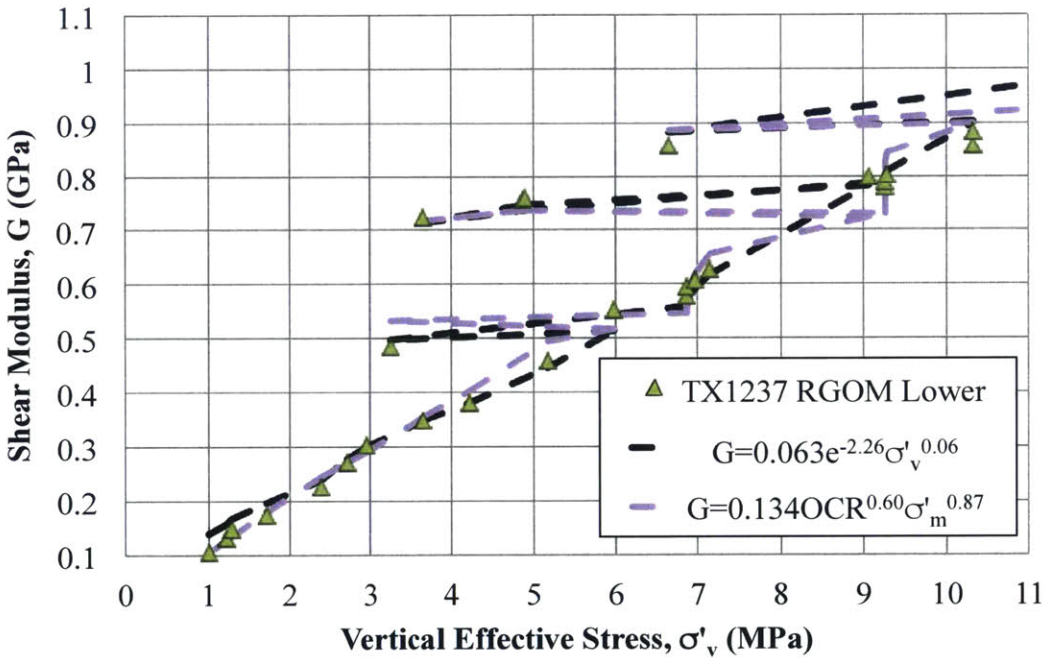

Figure 6-6: The two forms of the Hardin-type equation are used on RGOM Lower – $G = a * e^b * \sigma_m^{'c}$ has better success, as expected by the R^2 values for the fitting parameters in Tables 6.1 and 6.3

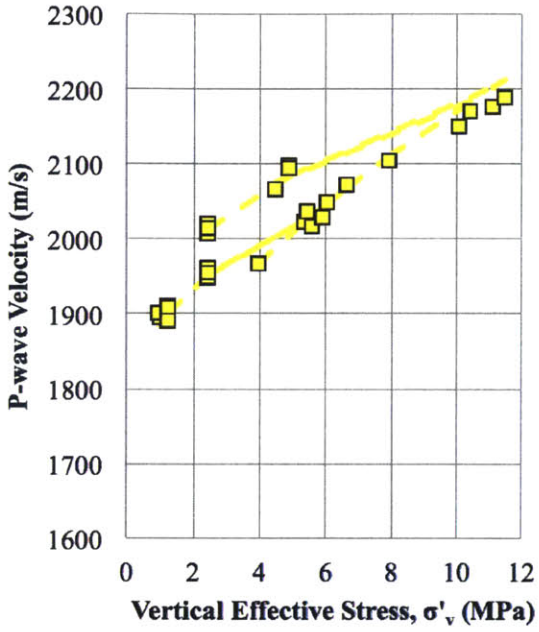

(a) Presumpscot Clay

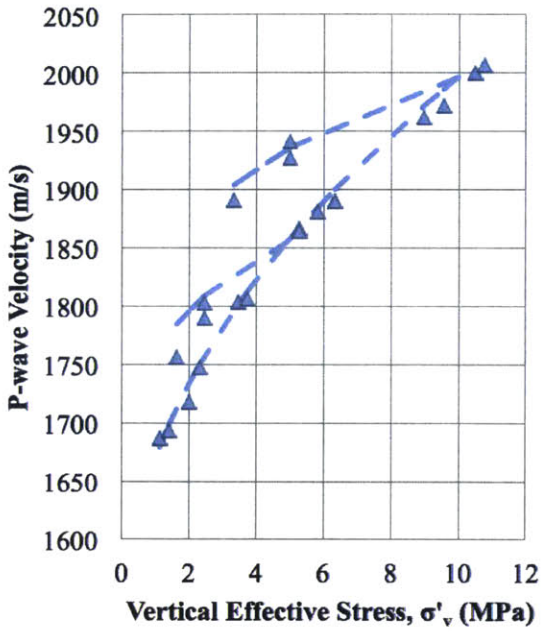

(b) RBBC

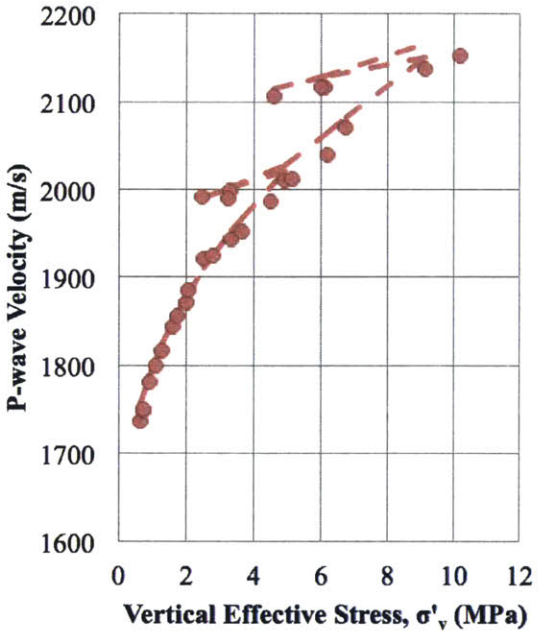

(c) RGOM-EI

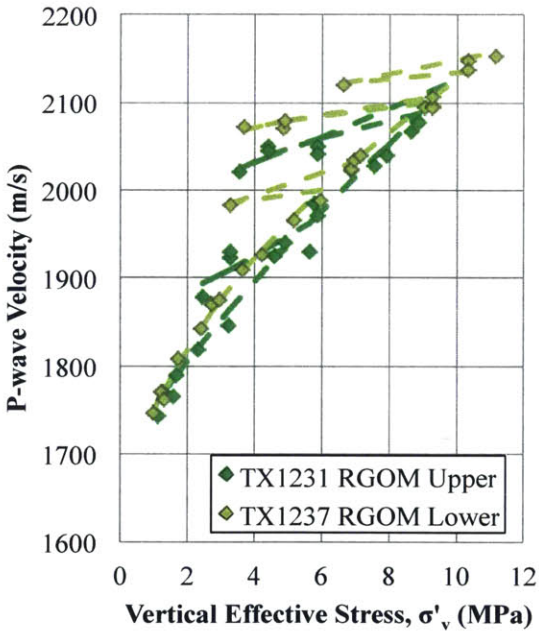

(d) RGOM Upper and Lower

Figure 6-7: V_p (solid symbols) are compared to the Bowers fit (dashed lines) based on the parameters in Table 6.5. For RBBC and RGOM-EI the Bowers fit is an average of multiple tests, thus more scatter is present

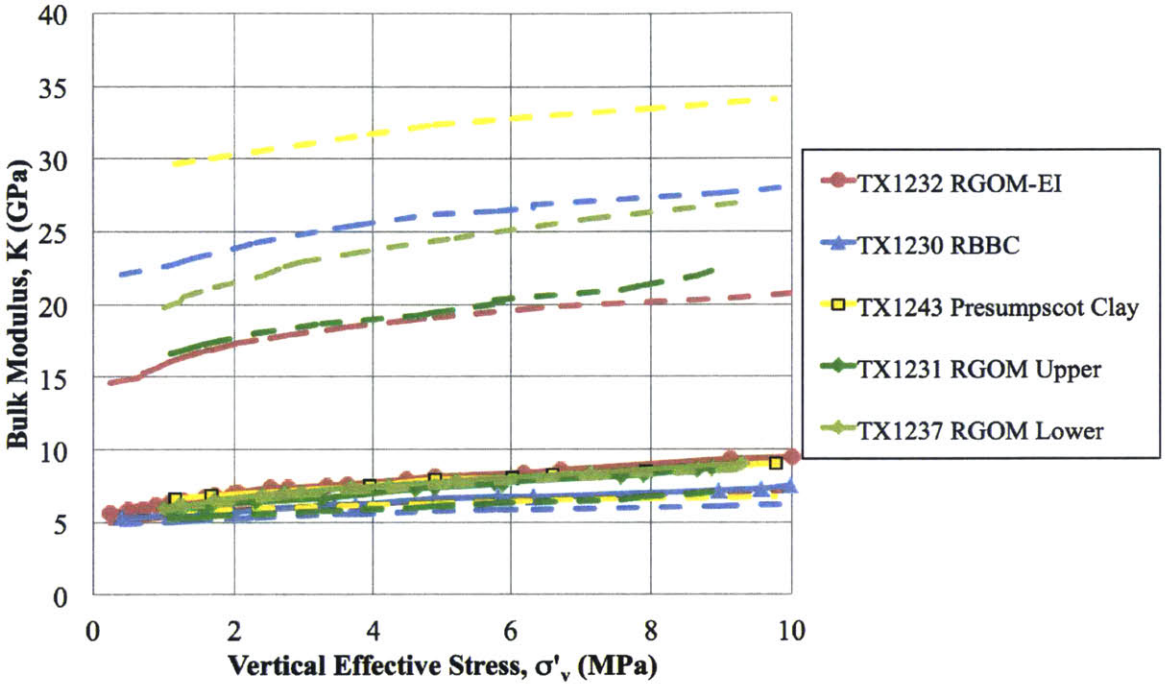

Figure 6-8: The Hashin-Schtrikman upper and lower bounds for bulk modulus are shown with dashed lines that agree with the color scheme of the material they represent. One set of experimental data are included for each material for reference

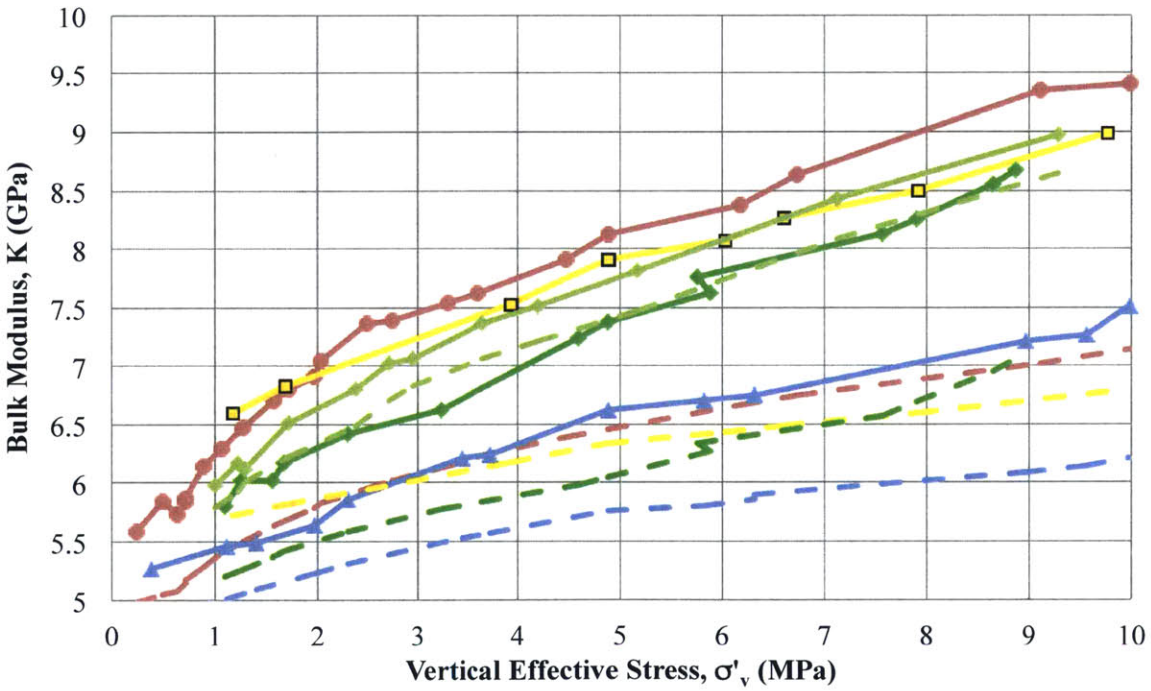

Figure 6-9: Zoomed-in version of the previous figure. Same legend applies

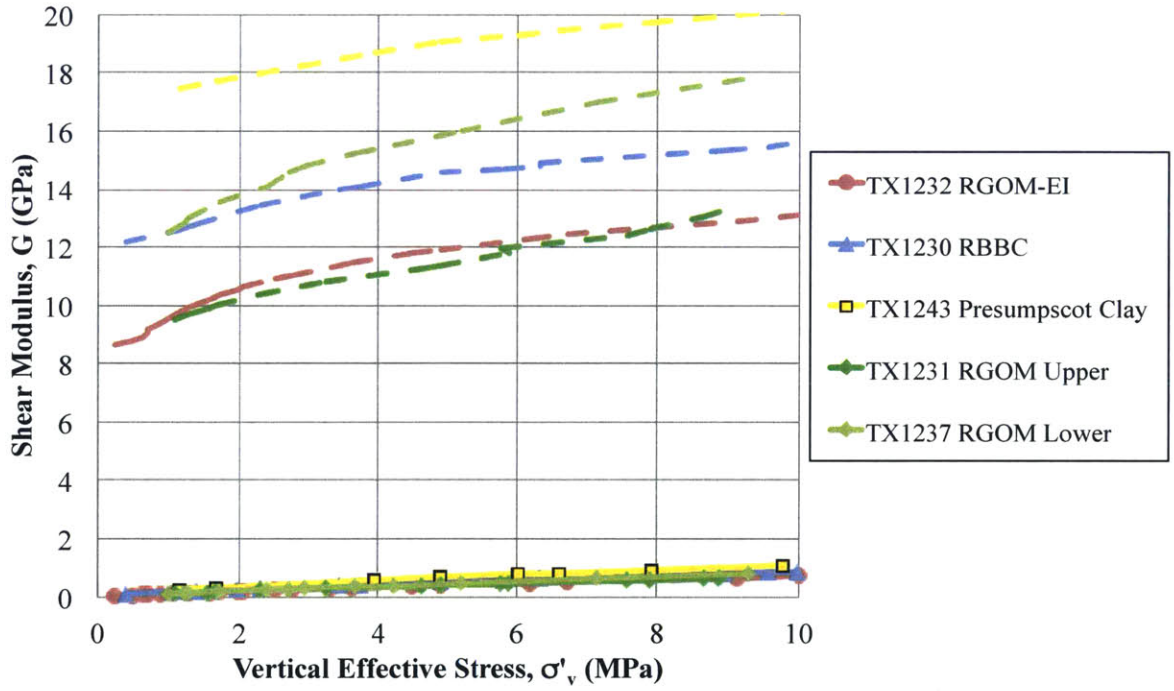

Figure 6-10: The Hashin-Schtrikman upper bounds for shear modulus are shown with dashed lines that agree with the color scheme of the material they represent. The lower bound is equal to zero, since water is assumed to have $G = 0$. One set of experimental data are included for each material for reference. Refer to Figure 5-24 for closeup of G curves for experiments

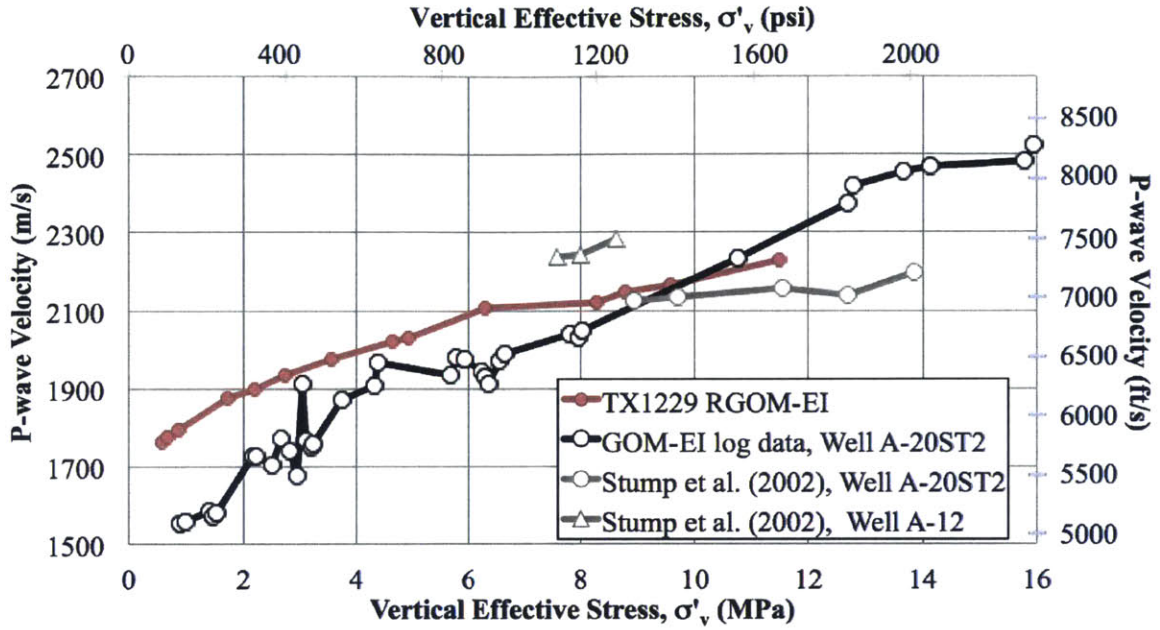

Figure 6-11: Laboratory measurements of RGOM-EI conducted by the author are compared to measurements taken by a logging tool in Well A-20ST2. In addition to the lab-tested RGOM-EI and the in-situ GOM-EI, lab-tested core results are presented in grey, performed by Stump and Flemings (2002)

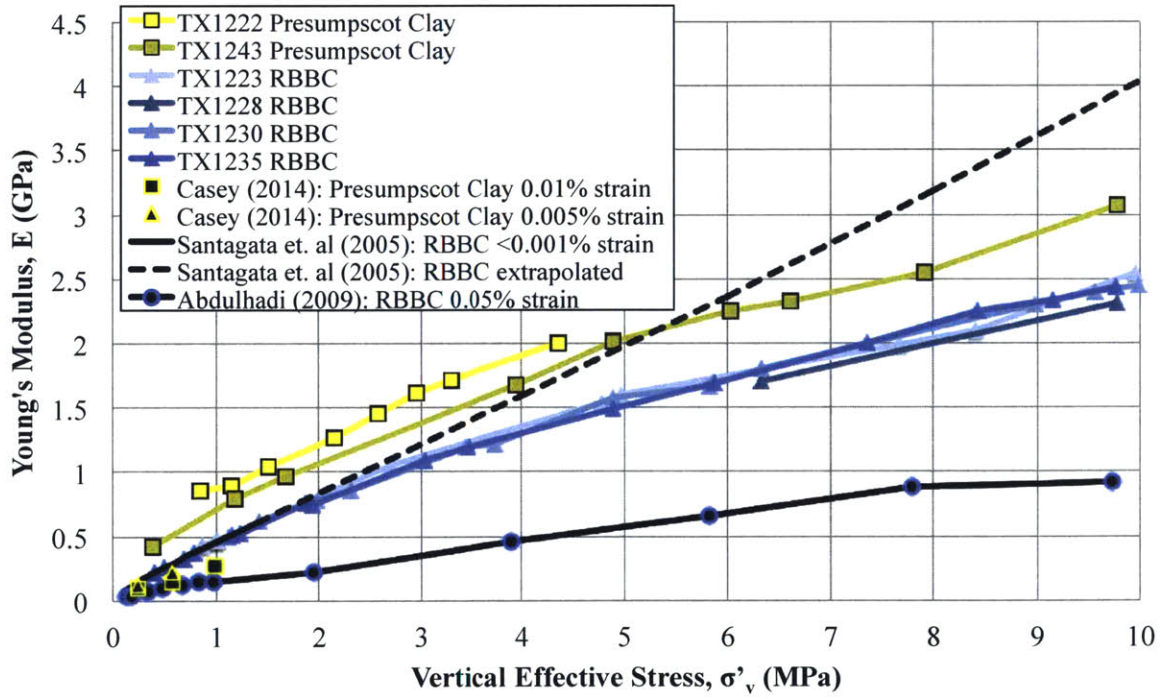

Figure 6-12: Published results based on specimen-mounted small-strain measurements (Santagata, 1998) and CK_0UC triaxial test results (Abdulhadi, 2009, Casey, 2014) are compared to the velocity-derived Young's modulus

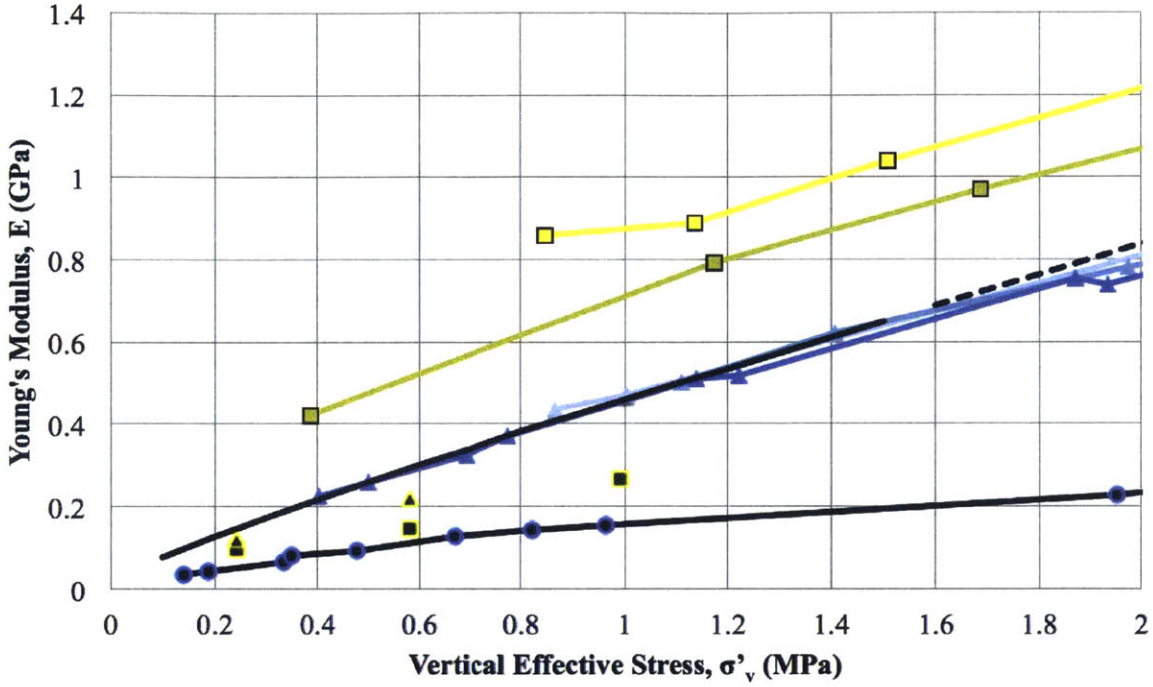

Figure 6-13: Zoomed-in version of previous figure. Legend is the same

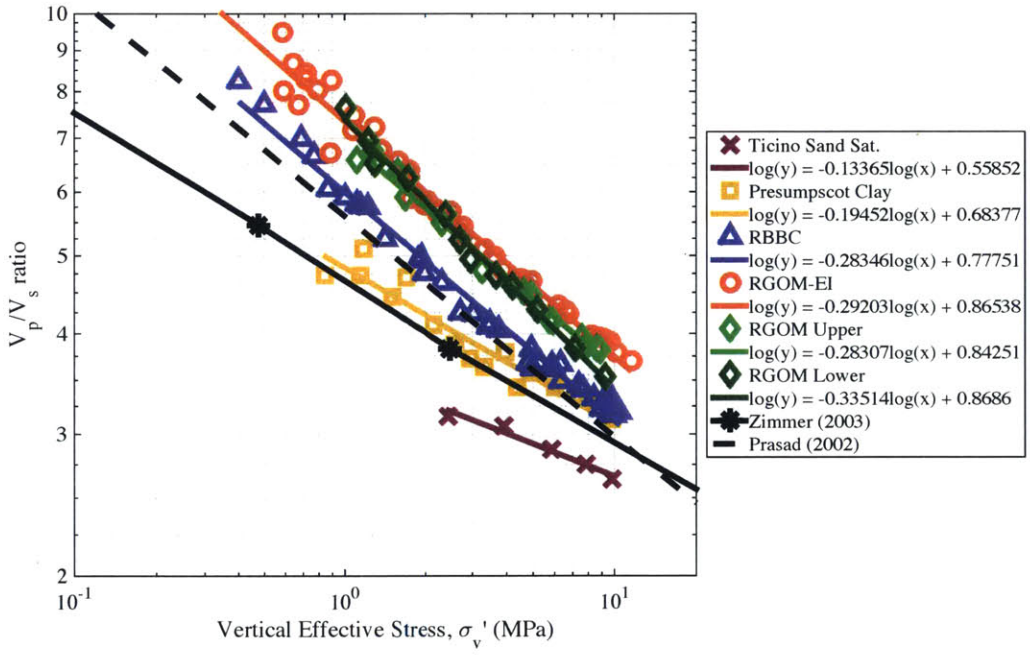

Figure 6-14: Published results based on velocity measurements are presented. Zimmer's data is a rough approximation based on his graphs, while Prasad's line is based on the following equation: $V_p/V_s = 5.6014\sigma_v'^{0.2742}$

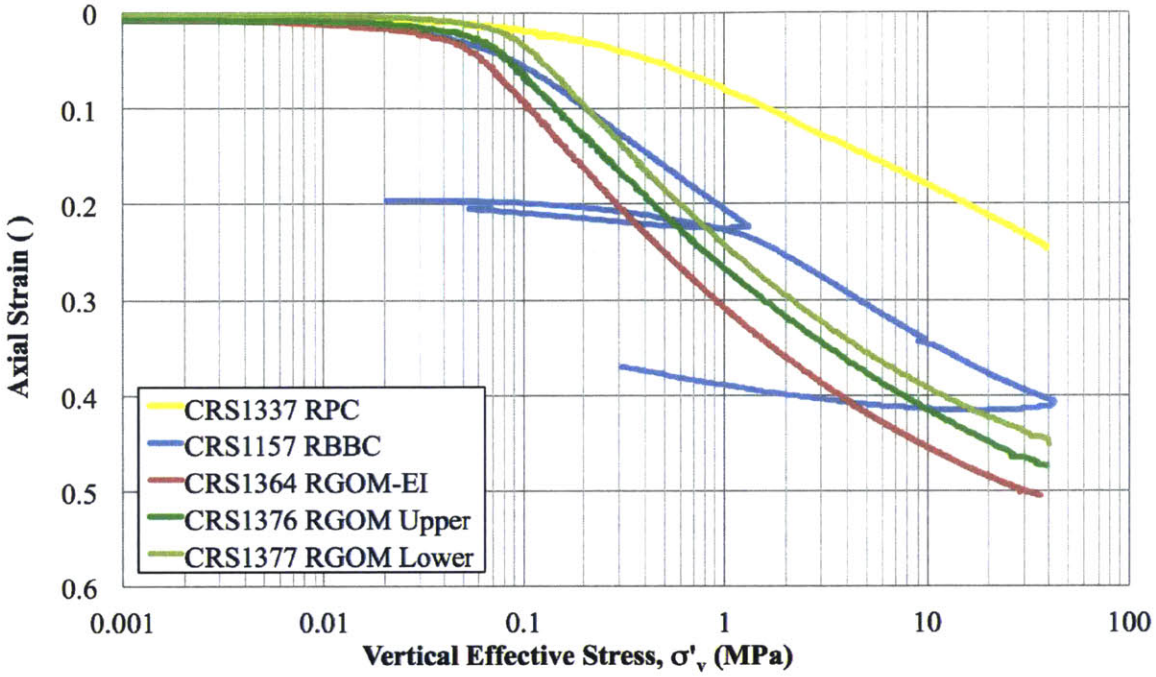

Figure 6-15: Axial strain curves obtained from a CRS test. The inverse slope of these lines is the constrained modulus. Tests were performed by Casey (2014) and Fahy (2014)

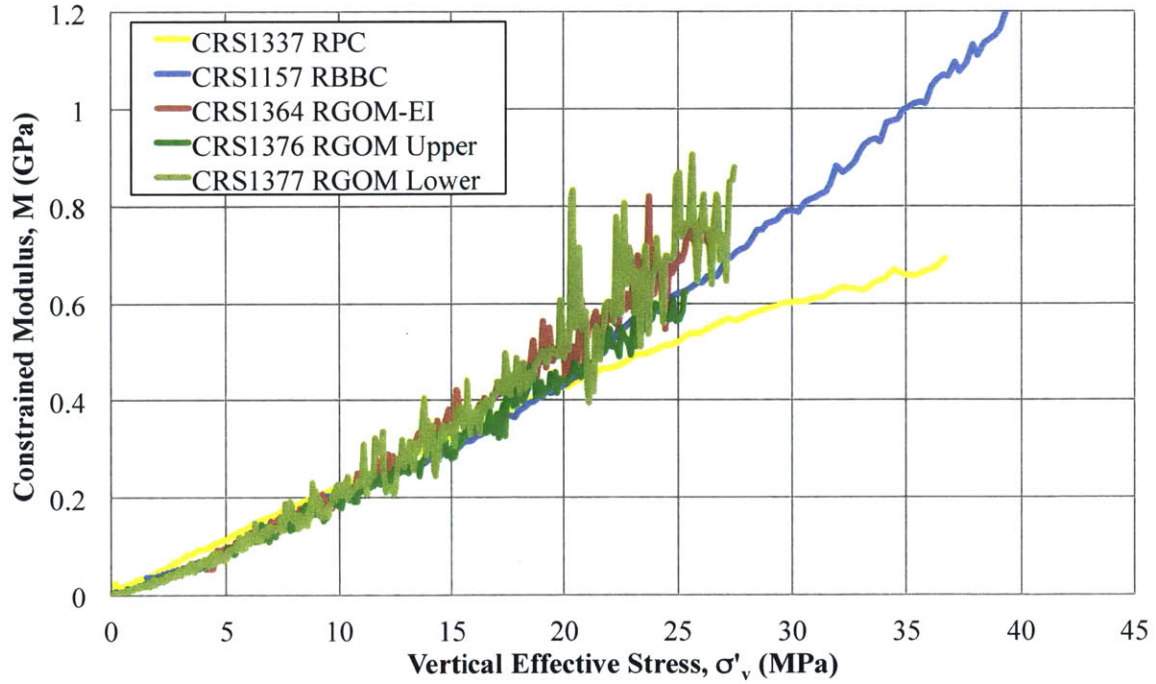

Figure 6-16: Constrained modulus obtained from a CRS test. It is representative of the modulus of the skeleton and is not affected by the water stiffness. Tests were performed by Casey (2014) and Fahy (2014)

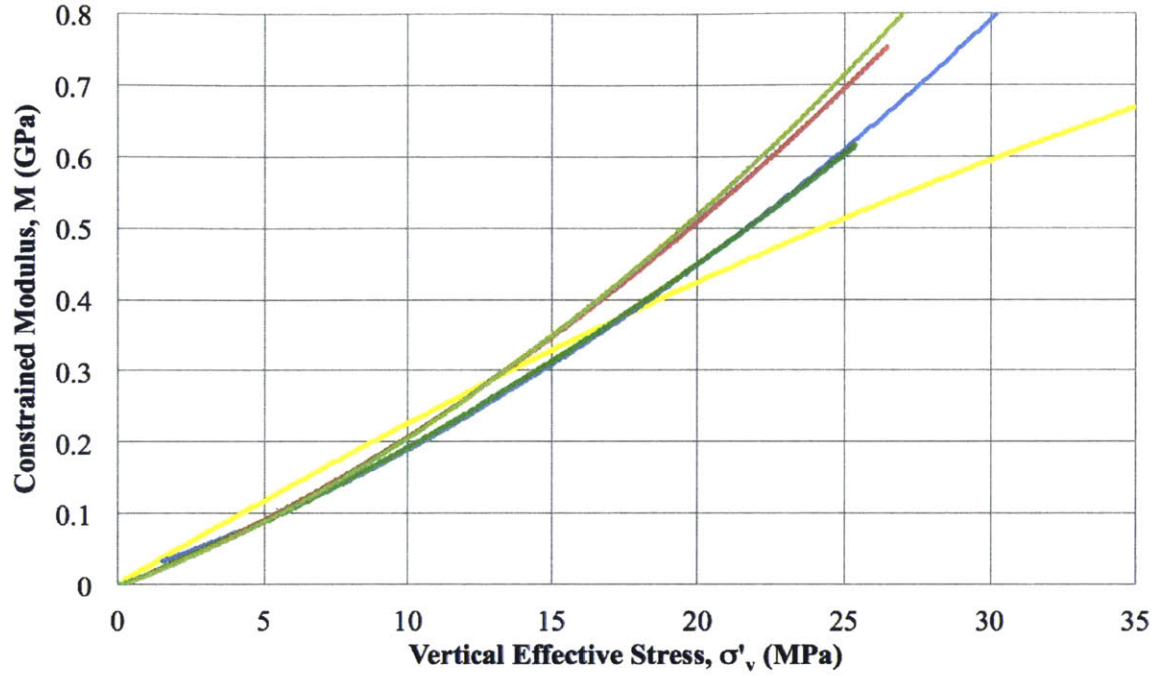

Figure 6-17: Same legend and comments as previous figure, with the lines smoothed out for clarity

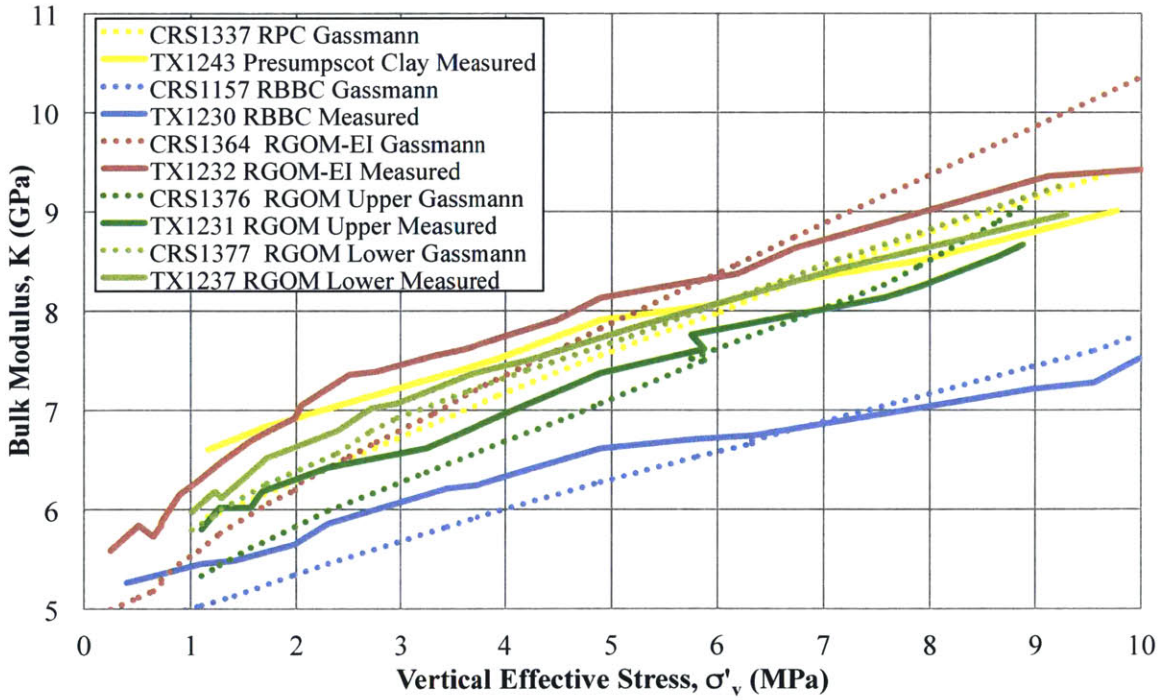

Figure 6-18: The statically-derived constrained modulus is used to calculate a wet bulk modulus using Gassmann fluid substitution and the X factor from Table 6.7. These values, listed as the "Gassmann" values, are compared to the velocity-derived "Measured" bulk modulus values

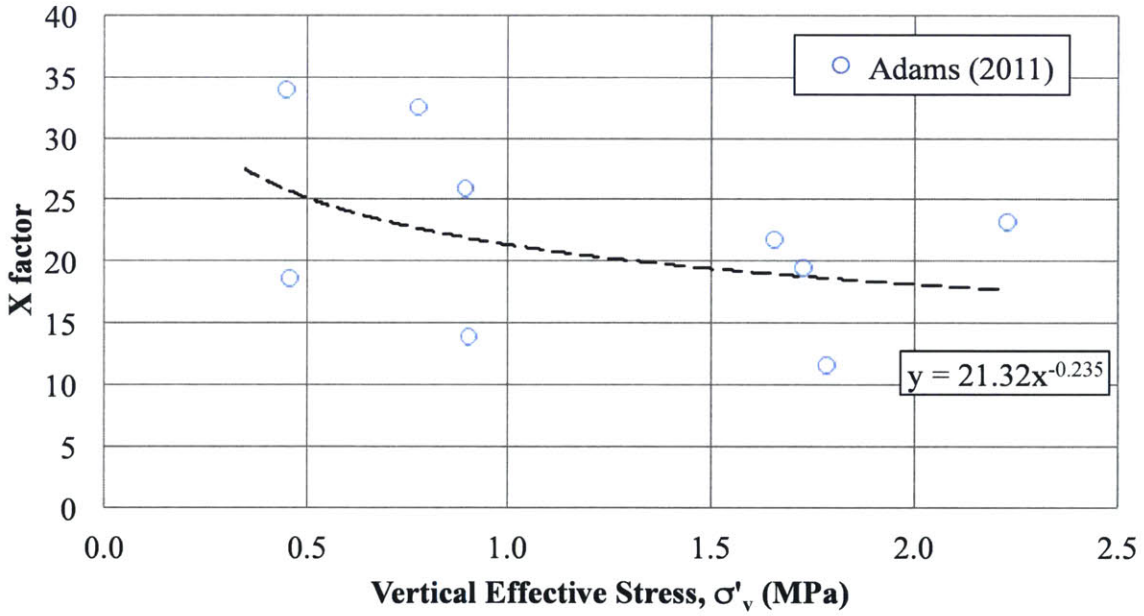

Figure 6-19: The X factor is calculated from CRS tests run by Adams (2011) on RBBC. The CRS tests included at least one unloading cycle, in some cases three. The best fit line is used to predict the Gassmann CRS-derived K in the next figure

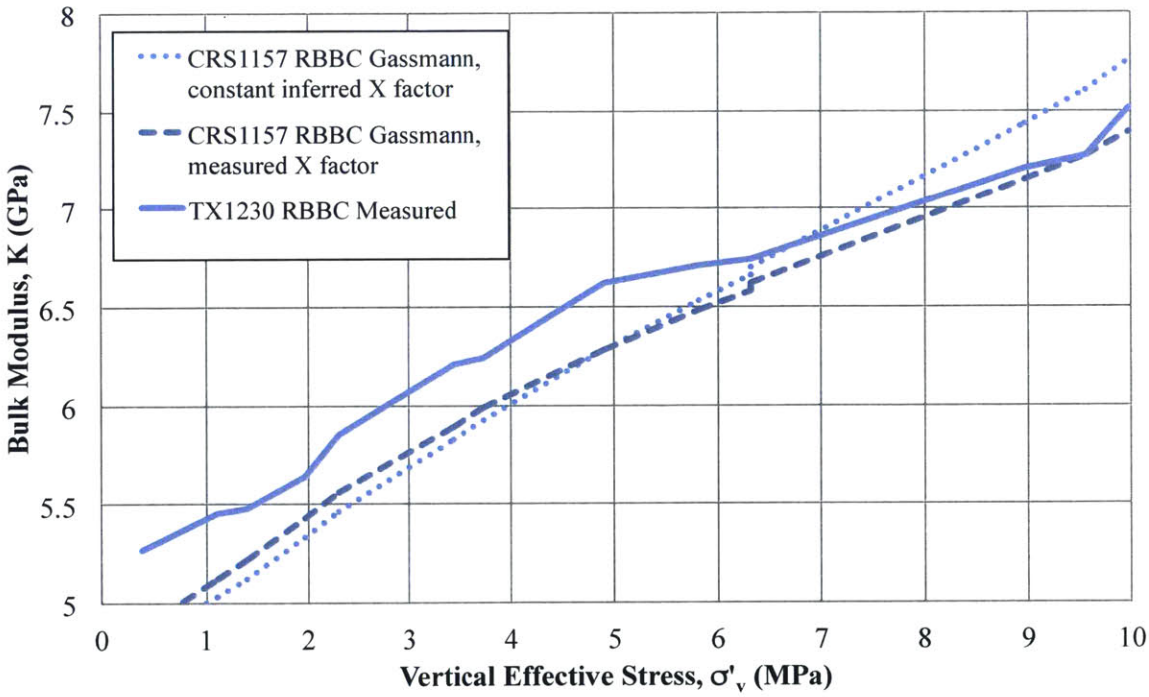

Figure 6-20: The constant X factor that is inferred to provide the best fit between the CRS-derived K is compared to the varying X factor that is measured from Figure 6-19. Both of these are also compared to the velocity-derived K, showing that the measured X factor fits very well with the velocity K, and the inferred X factor provides a decent fit as well

Chapter 7

Conclusion

7.1 Overview

A better understanding of wave propagation through clays is necessary to improve stress behavior predictions in the field and for geophysical interpretations. The velocity through soils varies as a function of the elastic stiffness of the material, thus by using wave propagation to measure the velocity through the soil, the stiffness of the material can be obtained.

The geotechnical methods for obtaining stiffness properties of clays, such as wave propagation via bender elements or internal stain measurements during CK_0UC tests, are usually stress-limited. Geotechnical testing typically has an upper limit of about 1.5 MPa, since this is the stress level encountered in geotechnical applications. On the other hand, studies that measure velocities at high stresses ($>$ 2 MPa) tend to be through sands and rocks – materials that have much higher stiffnesses, and usually performed by the geophysics field or the oil industry. This research spans the gap between these two testing types, by measuring the stiffness properties of a single clay specimen over a wide stress range. Clay can be found in the first 5 km of the Earth's crust, which corresponds up approximately 50 MPa. Furthermore, mudrocks, which are primarily composed of clay, are the most abundant type of sedimentary rock. The need to understand the behavior of clays over a wide stress range (up to 100 MPa), has recently become very important, as many shallow reservoirs have been discovered

to have a high clay content. The uncertainty in clay behavior during drilling has highlighted the need to characterize clay behavior at higher stresses for safer wellbore designs. This research begins to populate the voids present in the knowledge on velocity behavior through clay.

7.2 Key Findings and Developments

Equipment development is a major contribution of this research. The novel implementation of piezoceramic P and S-wave actuators in triaxial endcaps designed to test medium stiffness clays enables the characterization of the velocity behavior over a wide stress range for different plasticity clays. The few attempts at using ultrasonic transducers on clays include Mondol et al. (2008) and Voltolini et al. (2008) in an oedometer cell, and Marion et al. (1992) in a triaxial cell on clay/sand mixtures under hydrostatic pressures. Neither tests natural clay samples, but rather fabricate their mixtures in an attempt to quantify the relative behavior with fractional changes in composition.

This research began with the fabrication and experimentation of bender elements (Marjanovic, 2012), with a significant amount of time focused on signal interpretation techniques. Bender elements (BE) are often used for testing soft materials due to the excellent coupling with the soil; however, there is an upper stress limit of 1.5 MPa. This transferrable knowledge was then used to set the groundwork for a transition into testing with ultrasonic transducers (UT). The use of UT's on clays is very limited. The major obstacle lies in obtaining an interpretable S-wave through a soft material using UT's due to the high impedance contrast between the piezomaterial and the clay. Since P-waves travel through water, excellent P-wave signals are easily obtained through clay. Significant work with electronics resulted in a setup that produces S-wave signals at stresses as low as 0.5 MPa.

Performing tests using both BE and UT has allowed for the comparison of different equipment. In addition to the low stress (BE) and medium stress (UT) setups, a high stress setup at Shell using ultrasonics transducers populates the high stress regime,

up to 70 MPa. The difficulty with using high stress equipment is the low sensitivity at low stress, thus when testing a clay beginning at low stresses, maintaining fine-tuned control in terms of stress and strain is an obstacle. Acquiring velocity results for a clay preconsolidated to 5 MPa and taken to 70 MPa is a rather difficult task, and in particular measuring a shear wave. Not only is this one of the first times that a resedimented clay has been taken to such a high stress level, but it is the first time that a continuous spectrum of S-wave velocity results are available for a single type of natural cohesive soil from 0.1 to 70 MPa, as well as the P-wave velocity results from 0.5 to 70 MPa. Despite the different consolidation sequence, with the medium stress test following constant rate of strain consolidation, while the high stress test following a step-wise incremental loading, the two stress regimes yield very consistent S-wave velocity curves. The P-wave velocity curves are not as consistent, however, the agreement is within an acceptable range of scatter. These results highlight the reproducibility of S-wave velocity results in two very different experimental setups, with slightly more consistent results than V_p, indicating that S-wave velocity results are generally more consistent and less sensitive to small errors in interpretations. This is also supported by the error analysis in Section 5.3, where small interpretation variability in P-wave arrival times causes significantly higher scatter than the equivalent variability in S-wave arrivals. This is only confirmed for the saturated samples tested, which are known to be fully saturated based on the resedimentation techniques and B-wave checks.

Characterizing the velocity behavior for a wide range of plasticities has formed a backbone for understanding what controls the stiffness parameters. The consistency in V_s as a function of plasticity indicates the strong dependence of shear modulus on the grain contacts, with the high smectite clays having fewer contacts due to the obstructive double layer. The V_p indicates a rough trend with the plasticity, with the exception of intact Presumpscot clay; however, the plasticity trend is inverse to that of the V_s, with high smectite clay having the highest V_p. Although counterintuitive at first, the trend seen in V_p is supported by the difference in salinity of each sample. V_p is known to be sensitive to pore fluid and the micro-structural organization of the

particles, both of which are largely affected by the salinity. Furthermore, the scatter in the intact Presumpscot samples highlights the benefits of testing with resedimented samples, which show a very high level of repeatability.

Although the individual velocity measurements are not able to predict the clay type, when the V_p/V_s is calculated, there is a clear trend in plasticity. We developed a model that can predict the V_p/V_s behavior of clays as a function of liquid limit. Liquid limit is selected for many reasons. It is an easy, inexpensive test commonly performed for geotechnical site investigations. To run the liquid limit test the material is reconstituted, thus having a highly disturbed sample such as from a drilling site, does not affect the results. Finally, it is a robust indicator of mineralogy, facilitating correlations based on soil composition.

A novel method that accounts for creep is introduced and implemented in the results. Creep is inevitable when testing OCR, since the specimen needs to equilibrate and allow particle rearrangement to achieve proper unloading behavior. The unloading behavior indicates low plasticity clays have a much more pronounced decrease in stiffness with OCR as compared to high plasticity clays. In terms of a density-velocity crossplot, unloading is indistinguishable from loading for high plasticity clays, thus this technique is not appropriate for predicting unloading or overpressure. Furthermore, it is observed that the compression behavior (e) is unlinked from the velocity behavior in terms of the rate of change as a function of log-stress. When the unloading velocity is normalized by the maximum past velocity and put in terms of OCR, it becomes clear that plasticity affects the results independent of OCR and maximum past stress. The methodology and preliminary unloading results are presented; however, far more work can be done in this field.

The frequency of the received S-wave signal is shown to increase as a function of stress, but decrease as a function of plasticity, while the P-wave frequency did not follow any trend with respect to stress or material. This frequency observation is believed to be an artifact of the transducers and their reaction with the material. The specimen stiffness affects how the piezomaterial takes on the charge, thus explaining the increase in frequency response with increasing stiffness of the material. The

increase of frequency with stress is supported by the piezomaterial behavior, whose capacitance changes as a function of stress. Frequency does not impact velocity, which is most evident in the comparison of the medium and high stress triaxial equipment, whose frequencies are different while their velocity results align very nicely. There is insufficient proof that the 2 - 4 wavelengths that occur within the specimen allow sufficient time for attenuation or dispersion behaviors to manifest.

This thesis compares many different methods of obtaining velocity or stiffness parameters for comparable materials:

Firstly, the RGOM-EI results are compared to the wire-line logging data available from the source wells of the material, as well as some laboratory ultrasonic transducer tests performed on intact samples by Stump and Flemings (2002). While the wire-line logging velocities do not match up as well to the RGOM-EI results, they are in the same general range. Considering the many differences in both the technology, possible aging, and disturbance caused by drilling, the results are encouragingly similar. The velocity results from the intact samples tested in the lab by Stump and Flemings (2002) agree extremely well with the resedimented GOM-EI results from this research. They are able to compare well with each other since only the normally consolidated region for the intact samples is selected. Once the specimens are loading in the NC region, movement of the particles is reactivated and the results are more comparable.

Secondly, intact Presumpscot clay E values based on velocity measurements are compared to Young's modulus values measured via static, external strain measurements on resedimented Presumpscot clay in the triaxial cell. These tests are comparable since both attempt to measure the elastic modulus. After K_0-consolidation and proper equilibration, the triaxial experiment measures the stress-strain behavior at the commencement of shearing. Due to the low resolution of the external strain measurements, the small-strain behavior is not captured, but rather a stiffness measurement that has experienced plastic deformation is reported. The strain softening that occurs due to plastic deformation explains the large underestimation of E based on the results from Casey (2014) via CK_0UC tests.

Thirdly, velocity-derived Young's modulus results of RBBC are compared to

statically-measured E of RBBC based on both internal and external strain measurements. Much like the Presumpscot clay, the external strain measurements during the beginning of shearing are not sensitive enough to capture the *elastic small strain* regime, but rather underestimated E by a factor of two or higher due to strain softening. On the other hand, the specimen-mounted yolk system with high resolution is able to capture the behavior under the elastic strain threshold, validating the technology used by Santagata (1998). Obtaining results for a static versus a dynamic test within the same range, let alone be in almost exact agreement, is extremely encouraging. This provides further evidence that static and dynamic methods both measure the same E, with no frequency effect. The comparison also points out that the equations used to fit Santagata's data cannot be extrapolated beyond the stresses she measured.

Finally, the sand results reported by Zimmer (2003) and Prasad (2002) fall into the range of V_p/V_s ratio that agrees with the Ticino sand tested in this research. Sand tested by Prasad (2002) are clean beach sands with a smaller mean particle size than Ticino sand, and sand tested by Zimmer (2003) encompassed a wide variety of sands, with the the largest mean particle size being much smaller than Ticino sand. It is not expected that all sand velocity results would agree with Ticino sand, and sand is not the focus of this thesis, but this comparison validates they are approximately in the same range despite the large differences in preparation, mineralogy and particle size distribution.

A number of fitting techniques are compared with the velocity data. The best fit achieved is a Hardin-type empirical correlation that included the OCR and mean effective stress, as well as a few fitting constants unique to each material. Mean effective stress seems to be a more appropriate parameter since it takes into account the K_0 differences between the tests. Equations to fit all the materials in the research are provided for G and K.

The loading constrained modulus obtained from a CRS test during plastic deformation grossly underestimates the material stiffness. A more appropriate M is measured during the very initial stage of the unloading portion, after sufficient equi-

libration is allowed. This small strain unloading portion is much closer to the elastic stiffness behavior. Based on this observation, a new method using loading CRS tests can be used to predict the elastic constrained modulus, and thus the V_p of a material, with the caveat that the loading-to-unloading relationship is known as a function of stress, and the G is needed to perform the Gassmann fluid substitution. An X factor for each material is shown to adequately predict the K curve as a function of stress for all the materials. The X factors are all reasonable estimates for the relationship between the unloading and loading stiffness. There is clear potential in formalizing a method that correlates CRS loading to elastic velocity measurements. Room for improvement is evident in devising a method that eliminates the need for the dynamic shear modulus in the prediction; however, the consistency between K, M, and G when using the unloading portion of the CRS tests is encouraging.

7.3 Recommendations for Future Work

The following topics related to this thesis are suggested for other researchers:

1. The trend in P-wave velocity seems to follow the trend of salinity. In order to prove that the trend is not solely dependent on pore fluid, but also on mineralogy, a new experimental program changing the salinity of a single clay is crucial. I would recommend using RGOM-EI in order to see the largest change in behavior based on salinity, since it is the most reactive soil tested in this research. Furthermore, monitoring the water salinity expelled during consolidation (as well as before and after the test) would shed light into whether the expelled water is coming from the free pore space or the double layer. Relating this to the P-wave velocity trends could be useful.

2. The entire experimental program in this thesis focuses on running K_0-consolidation tests. There are a few extensions of this work that seem logical. Firstly, altering the stress paths would provide more insight into the sensitivity of the velocities as a function of anisotropic loading. Secondly, all the tests are loaded and

unloaded, without ever failing the specimens. The current triaxial equipment allows for shearing in both compression and extension. Measuring velocity during these experimental programs could provide some insight into the stiffness behavior of clay during shearing. It would be interesting to look at how the stiffness changes as failure is occurring

3. More unloading characterization is needed. This research only scratched the surface of the unloading behavior due to the difficulty of establishing the technology and an experimental protocol. The further characterization of unloading, extended to larger OCR's and higher maximum past stresses would validate the trend in stiffness evolution as a function of stress. This would also require entering a higher stress regime, up to 100 MPa. This thesis tests up to 70 MPa but does not conduct unloading cycles past 10 MPa. Furthermore, the strain rate during the loading and unloading portion needs to be investigated. A constant loading and unloading strain rate is used for each soil, with the low smectite clays using 0.15%/hr while the high smectite clays using 0.08%/hr. How the unloading strain rate alters the unloading creep behavior is unknown.

4. Improve the electronics of the pulse generation system to even further reduce the noise and variability of arrival time interpretation. There are a few artifacts in the signals that have not been fully explained, such as the precursory down-dip in the S-wave, that can be better explained with further electronic processing.

5. The predictive method presented in Section 6.5 that compares the velocity-derived modulus to the statically-derived CRS modulus is validated with results from RBBC CRS tests run by Adams (2011). More validation is needed for the rest of the clays in order to completely validate this method. Furthermore, a more detailed look at the loading and unloading stiffness in CRS tests is desirable.

6. The attempts at fitting empirical equations to the results in this research are based on other researchers' established equations. No attempt is made at deriv-

ing a new, unique form of equation that can better characterize the behavior. There is much work that can be done in this regard, with incorporating liquid limit, as well as OCR, σ'_v, σ'_{vmax}, and e. This would also require obtaining velocity results up to at least 100 MPa to establish a robust relationship that is not stress-limited

7. A closer look at the microstructure and its link to velocity behavior is needed. Although this research has a few SEM images in the appendix for RBBC and RGOM (Figure A-13), a more detailed analysis of the pore size evolution is needed.

Appendix A

Figures

Table A.1: Summary of swelling index, C_s, values for each unloading cycle

Unloading Cycle	TX1229 RGOM-EI	TX1230 RBBC	TX1231 RGOM Upper	TX1232 RGOM-EI	TX1235 RBBC	TX1237 RGOM Lower	TX1240 RGOM-EI	TX1243 Presumpscot Clay
1	-0.0361	-0.0445	-0.0199	-0.0115	-0.0428	-0.0135	-0.0512	-0.0213
2	-0.0396	-0.0427	-0.0427	-0.0101	-0.0431	-0.0166		-0.0228
3				-0.0101	-0.0413	-0.0025		

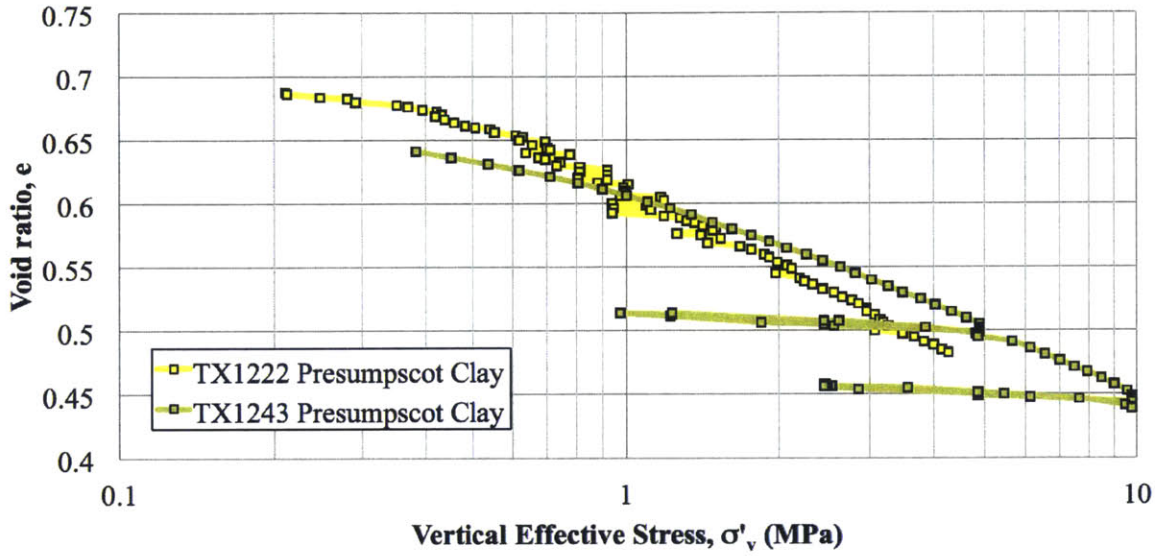

Figure A-1: Compression curve for Presumpscot clay

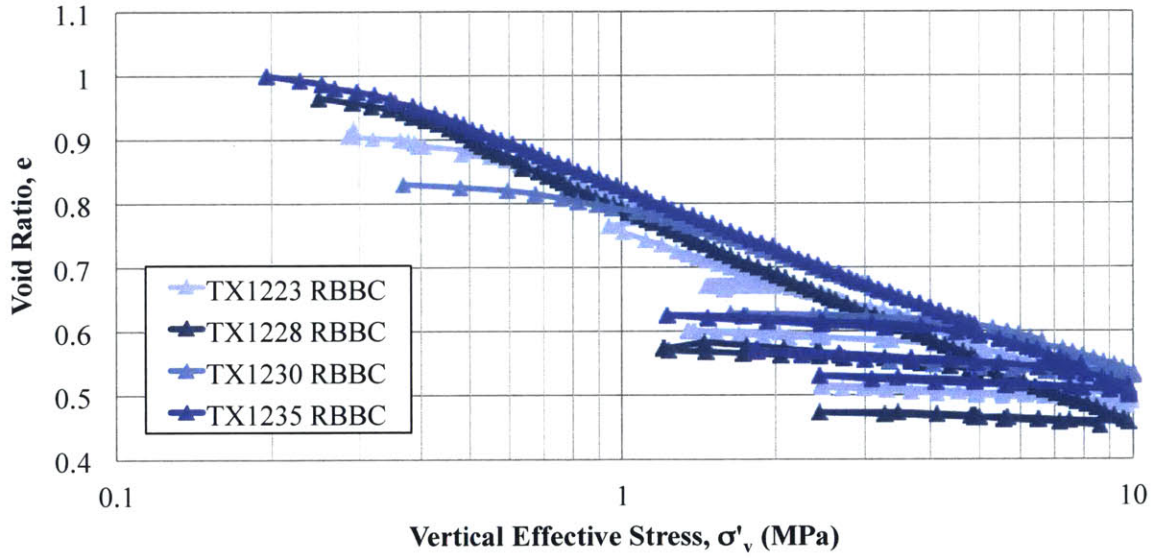

Figure A-2: Compression curve for RBBC

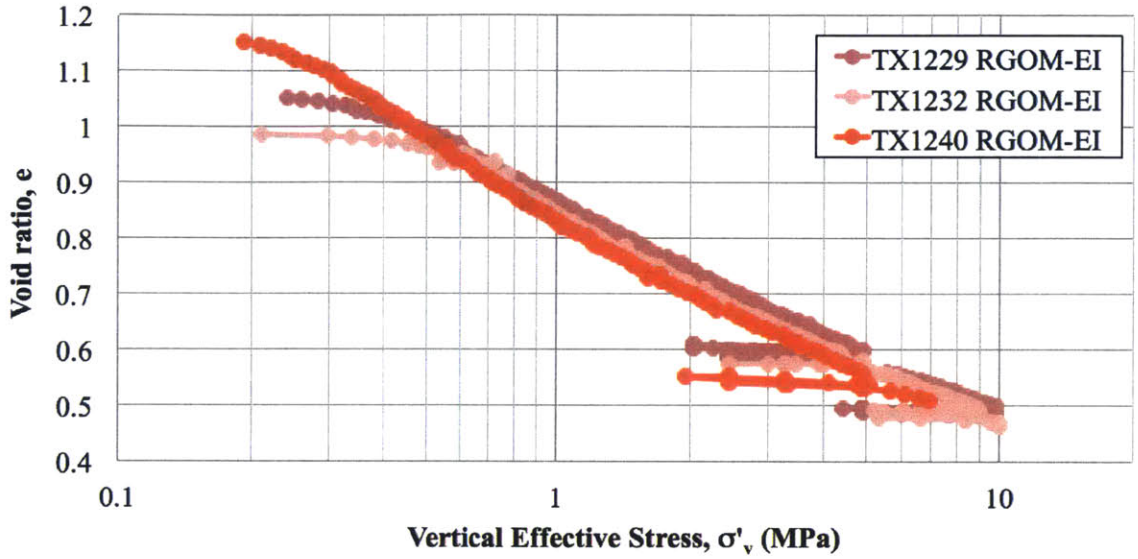

Figure A-3: Compression curve for RGOM-EI

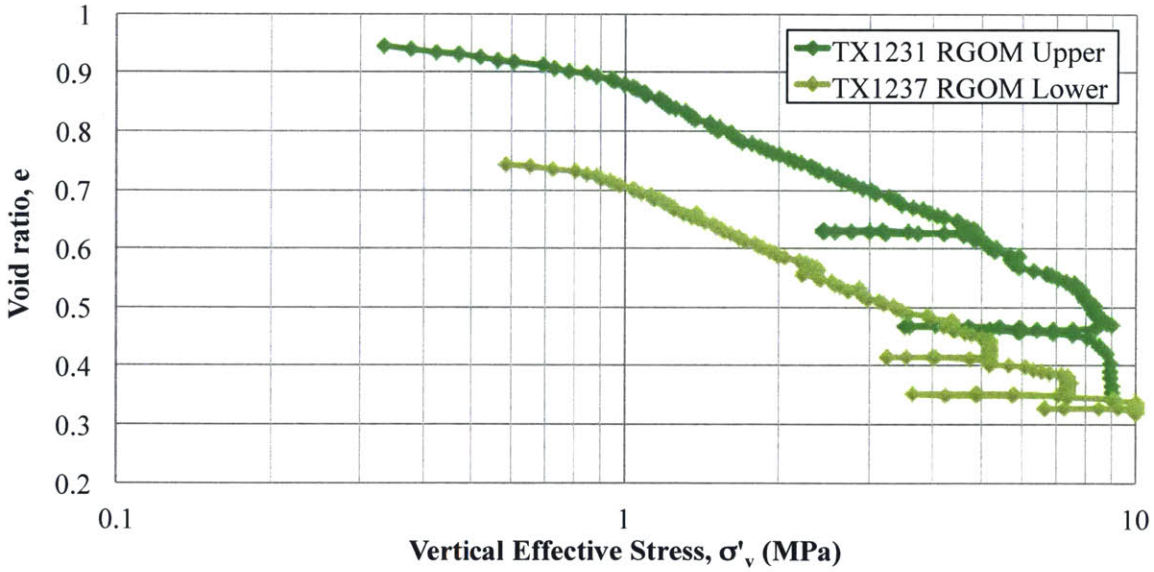

Figure A-4: Compression curve for RGOM Upper and Lower

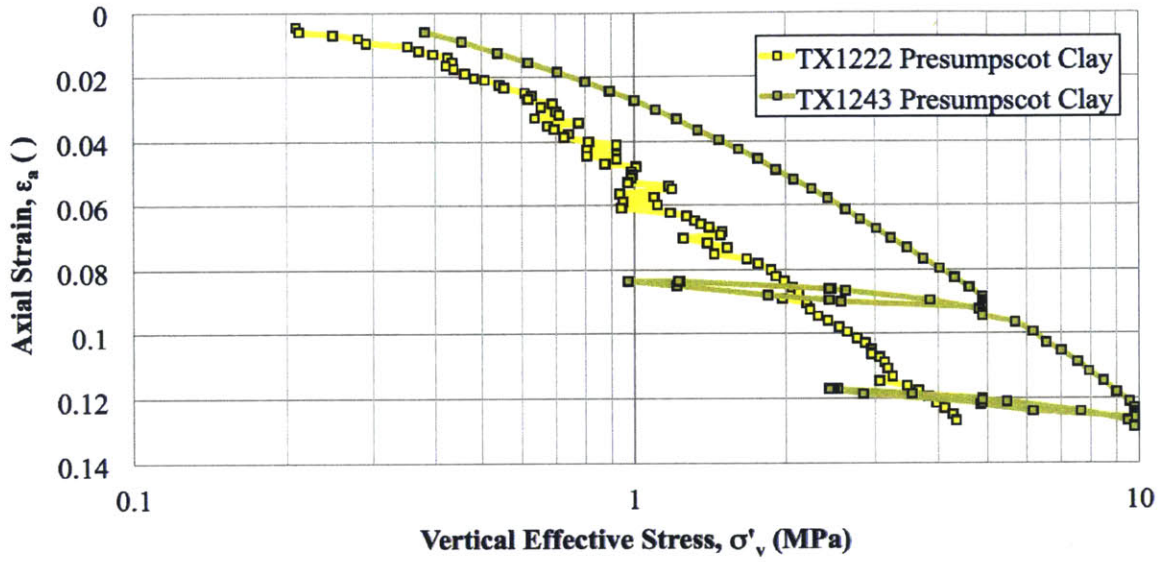

Figure A-5: Strain curve for Presumpscot clay

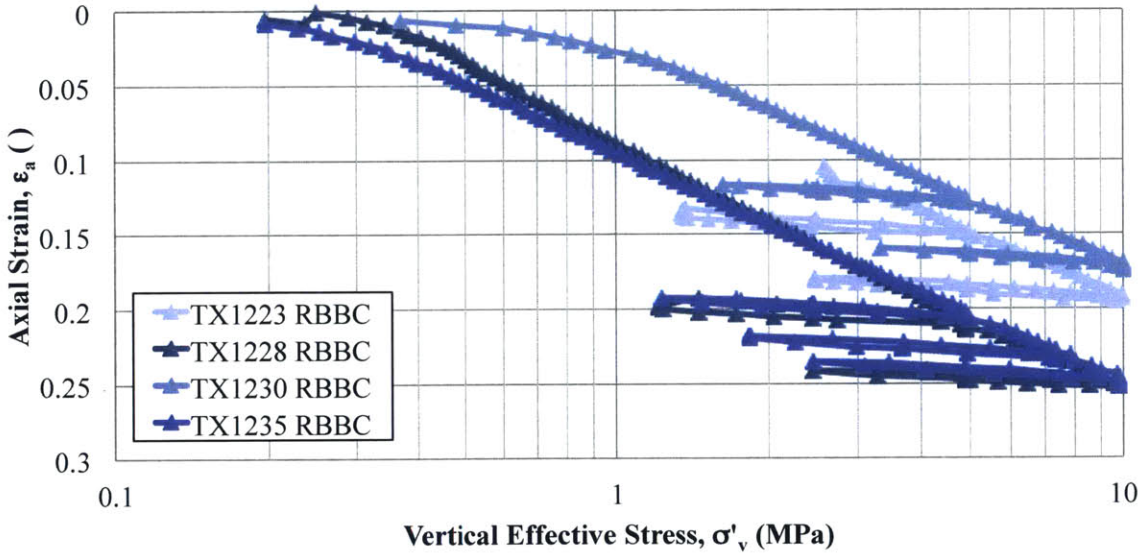

Figure A-6: Strain curve for RBBC

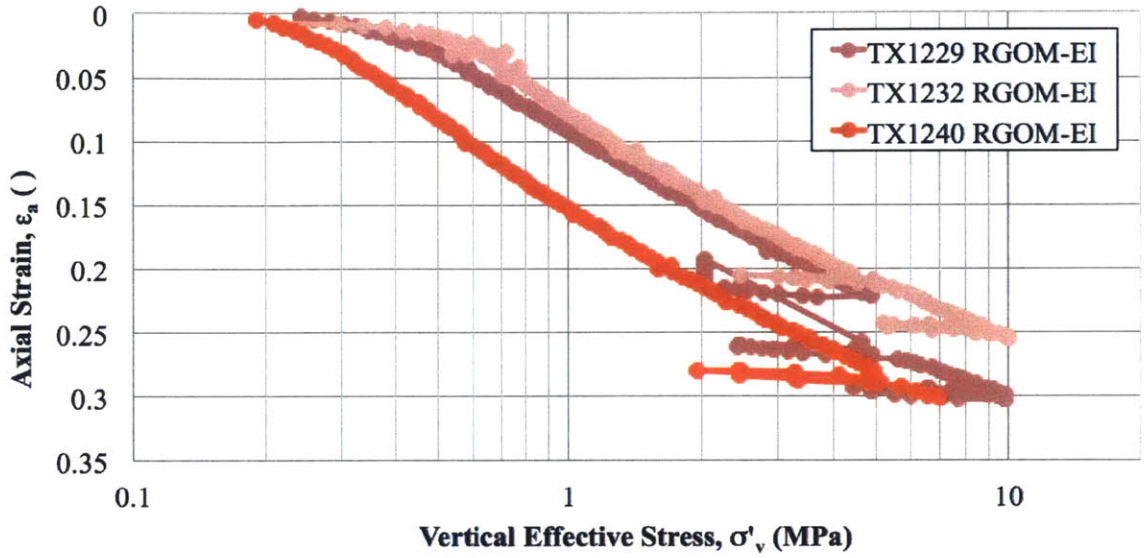

Figure A-7: Strain curve for RGOM-EI

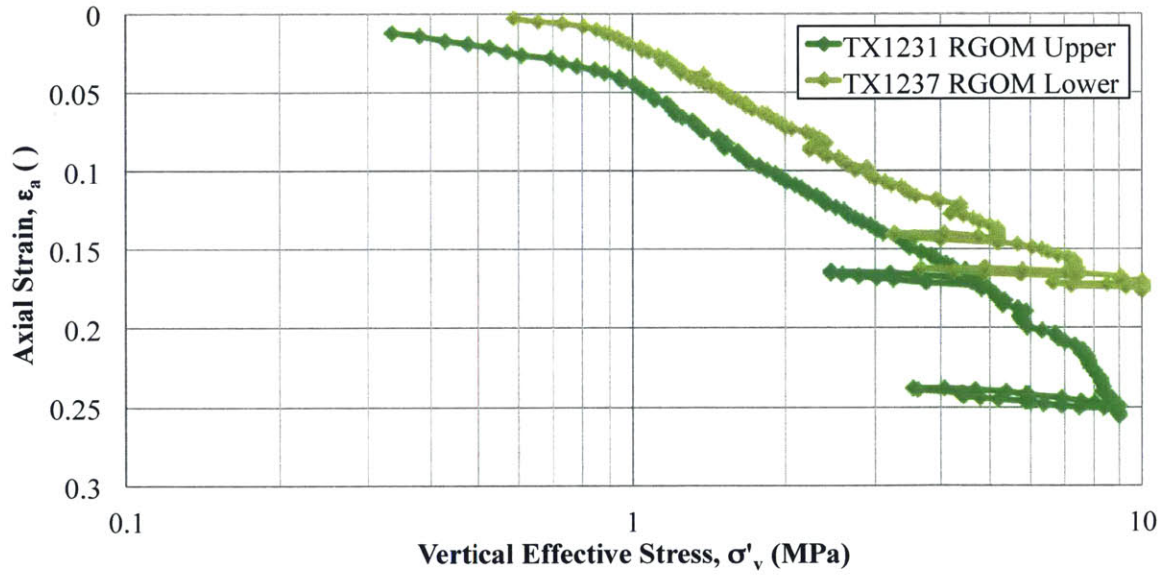

Figure A-8: Strain curve for RGOM Upper and Lower

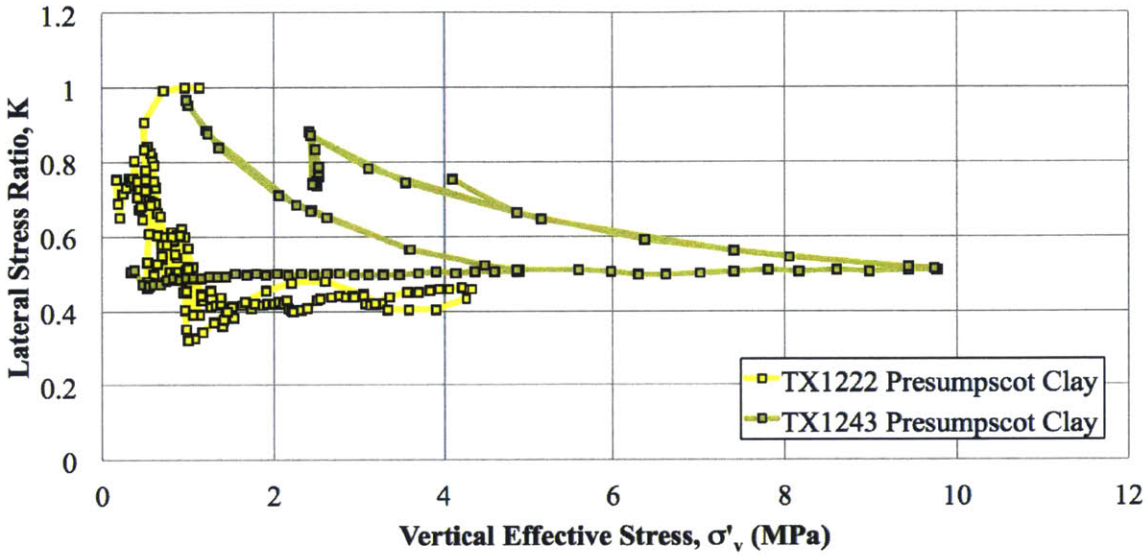

Figure A-9: K_0 curve for Presumpscot clay

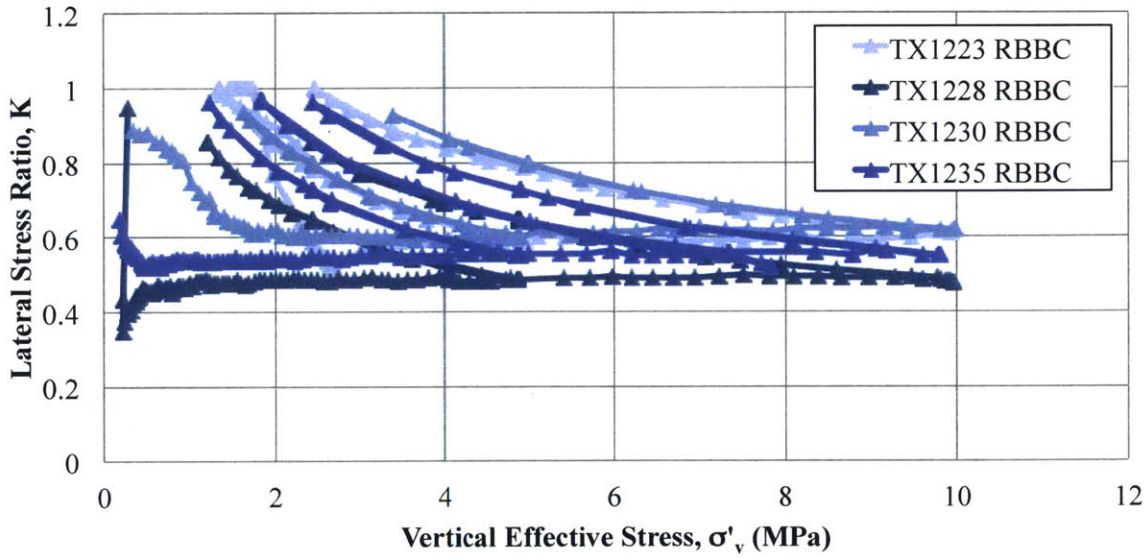

Figure A-10: K_0 curve for RBBC

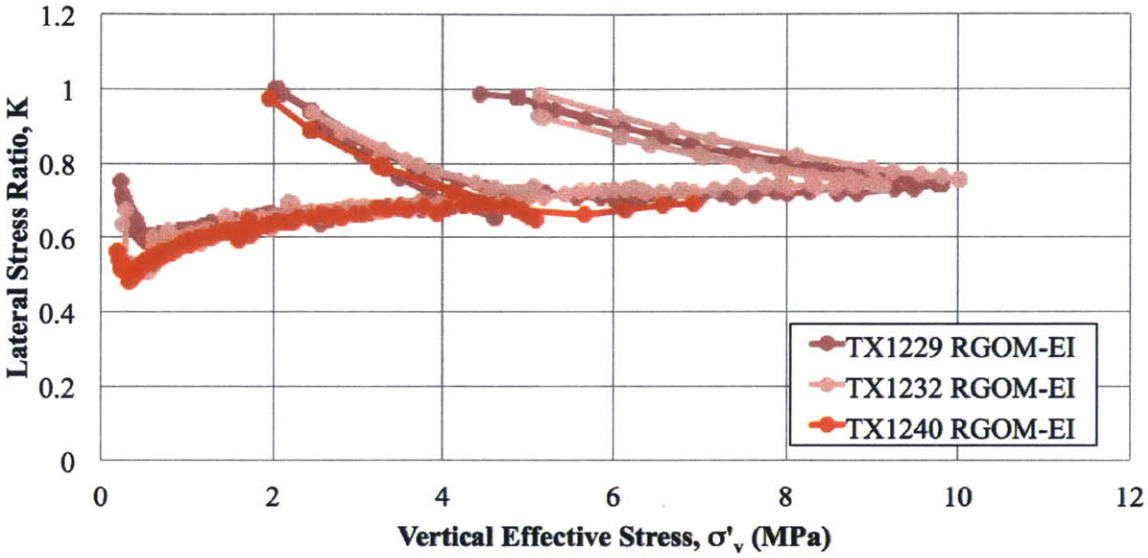

Figure A-11: K_0 curve for RGOM-EI

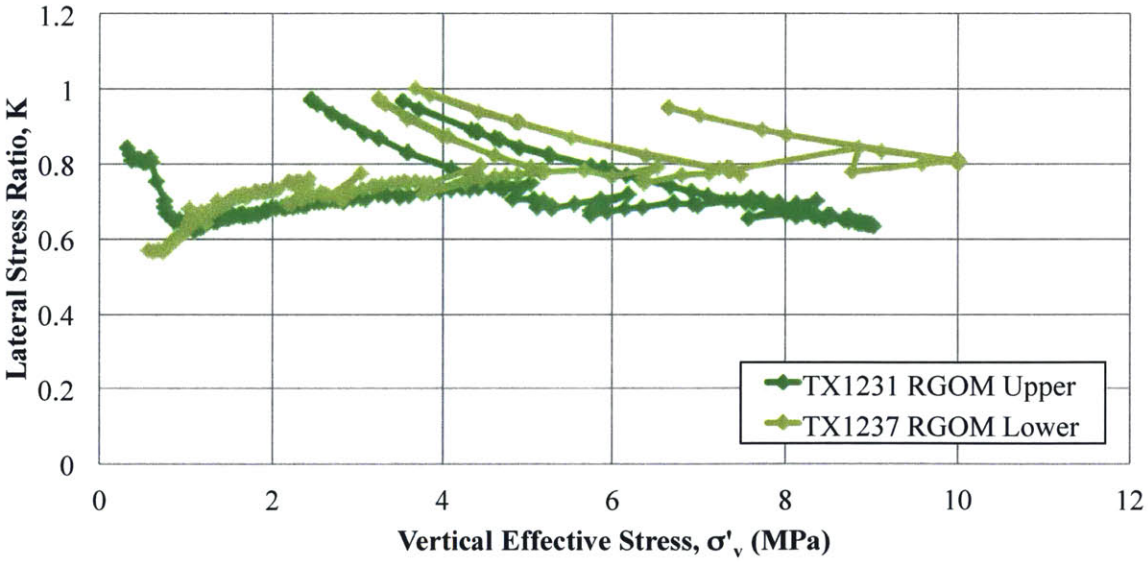

Figure A-12: K_0 curve for RGOM Upper and Lower

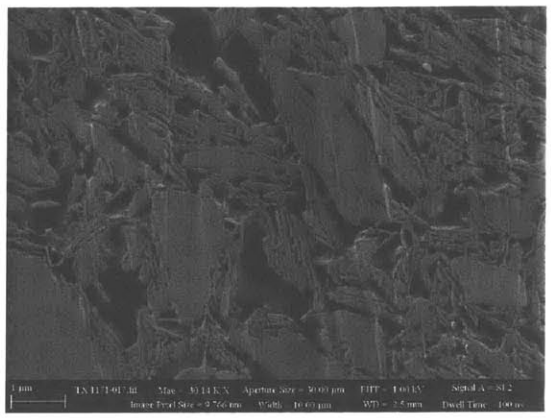

(a) RBBC 0.2 MPa

(b) RGOM-EI 0.2 MPa

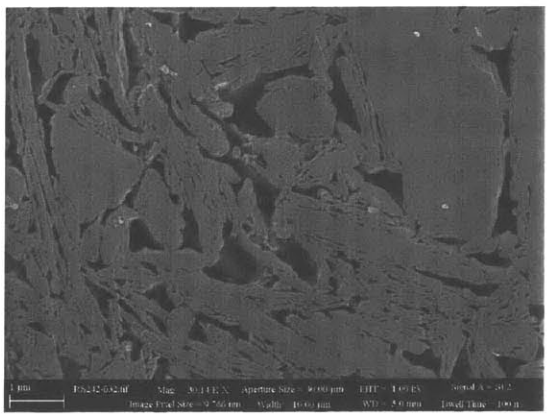

(c) RBBC 1 MPa

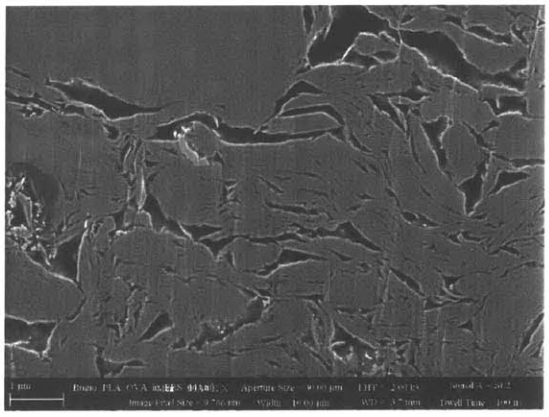

(d) RGOM-EI 1 MPa

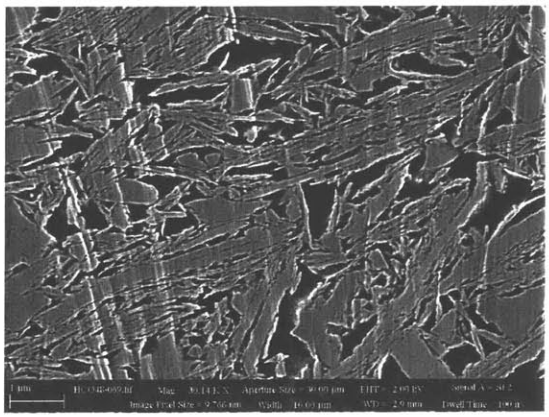

(e) RBBC 10 MPa

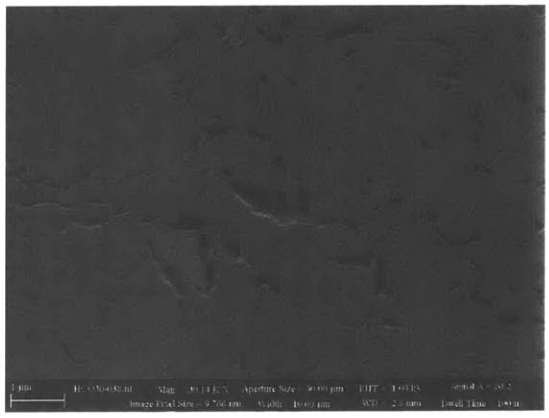

(f) RGOM-EI 10 MPa

Figure A-13: SEM Images from Deirieh (2015) for RBBC and RGOM-EI at different stress levels

Bibliography

Abdulhadi, N. O. (2009). *An Experimental Investigation into the Stress-Dependent Mechanical Behavior of Cohesive Soil with Application to Wellbore Instability.* PhD thesis, Massachusetts Institute of Technology, Cambridge, MA, USA.

Abdulhadi, N. O. and Barghouthi, A. F. (2012). Measurement of stiffness of rock from laboratory and field tests. *JEA Conference.*

Adams, A. L. (2011). Laboratory evaluation of the constant rate of strain and constant head techniques for measurement of the hydraulic conductivity of fine grained soils. Master's thesis, Massachusetts Institute of Technology, Cambridge, MA, USA.

Adams, A. L. (2014). *Permeability Anisotropy and Resistivity Anisotropy of Mechanically Compressed Mudrocks.* PhD thesis, Massachusetts Institute of Technology, Cambridge, MA, USA.

Alberty, M. W., McLean, M. R., et al. (2003). Emerging trends in pressure prediction. In *Offshore Technology Conference.* Offshore Technology Conference.

Andersen, G. (1991). *Physical Mechanisms Controlling the Strength and Deformation Behavior of Frozen Sand.* Thesis, Massachusetts Institute of Technology.

Ayres, A. and Theilen, F. (1999). Relationship between p-and s-wave velocities and geological properties of near-surface sediments of the continental slope of the barents sea. *Geophysical prospecting*, 47(4):431–441.

Bailey, W. (1961). Effects of salt on the shear strength of boston blue clay. Master's thesis, Massachusetts Institute of Technology, Cambridge, MA, USA.

Berman, D. R. (1993). Characterization of the engineering properties of boston blue clay at the mit campus. Master's thesis, Massachusetts Institute of Technology, Cambridge, MA, USA.

Betts, W. S. (2014). Compressibility and permeability of gulf of mexico mudrocks, resedimented and in-situ. Master's thesis, University of Texas at Austin, Austin, TX, USA.

Biot, M. (1962). Generalized theory of acoustic propagation in porous dissipative media. *The Journal of the Acoustical Society of America*, 34(9A):1254–1264.

Biot, M. A. (1956). Theory of propagation of elastic waves in a fluid-saturated porous solid. i. low-frequency range. *the Journal of the Acoustical Society of America*, 28(2):168–178.

Bowers, G. L. (1995). Pore pressure estimation from velocity data: Accounting for overpressure mechanisms besides undercompaction. *SPE Drilling and Completion*, 10(2):89–95.

Brignoli, E., Gotti, M., and Stokoe, K. H. (1996). Measurement of shear waves in laboratory specimens by means of piezoelectric transducers. *ASTM geotechnical testing journal*, 19(4):384–397.

Casey, B. A. (2011). The significance of specimen end restraint in high pressure triaxial testing of cohesive soil. Master's thesis, Massachusetts Institute of Technology, Cambridge, MA, USA.

Casey, B. A. (2014). *The Consolidation and Strength Behavior of Mechanically Compressed Fine-Grained Sediments.* PhD thesis, Massachusetts Institute of Technology, Cambridge, MA, USA.

Castagna, J., Batzle, M., and Kan, T. (1993). Rock physics–the link between rock properties and avo response, from: Offset-dependant reflectivity–theory and practice of avo analysis, published by the society of exploration geophysicists, edited by castagna. *J, and Backus, M.*

Castagna, J. P. and Backus, M. (1993). Avo analysis-tutorial and review. *Offset-dependent reflectivity: theory and practice of AVO analysis*, pages 3–36.

Castagna, J. P., Batzle, M. L., and Eastwood, R. L. (1985). Relationships between compressional-wave and shear-wave velocities in clastic silicate rocks. *Geophysics*, 50(4):571–581.

Cauble, D. (1996). *An Experimental Investigation of the Behavior of a Model Suction Caisson in a Cohesive Soil.* PhD thesis, Massachusetts Institute of Technology, Cambridge, MA, USA.

Cho, W. and Finno, R. J. (2010). Stress-strain responses of block samples of compressible chicago glacial clays. *Journal of Geotechnical and Geoenvironmental Engineering*, 136(1):178–188.

Cho, Y. and Mandai, Y. (1995). Dynamic measurement of capacitance variation of piezoelectric ceramics with stress. *Japanese journal of applied physics*, 34(3R):1591.

Chopra, S. and Huffman, A. R. (2006). Velocity determination for pore-pressure prediction. *The Leading Edge*, 25(12):1502–1515.

Claerbout, J. F. and Green, I. (2008). *Basic earth imaging.* Citeseer.

Clayton, C. (2011). Stiffness at small strain: research and practice. *Géotechnique*, 61(1):5–37.

Da Re, G. (2000). *Physical mechanisms controlling the pre-failure stress-strain behavior of frozen sand.* Thesis, Massachusetts Institute of Technology.

Day-Stirrat, R. J., Schleicher, A. M., Schneider, J., Flemings, P. B., Germaine, J. T., and van der Pluijm, B. A. (2011). Preferred orientation of phyllosilicates: Effects of composition and stress on resedimented mudstone microfabrics. *Journal of Structural Geology*, 33(9):1347–1358.

Deirieh, A. (2015). *From Clay Slurries to Mudrocks: A Cryo-SEM investigation of the Development of the Porosity and Microstructure.* PhD thesis, Massachusetts Institute of Technology, Cambridge, MA, USA.

Del Grosso, V. A. (1974). New equation for the speed of sound in natural waters (with comparisons to other equations). *The Journal of the Acoustical Society of America*, 56(4):1084–1091.

Delage, P. and Lefebvre, G. (1984). Study of the structure of a sensitive champlain clay and of its evolution during consolidation. *Canadian Geotechnical Journal*, 21(1):21–35.

Dewhurst, D. N., Siggins, A. F., Raven, M. D., et al. (2002). Influence of pore pressure, composition and microstructure on the acoustic properties of shales. In *SPE/ISRM Rock Mechanics Conference*. Society of Petroleum Engineers.

Dewhurst, D. N., Siggins, A. F., Sarout, J., Raven, M. D., and Nordgård-Bolås, H. M. (2011). Geomechanical and ultrasonic characterization of a norwegian sea shale. *Geophysics*, 76(3):WA101–WA111.

Domenico, S. N. (1984). Rock lithology and porosity determination from shear and compressional wave velocity. *Geophysics*, 49(8):1188–1195.

d'Onofrio, A., Silvestri, F., and Vinale, F. (1999). A new torsional shear device. *ASTM geotechnical testing journal*, 22(2):107–117.

Dvorkin, J., Mavko, G., and Nur, A. (1995). Squirt flow in fully saturated rocks. *Geophysics*, 60(1):97–107.

Dvorkin, J. and Nur, A. (1993). Dynamic poroelasticity: A unified model with the squirt and the biot mechanisms. *Geophysics*, 58(4):524–533.

Dvorkin, J. and Nur, A. (1996). Elasticity of high-porosity sandstones: Theory for two north sea data sets. *Geophysics*, 61(5):1363–1370.

Dvorkin, J. P. (2008). Yet another vs equation. *Geophysics*, 73(2):E35–E39.

Ebrom, D., Mueller, M., Heppard, P., Shah, H., and Thomsen, L. (2002). Vsp-derived vp/vs ratios for pressure prediction ahead of the bit. In *64th EAGE Conference and Exhibition*.

Ellis, E., Soga, K., Bransby, M., and Sato, M. (2000). Resonant column testing of sands with different viscosity pore fluids. *Journal of geotechnical and geoenvironmental engineering*, 126(1):10–17.

Emmanuel, S., Anovitz, L. M., and Day-Stirrat, R. J. (2015). Effects of coupled chemo-mechanical processes on the evolution of pore-size distributions in geological media. *Rev Mineral Geochem*, 80:45–60.

Fahy, B. P. (2014). The influence of salinity on the mechanical behavior of high plasticity soils. Master's thesis, Massachusetts Institute of Technology, Cambridge, MA, USA.

Fawad, M., Mondol, N. H., Jahren, J., and Bjørlykke, K. (2011). Mechanical compaction and ultrasonic velocity of sands with different texture and mineralogical composition. *Geophysical Prospecting*, 59(4):697–720.

Ferreira, C., Fonseca, A., and Santos, J. A. (2007). Comparison of simultaneous bender elements and resonant column tests on porto residual soil. In Ling, H. I., Callisto, L., Leshchinsky, D., Koseki, J., and Gladwell, G., editors, *Soil Stress-Strain Behavior: Measurement, Modeling and Analysis*, volume 146 of *Solid Mechanics and Its Applications*, pages 523–535. Springer Netherlands. 10.1007/978-1-4020-6146-2-34.

Fioravante, V. and Capoferri, R. (2001). On the use of multi-directional piezoelectric transducers in triaxial testing. *Geotechnical Testing Journal (GTJ)*, 24(3):243–255.

Flores, R. D. V., Emidio, G. D., and Van Impe, W. F. (2010). Small-strain shear modulus and strength increase of cement-treated clay. *Geotechnical Testing Journal (GTJ)*, 33(1):1–10.

Freed, R. L. and Peacor, D. R. (1989a). Geopressured shale and sealing effect of smectite to illite transition. *AAPG bulletin*, 73(10):1223–1232.

Freed, R. L. and Peacor, D. R. (1989b). Variability in temperature of the smectite/illite reaction in gulf coast sediments. *Clay Minerals*, 24(2):171–180.

Gajo, A., Fedel, A., and Mongiovi, L. (1997). Experimental analysis of the effects of fluid-solid coupling on the velocity of elastic waves in saturated porous media. *Géotechnique*, 47(5):993–1008.

Gal, D., Dvorkin, J., and Nur, A. (1998). A physical model for porosity reduction in sandstones. *Geophysics*, 63(2):454–459.

Gardner, G., Gardner, L., and Gregory, A. (1974). Formation velocity and density-the diagnostic basics for stratigraphic traps. *Geophysics*, 39(6):770–780.

Gardner, G., Harris, M., et al. (1968). Velocity and attenuation of elastic waves in sands. In *SPWLA 9th Annual Logging Symposium*. Society of Petrophysicists and Well-Log Analysts.

Gassmann, F. (1951a). Elastic waves through a packing of spheres. *Geophysics*, 16(4):673–685.

Gassmann, F. (1951b). Elasticity of porous media. *Vierteljahrsschrder Naturforschenden Gesselschaft*, 96:1–23.

Germaine, J. T. (1982). *Development of the Directional Shear Cell for Measuring Cross Anisotropic Clay Properties*. PhD thesis, Massachusetts Institute of Technology, Cambridge, MA, USA.

Gist, G. (1994). Interpreting laboratory velocity measurements in partially gas-saturated rocks. *Geophysics*, 59:1100.

Grande, L., Mondol, N., et al. (2013). Geomechanical, hydraulic and seismic properties of unconsolidated sediments and their applications to shallow reservoirs. In *47th US Rock Mechanics/Geomechanics Symposium*. American Rock Mechanics Association.

Greenberg, M. and Castagna, J. (1992). Shear-wave velocity estimation in porous rocks: Theoretical formulation, preliminary verification and applications1. *Geophysical prospecting*, 40(2):195–209.

Gregory, A. (1976). Fluid saturation effects on dynamic elastic properties of sedimentary rocks. *Geophysics*, 41(5):895–921.

Han, D.-h., Nur, A., and Morgan, D. (1986). Effects of porosity and clay content on wave velocities in sandstones. *Geophysics*, 51(11):2093–2107.

Hardin, B. O. (1978). The Nature of Stress-Strain Behavior for Soils. In *From Volume I of Earthquake Engineering and Soil Dynamics–Proceedings of the ASCE Geotechnical Engineering Division Specialty Conference, June 19-21, 1978, Pasadena, California. Sponsored by Geotechnical Engineering Division of ASCE in cooperation with:*, pages 3–90. ASCE.

Hardin, B. O. and Blandford, G. E. (1989). Elasticity of Particulate Materials. *Journal of Geotechnical Engineering*, 115(6).

Hardin, B. O. and Richart Jr, F. (1963). Elastic wave velocities in granular soils. *Journal of Soil Mechanics & Foundations Div*, 89(Proc. Paper 3407).

Hemes, S., Desbois, G., Urai, J. L., Schröppel, B., and Schwarz, J.-O. (2015). Multi-scale characterization of porosity in boom clay (hades-level, mol, belgium) using a combination of x-ray μ-ct, 2d bib-sem and fib-sem tomography. *Microporous and Mesoporous Materials*, 208:1–20.

Heppard, P. and Ebrom, D. (2010). Compaction and overpressure in shales: Practice and theory.

Hofmann, R. (2006). *Frequency Dependent Elastic and Anelastic Properties of Clastic Rocks.* PhD thesis, Colorado School of Mines, Golden, CO, USA.

Holt, R. M., Bhuiyan, M. H., Kolstø, M. I., Bakk, A., Stenebraten, J. F., and Fjær, E. (2011). Stress-induced versus lithological anisotropy in compacted claystones and soft shales. *The Leading Edge*, 30(3):312–317.

Horan, A. J. (2012). The mechanical behavior of normally consolidated soil as a function of pore fluid salinity. Master's thesis, Massachusetts Institute of Technology, Cambridge, MA, USA.

Houben, M., Desbois, G., and Urai, J. (2014). A comparative study of representative 2d microstructures in shaly and sandy facies of opalinus clay (mont terri, switzerland) inferred form bib-sem and mip methods. *Marine and Petroleum Geology*, 49:143–161.

House, R. (2012). A comparison of the behavior of intact and resedimented boston blue clay. Master's thesis, Massachusetts Institute of Technology, Cambridge, MA, USA.

Hu, Y., Wenliang, M., and Zhaoba, W. (2015). A study of ultrasonic guided wave ndt technique based on peek rod. *compare*, 8(8).

Isenhower, W. M., Stokoe, K., and Allen, J. (1987). Instrumentation for torsional shear/resonant column measurements under anisotropic stresses. *ASTM International*, 10(4):183–191.

Iwasaki, T., Tatsuoka, F., and Takagi, Y. (1978). Shear moduli of sands under cyclic torsional shear loading. *Soils and Foundations*, 18(1):39–56.

Janbu, N. (1965). Consolidation of clay layers based on non-linear stress-strain. In *Proceedings 6th International Conference on Soil Mechanics and Foundation Engineering, Montreal*, volume 2, pages 83–87.

Jensen, E. H., Andersen, C. F., and Johansen, T. A. (2011). Estimation of elastic moduli of mixed porous clay composites. *Geophysics*, 76(1):E9–E20.

Johnson, S. M. (2011). Modeling a bender element test using abaqus finite element program. Master's thesis, Massachusetts Institute of Technology, Cambridge, MA, USA.

Kawaguchi, T. and Tanaka, H. (2008). Formulation of gmax from reconstituted clayey soils and its application to gmax measured in the field. *Soils and Foundations*, 48(6):821–831.

Kenney, T. C. (1964). Sea-Level Movements and the Geologic Histories of the Post-Glacial Marine Soils at Boston, Nicolet, Ottawa and Oslo. *Géotechnique*, 14(3):203–230.

Knight, R., Dvorkin, J., and Nur, A. (1998). Acoustic signatures of partial saturation. *Geophysics*, 63(1):132–138.

Krushin, J. (2014). Quantifying shale pore pressure by modeling the controls on compaction and porosity. *Interpretation*, 2(1):SB79–SB88.

Kuster, G. T. and Toksöz, M. N. (1974). Velocity and attenuation of seismic waves in two-phase media: Part i. theoretical formulations. *Geophysics*, 39(5):587–606.

Ladd, C. (1996). Nature of soil: II-2 soil structure and environmental effects. Massachusetts Institute of Technology Lecture for 1.361 Soil Mechanics.

Lambe, T. and Whitman, R. (1969). Soil mechanics. *New York*, 553.

Lambe, T. W. (1958). The engineering behavior of compacted clay. In *Proceedings of the American Society of Civil Engineers*, volume 84, page 35.

Lee, M. W. and Waite, W. F. (2009). *High-Frequency Normal Mode Propagation in Aluminum Cylinders*. US Geological Survey.

Leong, E. C., Cahyadi, J., and Rahardjo, H. (2009). Measuring shear and compression wave velocities of soil using bender-extender elements. *Canadian Geotechnical Journal*, 46(7):792–812.

Li, X. S. and Dafalias, Y. F. (2002). Constitutive modeling of inherently anisotropic sand behavior. *Journal of Geotechnical and Geoenvironmental Engineering*, 128(10):868–880.

Lohani, T., Imai, G., Tani, K., and Shibuya, S. (2001). g_{MAX} of fine-grained soils at wide void ratio range, focusing on time-dependent behavior. *SOILS AND FOUNDATIONS*, 41(5):87–102.

Losh, S., Walter, L., Meulbroek, P., Martini, A., Cathles, L., and Whelan, J. (2002). Reservoir fluids and their migration into the South Eugene Island Block 330 reservoirs, offshore Louisiana. *AAPG Bulletin*, 86(8).

March, A. (1932). Mathematische theorie der regelung nach der korngestah bei affiner deformation. *Zeitschrift für Kristallographie-Crystalline Materials*, 81(1):285–297.

Marion, D., Nur, A., Yin, H., and Han, D.-H. (1992). Compressional velocity and porosity in sand-clay mixtures. *Geophysics*, 57(4):554–563.

Marjanovic, J. (2012). The Study of Shear and Longitudinal Velocity Measurements of Sands and Cohesive Soils. S.M. Thesis, Massachusetts Institute of Technology, Cambridge, MA.

Marjanovic, J. and Germaine, J. T. (2013). Experimental study investigating the effects of setup conditions on bender element velocity results. *Geotechnical Testing Journal*, 36(2):1–11.

Mavko, G., Mukerji, T., and Dvorkin, J. (2003). *The Rock Physics Handbook: Tools for Seismic Analysis of Porous Media*. Stanford-Cambridge Program. Cambridge University Press.

Mavko, G. and Nur, A. (1975). Melt squirt in the asthenosphere. *Journal of Geophysical Research*, 80(11):1444–1448.

McBride, M. and Baveye, P. (2002). Diffuse double-layer models, long-range forces, and ordering in clay colloids. *Soil Science Society of America Journal*, 66(4):1207–1217.

Mesri, G. and Olson, R. E. (1971). Mechanisms controlling the permeability of clays. In *From Soil Behavior Fundamentals to Innovations in Geotechnical Engineering@ sHonoring Roy E. Olson*, pages 88–95. ASCE.

Miller, D., Plumb, R., and Boitnott, G. (2013). Compressive strength and elastic properties of a transversely isotropic calcareous mudstone. *Geophysical Prospecting*, 61(2):315–328.

Mitchell, J. (1993). *Fundamentals of soil behavior*. John Wiley and Sons Inc, New York.

Mitchell, J. K. (1956). *The importance of structure to the engineering behavior of clay*. PhD thesis, Massachusetts Institute of Technology, Cambridge, MA, USA.

Mondol, N. H., Bjørlykke, K., Jahren, J., and Høeg, K. (2007). Experimental mechanical compaction of clay mineral aggregates?changes in physical properties of mudstones during burial. *Marine and Petroleum Geology*, 24(5):289–311.

Mondol, N. H., Jahren, J., Bjorlykke, K., and Brevik, I. (2008). Elastic properties of clay minerals. *The Leading Edge*, 27(6):758–770.

Montoya, B. M., Gerhard, R., Dejong, J. T., Wilson, D. W., Weil, M. H., Martinez, B. C., and Pederson, L. (2012). Fabrication, Operation, and Health Monitoring of Bender Elements for Aggressive Environments. *ASTM geotechnical testing journal*, 35(5):728–742.

Mori, T. and Tanaka, K. (1973). Average stress in matrix and average elastic energy of materials with misfitting inclusions. *Acta metallurgica*, 21(5):571–574.

Muller, T. M., Gurevich, B., and Lebedev, M. (2010). Seismic wave attenuation and dispersion resulting from wave-induced flow in porous rocks — a review. *Geophysics*, 75(5):75A147–75A164.

Nishimura, S. (2005). *Laboratory Study on Anisotropy of Natural London Clay.* PhD thesis, Imperial College London, London, UK.

Olsen, H. W. (1962). Hydraulic flow through saturated clays. In *Proceedings of 9th National Conference on Clays and Clay Minerals*, volume 9, pages 131–161.

Pervukhina, M., Gurevich, B., Dewhurst, D. N., and Siggins, A. F. (2010). Applicability of velocity-stress relationships based on the dual porosity concept to isotropic porous rocks. *Geophysical Journal International*, 181(3):1473–1479.

Pestana-Nascimento, J. M. (1994). *A Unified Constitutive Model for Clays and Sands.* PhD thesis, Massachusetts Institute of Technology, Cambridge, MA, USA.

Pickett, G. R. et al. (1963). Acoustic character logs and their applications in formation evaluation. *Journal of Petroleum technology*, 15(06):659–667.

Prasad, M. (1988). *Experimental and theoretical considerations of velocity and attenuation interactions with physical parameters in sands.* PhD thesis, Kiel University.

Prasad, M. (2002). Acoustic measurements in unconsolidated sands at low effective pressure and overpressure detection. *Geophysics*, 67(2):405–412.

Prasad, M. and Meissner, R. (1992). Attenuation mechanisms in sands: Laboratory versus theoretical (biot) data. *Geophysics*, 57(5):710–719.

Rae, P. and Dattelbaum, D. (2004). The properties of poly (tetrafluoroethylene)(ptfe) in compression. *Polymer*, 45(22):7615–7625.

Rampello, S., Viggiani, G. M. B., and Amorosi, A. (1997). Small-strain stiffness of reconstituted clay compressed along constant triaxial effective stress ratio paths. *Géotechnique*, 47(3):475–489.

Raymer, L., Hunt, E., Gardner, J. S., et al. (1980). An improved sonic transit time-to-porosity transform. In *SPWLA 21st annual logging symposium.* Society of Petrophysicists and Well-Log Analysts.

Reynolds, R. T. and Germaine, J. T. (2007). Benefits and Pitfalls of Multistage Embankment Construction. In *7th FMGM 2007*, pages 1–12. American Society of Civil Engineers.

Roesler, S. K. (1979). Anisotropic shear modulus due to stress anisotropy. *Journal of the Geotechnical Engineering Division*, 105(7):871–880.

Santagata, M. C. (1998). *Factors Affecting the Initial Stiffness and Stiffness Degradation of Cohesive Soils.* PhD thesis, Massachusetts Institute of Technology, Cambridge, MA, USA.

Santagata, M. C., Germaine, J. T., and Ladd, C. C. (2005). Factors Affecting the Initial Stiffness of Cohesive Soils. *Journal of Geotechnical and Geoenvironmental Engineering*, 131(4):430–441.

Sarout, J. and Gueguen, Y. (September-October 2008). Anisotropy of elastic wave velocities in deformed shales: Part 1 âĂŤ experimental results. *Geophysics*, 73(5):D75–D89.

Sayers, C. M. and den Boer, L. D. (2011). Rock physics-based relations for density and S-velocity versus P-velocity in deepwater subsalt Gulf of Mexico shales. *The Leading Edge*, 30(12):1376–1381.

Schneider, J., Flemings, P. B., Day-Stirrat, R. J., and Germaine, J. T. (2011). Insights into pore-scale controls on mudstone permeability through resedimentation experiments. *Geology*, 39(11):1011–1014.

Scholey, G. K., Frost, J. D., Lo Presti, D. C. F., and Jamiolkowski, M. (1995). A review of instrumentation for measuring small strains during triaxial testing of soil specimens. *ASTM geotechnical testing journal*, 18(2):137–156.

Seah, T. H. (1990). *Anisotropy of resedimented Boston Blue Clay.* Thesis, Massachusetts Institute of Technology.

Sheahan, T. C. T. C. (1991). *An experimental study of the time-dependent undrained shear behavior of resedimented clay using automated stress path triaxial equipment.* Thesis, Massachusetts Institute of Technology.

Shearer, P. M. (2009). *Introduction to seismology.* Cambridge University Press.

Shibuya, S. (2000). Assessing structure of aged natural sedimentary clays. *Soils and Foundations*, 40(3):1–16.

Shibuya, S., Hwang, S., and Mitachi, T. (1997). Elastic shear modulus of soft clays from shear wave velocity measurement. *Geotechnique*, 47(3):593–601.

Shibuya, S., Mitachi, T., Yamashita, S., and Tanaka, H. (1995). Effect of sample disturbance on g_{max} of soils – a case study. *Prefailure Deformation of Geomaterials*, pages 77–82.

Shirley, D. J. and Hampton, L. D. (1978). Shear-wave measurements in laboratory sediments. *The Journal of the Acoustical Society of America*, 63(2):607–613.

Spencer, J. W. (1981). Stress relaxations at low frequencies in fluid-saturated rocks: Attenuation and modulus dispersion. *Journal of Geophysical Research: Solid Earth (1978–2012)*, 86(B3):1803–1812.

Sridharan, A. and Prakash, K. (1998). Liquid limits and fall cones: Discussion. *Canadian geotechnical journal*, 35(2):407–408.

Stein, S. and Wysession, M. (2003). *An Introduction to Seismology, Earthquakes, and Earth Structure.* Blackwell Pub.

Stump, B. B. and Flemings, P. B. (2002). Consolidation state, permeability, and stress ratio as determined from uniaxial strain experiments on mudstone samples from the eugene island 330 area, offshore louisiana. *MEMOIRS-AMERICAN ASSOCIATION OF PETROLEUM GEOLOGISTS*, pages 131–144.

Tatham, R. H. (1982). Vp/vs and lithology. *Geophysics*, 47(3):336–344.

Tosaya, C. A. (1982). *Acoustical properties of clay-dearing rocks.* PhD thesis, Stanford University.

Valle-Molina, C. (2006). *Measurements of Vp and Vs in dry, unsaturated and saturated sand specimens with piezoelectric transducers.* PhD thesis, THE UNIVERSITY OF TEXAS AT AUSTIN.

Van Der Hilst, R. (2004). Massachusetts Institute of Technology: MIT OpenCourseWare. Accessed 1 May, 2012, License: Creative Commons BY-NC-SA.

Voltolini, M., Wenk, H.-R., Mondol, N. H., Bjørlykke, K., and Jahren, J. (2008). Anisotropy of experimentally compressed kaolinite-illite-quartz mixtures. *Geophysics*, 74(1):D13–D23.

Vucetic, M. (1994). Cyclic threshold shear strains in soils. *Journal of Geotechnical engineering*, 120(12):2208–2228.

Vucetic, M. and Dobry, R. (1991). Effect of Soil Plasticity on Cyclic Response. *Journal of Geotechnical Engineering*, 117(1):89–107.

Wair, B., DeJong, J., and Shantz, T. (2012). Guidelines for estimating vs based on in-situ tests. Technical report, PEER Report 2012/08.

Wei, Z. (2009). *Nanoindentation behavior of clay minerals and clay-based nanostructured multilayers.* PhD thesis, Tsinghua University, China, 1994.

Winkler, K. W. and Nur, A. (1982). Seismic attenuation: Effects of pore fluids and frictional-sliding. *Geophysics*, 47(1):1–15.

Wissa, A. E., Christian, J. T., Davis, E. H., and Heiberg, S. (1971). Consolidation at constant rate of strain. *Journal of the Soil Mechanics and Foundations Division*, 97(10):1393–1413.

Wyllie, M., Gregory, A., and Gardner, G. (1958). An experimental investigation of factors affecting elastic wave velocities in porous media. *Geophysics*, 23(3):459–493.

Wyllie, M. R. J., Gregory, A. R., and Gardner, L. W. (1956). Elastic wave velocities in heterogeneous and porous media. *Geophysics*, 21(1):41–70.

Xu, S. and White, R. E. (1995). A new velocity model for clay-sand mixtures. *Geophysical prospecting*, 43(1):91–118.

Yamashita, S., Fujiwara, T., Kawaguchi, T., and Mikami, T. (2004). *International Parallel Test on the Measurement of Gmax Using Bender Elements Organized by TC-29.* Japanese Domestic Committee for TC-29.

Yao, Y.-P., Yamamoto, H., and Wang, N.-D. (2008). Constitutive model considering sand crushing. *Soils and foundations*, 48(4):603–608.

Yin, H., Nur, A., et al. (1992). Stress-induced ultrasonic velocity and attenuation anisotropy of rocks. In *SEG Technical Program Expanded Abstracts*, pages 1073–1076.

Youn, J.-U., Choo, Y.-W., and Kim, D.-S. (2008). Measurement of small-strain shear modulus gmax of dry and saturated sands by bender element, resonant column, and torsional shear tests. *Canadian Geotechnical Journal*, 45(10):1426–1438.

Zhou, W., Fan, D., Liu, Y., and Xie, H. (2011). Measurements of wave velocity and electrical conductivity of an amphibolite from southwestern margin of the tarim basin at pressures to 1.0 gpa and temperatures to 700ř c: comparison with field observations. *Geophysical Journal International*, 187(3):1393–1404.

Zimmer, M. A. (2003). *Seismic Velocities in Unconsolidated Sands: Measurements of Pressure, Sorting, and Compaction Effects.* PhD thesis, Stanford University, Stanford, CA, USA.